Universidad de Granada

Programa de Doctorado en Física y Matemática

PhilosophiæDoctor (PhD) Thesis

Multi-wavelength polarimetric studies of relativistic jets in active galactic nuclei

Carolina Casadio

Instituto de Astrofísica de Andalucía (CSIC)

Director:

Dr. José Luis Gómez Fernández

co-Director:

Dr. Juan Iván Agudo Rodríguez

Granada, 2016

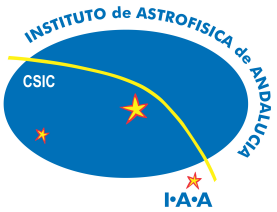

Editor: Universidad de Granada. Tesis Doctorales
Autora: Carolina Casadio
ISBN: 978-84-9125-910-7
URI: http://hdl.handle.net/10481/43886

Abstract

This Thesis is focussed on the study of relativistic jets, commonly present in multiple astrophysical sites, from active galactic nuclei (AGN), to micro-quasars or gamma-ray bursts (GRBs). In the case of AGN, huge amounts of energy across the whole electromagnetic spectrum are released as a consequence of the accretion of material onto a supermassive back hole (SMBH) lurking at their centers. The accretion leads to the formation of a pair of very powerful and highly collimated jets extending far beyond the size of the host galaxy.

We analyzed the correlation between the multi-wavelength emission and the radio jet in three powerful AGN, the radio galaxies 3C 120 and M 87, and the quasar CTA 102. The main goal of this Thesis is to obtain a better understanding of the jet dynamics and the role played by the magnetic field, and to determine what are the sites and mechanisms for the production of the γ-ray emission observed in these sources.

We have performed multi-wavelength studies of the radio galaxy 3C 120 and the blazar CTA 102 during unprecedented γ-ray flares for both sources. The NASA satellite *Fermi* registered in September-October 2012 a bright γ-ray flare in CTA 102, and between December 2012 and October 2014 a prolonged γ-ray activity in the radio galaxy 3C 120. In both studies, to determine where the γ-ray emission is produced, the analysis of *Fermi* data has been compared with a detailed study of the morphology and evolution of the parsec scale jet through a series of extremely-high angular resolution Very Long Baseline Array (VLBA) images at 43 GHz from the Boston University blazar monitoring program, in which our research group is actively participating. In the case of 3C 120 we have also collected 15 GHz VLBA data from the MOJAVE monitoring program, extending our study of the

radio jet from June 2008 to May 2014. For the study of CTA 102 a total of 80 VLBA images at 43 GHz have been analyzed and compared with observations across the whole electromagnetic spectrum between June 2004 and June 2014. These include observations at millimeter, near-infrared, and optical bands from observatories across the world, as well as ultraviolet and X-ray data from the *Swift* satellite.

Our multi-wavelength observations of 3C 120 and CTA 102 have revealed very similar properties during γ-ray events in both sources, despite representing very different classes of AGN. We found that in both sources the γ-ray flares are associated with the passage of knew superluminal components through the millimeter VLBI core, corresponding to the bright emission at the upstream end of the jet. But not all ejections lead to γ-ray emission; in fact bright superluminal components have been observed crossing the millimeter VLBI core without having a counterpart at γ-ray energies. We have found that in both sources γ-ray flares occurred only when the new component is moving in a direction closer to our line of sight. We located the γ-ray dissipation zone a short distance downstream of the radio core but outside of the broad line region, suggesting synchrotron self-Compton scattering as the probable mechanism for the γ-ray production. In addition, during the multi-wavelength outburst observed in CTA 102 the optical polarized emission displayed intra-day variability and a clear clockwise rotation of the polarization vectors, which we associated with the path followed by the component as it moves along helical magnetic field lines. These results have been reported in two papers published in high-impact peer-reviewed journals (Casadio et al., 2015a,b) that we present here in their original form.

The location of γ-ray activity close to the radio core and far from the black hole in both 3C 120 and CTA 102 implies that we need a mechanism to reaccelerate particle in situ; this leads to consider the core as a recollimation shock. Hence, it is important to understand the physics of recollimation shocks and what could be the related observational evidences.

For this purpose we have performed polarimetric studies of the jets in the radio galaxies 3C 120 and M 87 aimed to understand the nature of the

peculiar emitting regions known as C80 and HST-1, located hundreds of parsecs from the core of the jet. In Agudo, Gómez, Casadio, et al. (2012) we analyzed polarimetric VLBA observations at 5, 8, 12, and 15 GHz of the jet in 3C 120 revealing that the stationary component C80 corresponds to the peak emission of a larger and more extended emission structure in arc, downstream of which other moving components are observed. The agreement between our observations and numerical simulations led us to conclude that the emitting region C80 corresponds in fact to a recollimation shock located ∼190 pc from the core of the jet.

Interestingly, our observations of the peculiar structure HST-1 in the radio-galaxy M 87 revealed a similar structure to that observed in C80 of 3C 120; in Giroletti et al. (2012) we found that HST-1 corresponds to an extended emission structure in which new components appear to be released from the stationary upstream end of HST-1. It has been suggested that very high-energy emission has been originated in the HST-1 region. However, our new VLBA and JVLA observations of M 87 confirmed that HST-1 was in a low energy state between 2011 and 2013, ruling out its implication in the high energy flare in M 87 in March 2012, as we pointed out also in Hada et al. (2014).

Resumen

Esta Tesis está enfocada en el estudio de los jets relativistas, comúnmente presentes en numerosos escenarios astrofísicos, desde los núcleos de galaxias activas (AGN) hasta los microcuásares y las explosiones de rayos gamma (GRBs). En el caso de los AGN, observamos una gran cantidad de radiación emitida a lo largo de todo el espectro electromagnético, debida a la acreción de material por parte de un agujero negro supermasivo (SMBH) situado en el interior de estas galaxias. La acreción de material lleva a la formación de dos jets relativistas muy brillantes y bien colimados que se extienden mucho mas allá de la extensión de la propia galaxia.

Hemos analizados la correlación entre la emisión multi-frecuencia y el jet en radio en tres AGN muy brillantes: las radio galaxias 3C 120 y M 87 y el cuásar CTA 102. El objetivo principal de esta Tesis es obtener un mejor conocimiento de la dinámica de los jets y del papel jugado por el campo magnético, así como determinar cuáles son las regiones y los mecanismos de emisión involucrados en la producción de emisión a energías γ observadas en estas fuentes.

Hemos realizado estudios multi-frecuencia de la radio galaxia 3C 120 y del blazar CTA 102 en coincidencia con extraordinarios flares de rayos γ observados en ambas fuentes. El satélite *Fermi* de NASA ha registrado en septiembre-octubre 2012 un flare γ brillante en CTA 102 y, entre diciembre de 2012 y octubre de 2014, actividad γ prolongada en la radio galaxia 3C 120. En ambos estudios, a fin de determinar dónde se ha producido la emisión γ, el análisis de los datos de *Fermi* ha sido comparado con un estudio detallado de la morfología y evolución del jet a escala del parsec, a través de una serie de imágenes interferometricas a muy alta resolución angular

obtenidas con el Very Long Baseline Array (VLBA) a 43 GHz. Estas observaciones forman parte del Boston University blazar monitoring program, en el cuál colabora nuestro grupo de investigación. En el caso de 3C 120 hemos también coleccionado datos VLBA a 15 GHz desde el MOJAVE monitoring program, extendiendo así el estudio del jet en radio desde junio de 2008 a mayo de 2014. Respecto al estudio de CTA 102, hemos analizado un total de 80 imágenes a 43 GHz y las hemos comparado con datos a lo largo de todo el espectro electromagnético, cubriendo el periodo de observación desde junio de 2004 hasta junio de 2014. Éstos últimos incluyen observaciones a longitudes de ondas milimetricas, del infrarrojo cercano y en la banda óptica, obtenidas con diferentes observatorios alrededor del mundo así como datos a frecuencias ultravioleta y rayos X, obtenidos con el satélite *Swift*.

Nuestros estudios multi-frecuencia de 3C 120 y CTA 102 han revelado características muy similares en ambas fuentes durante los flares en rayos γ, de especial relevancia teniendo en cuenta que éstas fuentes representan clases muy distintas de AGN. Hemos encontrado que los flares γ en ambas fuentes están asociados con el paso de una nueva componente superlumínica a través del mm-VLBI core, correspondiente a la región mas brillante desde donde se extiende el jet. No obstante, no todas las eyecciones de componentes producen emisión en γ; de hecho hemos observado las eyecciones de nuevas componentes superluminicas sin una contrapartida en rayos γ. Hemos observado que en ambas fuentes la emisión en rayos γ se produce solamente cuando la nueva componente se mueve en una dirección cercana a nuestra linea de visión. Hemos determinado que la zona de emisión γ se produce a una pequeña distancia desde el core radio y lejos de la broad line region (BLR), y por ello sugerimos el proceso de scatterring synchrotron self-Compton (SSC) como el mecanismo más probable de producción de fotones γ. Por otra parte, durante el flare multi-frequencia observado en CTA 102, la emisión óptica polarizada muestra una variabilidad en escalas de horas y también una clara rotación de los vectores de polarización que asociamos al paso de la componente por la región de aceleración y colimación del jet en el que las lineas del campo magnético tienen una estructura helicoidal.

Estos resultados han sido presentados en dos artículos, publicados en una revista internacional con arbitraje y de alto factor de impacto (Casadio et al., 2015a,b), que se incluyen en esta Tesis en su formato original.

La localización de la actividad γ cerca del radio core y lejos del agujero negro tanto en 3C 120 como en CTA 102, implica que necesitamos un mecanismo de aceleración de partículas in situ; esto lleva a considerar el core como un choque de recolimación. Por lo tanto, es importante entender la física de los choques de recolimación y cuáles podrían ser las evidencias observacionales relacionadas con estos choques. A tal propósito hemos realizado estudios polarimétricos de los jets de las radio galaxias 3C 120 y M 87 para estudiar la naturaleza de las regiones de emisión conocidas como C80 y HST-1 y localizadas a cientos de parsec del core del jet. En Agudo, Gómez, Casadio, et al. (2012) hemos analizados observaciones VLBA polarimétricas a 5, 8, 12 y 15 GHZ del jet de 3C 120 que han revelado que la componente estacionaria C80 en realidad corresponde al pico de emisión de una región mas alargada y extensa con forma de arco, detrás de la cuál salen otras componentes que luego viajan a lo largo del jet. La concordancia entre nuestras observaciones y las simulaciones numéricas nos lleva a concluir que la región de emisión C80 corresponde efectivamente a un choque de recolimación situado a $\sim$190 pc desde el core del jet. Curiosamente, nuestras observaciones de la peculiar estructura HST-1 en la radio galaxia M 87 revelan una estructura similar a la que observamos en la componente C80 en 3C 120; en Giroletti et al. (2012) hemos encontrado que HST-1 corresponde a una región de emisión extensa en la que nuevas componentes parecen originarse desde el extremo estacionario de HST-1. Previos estudios han sugerido que algunos eventos de emisión a altas energías observados en M 87 tienen a HST-1 como origen. Sin embargo, nuestras nuevas observaciones con el VLBA y JVLA de M 87 confirman que, entre 2011 y 2013, HST-1 se encuentra en un estado de baja emisión que excluiría su implicación en el flare de alta energía observado en M 87 en marzo 2012, como también puntualizamos en Hada et al. (2014).

A mia madre

"Il mondo è nelle mani di coloro che hanno il coraggio di sognare e di correre il rischio di vivere i propri sogni. Ciascuno con il proprio talento."

Paulo Cohelo

Contents

List of Figures

LIST OF FIGURES

1 Introduction

1.1 Active Galaxies

Black holes (BH) are one of the greatest mysteries in astronomy. They exist in different sizes: stellar-mass black holes, the final product of a massive star explosion (supernovae), or supermassive black holes (SMBH) when they have a mass between 10^6 and 10^9 solar masses. SMBH are found in the center of galaxies, including our galaxy, but not all of them show signs of activity. Those galaxies hosting a SMBH and showing nuclear activity (see below) are called active galaxies and they are mentioned with the acronym AGN (Active Galactic Nuclei). The two largest subclasses of AGN are Seyfert galaxies and quasars. The main difference between these two subclasses is that the amount of radiation emitted by nuclear regions at visible wavelength is comparable to the energy emitted by all of the stars in the galaxy ($\sim 10^{11} M_{\odot}$) in Seyfert galaxies and greater by a factor of 100 or more in quasars. The luminosity coming from these bright nuclei cannot be explained by conventional nuclear fusion that powers stars.

The current understanding of AGNs is that their emission is produced by the accretion of material onto the black hole located in the center of the galaxy. Material

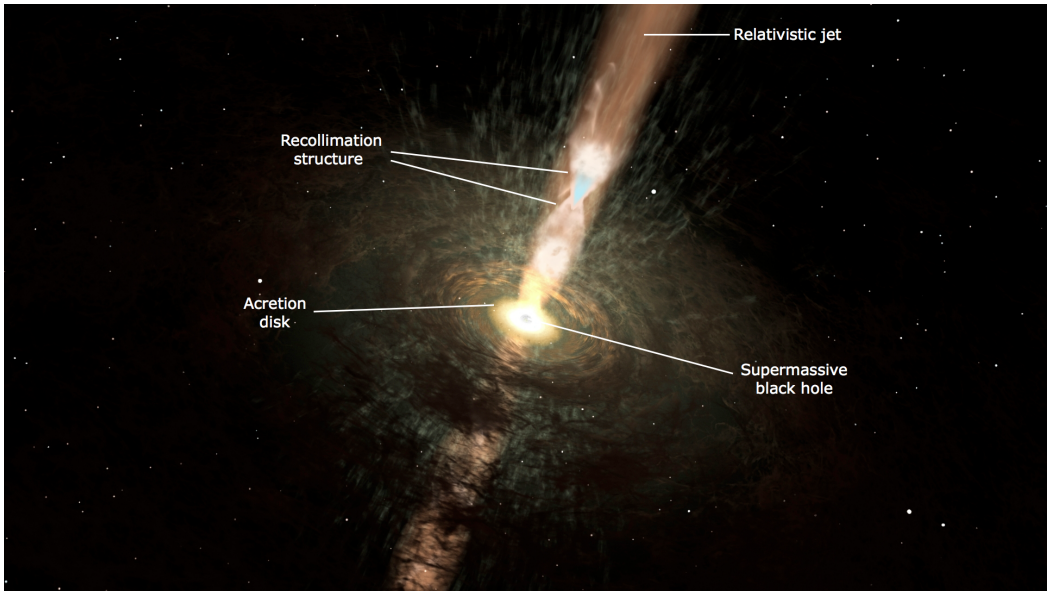

Figure 1.1: Artistic representation of the inner regions of an AGN. Credits: W. Steffen, UNAM & Cosmovision.

surrounding the black hole forms a rotating disk that gets heated through the viscous dissipation of gravitational energy and then radiates thermal emission mainly at UV and X-ray energies. In the case of *radio loud* AGN the accretion process also leads to the formation of well collimated jets of plasma perpendicular to the accretion disk (see Figure 1.1), with the radiative power of the jets being a significant fraction of the total bolometric luminosity of these AGN. The jets are launched from a rotating black hole or accretion disk and transport material at relativistic speeds to distances far beyond the size of the host galaxy (Blandford & Znajek, 1977; Blandford & Payne, 1982). Jets observed in *radio quiet* AGN instead are usually not so powerful and bright.

A useful criterion to distinguish between *radio loud* and *radio quiet* AGN is related to the ratio (R_{r-o}) of radio (at 6 cm) to optical (at 4400 Å) specific fluxes, being R_{r-o} in the range 10-100 for radio loud objects and $0.1<R_{r-o}< 1$ for radio quiet ones (Kellermann et al., 1989). Although this criterion leaves some doubts on the range of values 1-10 and nowadays astronomers consider $R_{r-o}>10$ for "radio-loudness" a reasonable criterion. Seyfert galaxies and radio quiet quasars belong to the *radio quiet* group, while radiogalaxies and blazars form the group of *radio loud* AGN. The characteristics of each of these class of objects are as follows:

- **Seyfert galaxies:** are spiral galaxies with luminous nuclei usually displaying slow, weak and poorly collimated flow. They are divided into two subclasses, type 1 Seyfert galaxies (Sy I) if they show broad (up to 10^4 km s^{-1}) and narrow (several 10^2 km s^{-1}) emission lines in their spectra, or type 2 Seyfert galaxies (Sy II) if they only show narrow emission lines;

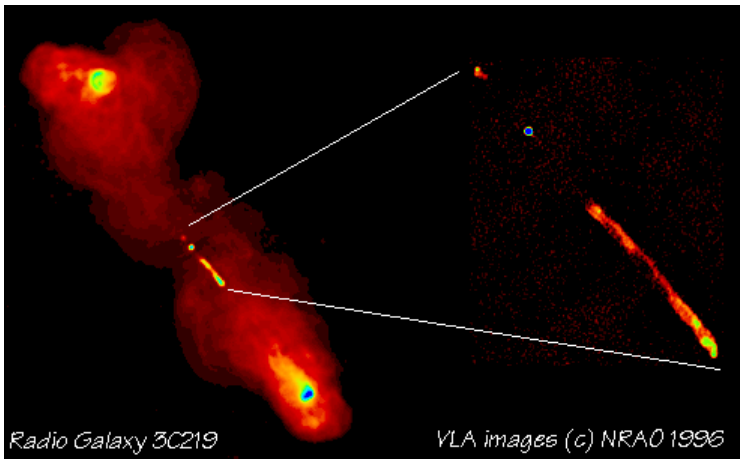

Figure 1.2: FRII radio galaxy. Radio images of the FR II radio galaxy 3C219. *Left:* VLA 1.4 + 1.6 GHz radio images superimposed. *Right:* VLA 8 GHz radio image. Credit: NRAO.

- **Quasars:** are the most luminous subclass of AGN and the objects that can be found at the farthest distances in the universe (the most distant quasar is at redshift 7.1). They are more compact than Seyfert galaxies and narrow lines in their spectra are generally absent or weaker than broad lines, while the opposite occurs in Seyfert;

- **Radiogalaxies:** are typically identified with giant elliptical galaxies, which are very bright at radio wavelength. Depending on their radio power, radio galaxies are divided into two subclasses, FRI and FRII radio galaxies (Fanaroff & Riley, 1974), where FR I show low 1.4 GHz radio power ($P_{1.4\ \mathrm{GHz}} < 10^{24.5}$ Watt/Hz) and FR II large radio power ($P_{1.4\ \mathrm{GHz}} > 10^{24.5}$ Watt/Hz). There are also differences in morphology between these two subclasses: FR II have powerful and well collimated jets that end in bright hot spots surrounded by luminous radio lobes, resulting from the interaction with the intergalactic medium (see Figure 1.2), while jets in FR I are usually less linear and they do not display bright radio

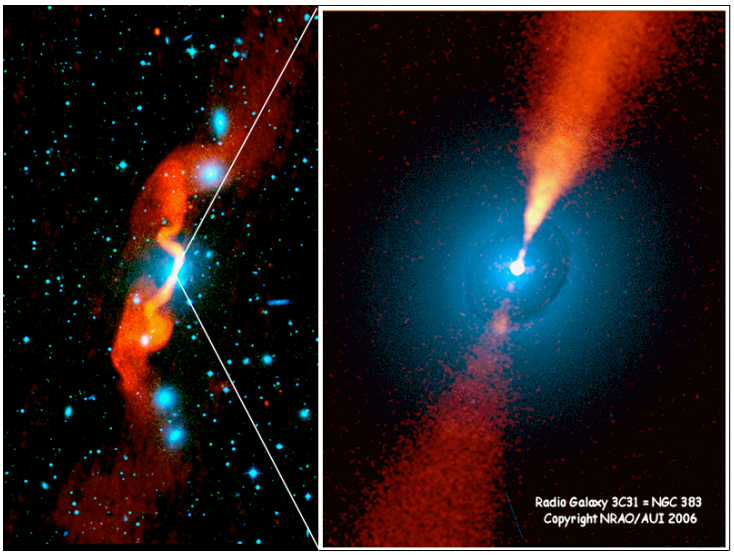

Figure 1.3: FRI radio galaxy. Superposition of an optical (blue) and radio (red) image of the FR I radio galaxy 3C31. The radio images have been taken with the VLA at a wavelength of 1.4 GHz (*left*) and 8.3 GHz (*right*). Credit: NRAO.

lobes at the end (see Figure 1.3). The collimation in FR II jets indicates an efficient transport mechanism of relativistic particles, whereas the dispersion and the darkened edge in FR I jets indicates slower relativistic particles that interact more with the surrounding medium and cool more rapidly. FRI radiogalaxies are usually broad line radio galaxies (BLRGs) while FR II only display narrow lines in their spectra (NLRGs). BLRGs and NLRGs are the radio loud analogs of Sy I and Sy II, respectively.

- **Blazars:** are bright, compact and highly variable AGN. They often display polarized emission at optical and radio frequencies. Variations in total and polarized flux range from less than a day to several months. Blazars get their name from the contraction of names of the two types of sources in which they are subdivided: BL Lacertae objects (BL Lacs) and Flat Spectrum Radio Quasars (FSRQ). BL Lacs are less luminous than FSRQs and they have weak or absent lines in their spectra, while FSRQs exhibit strong broad emission lines. They differ also in redshifts: BL Lacs objects tend to be located at smaller redshift ($z \lesssim 0.1$) than FSRQs ($z \gtrsim 0.5$).

1.2 The Unified Model

It was clear since the discovery of the first quasars that the identification and classification of a so wide variety of objects was quite complex. Kellermann (2013) provides some interesting historical details about the physics of quasars, highlighting how the different characteristics of these objects made their classification very confusing. Here we learn that the discovery of quasars was followed by an interesting finding: the optical counterparts of these objects were unusual blue.

In an attempt to find a correspondence between 'blue stellar objects' (BSOs) and the known radio sources, Alan Sandage (1926-2010) noticed that many BSOs had no radio source associated. He also estimated that those BSOs without a counterpart among known radio sources, that he called 'quasi-stellar galaxies' (QSGs), were about 10^3 times more compact than radio sources in the 3C catalog. He reported these findings in a paper sent to *The Astrophysical Journal* (ApJ) on 15 May of 1965. The Editor of the journal was so impressed that he delayed the other publications and he published the article in the 15 May issue, without sending it to a referee. This obviously caused some controversy within the astronomical community. Fritz Zwicky (1898 - 1974) in a letter to the editor (Zwicky, 1965) pointed out that:

> "All of the five quasi-stellar galaxies described individually by Sandage (1965) evidently belong to the subclass of compact galaxies with pure emission spectra previously discovered and described by the present writer."

In fact, Zwicky during the April 1963 meeting of the *American Astronomical Society* (AAS) reported that:

> "*Very compact galaxies* have been found.... The objects found form a continuos sequence of what appear to be detached red nuclei of galaxies, isolated in intergalactic space, to exceedingly compact blue objects, which show emission lines. Radio stars are thought as lying at the luminous end of this sequence" (Zwicky, 1963).

Unlike Sandage's paper, Zwicky's paper on the same subject was rejected by Subrahmanyan Chandrasekhar (1910-1995), the then editor of ApJ, who replied that : "Communications of this character are outside the scope of this journal."

Afterwards, T. Kinman working at Lick observatory and R. Lynds and C. Villere working at the Kitt Peak national observatory, suggested that most of the BSO objects

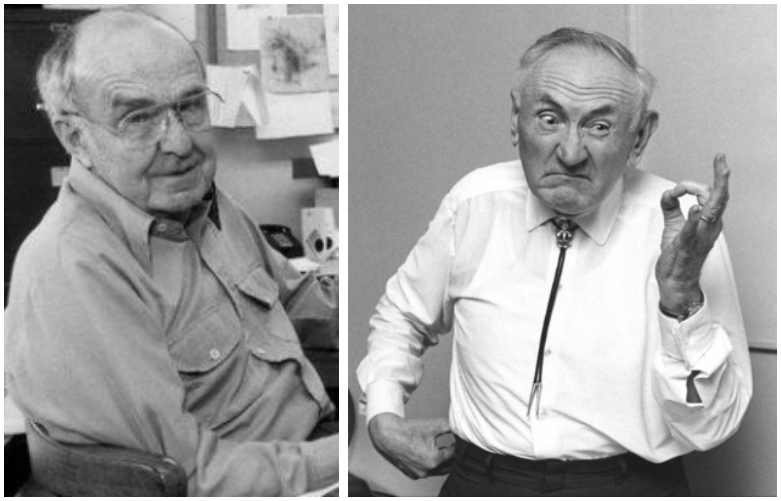

Figure 1.4: *Left:* Alan Sandage (courtesy: Carnegie Observatories) *Right:* Fritz Zwicky (courtesy: Caltech Archives)

discovered by Sandage were inside our Galaxy, not compact external galaxies. Nowadays we know that, apart from radio loud quasars, there is also a radio silent class of quasars (radio quiet).

The term 'quasar' was formally accepted by ApJ in 1970, when Maarten Schmidt, who was the first to observe a quasar (3C 273), wrote in his paper (Schmidt, 1970):

> "We use the term "quasar" for the class of objects of starlike appearance (or those containing a dominant starlike component) that exhibit redshifts much larger than those of ordinary stars in the Galaxy. QSOs are quasars selected on the basis of purely optical criteria, while QSSs are quasars selected on both the optical and radio criteria."

In the same paper we found a footnote from the Editor in which he reports:

> "The Astrophysical Journal has until now not recognized the term "quasar"; and it regrets that it must now concede: Dr. Schmidt feels that, with his precise definition, the term can no longer be ignored. – S. Chandrasekhar."

Since then, the term 'quasar' also started to populate scientific literature and subsequently many subclasses have been defined depending on observational properties, such as, for example, Low-Ionization nuclear emission line region (LINERS), Broad Absorption Line Quasars (BALQs) based on their optical spectra, or Flat Spectrum Radio Quasars (FSRQs) and Steep Spectrum Radio Quasars (SSRQs) based on their radio

spectra and morphology.

The latter classification depends strongly on the viewing angle of these objects. The emission coming from extended regions, such as that from lobes, dominates at lower frequencies, thus being responsible for the steeper spectrum when we see the extended part of the AGN. The observation of extended regions in AGN also depends on the viewing angle, as we are only able to observe these regions when the jet is oriented at a large viewing angle. If instead the jet points almost toward us, as the emission from the jet is beamed and particles move at relativistic speeds, it is subject to relativistic effects that amplify the emission itself (see § 2.2 for more details). In this case the emission from the jet, whose contribution is greater at higher radio frequencies, dominates over the extended part and the spectrum is flatter. Therefore, the slope of the radio spectrum is a first indication of the viewing angle.

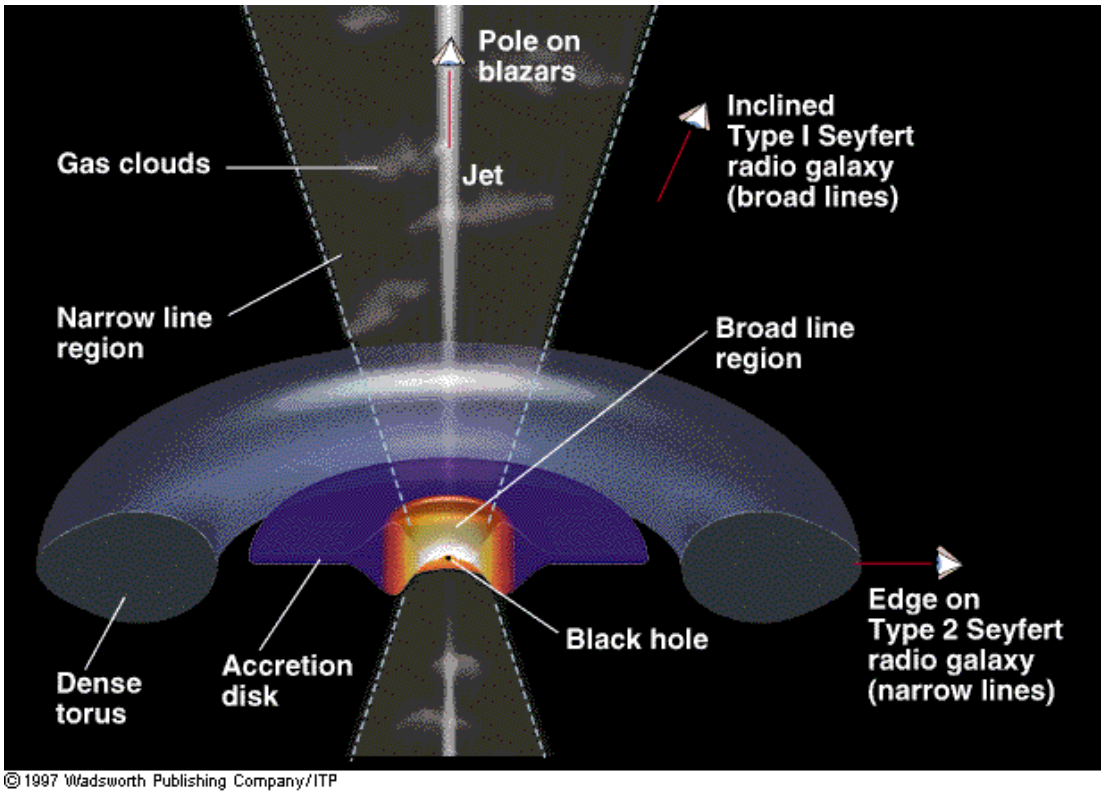

Figure 1.5: AGN model. Artistic representation of the unified AGN model. Credit: Wadsworth Publishing Company/ITP

Many other observational features in AGNs seem to depend on the viewing angle,

and it is exactly on the viewing angle that the "unified model" of AGNs is based, elaborated on by Robert Antonucci, Claudia Megan Urry and Paolo Padovani in the 90's (e.g., Antonucci, 1993; Urry & Padovani, 1995). This model unifies all the different types of AGN into a standard model in which the only physical parameter that can vary among them is the intrinsic power, while the other observational differences are explained in terms of obscuration and beaming that vary depending on the angle from which the observer sees the source. Figure 1.5 presents a schematic view of this model.

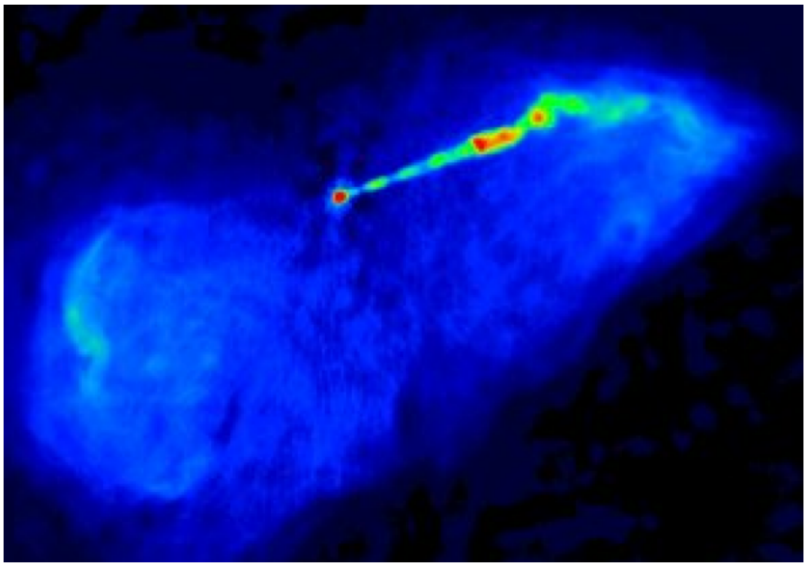

Figure 1.6: M 87. VLA image at 1.4 GHz of the radio galaxy M 87. The field of view in the image is of 5 Kpc. Credit: NRAO.

The responsible for obscuration is a molecular torus located at several parsecs from the black hole which partially absorbs the radiation emitted in the inner components and re-emits it in the infrared. Depending on the viewing angle at which we observe the AGN, the torus could hide some internal zones, such as a region of small clouds located at a distance of $\sim 10^{15}$–10^{18} cm (less then a parsec) from the black hole moving rapidly (1000-10,000 km s^{-1}), usually called the Broad Line Region (BLR). These clouds are in fact responsible for the broad emission lines directly observed in AGNs seen almost

face-on, or in polarized emission in those AGNs observed almost edge-on, as in this case the torus obscured the BLR. At a greater distance ($\sim$ 100 pc) there is another region where slower moving clouds produce narrower emission lines (300-500 km s^{-1}). According to the unified model, we have a Type 1 object when we observe at smaller viewing angles respect to the direction of the jet and we are able to see the BLR, while we see a Type 2 object when we observe at larger viewing angles and we only have a direct view of the Narrow Line Region (NLR).

Another phenomena, referred to as relativistic beaming, can change the observational properties of the AGN depending on its viewing angle. An example is the enhancement of the luminosity of the jet that points toward us, and the corresponding de-boosting of the jet pointing in the opposite direction which could be even undetectable if the viewing angle is small, as in the case of blazars, or quite large, as occurs in the radio galaxy M 87, in Figure 1.6. We will explain this effect and other relativistic effects relevant to the understanding of the physics of jets in AGNs in Chapter 2.2.

Research into AGN's not only provides knowledge of this type of objects, but also allows us to probe into extreme physics near black holes, to understand the jet formation mechanism and the production of high energy emission. This makes the study of AGN an excellent tool for understanding fundamental physics.

2

The physics of AGN jets

2.1 Emission processes

The non-thermal radio continuum emission observed in relativistic AGN jets is produced by synchrotron and inverse Compton processes. In this chapter we provide an overview of these two radiative processes and we discuss other aspects related to the physics of AGN jets that are necessary to understand the work contained in this Thesis. A more detailed description of the synchrotron and inverse Compton radiation processes can be found in Pacholczyk (1970), Rybicki & Lightman (1979) and Ghisellini (2013).

2.1.1 Synchrotron emission

According to classical electromagnetism, the power emitted by a charged particle (q) subjected to acceleration (a), is obtained from the Larmor formula:

$$P(t) = -\frac{dE}{dt} = \frac{2}{3}\frac{q^2}{c^3}a^2(t) = \frac{2}{3}\frac{q^2}{m^2c^3}\left(\frac{d\vec{p}}{dt}\right)^2 \tag{2.1}$$

where $\vec{p} = m\vec{v}$ is the particle momentum. We note that the emitted power depends

inversely on the square of the particle mass. This means that an electron or positron radiates $\sim 3\times10^6$ times more than a proton. For this reason we will focus our attention on electrons, indicating with m_e and e the mass at rest and the charge, respectively.

If the particle is relativistic ($v \approx c$) then the Lorentz factor $\gamma = 1/\sqrt{1-(v/c)^2}$ is greater than one and we need to consider the Lorentz transformations that relate quantities between two different reference frames. We know that the emitted power is Lorentz invariant, hence we can simply write:

$$P = P' = \frac{2}{3}\frac{e^2}{c^3}a'^2 = \frac{2}{3}\frac{e^2}{c^3}\left(a'^{\,2}_{\parallel} + a'^{\,2}_{\perp}\right) \tag{2.2}$$

where primed quantities refer to the rest frame of the particle and the other quantities to the observer's reference frame. In the above equation we have decomposed the acceleration in two terms, parallel and perpendicular to the direction of motion. These are Lorentz transformed as (Rybicki & Lightman, 1979):

$$a'_{\parallel} = \gamma^3 a_{\parallel} \tag{2.3}$$

$$a'_{\perp} = \gamma^2 a_{\perp} \tag{2.4}$$

Hence, we can write:

$$P = P' = \frac{2}{3}\frac{e^2}{c^3}\left(a'^{\,2}_{\parallel} + a'^{\,2}_{\perp}\right) = \frac{2}{3}\frac{e^2}{c^3}\gamma^4\left(\gamma^2 a^2_{\parallel} + a^2_{\perp}\right) \tag{2.5}$$

For an electron moving in a magnetic field ($\vec{B}$) the only acting force is the Lorentz force:

$$F_L = \frac{d}{dt}(\gamma m_e \vec{v}) = \frac{e}{c}\vec{v}\times\vec{B} = \frac{e}{c}vB\sin\phi \tag{2.6}$$

where ϕ is the *pitch angle*, that is the angle between the velocity vector and the magnetic field. It follows from the vectorial product that the only acting force is perpendicular to the magnetic field lines. Then the acceleration related to this force is also perpendicular to the magnetic field and is:

$$a_{\perp} = \frac{evB\sin\phi}{\gamma m_e c} \tag{2.7}$$

Substituting $a_{\perp}$ in the generalized Larmor formula (eq. 2.5) and considering $v \approx c$, we obtain the power emitted by an electron subject to the Lorentz force:

$$P_s(\phi) = \frac{2e^4}{3m_e^2c^3} B^2\gamma^2\beta^2\sin^2\phi \tag{2.8}$$

where the subscript "s" indicates the synchrotron emission process and β is equal to v/c. Knowing the formula for the electron energy ($E = \gamma \mathrm{m}_e \mathrm{c}^2$) we can insert it in the equation, obtaining:

$$P_s(\phi) = \frac{2}{3}\frac{e^4}{m_e^2c^3}\left(\frac{E}{m_ec^2}\right)^2 B^2\sin^2\phi \tag{2.9}$$

Using this notation we can immediately note that the power emitted is proportional to the squares of the electron energy and the magnetic field. Equation 2.9 is referred to a single electron with a pitch angle ϕ. When we deal with an ensemble of particles we can assume an isotropic distribution of pitch angles and average the term $\sin^2\phi$ over the solid angle, being 2/3. Then in the case of an ensemble of particles we simply replace $B^2\sin^2\phi$ with $\frac{2}{3}B^2$.

We can also write equation 2.8 introducing the Thomson scattering cross section, whose formula is:

$$\sigma_T = \frac{8\pi}{3}\left(\frac{e^2}{m_ec^2}\right)^2 = 6.65\times10^{-25}cm^2 \tag{2.10}$$

and obtaining for the emitted power by a single relativistic electron the following formula:

$$P_s(\phi) = 2c\sigma_T\gamma^2\beta^2\frac{B^2\sin^2\phi}{8\pi} = 2c\sigma_T\gamma^2\beta^2U_B \tag{2.11}$$

where insert $U_B{\equiv}B^2/8\pi$ that is the magnetic energy density.

For a non-relativistic particle, the pattern of the emitted power over the solid angle has the characteristics of a dipole, as plotted in Figure 2.1. In the relativistic case, we have a dipole radiation pattern only in the reference frame of the electron, where the electron itself is at rest.

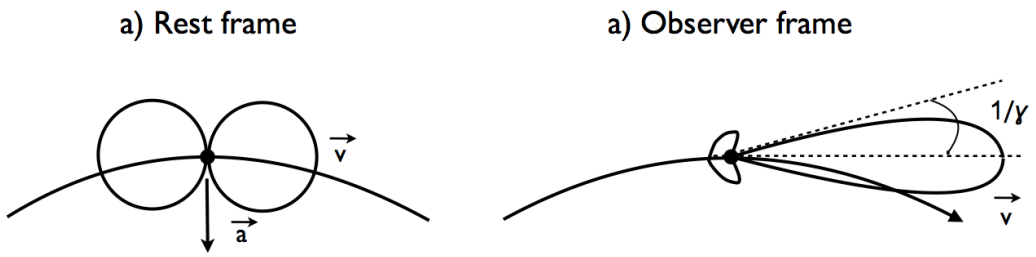

Figure 2.1: Angular distribution of the synchrotron radiation. Diagram showing a) the dipole radiation pattern from a non-relativistic accelerated particle (i.e., in the particle rest frame in the relativistic case), b) the dipole radiation pattern from a relativistic particle.

To obtain the angular distribution of radiation in the reference frame of the observer we need to transform the angles between the two reference frames through the relativistic formula of the aberration of light. We indicate with α and α' the angle in the observer and the electron reference frame, respectively, measured with respect to the velocity direction. These are related by (Ghisellini, 2013):

$$\sin\alpha = \frac{\sin\alpha'}{\Gamma(1+\beta\cos\alpha')}$$
$$\cos\alpha = \frac{\cos\alpha'+\beta}{1+\beta\cos\alpha'} \tag{2.12}$$

Only when β=0 the two angles are the same, in all the other cases α is smaller than α'. Note that, if α'=90°, we have $\sin\alpha = 1/\Gamma$ and $\cos\alpha = \beta$.

If we consider a semi-plane in the electron reference system (α'=$\pm$90°), for $\gamma \gg 1$ we have that $\beta \sim 1$ and then:

$$\alpha \approx \tan\alpha = \frac{1}{\gamma} \tag{2.13}$$

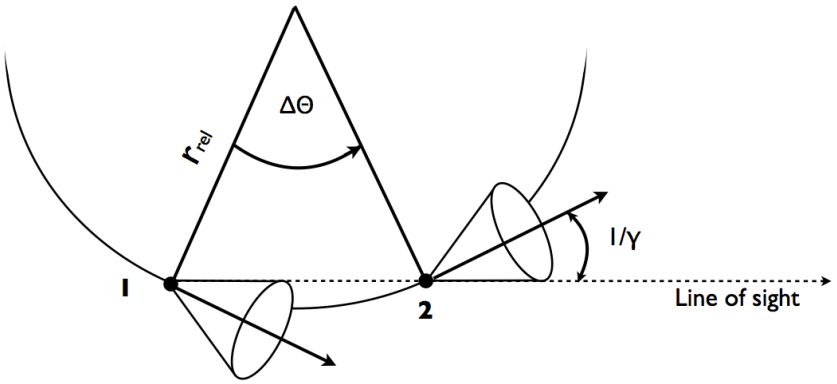

Figure 2.2: Pulse duration. A relativistic electron moving in a circular orbit around magnetic field lines with a pitch angle of 90°. Due to aberration the observer receives the emitted radiation only when the cone of semi-aperture $1/\gamma$ points toward him. The radiation received from a single electron is then in the form of pulses.

Therefore in the case of relativistic electrons almost half of the emitted radiation is concentrated in a cone of semi aperture $1/\gamma$ (Figure 2.1). It follows that, as the electron moves on its orbit around magnetic field lines, the observer receives the emitted radiation only when the cone points in his direction, as we observe in Figure 2.2. The emission of a single electron is then received in the form of pulses.

We use Figure 2.2 for a visual description of what happens when the relativistic electron follows its orbit and emits synchrotron radiation. Let us consider $\Delta\theta = 2/\gamma$ the aperture of the cone within which the radiation is emitted. When the electron is in position 1, the cone of emission starts to point toward the observer. The pulse stops when the electron is in position 2. From position 1 to 2 the electron moves by Δl, that is the length of the arc from point 1 to point 2. If we approximate the arc with the chord whose endpoints are points 1 and 2, we can write $\Delta l \approx \Delta\theta r_{rel}$. The radiation emitted in point 1 by the electron, reaches point 2 in $\Delta t_1 = \Delta l/c$, while the electron moves from point 1 to 2 in $\Delta t_2 = \Delta l/v$. Then, the effective duration of the pulse is:

$$\tau = \Delta t_2 - \Delta t_1 \approx \Delta\theta r_{rel}\left(\frac{1}{v} - \frac{1}{c}\right) = \frac{\Delta\theta}{\omega_{rel}}(1-\beta) \tag{2.14}$$

where $\omega_{rel} = v/r_{rel}$ is the frequency of gyration of the relativistic electron along its circular orbit. This is the duration of the pulse of a single emitting electron. Obviously, due to the huge amount of electrons present in a radio source, we do not observe this discontinuity because the sum of pulses emitted by electrons in different times makes the signal continuos in time.

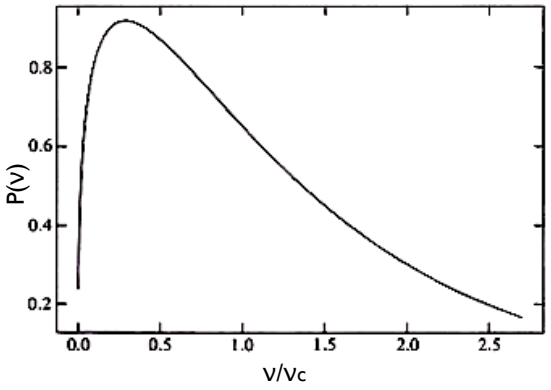

Figure 2.3: Synchrotron spectrum of a single electron. The power radiated by a single relativistic electron as a function of the critical frequency (ν_c). Reproduced from Hughes (1991).

For a non-relativistic motion, the gyration frequency ω_{rel} gives directly the frequency of the emitted radiation $\nu = 2\pi\omega_{rel}$. In the synchrotron case, the spectral distribution of the radiation is mainly concentrated around a *critical frequency* (ν_c), as we appreciate in Figure 2.3, where ν_c is related to the duration of the pulse (τ) and is (Pacholczyk, 1970):

$$\nu_c \sim \frac{1}{\tau} = \frac{3}{4\pi}\frac{eB\sin\phi}{m_e^3 c^5}E^2 \tag{2.15}$$

More specifically, the peak of the emission is centered at a frequency $\nu_p = \nu_c/3$. We note that the critical frequency is proportional to the square of the electron energy.

2.1.1.1 Emission from an ensemble of electrons

Now we discuss the case of an ensemble of relativistic electrons. Since the synchrotron process is a non-thermal process, the energy distribution of electrons does not follow a Maxwell-Boltzmann distribution.

We assume a *power law* energy distribution of relativistic electrons:

$$N(E)dE = N_0 E^{-p} dE \qquad (E_{min} \leq E \leq E_{max}) \tag{2.16}$$

This indicates the number of particles per unit volume between a minimum (E_{min}) and a maximum (E_{max}) values of energy. We introduce the *specific emissivity* j_ν, that is the power emitted per unit volume, per frequency interval, per steradian. The synchrotron emissivity of an ensemble of electrons is obtained integrating $N(E)dE$ times the power emitted by a single electron (eq. 2.9):

$$j_\nu d\nu = \int P_s(\nu, E) N(E) dE \tag{2.17}$$

where we have considered $E_{min} = 0$ and $E_{max} = \infty$, taking into account that at very low energies we have more electrons but contributing less to the emission and at higher energies we have less electrons but contributing more. The solution of the integral is found to be (Hughes, 1991):

$$j_\nu = c_5(\alpha) N_0 (B \sin\theta)^{\alpha+1} \left(\frac{\nu}{2c_{\gamma 1}}\right)^{-\alpha} \tag{2.18}$$

where $\alpha = \frac{p-1}{2}$ is the *spectral index* of the synchrotron radiation and both $c_5(\alpha)$ and $c_{\gamma 1}$ are constants. The angle θ here represents the direction between the magnetic field and the line of sight. Then we have that the emissivity and then the power emitted by an ensemble of electrons depend on N_0, on B and follows a power law that depends on $\nu^{-\alpha}$ where α in turn depends on the initial electrons energy density distribution. The assumed power law distribution of the electrons energy density leads to a power spectrum that is similar to what we observe in the case of an *optically thin* source, then the initial assumption is found valid in the case of synchrotron emission and usually, in AGN jets, "p" assumes values between 1 and 3.

The basics outline of the relativistic jet model in AGN can be find for example in Blandford & Königl (1979). Here the authors considered a conical relativistic jet that they assumed expanding adiabatically. With the adiabatic expansion the electron energy spectrum coefficient N_0 is observed to decrease radially along the jet as $N_0 \propto r^{-2(p+2)/3}$. Also the magnetic field in adiabatic expansion is observed to decrease with the distance; in particular the component of the magnetic field parallel to the jet flow scales as $B_{\parallel} \propto r^{-2}$ whereas the perpendicular component as $B_{\perp} \propto r^{-1}$. The dependence of N_0 and B with the distance along the jet in relation with equation 2.18 explain for example why do not observe emission at large distances from the core.

2.1.1.2 Synchrotron Self-Absorption

We consider the *specific intensity* I_ν, being the power emitted per unit area, per frequency interval, per steradian. If the source is *optcially thick*, the specific intensity entering the volume element $d_V = dsd\sigma$ of the source, may be reduced by absorption or scattering processes. In this case we need to solve the radiative transfer equation:

$$dI_\nu = j_\nu ds - k_\nu I_\nu ds \tag{2.19}$$

where the specific intensity gives by an infinitesimal element of length ds, j_ν, is reduced by $k_\nu I_\nu ds$, where k_ν is the *absorption coefficient* and $d\tau_\nu = k_\nu ds$ indicates the *optical depth*. When $\tau_s > 1$ the source is optically thick, meaning that it absorbs its own radiation, while for $\tau_\nu < 1$ is optically thin, the radiation can escape from the source without being absorbed. Dividing the previous equation by $d\tau_\nu$ we obtain:

$$\frac{dI_\nu}{d\tau_\nu} = S_\nu - I_\nu \tag{2.20}$$

where S_ν is the source function and is equal to $\frac{j_\nu}{k_\nu}$. To obtain the contribution of each infinitesimal element along our line of sight we have to ingrate the previous equation. The solution of the integral for an homogeneous source is (Pacholczyk, 1970):

$$I_\nu(\tau_\nu) = S_\nu(1 - e^{-\tau_\nu}) \tag{2.21}$$

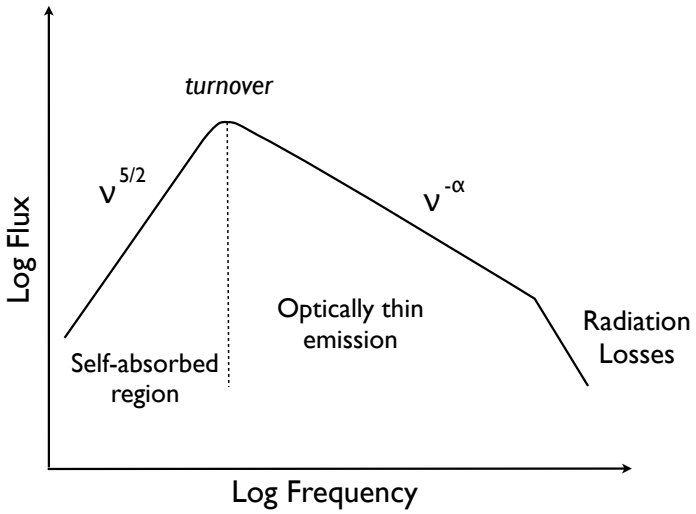

Figure 2.4: Synchrotron spectrum. A plot representing the synchrotron spectrum in the case of a partially self-absorbed source.

For an optically thick source ($\tau_\nu \gg 1$) we have $I_\nu(\tau_\nu) = S_\nu \equiv \frac{j_\nu}{k_\nu}$.

We already found the solution for the specific emissivity, j_ν, then now we need to know the solution for the absorption coefficient, k_ν, in order to have the specific intensity from an optically thick source. The solution for k_ν is found to be (Pacholczyk, 1970):

$$k_\nu = c_6 N_0 (B \sin\theta)^{\frac{p+2}{2}} \nu^{\frac{-(p+4)}{2}} \left[1 \pm \frac{p + 10/3}{p+2}\right] \tag{2.22}$$

where c_6 is a constant. Given the frequency dependences of j_ν and k_ν as found in equations 2.18 and 2.22, respectively, we obtain the following frequency dependence for the specific intensity when $\tau_\nu \gg 1$:

$$I_\nu(\tau_\nu) \propto \nu^{5/2} \tag{2.23}$$

In Figure 2.4 we display the synchrotron spectrum of a partially absorbed source where we appreciate the frequency dependences found in case of optically thick and optically thin regimes. The frequency at which we have the transition between the two regimes

is called the *turnover frequency* and produces a low-frequency cutoff of the spectrum, meaning that if we observe at higher frequencies we have less absorption and we can see deeper into the source.

The optically thin part of the spectrum (Figure 2.4) shows a steepening at higher frequencies due to radiative losses of the most energetic electrons that cool more rapidly since energy losses for synchrotron process are proportional to the square of the electron energy, as seen in equation 2.9.

The dependence of k_ν with N_0 and B that, as seen previously, decrease both along the jet due to adiabatic expansion, indicates that the emission is more absorbed close to the core than at large distances. Moreover, the exponential dependence with ν of the absorption coefficient suggests that higher frequency emission is less absorbed, meaning that we need to observe at high frequency to probe deeper in the formation regions.

2.1.1.3 Polarization

One of the distinguishing features of synchrotron radiation is that it exhibits detectable linear polarization. To investigate this, we consider first the case of the *cyclotron radiation*, produced by a non-relativistic electron on a circular orbit around magnetic field lines (Fig. 2.5, *left panel*). Observing along the orbital plane, the radiation is completely linearly polarized with the electric vector oscillating perpendicular to the magnetic field line. Observing along the direction of the magnetic field, the radiation is instead completely circularly polarized. If the electron moves at relativistic speed we have shown in § 2.1.1 that the radiation is beamed along the direction of motion in a cone of semi aperture $1/\gamma$ (Fig. 2.5, *right panel*) . In this case the two components of circular polarization, being oriented in opposite directions (right and left hand), will cancel each other out, whereas the linear polarization will survive.

In the case of an optically thin homogeneous source without Faraday rotation and considering a power law energy distribution of electrons such as that in eq. 2.16, the degree of linear polarization, defined as the ratio between the polarized signal over the total intensity, is (Pacholczyk, 1970):

$$\Pi = \frac{P}{I} = \frac{3p+3}{3p+7} \tag{2.24}$$

From the observed spectral indices we estimate that $2 < p < 3$, implying a maximum

theoretical linearly polarized flux of almost 70% (Hughes, 1991). Moreover, any disordering of the magnetic field reduces the degree of polarization, since different orientations of magnetic field lines produce polarization vectors oriented in different directions that cancel each other out. We note that the degree of polarization is independent of frequency and this is true also for optically thick sources, although in that case the degree of polarization is less than in optically thin sources and can be expressed as follows (Pacholczyk, 1970):

$$\Pi = \frac{3}{6p + 13} \tag{2.25}$$

that, for typical values of p, is only $\sim$10%.

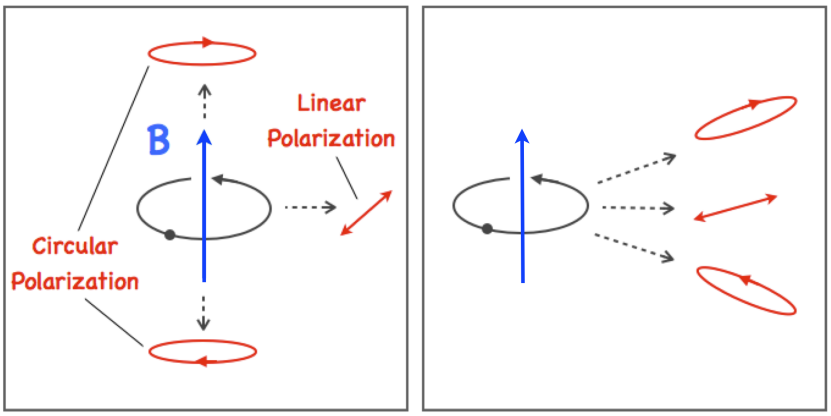

Figure 2.5: Polarization. *Left:* The case of cyclotron radiation. In red we have the polarized emission perceived by the observer from different orientations. *Right:* The case of synchrotron radiation, where the emission is concentrated in a cone of semi-aperture $1/\gamma$. Blue and red lines indicate the same as in *left panel*.

Synchrotron radiation may provide a small amount of circular polarization in the most compact regions of radio jets, observed usually close to the synchrotron self-absorbed jet cores with degrees of polarization that range between 0.3% and 1% (Homan & Wardle, 1999; Homan et al., 2001).

The polarization properties of an electromagnetic wave are usually characterized in terms of four parameters introduced by Sir George Stokes in 1852. The Stokes parameters are related to the amplitudes of the components of the electric field, E_x and

E_y, in the plane perpendicular to the direction of propagation of the electromagnetic wave. Thus, if E_x and E_y are represented respectively by $\epsilon_x(t)\cos(2\pi\nu t+\delta_x(t))$ and $\epsilon_y(t)\cos(2\pi\nu t+\delta_y(t))$, where ϵ_x and ϵ_y are the amplitude of the vibrations while $\delta_x(t)$ and $\delta_y(t)$ are the phases, the Stokes parameters are defined as follows:

$$\begin{aligned} I &= \langle\epsilon_x^2(t)\rangle + \langle\epsilon_y^2(t)\rangle \\ Q &= \langle\epsilon_x^2(t)\rangle - \langle\epsilon_y^2(t)\rangle \\ U &= 2\langle\epsilon_x(t)\epsilon_y(t)\cos(\delta_x(t)-\delta_y(t))\rangle \\ V &= 2\langle\epsilon_x(t)\epsilon_y(t)\sin(\delta_x(t)-\delta_y(t))\rangle \end{aligned} \tag{2.26}$$

where the angular brackets denote the average in time. Of the four Stokes parameters, I represents the total intensity, Q and U measure the linearly polarized intensity and V represents the circularly polarized component. Combining the Stokes parameters we obtain the following physical parameters of the polarized signal:

$$\Pi_L = \frac{\sqrt{Q^2+U^2}}{I} \tag{2.27}$$

$$\Pi_C = \frac{V}{I} \tag{2.28}$$

$$\Pi = \frac{\sqrt{Q^2+U^2+V^2}}{I} \tag{2.29}$$

$$\chi = \frac{1}{2}\arctan\left(\frac{U}{Q}\right) \tag{2.30}$$

where Π_L, Π_C and Π are the degrees of linear, circular and total polarization respectively, and χ is the position angle of the plane of linear polarization, or more commonly the electric vector position angle (EVPA), since it indicates the direction of the oscillation plane of the electric field. This is always perpendicular to the magnetic field and to the direction of propagation of the electromagnetic wave. However, when we try to infer the direction of the magnetic field in the emitting source from the observed direction of the EVPAs we have to consider that we are dealing with different reference frames (the observer and the source frames). Therefore, we have to consider the relativistic Lorentz transformations which establish that the components of the magnetic

field perpendicular and parallel to the velocity vector of the plasma transform in different ways (e.g. Blandford & Königl, 1979; Lyutikov et al., 2005). This implies that the orientation of the magnetic field in the emitting source could be different from what we measure in our reference frame.

2.1.1.4 Faraday Rotation

Faraday rotation of the polarization angle occurs when the electromagnetic wave propagates through a magnetized plasma, as for example the thermal plasma in the environment of the inner regions of relativistic jets. The linearly polarized electromagnetic wave can be constructed via a superposition of right and left hand circularly polarized waves of equal amplitudes which propagate with different velocities when they cross the magnetized plasma, causing a rotation in the plane of linear polarization by:

$$\Delta\chi = RM\lambda^2 \tag{2.31}$$

where λ is the wavelength of the electromagnetic wave and RM is the rotation measure defined as (Gabuzda et al., 2015):

$$RM = \frac{e^3}{8\pi^2\epsilon_0 m_e^2 c^3}\int n_e B_{\parallel}\, dl \quad [\text{rad m}^{-2}] \tag{2.32}$$

where e is the electron charge, m_e the electron mass, n_e the electron density, ϵ_0 the dielectric constant of the medium, c the speed of light and $B_{\parallel}$ is the component of the magnetic field along the line of sight. Therefore, the observed EVPAs (χ) affected by Faraday rotation can be expressed as $\chi = \chi_0 + \Delta\chi$, where χ_0 is the intrinsic value of the EVPAs in the source. Due to the dependence of $\Delta\chi$ on the square of the wavelength, in order to obtain the rotation measure values it is necessary to measure χ over a range of frequencies , as we observe in Figure 2.6.

The Faraday rotation can be produced inside or outside of the emitting region, in the interstellar or intergalactic medium between the source and the observer. External Faraday rotation follows the λ^2 law (see Figure 2.6), while internal Faraday rotation can deviate from this (e.g. Gómez et al., 2008; Wardle, 2013). If the Faraday rotation is internal to the emitting source the electromagnetic waves coming from the farthest parts

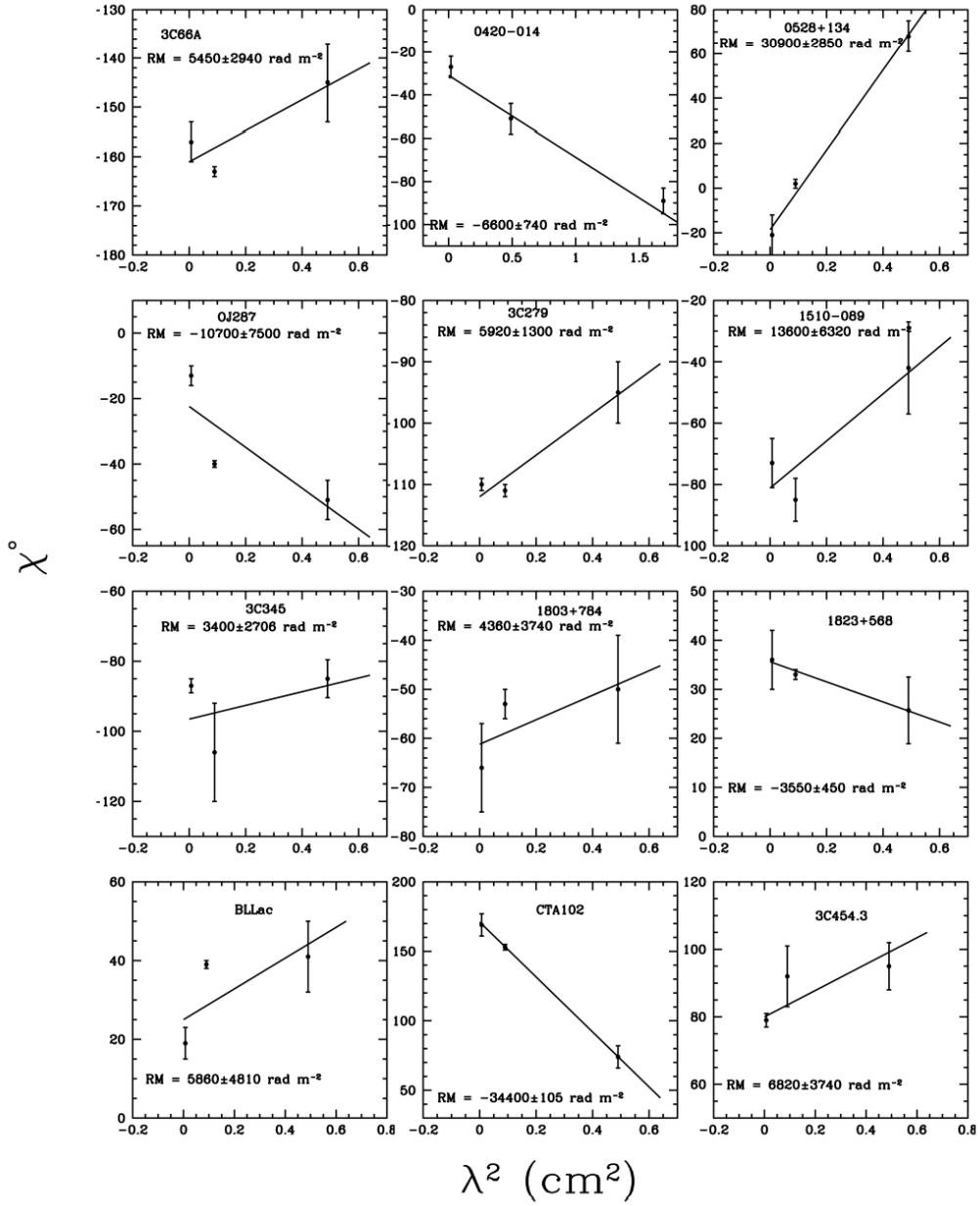

Figure 2.6: Rotation measure determinations of a sample of AGNs. The ordinate axis reports the measured EVPAs and the abscissa the values of the squared wavelengths of observations. The slope of the solid line gives the value of the estimated RM for each source. The image is reproduced from Jorstad et al. (2007)

of the source rotate more than those coming from parts closer to the observer, producing a partial cancelation between each other. The net effect can be a depolarization of the signal and a consequent deviation from the λ^2 law.

2.1.2 Inverse Compton process

The inverse Compton process involves the scattering of low energy photons to high energies by relativistic electrons so that the photons gain and the electrons lose energy. The term *inverse* distinguishes this process from the *direct* Compton scattering, in which the electron gains energy during the collision while the photon loses part of its energy. During this process the photon can gain sufficient energy to pass from frequencies in the optical to X-rays and γ-ray energies if the relativistic electron is sufficiently energetic. Depending on the photon energy in the rest frame of the electron we can distinguish between two scattering cross sections and therefore between two regimes: the *Thomson* and the *Klein-Nishina* regimes. When the energy of the incoming photon in the rest frame of the electron is smaller than the rest mass energy of the electron ($h\nu \ll m_e c^2$) we are in the Thomson regime; in the opposite case ($h\nu \gg m_e c^2$) we are in the Klein-Nishina regime. This is the same as saying that in the classical limit of the problem, when $\lambda \gg \lambda_c$, where λ_c is the *Compton wavelength* and is defined by (Rybicki & Lightman, 1979):

$$\lambda_c \equiv \frac{h}{mc} = 0.02426\,\text{Å} \quad (\text{for electrons}) \tag{2.33}$$

we are in the Thomson regime; otherwise we have to consider the quantum approach of the Klein-Nishina regime. The principal effect in the Klein-Nishina regime is the reduction of the scattering cross section with respect to the classical value, leading to a lower probability of scatter than in the classical case, although in this case the recoil of the electron is not negligible and the electron loses most of its energy during the collision. Due to the low probability of having Klein-Nishina interactions the quantum effects on the inverse Compton process are usually neglected in the study of the spectral evolution of relativistic electrons in jets.

2.1.2.1 Thomson regime

In the rest frame of the electron the scattering is closely elastic and we can assume that there is no change in the photon energy. But, this is not true in the observer rest frame where, in the collision, the photon gains energy and its final energy ranges between $x/4\gamma^2$ and $4\gamma^2 x$, where x is the energy of the photon before the collision (see for example Ghisellini, 2013). The maximum gain occurs when the angle between the electron velocity and the incoming photon is π (*head-on collision*) and the minimum gain occurs when the angle is $0°$, meaning that the photon comes from behind (*tail-on collision*). Considering an isotropic distribution of incoming photons, the mean photon energy after the scattering is $\frac{4}{3}\gamma^2 x$.

The energy loss rate of electrons during the scattering in the Thomson regime is given by (Rybicki & Lightman, 1979):

$$P_c = \frac{dE}{dt} = \frac{4}{3}\sigma_T c \gamma^2 \beta^2 U_{ph} \tag{2.34}$$

where σ_T is the Thomson scattering cross section and U_{ph} is the initial photon energy density.

There are many analogies among the energy loss rate of electrons due to synchrotron and inverse Compton processes, as we observe from eq. 2.11 and 2.34. If in eq. 2.34 we replace U_{ph} with U_B, the magnetic energy density, we obtain eq. 2.11. Then if electrons travel in a medium with some radiation and magnetic fields, they will emit both for the synchrotron and the inverse Compton process.

Another analogy is the spectral distribution of photons after the inverse Compton scattering and that one resulting from the synchrotron process. If we consider an initial power law distribution for the population of relativistic electron, as that in eq. 2.16, the spectral distribution of photons after the scattering will be again a power law with spectral index $\alpha = (p-1)/2$, as occurs in the synchrotron process for optically thin emission.

2.1.3 The SED

The spectral energy distribution (SED) of most radio loud AGNs has the typical double-hump form as that shown in Figure 2.7.

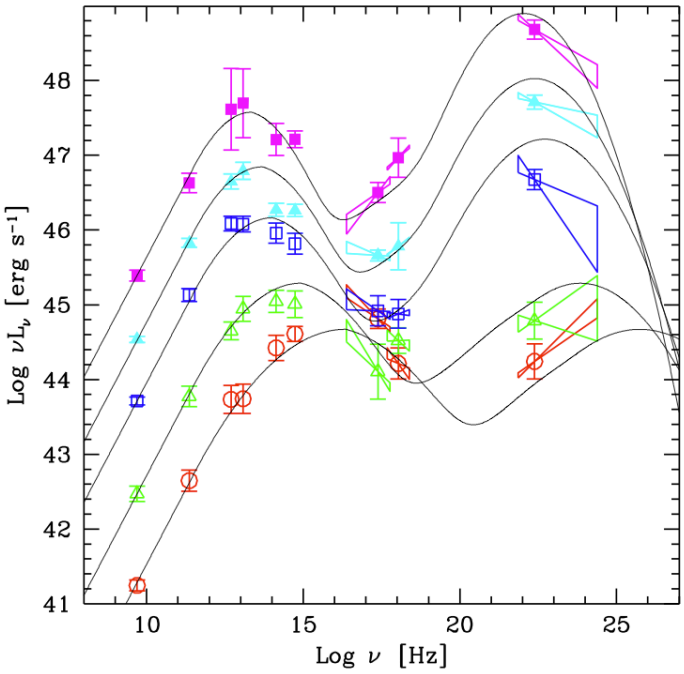

Figure 2.7: Blazar Sequence. The spectral blazar sequence as reported in Donato et al. (2001) and adapted from Fossati et al. (1998).

The first peak falls in the range of mm and soft X-ray frequencies and the second one at γ-ray frequencies, in the MeV-TeV energy range. The first hump is produced by the synchrotron process and the second hump by the inverse Compton scattering of the same photons produced by synchrotron emission (*Synchrotron Self Compton, SSC*) or the inverse Compton scattering of an external photon field (*External Compton, EC*). The candidates for the external photon field are the accretion disk (e.g. Dermer et al., 1992), the broad line region (e.g. Sikora et al., 1994), the dusty torus (e.g. Tavecchio et al., 2011) or a relatively slow sheath surrounding the jet (e.g. Marscher et al., 2010).

The series of SEDs reported in Figure 2.7 represent the spectral sequence of blazars and, as noted by Fossati et al. (1998), when the luminosity increases the two peaks shift to lower frequencies and the high energy peak becomes more prominent. This sequence also marks the difference between the more powerful FSRQs, that are represented by the SEDs at higher luminosities in Figure 2.7, and BL Lacs, less powerful, represented by SEDs at lower luminosities. This differentiation was interpreted by Ghisellini et al. (1998) as due to a more severe cooling suffered by FSRQs than by BL Lacs. FSRQs are

more powerful sources than BL Lacs and electrons suffer a stronger inverse Compton cooling due to the presence of external photon fields (disk, BLR and molecular torus) observed in FSRQs and not in BL Lacs. Hence, typical electron energies in FSRQs are smaller than in BL Lacs and the second peak, due to the Compton scattering, is more prominent.

2.2 Relativistic effects in jets

Special relativity teaches us that lengths and times measured in two different reference frames differ from each other. If we measure a ruler when it is at rest and when it is moving we find that the ruler is shorter when it is moving and the opposite effect is observed in the case of intervals of time, which are longer when the reference frame is moving.

Furthermore, if we measure distances using photons we also have to take into account the different travel paths of photons. If the object we want to measure is moving at velocities close to the speed of light, we have to take into account that these photons have been emitted at different times, when the object was at different locations in space. This is what happens in AGNs, where information is carried to the observer by photons and the plasma in the jet moves relativistically. Besides usual Lorentz transformations we have to consider also the *Doppler factor* (δ), a parameter related to both the velocity and the viewing angle of the jet, and important in the understanding of several observed properties of radio loud AGNs. Through this considerations we can explain for example superluminal motions observed in many blazars (e.g Jorstad et al., 2005; Lister et al., 2009) and radiogalaxies (e.g Gómez et al., 2000; Lister et al., 2013) as well as intraday variability observed in total and polarized flux in many sources (see e.g. reviewed by Wagner & Witzel, 1995).

2.2.1 Superluminal motions

A peculiar phenomenon observed commonly in blazars is superluminal motions, namely velocities larger than the speed of light as measured projected in the plane of the sky. These apparent superluminal velocities are observed in bright regions of the jet commonly known as "Components" (see § 2.3 for more details). These components, which move relativistically toward the observer, running after their own emitted photons and

this makes the observed time lapse smaller and the apparent velocity larger than c. Superluminal motions were first predicted by Martin Rees in his PhD thesis (1966) and then actually measured in 1971 (Whitney et al., 1971) thanks to the first Very Long Baseline Interferometer (VLBI) observations at radio wavelength, the only technique able to achieve the necessary angular resolution to discern these motions.

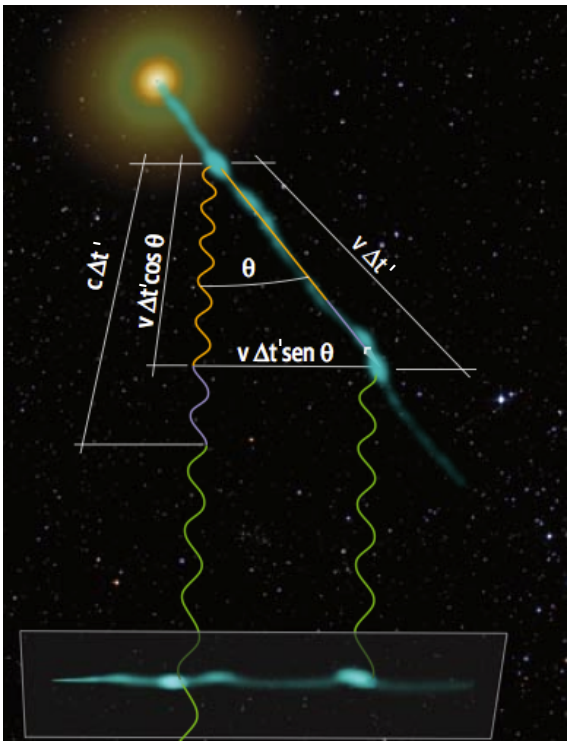

Figure 2.8: Superluminal Motions. Artistic view of a moving component along a jet oriented at viewing angle θ. This component emits radiation in two separated instants of time. The time measured between the two pulses by the observer differs from the real time lag $\Delta t^{'}$. Reproduced by Wolfgang Steffen.

To understand better this phenomenon we consider the artistic reproduction in Figure 2.8, where we have a jet oriented at a viewing angle θ, in which we distinguish the motion of a bright component. We detect radiation from the component at two different instants separated by an interval of time $\Delta t^{'}$. Between the two pulses, the component moves along the jet a distance vΔt and, at the same time, the first pulse travels a distance $c\Delta$t. The second pulse has to travel a shorter distance to reach us respect to the distance traveled by the first pulse. This results in a time interval (Δt),

as measured by the observer, shorter than the real time interval $\Delta t^{'}$ at which the source has emitted the two pulses. Concretely, the time interval in the observer's reference frame is equal to the time spent by the second pulse to reach the first pulse (the path in violet in Figure 2.8). The path difference is equal to $c\Delta t^{'}$ - $v\Delta t\cos\theta$, hence the interval of time need to the second pulse to reach the first one is $\Delta t=(c\Delta t^{'}$ - $v\Delta t^{'}\cos\theta)/c$. As shown in Figure 2.8, what we measure in our reference frame is the distance traveled by the component between the two pulses, projected in the plane of the sky which is ($v\sin\theta\Delta t$). The apparent velocity at which the component is seen moving that distance is:

$$v_{app} = \frac{\Delta t v \sin\theta}{\Delta t} = \frac{v\sin\theta}{\Delta t(1-\frac{v}{c}\cos\theta)} \tag{2.35}$$

If we express the apparent velocity in function of c we obtain the knowing formula:

$$\beta_{app} = \frac{\beta\sin\theta}{1-\beta\cos\theta} \tag{2.36}$$

where the observed apparent velocity depends on the real speed of the component and the angle between its velocity vector and the line of sight. It is easy to see that when θ=90° the apparent velocity is equal to the real velocity of the component, in fact in this case all photons travel the same path, and when θ=0° the apparent velocity is zero since we can not detect the proper motion of a component moving exactly along our line of sight.

In Figure 2.9 we plot the values of β_{app} for different viewing angles and Lorentz factors, Γ. It is easy to see that for each Γ there is a value of viewing angle for which the apparent velocity is maximum, and this value corresponds to θ_{max}=$\arccos\beta$. For smaller viewing angles the apparent velocity decreases, due to projection effects.

From eq. 2.36 we can derive some constraints on the physical parameters of relativistic jets using the observed apparent velocity of the components. For example, for a certain β_{app} we can calculate the upper limit of the viewing angle of the jet, θ_{sup}, which is obtained considering that the component is moving at the maximum possible speed ($\beta = 1$). In this case we have:

$$\beta_{app} = \frac{\sin\theta_{sup}}{1-\cos(\theta_{sup})} = \frac{1}{\tan(\theta_{sup}/2)} \tag{2.37}$$

and a corresponding upper limit of $\theta_{sup} = 2\arctan(1/\beta_{app})$. For example, for an observed apparent velocity of $\beta_{app} = 5$, the jet has to be oriented at a viewing angle $\leq 23°$. From similar considerations we can also put a constraint on the minimum value of β necessary to have the observed β_{app}, independently of the viewing angle of the jet, as we can also appreciate from Figure 2.9. The value of β_{min} for a certain β_{app} is obtained for θ=θ_{max}, as follows:

$$\beta_{min} = \frac{\beta_{app}}{\sqrt{1+\beta_{app}^2}} \tag{2.38}$$

Then for $\beta_{app} = 5$, for example, we have $\beta_{min} = 0.98$ and a corresponding $\Gamma_{min} = 5$.

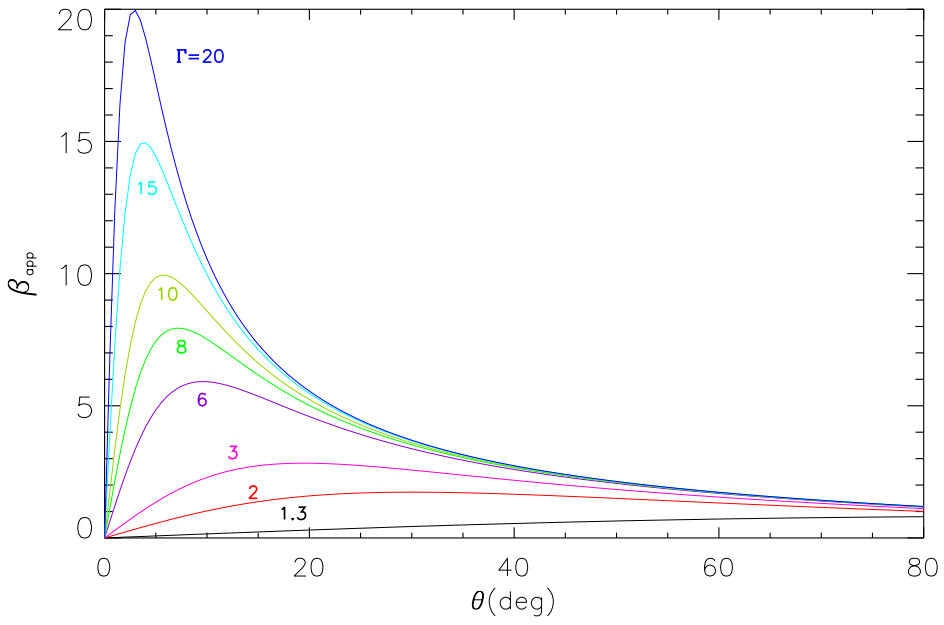

Figure 2.9: Apparent velocity trend. The trend of the apparent velocity depending on the viewing angle (θ) and the Lorentz factor (Γ).

In some blazars superluminal components with speeds up to 40 times the speed

of light are routinely measured (Jorstad et al., 2005), although more moderate superluminal motions up to $\sim 10c$ are more typical for this class of AGNs (e.g. Gómez et al., 2001a; Marscher et al., 2008; Agudo et al., 2011; Ramakrishnan et al., 2014). Superluminal motions are not common in radiogalaxies, but some of them, such as the radiogalaxies 3C 120 (Gómez et al., 1998, 2001b; Casadio et al., 2015a), 3C 111 (Chatterjee et al., 2011) and M 87 (Cheung et al., 2007; Giroletti et al., 2012) usually display these type of motions.

2.2.2 Doppler boosting

We consider for example the component in Figure 2.8 that moves with a velocity v=βc along the jet oriented at viewing angle θ. This component emits a pulse at a frequency $\nu^{'}$. Due to the relativistic time dilation the frequency will redshift by a factor $1/\gamma$, while the Doppler effect causes a shift in frequency by a factor $(1\text{-}\beta\cos\theta)^{-1}$. The latter rescales the frequency to high values (blu-shift) if the source is moving toward us and to low values (red-shift) if the source is moving in the opposite direction, note that $\cos\theta$ can have opposite signs. Considering both effects, we obtain the frequency in our reference frame, that is:

$$\nu = \nu' \frac{1}{\gamma} \frac{1}{(1-\beta\cos\theta)} = \nu'\delta \tag{2.39}$$

where δ is the *Doppler factor*.

We are also interested in determining how the intensity Lorentz transforms between the fluid and observers' reference frames. The specific intensity that we already mentioned in sec. 2.1.1.2, is the energy emitted per unit of time (the power), per unit area, per frequency interval and solid angle ($d\Omega$):

$$I_\nu = \frac{h\nu dN}{dtdAd\nu d\Omega} \qquad [erg \cdot cm^{-2} \cdot s^{-1} \cdot Hz^{-1} \cdot ster^{-1}] \tag{2.40}$$

where we have considered an ensemble of photons (dN) with energy ($h\nu$). The only invariant quantities between the two reference frames are dN, as it is a number, and dA, that is a surface and only rotates due to relativistic effects. Therefore the specific

intensity Lorentz transforms as:

$$I_\nu = \frac{h\delta\nu' dN'}{(dt'/\delta)\delta d\nu'(d\Omega'/\delta^2)dA'} = \delta^3 I'_{\nu'} \tag{2.41}$$

where we introduced the transformation of the solid angle between the two reference frames ($d\Omega = d\Omega'/\delta^2$), as well as those of the time intervals and frequencies discussed previously.

Depending on the value of the *Doppler factor* (δ), the specific intensity can be significantly amplified by the δ^3 factor, favoring the observation of faint sources or components when their jets point toward us.

2.3 Theoretical model of relativistic jets in AGN

Extragalactic jets are the fascinating product of accretion into unexplored black holes and despite many years of observations and theoretical studies, their most fundamental aspects are still mysterious. It is still unclear how they are launched, accelerated and collimated up to large distances from the galaxy's nucleus; why in some AGN they are visible and powerful, while in others they are not; and whether they are dynamically dominated by matter or magnetic fields. Many models are able to interpret the physics and formation of jets, but we cannot still confirm observationally which of these models reflects the reality and whether all or none of them are valid in explaining the wide variety of AGN.

The first very long baseline interferometric (VLBI) observations of AGN suggested that the radio emission may arise from relativistic jets where relativistic electrons emit at radio frequencies through synchrotron process (e.g. Readhead et al., 1979). Prior to these observations, such a scenario had been proposed theoretically by Blandford & Rees (1978) and Blandford & Königl (1979). The most promising model for launching relativistic jets in AGN involves the rotation of large-scale magnetic fields (Blandford & Payne, 1982; Blandford & Znajek, 1977). The differential rotation of plasma in the accretion disk or a black hole magnetosphere causes the polar component of magnetic field lines to wind up into a helix.

The toroidal component of the magnetic field provides a force directed toward the jet axis that allows the jet confinement. The expansion of the magnetic field with

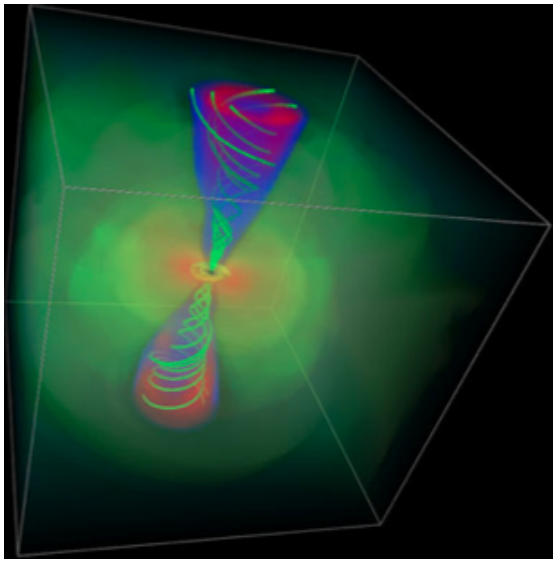

Figure 2.10: Magnetic tower. Helical magnetic field driving magnetized plasma into the jets. Reproduced from McKinney & Blandford (2009)

the distance from the black hole reduces the magnetic pressure, creating a pressure gradient along the jet which drives the flow. Such outflow can become relativistic if the magnetic energy density exceeds the rest mass energy density. Hence, the jet is initially dominated by Pointing flux that is transferred to the kinetic flux of the particles until reaching the equipartition between the kinetic and the magnetic energy density. Magnetic acceleration and gas dynamical models predict also that the intrinsic opening angle of the jet is inversely proportional to the Lorentz factor of the flow, as observed in many AGN (Jorstad et al., 2005).

Therefore, the scenario that emerges from these theoretical models is that of a jet formed by an electrons-protons plasma or electrons-positrons plasma or a combination of the two (this is still unclear) that is driven and collimated by a toroidal magnetic field and accelerated by a decreasing magnetic pressure gradient and eventually subject to internal instabilities, causing a local enhancement of the emission. The latter can be of different type and origin; in the following section we will analyze those of major interest and that we have dealt with during this thesis.

2.3.1 Shock waves and related polarization

Variations in the velocity or energy density of the particles injected into the jet can produce internal shocks waves (Marscher, 2009, e.g.). These shocks accelerate the particles of the plasma they cross, resulting in a region brighter than the underlying plasma that we usually called *component*.

A shock compresses the plasma so that the density of the shocked plasma results a factor $1/\eta$ greater than the density of the unshocked part (as we can appreciate in simulation in Figure 2.11), where η is <1 and is defined as (Hughes et al., 1989; Gomez et al., 1993):

$$\eta = \frac{n_u}{n_d} = \Gamma'_u(8{\Gamma'_u}^4 - 17{\Gamma'_u}^2 + 9)^{-0.5} \tag{2.42}$$

whit n_u and n_d being the particle density upstream and downstream, respectively, and Γ'_u the Lorentz factor of the upstream flow as calculated in the shock's frame. The upstream flow is the quiescent flow that has not crossed yet the shock front, while the downstream flow is the flow reprocessed by the shock front.

The magnetic field component that lies parallel to the shock front is compressed by the shock front and increases by the same $1/\eta$ factor, while the component transverse to shock front direction, and usually almost parallel to the jet axis, does not change. This imposes order even on a magnetic field that is completely chaotic in front of the shock. The geometry and degree of order of the magnetic field are therefore key indicators of the physical conditions in a jet.

There is another type of shock, often labeled as "recollimation" or "external" shocks, since they are related to instabilities coming from the outside of the jet unlike the "internal" ones. The jet during its path tends to reach the pressure balance with the external medium, expanding and contracting its cross-sectional area. Since both the external medium and the plasma inside the jet are subject to variations of pressure, they can undergo mismatches in pressure between each other (see Figure 2.11). The jet edges experience first the mismatch and communicate it to the interior of the jet through sound waves. When the mismatch is great, a shock wave forms to adjust the imbalance more rapidly. These recollimation shocks are observed to be oblique shocks

waves (Gomez et al., 1995; Marti et al., 1995) or conical if the jet is circularly symmetric (Cawthorne & Cobb, 1990; Cawthorne, 2006).

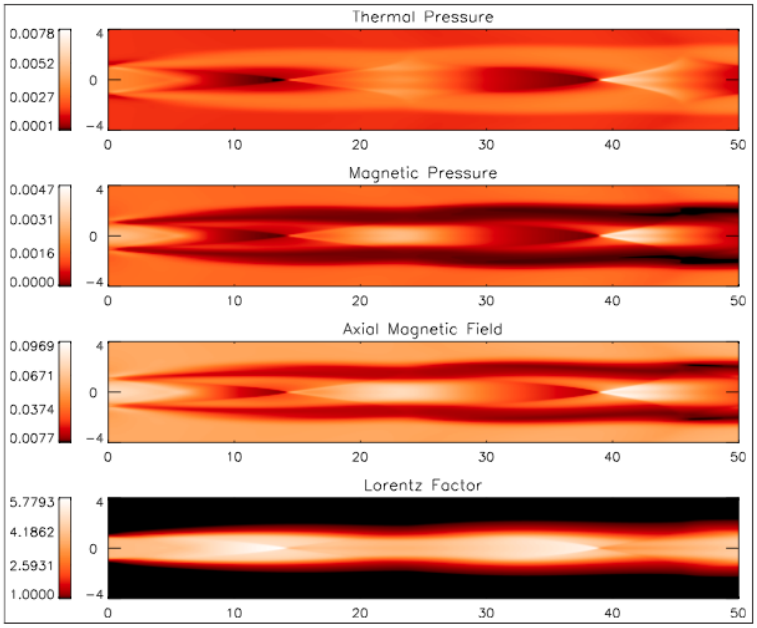

Figure 2.11: RMHD simulations. Relativistic magnetohydrodynamical simulation of a jet with a pitch angle of 0°. A series of recollimation shocks form along the jet. Reproduced from Mar Roca-Sogorb's PhD thesis.

In optically thin regions, the observed polarization vectors and the associated magnetic fields are considered orthogonal to each other (see § 2.1.1.3), then in transverse or orthogonal shock models (Marscher & Gear, 1985; Hughes et al., 1985) the EVPAs are expected to be aligned with the jet axis while in conical shock models (Cawthorne & Cobb, 1990; Cawthorne, 2006) are expected to cover a wide range of angles that depend on the opening angle of the cone and the viewing angle. Therefore, the fractional polarization and direction of EVPAs are a powerful tool to identify distinct features in the jet.

2.3.2 Models for the core, stationary and superluminal knots

The most prominent features on VLBI images of jets in radio loud AGN are the *core* and the so called *knots* or *components* of the jets (mentioned in the previous section). The radio *core* is usually the bright, compact feature at the upstream end of a one-

sided jet and it is generally the most compact feature at any observing frequency in the jet. The core may correspond to the transition region between optically thick and thin emission (see Konigl, 1981) or to the first "recollimation" shock as results from numerical simulations (i.e., Gomez et al., 1995; Gómez et al., 1997). In the first case, the position of the core should move toward the central engine with increasing of frequency of observation, as we appreciate in Figure 2.12. This effect has been observed in some objects (e.g., Lobanov, 1998; Hada et al., 2011) but not in others (e.g., Mittal et al., 2006).

Besides the core there are often other bright features in the jet that could be stationary or moving at subluminal apparent speeds or others moving at superluminal apparent speeds.

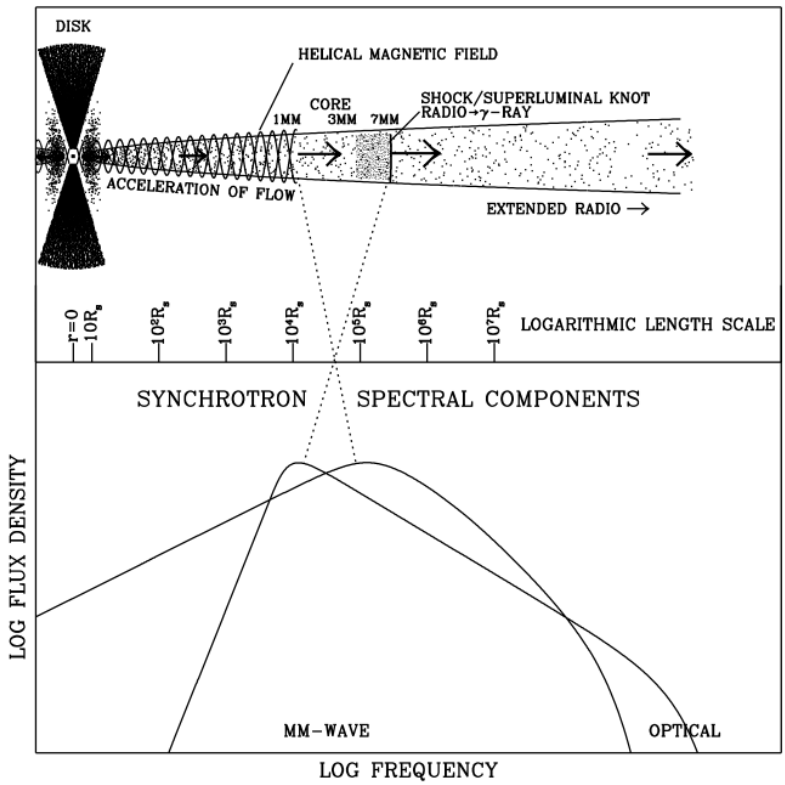

Figure 2.12: Shock-in-jet model. Reproduced from Jorstad et al. (2007)

These *knots* or *components* if stationary, can be produced by recollimation shocks or instabilities in the jets that compress the flow, accelerate particle and amplify the

magnetic field enhancing the emission. Shock waves are the most common and tested interpretation of superluminal knots so far. Many theoretical models are able to reproduce the time variability of the flux, polarization and continuum spectra of blazar (e.g. Hughes et al., 1985; Marscher & Gear, 1985) identifying moving knots with shocks that propagate along the jet. In the shock-in-jet model of Marscher & Gear (1985) for example, electrons are accelerated at the shock front and they lose energy because of expansion and cooling as the flow in which they are imbedded, propagates downstream the shock front. This results in energy stratification of electrons, with higher energy electrons locating in a thin layer close to the shock front and progressively lower energy electrons occupying larger volumes. When applied to an outburst or a flare, this leads to time lags among different frequencies emission whit higher frequencies variations leading those at lower frequencies.

3

Multi-wavelength studies of AGN

3.1 High-energy emission in AGN

So far extragalactic sources detected at γ-ray frequencies are mostly active galactic nuclei, γ-ray bursts and starburst galaxies. As expected, the majority of detected AGN are blazars, having the jets point toward the observer. Their radiation is expected to be enhanced and shift to higher frequencies by Doppler boosting effects (see § 2.2). On the other hand, although they are a small fraction of γ-ray AGN, also some AGN whose jets have larger viewing angles are detected at γ-ray frequencies. Radio galaxies of type I (FRI) and type II (FR II) belong to these misaligned AGN (MAGN).

The γ-ray satellite EGRET (1991-2000), observing in the energy range of 20 MeV to 30 GeV, allowed to catalog for the first time the extragalactic sky at γ-ray frequencies. But it has been with the present generation of satellite in the MeV-GeV energy range (AGILE and *Fermi*) and ground based Cherenkov Telescopes in the TeV energy range (HESS, MAGIC and VERITAS), that the field of extragalactic γ-ray astronomy has become more crowded and extended.

One of the major uncertainties on the high-energy emission in AGN concerns the location of γ-ray emission site. The debate lies in whether γ-ray are produced close

to the central engine, as proposed in the pair cascade model of Blandford & Levinson (1995) or in shocks located in the parsec scale jets, as the mm-VLBI *core*, as proposed in Jorstad et al. (2001).

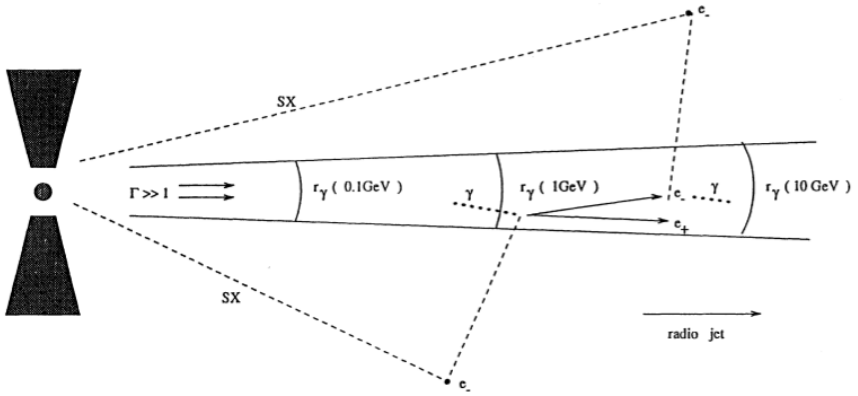

Figure 3.1: Pair cascade model. Reproduced from Blandford & Levinson (1995)

In the model of Blandford & Levinson (1995), soft X-ray photons coming from regions near the black hole are Thomson-scattered by electrons in the surrounding medium and then they can interact with electron/positrons or other γ-ray photons already in the jet. The interaction with another γ-ray photon, if the sum of their energies exceeds 1.022 MeV (the sum of the rest mass energies of an electron and positron), produces an electron positron pair. The interaction with electrons or positrons instead can produce γ-ray photons through inverse Compton scattering. In this way a pair cascade can develop, leading to pair-production opacity. This opacity is energy dependent and gives rise to unity opacity surfaces for the γ-ray photons, whose radius increases with energy. This means that the lower energy photons come from regions closer to the black hole. In Figure 3.1 we report a schematic view of this model.

The scenario proposed in the model that locates the γ-ray dissipation zone in the parsec scale jet, is different (Jorstad et al., 2001; Marscher, 2005). Here the radio and the γ-ray emission originate from the same shocked area that locates close to the radio core rather than closer to the central engine. The electrons, that are accelerated in shocks, scatter photons to γ-ray energies via synchrotron self Compton or external Compton (see § 2.1.2 and § 2.1.3). For a schematic representation, we refer to Figure 2.12.

The fast variability observed at high energies initially pointed to locate the emission site close to the black hole, where the jet has a smaller cross-section (e.g. Tavecchio et al., 2010). However, the short time scales of variability only imply the compactness of the emitting region, which has to be $R < c\Delta t\delta$, where c is the speed of light, Δt is the variability time scale and δ is the Doppler factor. Then, we can not discard emitting regions far away from the central engine if we associate the γ-ray emission to compact knots in the jet (e.g. Tavecchio et al., 2011) or if we treat the jet as divided in many turbulent cells (Marscher, 2014). Depending on the location of the high-energy dissipation zone, the production mechanism of this emission could be different. Some authors suggest external Compton emission with external photons coming from the broad line region (Ghisellini et al., 2010), while other authors locate the emission at parsecs scale with external photons coming from the dusty torus or synchrotron self Compton emission if we have no contribution from an external photon field (Sikora et al., 2009; Bonnoli et al., 2015). However, in many cases SED modeling does not provide a unique answer to the above questions and more observational constraints are needed.

The location and production mechanism of the high-energy emission are not the only open questions on our understanding of AGN. The main uncertainties concern the formation, acceleration and collimation of jets, as well as their composition. It is also largely unknown what is the role of the magnetic field in dynamic of jets.

3.2 Combining high spatial resolution radio observations with higher energy data: the multi-waveband tools.

Many studies of AGN involve a single technique and at only one waveband, which is usually inadequate to reveal the complex physics behind of these objects. Our understanding has improved with the increase of available data from many astronomical instruments at different wavelength. Multi-waveband polarimetric observations of individual objects that undergo high energy events can provide a wealth of informations on the physics of jets through the following tools:

- *creation of the spectral energy distribution (SED) at several epochs using measurements of flux density at different frequencies*: this gives informations on the

emission processes and separate components responsible for the emission at the different epochs;

- *study of the variability at the different wavelength*: the minimum time scale observe in flux variations at any wavelength is related to the maximum size of the emitting region; cross-frequency time lags help to locate the emission region;

- *radio interferometric imaging (in particular, mm-VLBI images)*: we can study the evolution of the parsec to kiloparscec scale jet with angular resolutions of 0.1 milliarcseconds or less. This give us informations on superluminal motions inside the jet, appearance or disappearance of radio knots that could be related with high energy flares and peculiar changes of the polarized flux on very small angular scales;

- *study of the polarized flux at different wave-bands*: polarization gives informations on the degree of ordering of the magnetic field and the mean direction of the field and it is also an additional tool for the cross-frequency identification of emission regions.

Radio interferometric images and, in particular, between them millimeter-VLBI images are the most powerful tool among those mentioned above. Infrared and higher-frequency observations have worst angular resolutions respect to mm-VLBI observations so multi-epoch VLBI images are necessary to determine where in the jet flares occur. Moreover, comparing the time scale of variability of radio knots with their size we can infer the Doppler factor related to each knots (e.g. Jorstad et al., 2005). This allows deriving the Lorentz factor and the angle between the direction of these knots and the line of sight. The Doppler factor, the Lorentz factor and the viewing angle are key parameters in revealing changes in the jet that can be related to events at the other frequencies.

In the studies presented in this thesis we collected data at different waveband and we performed the analysis of data making use of all the techniques described above. In particular, the γ-ray data come from the NASA's satellite *Fermi* and the VLBI data from observations at different frequencies performed with the Very Long Baseline Array (VLBA). Also low resolution observations with the Karl G. Jansky Very Large Array (JVLA) have been performed in the analysis of M 87 jet (see Chapter 5).

In the following sections, after a brief description of the main instruments involved in our studies, we explain how we performed the calibration process of VLBI data. In fact, while the calibration of *Fermi* data is well explained in both studies in which we used γ-ray data (Casadio et al., 2015a,b), the calibration of VLBA data is not explained in detailed in none of the three presented articles.

3.2.1 The *Fermi* satellite

The *Fermi* satellite was launched by NASA on 11 June 2008 as the *γ-ray Space Telescope* (GLAST) and renamed *Fermi γ-ray Space Telescope* when the mission started (04 August 2008). It orbits around the earth at $\sim$565 km of altitude with an orbital period of about 96 minutes.

Figure 3.2: The *Fermi* satellite. An artistic image of the NASA's space telescope Fermi. Credit: NASA artist's concept.

On board there are two scientific instruments, the Large Area Telescope (LAT) and the γ-ray Burst Monitor (GBM). The LAT is a pair-conversion telescope designed to measure the directions, energies (from 20 MeV to 300 GeV) and arrival times of γ-ray

photons over a large field of view, while rejecting a large background of cosmic rays. In order to take full advantage of the LAT large field of view, *Fermi* operates primarily in scanning survey mode in which the telescope is pointed north and south of zenith in alternate orbits. As a result, after two orbits, about 3 hours, an almost uniform sky exposure is obtained. With the results of surveys, the *Fermi*-LAT collaboration have produced until now three catalogs with the detected γ-ray sources and the corresponding counterparts at lower energies when possible: the first *Fermi*-LAT catalog (1FGL; Abdo et al. (2010)), the second catalog (2FGL; Nolan et al. (2012)) and the third catalog (3FGL; Acero et al. (2015)). In addition to these catalogs containing all the γ-ray sources detected by *Fermi*, others catalogs containing only the AGN lists and related studies have been reported in the LAT Bright AGN Sample (LBAS; Abdo et al. (2009)), 1LAC (Abdo et al., 2010), 2LAC (Ackermann et al., 2011) and 3LAC (Ackermann et al., 2015), the first, second and third LAT AGN catalogs, respectively.

The number of detected sources has increased among the successive catalogs, then here we report only the statistic contained in the 3FGL and 3LAC catalogs. The 3FGL catalog includes 2192 γ-ray sources detected at Galactic latitude greater than 10° and among them the 71% are associated with AGN, which constitute the 3LAC. Only the 2% of these AGN are non-blazar AGN and among them the majority is of radio galaxies. The radio galaxies, that belong to misaligned AGN, are not favored GeV sources, as previously explained at the beginning of the Chapter.

3.2.2 The Very Long Baseline Array

The VLBA consists in 10 antennas of 25 meters across each, located in American territories and controlled remotely from the National Radio Astronomy Observatory in Socorro (New Mexico).

The antennas are located in such a way as to have a good sampling at shorter baselines, necessary to study extended and weaker structures, as well as at longer baselines to have a good resolution. In the astronomical interferometry the maximum baseline length between two antennas represents the "equivalent diameter" (D) of the instrument, which provides an estimate of the angular resolution (θ) that can be achieved by the instrument according to formula $\theta \propto \lambda/D$.

The sites hosting the antennas are: Mauna Kea (Hawaii), Brewster (Washington), Owens Valley (California), Kitt Peak (Arizona), Pie Town (New Mexico), Los Alamos

(New Mexico), Fort Davis (Texas), North Liberty (Iowa), Hancock (New Hampshire), St. Croix (Virgin Islands). The maximum baseline length of the VLBA is about 8600 km and corresponds to the baseline between Mauna Kea and St. Croix antennas, providing for 7 mm observations an angular resolution of ∼0.15 mas, for example.

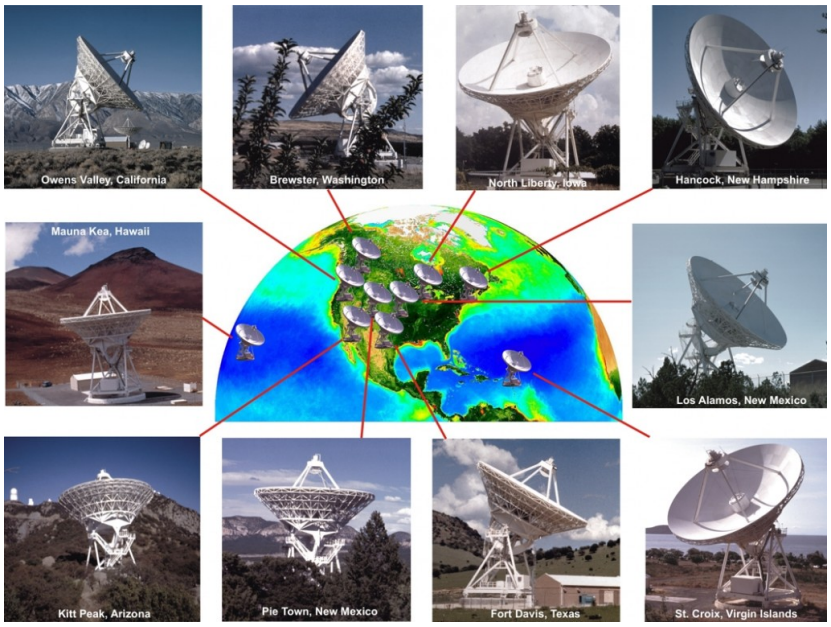

Figure 3.3: The Very Long Baseline Array. Panoramic view and localization of the 10 antennas forming the VLBA. Credit: NRAO/AUI and for the Earth image, the SeaWiFS Project NASA/GSFC and ORBIMAGE.

3.2.3 The Jansky Very Large Array

The Very Large Array (VLA), built at the end of 70' in Socorro (New Mexico, USA), is one of the oldest astronomical radio observatories in the world. It is formed by 27 antennas, each of 25 across and arranged along the arms of an upside-down Y, as visible in Figure 3.4. The antennas can move along the arms forming four different configurations denoted as D, C, B and A, from the closest to the most extended one. All VLA antennas have eight receivers providing continuous frequency coverage from 1 to 50 GHz. The recent improvement of the receivers bandwidth leads to achieve a better sensitivity and a better coverage in frequency. The new improved VLA was renamed Karl G. Jansky Very Large Array (JVLA).

Figure 3.4: The Jansky Very Large Array. Part of the JVLA antennas in Socorro (New Mexico) at the twilight. Credit: NRAO.

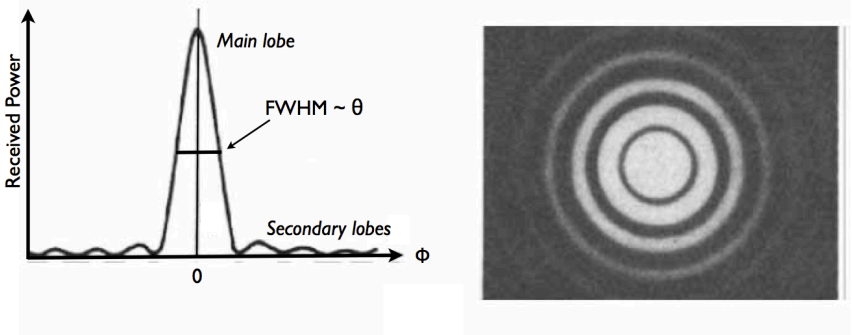

Figure 3.5: The antenna power pattern. In both figures we appreciate the main lobe and the secondary lobes of the diffraction pattern produced observing a point source. In the graphic, the x-axis represents the angular distance respect to the axis of the antenna and the y-axis represent the power received by the antenna. The FWHM gives an estimation of the resolution of the antenna (θ).

3.2.3.1 Interferometric data

Each antenna forming the interferometer register the electromagnetic waves coming from the observed source. Then, all the signals coming from the antennas are collected at the correlator center, where are combined and corrected for time delays due to the different arrival times of the signals at the different sites where the antennas are located. The output of the correlator is a complex function called "fringe visibility" or more simply "visibility", whose amplitude and phase are the Fourier components of the sky brightness convolved with the *beam* of the instrument. The *beam* or *power pattern* or *Point Spread Function* (PSF), the latter mainly used at optical wavelength, is the response of the antenna to the observation of a point source in the center of the field and describes how the energy of a plane wavefront is distributed on the focal plane of the instrument. An example of power pattern is shown in Figure 3.5, where the full width half maximum (FWHM) of the main lobe gives an estimation of the resolution of the instrument (θ).

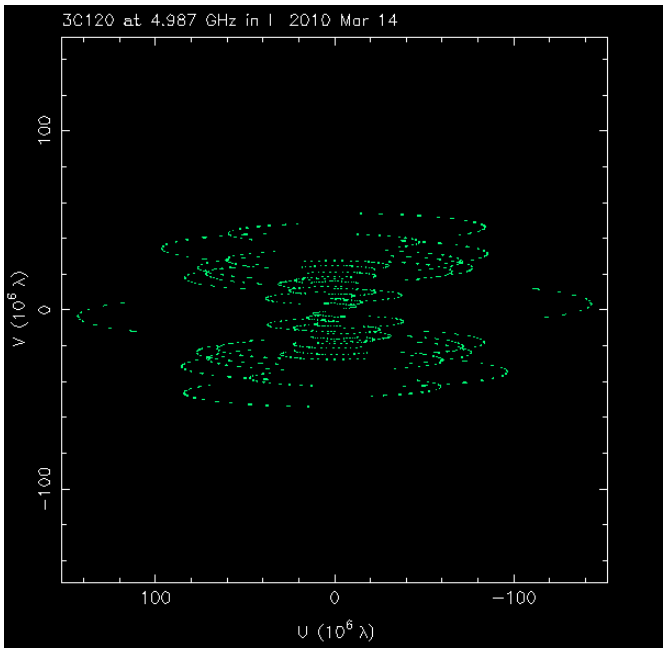

Figure 3.6: The UV plane. The UV plane related to the observation of 14th March 2010 of the radio galaxy 3C 120 with the VLBA at 5 GHz.

The visibility function, V(u,v), depends on coordinates of the uv plane, which is the reference plane tangent to the celestial sphere in the direction of the observed source

and where are impressed, continuously during the observation, the baselines between all the antennas as are seen from the source (Figure 3.6).

The u-axis represents the East-West direction and the v-axis the North-South direction. The rotation of the Earth makes the locations of the antennas, as seen by the source, changing with time and this produces a better coverage of the uv plane that later translates into a better image of the source.

After the correlation, data are ready to be analyzed, but before to produce an image we have to verify that amplitudes and phases of the visibility function are sufficiently corrected. Calibration of amplitudes is important because errors in amplitude can simulate inexistent structures and even more important is the calibration of phases that are subject to variations in time (*rates*) and inside the observing waveband (*group delays*) due to many causes: changes in the electronic of the instrument related to changes in temperature, extra path introduced by different antennas cables, changes in atmospheric conditions, imprecisions in pointing of some antennas, delays due to the ionosphere, etc..

3.2.3.2 Amplitude and phase calibration

Calibration of the VLBA data has been performed within the Astronomical Image Processing System (`AIPS`) following the standard procedure for VLBI polarimetric observations (Leppanen et al., 1995).

We first correct phases for the dispersive delays introduced by the ionosphere using Global Position System (GPS) models of the electron content in the ionosphere. Then we apply time dependent corrections of the Earth Orientation Parameters (EOPs) which takes into account the different orientation of the antennas in time respect to the source, due to the earth rotation. Afterwards we proceed to the amplitude calibration which uses informations contained in two tables, the GC (Gain Curve) and TY (System Temperature) table. The GC table contains measurements of the efficiency of each antenna, which depends mainly on the elevation of the antenna and then on the position of the source in the sky. The TY table contains measurements of the system temperature of antennas which are related to weather conditions and performance of the receiver. The amplitude calibration also converts the amplitudes values of the visibility function into physical units (i.e, Janskys).

At this point, if the amplitude calibration is satisfactory, we proceed to calibrate the phases of the visibility data. First we correct phases considering the parallactic angle of each antenna, which changes in time with the source tracking. This calibration is important for polarimetric experiments because the two (orthogonally polarized) receivers involved in a polarimetric observation, the right circular polarized (RCP) and the left circular polarized (LCP) one, rotate in position angle respect to the source during the observation and this introduces a geometric effect which has to be corrected.

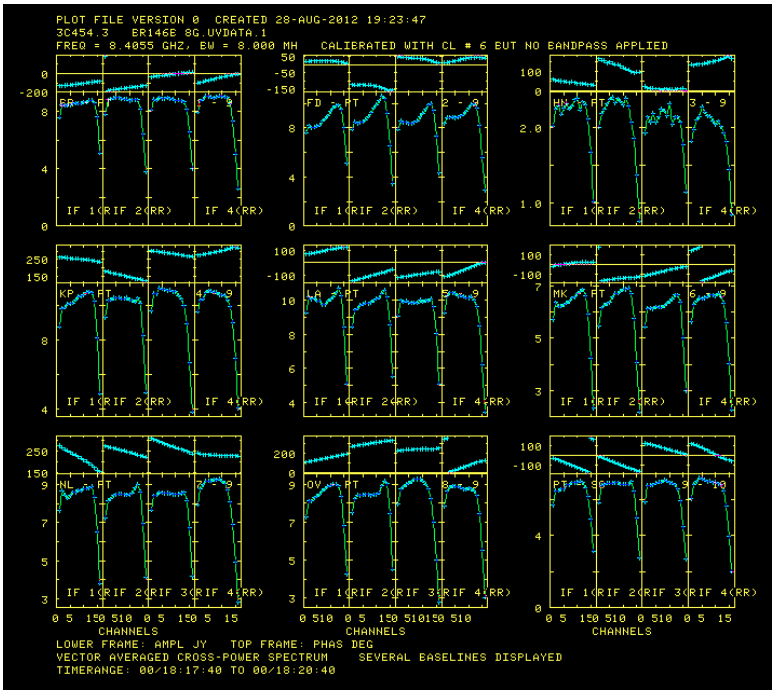

Figure 3.7: The visibility data with phases affected by delays. The data displayed are from one of 8 GHz VLBA observations of 3C 120 presented in Agudo et al. (2012). The nine plots, representing visibility data between the antenna in Pie Town and the other 9 VLBA antennas, contain the phases (panels above) and the amplitudes (panels below) of the visibility function. The bandwidth of the receiver of each antenna is divided into four intermediate frequencies (IF) and each IF is subdivided into 16 channels (the blue points). The phases here are affected by delays.

The next step is to correct phase variations along the observing frequency bandwidth (the delays) introduced by the passage of the signal thought electronics of the VLBA instruments. An example of data affected by these delays is shown in Figure 3.7. These delays are removed using the "pulse-cal" system, which consists of a series of

pulses of well-known time and frequency interval introduced during the observation and obtaining in output a pulse-cal (PC) table to apply to data. In Figure 3.8 we appreciate how phases displayed in Figure 3.7 have been corrected by the pulse calibration.

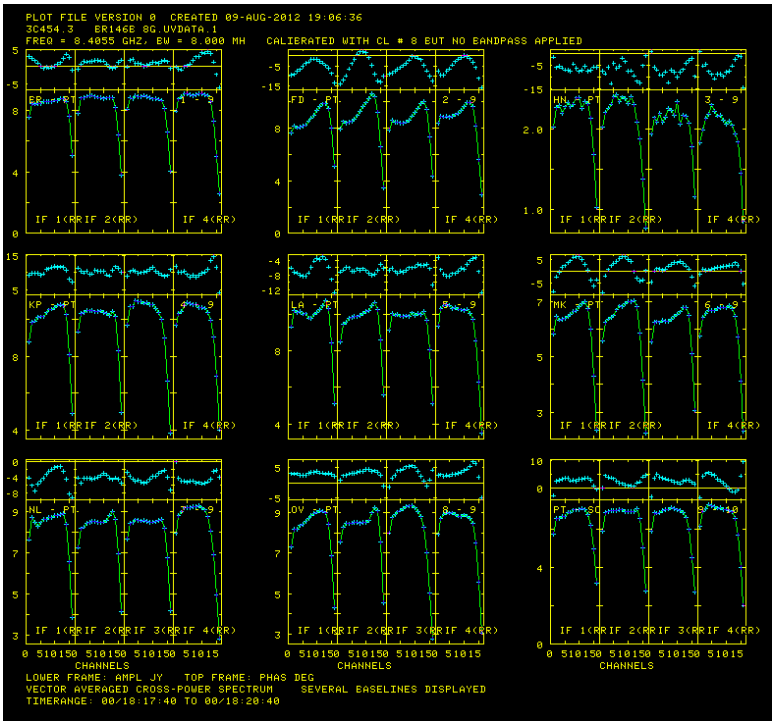

Figure 3.8: The visibility data with phases corrected for delays. The visibility data of the scan in Figure 3.7 after the correction using the pulse calibration. The phases now do not exhibit abrupt changes among the IFs (note the different scales of the plot of phases respect to Figure 3.7.)

The phases after the pulse calibration can still exhibit residual rates and second order delays. The last step of the phase calibration is the *global fringe-fitting* as described by Schwab & Cotton (1983). The global fringe-fitting searches peaks in amplitude and phase (the fringes) in a determined integration time. The integration time used to search for fringes, usually between 1 and 3 minutes, it has to be sufficiently large to have a good signal to noise ratio and not so large to not loose coherence in the signal because of ionospheric and tropospheric variations. When the source of interest is bright enough, as in our case, the fringe fitting can be done directly on the source while in case of weak sources a phase calibrator is needed. After applying fringe-fitting solutions, the visibility data are ready for imaging and self-calibration using a combination

of `AIPS` and the Differential Mapping (`Difmap`) packages.

3.2.3.3 Imaging and self-calibration

The amplitudes and phases of data can still display minor errors which, together with secondary lobes (due to the *beam*) and grating lobes (due to lack of points in the uv plane), make the image we can obtain after the calibration incomprehensible ("dirty"). This means that the image construction is tricky and it is necessary to pay attention because there is not a unique solution. The problem of image construction consists in fact in choosing plausible visibility distributions for that points of the uv plane where we do not have informations and, at the same time, we have to take care with the true distribution of any emission in the dirty image because secondary lobes can be confusing.

There are many methods to reconstruct an image but the longer used is the CLEAN algorithm (Högbom, 1974). The CLEAN starts selecting the region containing the source and choosing the number of iterations to perform. In each iteration, the CLEAN searches for the intensity peak inside the selected region and after convolving it with the dirty beam, it subtracts it from the dirty map. In this way the CLEAN removes the intensity peaks of the map together with secondary lobes due to the beam and it also records the position and values of the point sources subtracted in a model. This process stops when the maximum value of the residual map (the map containing the remained flux after the subtraction) is smaller than the estimated noise of the image. Then the image is reconstructed adding to the last residual map the components found by CLEAN but only after having convolved them with a cleaned beam, usually a gaussian function with the same FWHM of the dirty beam, in order to maintain the resolution proper of the observation.

The CLEAN components generate a source model used to self-calibrate visibility data usually in an iterative process. This iterative process generates models which progressively better adjust to the visibility function. When the differences between the model and the visibility data are no longer considerable we can obtain the final image.

3.2.3.4 Polarization calibration

The phases and delays corrected in previous steps were mainly related to Right Right (RR) and Left Left (LL) offsets between different antennas. But also corrections of

cross-hand circular polarization (Right Left and Left Right) phases and delays are important, being the calibration of RL and LR data necessary for polarimetric observations. In fact the determination of the R-L phase difference is equivalent to the determination of the polarization position angle (mentioned in § 2.1.1.3). We use a specific task in `AIPS` named RLDLY to correct R-L delays differences and after that the RL and LR phases should be continuos over frequencies and flat if the RR and LL phases are flat, meaning without residual delays.

Once the cross-hand calibration has been completed it is also necessary to correct for the instrumental polarization also known as "D-terms". In `AIPS` there are many tasks that correct for D-terms and they all write corrections in the antenna table (AN) that is later on applied to data. Then, after executing one of these tasks, the AN table contains corrections for D-terms associated to each antenna. The D-terms change slowly with time and for this, as shown in Gómez et al. (2002), they can be used to calibrate the absolute orientation of VLBA EVPAs. In fact, the real orientation of polarization angles is usually obtained observing a calibrator having stable EVPAs, but this type of sources are almost inexistent for VLBA observations because it is very difficult to find sources with electric vector position angles stable on milliarcsecond or submilliarcsecond scales.

When quasi simultaneous low resolution observations, as those performed with the Very Large Array (VLA) or single-dishes, are available we achieve the absolute calibration of VLBA EVPAs comparing EVPAs in low resolution observations with an integrated value of EVPAs in VLBA images. Once we have the absolute orientation of EVPAs in at least one epoch, we can use the D-terms to obtain the absolute calibration at all the other epochs. If we use the same reference antenna during the calibration of data in all epochs and if there were no changes in antennas instrumentation, the D-terms remain constant and are used to the relative calibration of EVPAs among epochs.

For the polarimetric study on the radio galaxy 3C 120 performed in Agudo et al. (2012), where we analyzed VLBA observations at three different frequencies (5, 8 and 12 GHz) during three observing epochs (December 2009, March and June 2010), we make use of both techniques. As described in details in the article which we include below, we performed the absolute calibration of EVPAs at 5 and 8 GHz in the first epoch (December 2009) taking advantage of informations contained in the VLA/VLBA

Polarization Calibration Program [1] and we used the D-terms for the relative calibration of 5 and 8 GHz EVPAs in May and June 2010. The VLA/VLBA Polarization Calibration Program, started in 1999 and halted in 2009 with the born of the new JVLA, was thought to have an ongoing VLA monitoring of VLBA polarization calibrators. The lack of 12 GHz data in the above program led us to use another method: we extrapolated the value of 12 GHz EVPAs from the Faraday rotation profile (described in § 2.1.1.4) where we included EVPAs values at 5, 8 and 15 GHz; the latter obtained from the MOJAVE Program. Moreover, also in this case, the D-terms stability among epochs at 12 GHz has been used as further proof for the EVPAs calibration.

In both multi-wavelength studies presented here (Casadio et al., 2015a,b), we collected 43 GHz VLBA data of our sources of interest (3C 120 and CTA102) from the VLBA-BU-BLAZAR program which includes regularly observations of 36 AGN. The calibration of total intensity and polarization of the entire data set has usually performed simultaneously for all the objects. In this case, we inferred the mean values of the D-terms from the sources that we consider better polarization calibrators and we applied them to all the sources in the sample. We compared the mean D-terms among epochs for the relative calibration of the electric vector position angles and, in addition, we took a look at some strong calibrators in the sample having knots in their jets with reasonably stable EVPAs which provide an additional comparison method.

A more detailed explanation on the data set analyzed in each study is included in the articles that we present in the following section.

3.3 Previous multi-wavelength studies.

The first studies of variability at radio wavebands in connection with the γ-ray activity were carried out by Valtaoja & Terasranta (1995) and Valtaoja & Teraesranta (1996). They compared sources observed at 22 and 37 GHz with the 13.7 meter Metsähovi radio telescope with γ-ray detections by EGRET. They found a correspondence between γ-ray detections and radio activity and they interpreted this result as an evidence of the common spatial location of the radio and γ-ray emission regions. Later on, radio monitoring using the Very Long Baseline Array (VLBA) at 22 and 43 GHz have been compared with γ-ray measurement with EGRET in Jorstad et al. (2001), where authors

[1] http://www.vla.nrao.edu/astro/calib/polar/

found that in most cases γ-ray flares were related to the appearance of new superluminal components.

Nowadays, in the era of the *Fermi* satellite the two most extended VLBA monitoring programs of the northern hemisphere are the VLBA−BU−BLAZAR program and the MOJAVE (Monitoring of Jets in Active Galactic Nuclei with VLBA Experiments) program. The VLBA-BU-BLAZAR program is pioneering in mm-VLBI and multi-frequency studies of AGN. It consists of monthly polarimetric observations of 36 γ-ray blazars and radio galaxies with the VLBA at 43 GHz (7 mm) plus observations of the 17 brightest AGN of the sample with the Global mm-VLBI Array (GMVA) at 90 GHz (3 mm) every 6 months (e.g. Jorstad et al., 2013). Moreover, several research groups collaborate to this program with data from many telescopes and at different wavelength in order to extend the monitoring of these 36 AGN to the entire electromagnetic spectrum. The research group in Granada participates in the collaboration with the ongoing polarimetric programs MAPI and POLAMI, where we observe the sample of AGN at 1 and 3mm with the 30m telescope of the Institut de Radioastronomie Millimétrique (IRAM) located at the Pico Veleta Observatory in Sierra Nevada (Granada, Spain) and with the MAPCAT program, where the same sample is observed with the optical telescope of Calar Alto Observatory in Almeria (Spain). During my PhD, I performed half of the observations planned with the IRAM telescope as well as I reduced part of the optical data obtained from the Calar Alto telescope. The MOJAVE program provides long-term systematic monitoring of an extended sample of AGN with the VLBA at 15 GHz (2 cm) (e.g. Lister et al., 2009). The major aim of this program is to characterize the kinematics and polarization evolution of AGN jets, providing also parsec-scale structural informations on over 100 AGN jets observed with the *Fermi* satellite.

Statistical studies between the MOJAVE sample and *Fermi* catalogs reveal that, among the brightest radio loud blazars in the sample, AGN non-detected by *Fermi* have lower Doppler factors respect to AGN displaying γ-ray emission where higher Doppler factors are in many cases related to jets oriented at smaller viewing angles (Pushkarev et al., 2014). Another result from the MOJAVE program is that synchrotron self Compton mechanism is favored for the γ-ray emission in BL Lac objects (Lister et al., 2011). We reported evidences of that also in Williamson et al. (2014) where we analyzed 4 years of multi-wavelength data of a sample of 33 γ-ray bright blazars. In Williamson

et al. (2014) we also reported how FSRQs display the highest amplitudes of γ-ray outbursts and the largest variations of γ-ray spectral indices between quiescent and active states while in BL Lac, where different activity states have similar characteristics, the same mechanism is responsible for quiescent and flaring γ-ray emission. From statistical studies on the AGN sample of the VLBA−BU−BLAZAR program is found that more than 50% of γ-ray flares occurred in the mm-core, which lies parsecs from the black hole in luminous blazars, and are associated with the ejection of a new superluminal component (Marscher et al., 2012), confirming previous results from VLBA and EGRET observations (Jorstad et al., 2001). Also X-ray emission in blazars seems to come predominantly from regions close to the mm-core (Marscher et al., 2004; Sokolov et al., 2004). However, we also observe cases of AGN where γ-ray or X-ray and optical flares occur before the flux density variation in the mm-core (e.g. Jorstad et al., 2005) or we observe the γ-ray spectral break at few GeVs due to pair production opacity (Poutanen & Stern, 2010); evidences that point to locate the high energy site closer to the central engine.

Many progresses toward revealing the location and mechanism of high energy emission in AGN have been done through multi-waveband monitoring observations. However, the variety of objects and characteristics displayed is so wide that still more studies are necessary to have the entire scenario complete.

4

Multi-wavelength polarimetric studies on the radio galaxy 3C 120 and the blazar CTA 102

In this section we present the multi-wavelength and polarimetric studies we performed on the radio galaxy 3C 120 and the blazar CTA 102 in their original form of publication in the international peer-reviewed journal *The Astrophysical Journal*.

Both sources have been observed in coincidence with unprecedented γ-ray flares registered by the *Fermi* satellite. The *Fermi* Large Area Telescope registered in September-October 2012 an extraordinary bright γ-ray outburst in the quasar CTA 102, and between December 2012 and October 2014 a prolonged γ-ray activity in the radio galaxy 3C 120. In CTA 102 also very bright flares at both optical and near infrared wavelengths have been observed in the same period. In both studies the analysis of γ-ray data has been compared with a series of 43 GHz VLBA images from the VLBA-BU-BLAZAR program, providing the necessary spatial resolution to probe the parsec scale jet evolution during the high energy events. In the case of 3C 120, in order to extend the observing period covered by radio data, we also used 15 GHz VLBA data from the MOJAVE sample. For the CTA 102 study we extend the analysis to the entire electromagnetic spectrum, collecting data from many ground telescopes and satellites.

4.1 The Connection between the Radio Jet and the Gamma-ray Emission in the Radio Galaxy 3C 120

The following article has been published in *The Astrophysical Journal* on August 1st, 2015 and it is presented here in its original form.

The reference for this article is: Casadio C., Gómez J. L., Grandi P., et al., 2015, ApJ, 808, 162.

The authors are: Carolina Casadio, José L. Gómez, Paola Grandi, Svetlana G. Jorstad, Alan P. Marscher, Matthew L. Lister, Yuri Y. Kovalev, Tuomas Savolainen and Alexander B. Pushkarev.

The Astrophysical Journal, 808:162 (11pp), 2015 August 1 doi:10.1088/0004-637X/808/2/162

THE CONNECTION BETWEEN THE RADIO JET AND THE GAMMA-RAY EMISSION IN THE RADIO GALAXY 3C 120

Carolina Casadio[1], José L. Gómez[1], Paola Grandi[2], Svetlana G. Jorstad[3,4], Alan P. Marscher[3], Matthew L. Lister[5], Yuri Y. Kovalev[6,7], Tuomas Savolainen[8,7], and Alexander B. Pushkarev[7,9,10]
[1] Instituto de Astrofísica de Andalucía, CSIC, Apartado 3004, E-18080, Granada, Spain
[2] Istituto Nazionale di Astrofisica-IASFBO, Via Gobetti 101, I-40129, Bologna, Italy
[3] Institute for Astrophysical Research, Boston University, 725 Commonwealth Avenue, Boston, MA 02215, USA
[4] Astronomical Institute, St. Petersburg State University, Universitetskij Pr. 28, Petrodvorets, 198504 St. Petersburg, Russia
[5] Department of Physics, Purdue University, 525 Northwestern Avenue, West Lafayette, IN 47907, USA
[6] Astro Space Center, Lebedev Physical Institute, Russian Academy of Sciences, Profsoyuznaya str. 84/32, Moscow 117997, Russia
[7] Max-Planck-Institut für Radioastronomie, Auf dem Hügel 69, D-53121 Bonn, Germany
[8] Aalto University Metsähovi Radio Observatory, Metsähovintie 114, FI-02540 Kylmälä, Finland
[9] Pulkovo Observatory, Pulkovskoe Chaussee 65/1, 196140 St. Petersburg, Russia
[10] Crimean Astrophysical Observatory, 98409 Nauchny, Crimea, Russia
Received 2015 January 20; accepted 2015 May 8; published 2015 July 30

ABSTRACT

We present the analysis of the radio jet evolution of the radio galaxy 3C 120 during a period of prolonged γ-ray activity detected by the *Fermi* satellite between 2012 December and 2014 October. We find a clear connection between the γ-ray and radio emission, such that every period of γ-ray activity is accompanied by the flaring of the millimeter very long baseline interferometry (VLBI) core and subsequent ejection of a new superluminal component. However, not all ejections of components are associated with γ-ray events detectable by *Fermi*. Clear γ-ray detections are obtained only when components are moving in a direction closer to our line of sight. This suggests that the observed γ-ray emission depends not only on the interaction of moving components with the millimeter VLBI core, but also on their orientation with respect to the observer. Timing of the γ-ray detections and ejection of superluminal components locate the γ-ray production to within ~0.13 pc from the millimeter VLBI core, which was previously estimated to lie about 0.24 pc from the central black hole. This corresponds to about twice the estimated extension of the broad line region, limiting the external photon field and therefore suggesting synchrotron self Compton as the most probable mechanism for the production of the γ-ray emission. Alternatively, the interaction of components with the jet sheath can provide the necessary photon field to produced the observed γ-rays by Compton scattering.

Key words: galaxies: active – galaxies: individual (3C120) – galaxies: jets – radio continuum: galaxies

Supporting material: machine-readable tables

1. INTRODUCTION

In the unified scheme of active galactic nuclei (AGNs), Fanaroff–Riley radio galaxies of type I (FRI) and II (FRII) are considered the parent population of BL Lacs and flat spectrum radio quasars (FSRQs), respectively. FRI and FRII radio galaxies belong to the misaligned AGN class, as they are oriented at larger viewing angles than blazars (the most luminous and variable BL Lac objects and FSRQs). Relativistic beaming amplifies the emission of jets pointing toward the observer, making blazars the brightest objects in the extragalactic sky also in the γ-ray band. In fact, among the more than 1000 extragalactic sources detected by the Large Area Telescope (LAT) on board the *Fermi* Gamma-Ray Space Telescope in 2 years, only 3% of them are not associated with blazar objects. FRI and FRII radio galaxies fall inside this 3%, with the predominance of nearby radio galaxies of type I (Grandi et al. 2012a). FRII radio galaxies with GeV emission are rare, 3C 111 being the only FRII so far with a confirmed *Fermi* counterpart. 3C 111 is also the first FRII radio galaxy where a γ-ray flare has been associated with the ejection of a new bright knot from the radio core (Grandi et al. 2012b). The simultaneity of the observed flare in millimeter, optical, X-ray and γ-ray bands led Grandi et al. (2012b) to claim that the GeV dissipation region is located at a distance of about 0.3 pc from the central black hole (BH).

The rapid γ-ray variability observed in FRI radio galaxies, with time scales of months in the case of NGC 1275 (Abdo et al. 2010; Kataoka et al. 2010), or even days for the case of the TeV variability in M87 (Aharonian et al. 2006; Harris et al. 2011), suggests that the γ-ray emission in these sources originates also in a very compact jet region. Results from over 10 years of multiwavelength observations of M87 (Abramowski et al. 2012) suggest that the very high energy flares may take place in the core (for the case of the 2008 and 2011 TeV flares), or in the HST-1 complex, about 0.″8 downstream of the jet (in the case of the 2005 TeV flare). More recently, Hada et al. (2014) found that the last TeV flare occurred in M87 in 2012 originates in the jet base, within 0.03 pc from the BH, but no correlation with the MeV–GeV light curve obtained by *Fermi* has been found.

Recently, the LAT detected an unprecedented γ-ray flare from the FRI radio galaxy 3C 120 on 2014 September 24th, when the source reached a daily flux ($E > 100$ MeV) of $1.0 \pm 0.3 \times 10^{-6}$ photon cm^{-2} s^{-1}, as reported in Tanaka et al. (2014). This recent flare appears to be associated with a higher state of γ-ray activity in the source. In fact, since 2012 December the radio galaxy 3C 120 registered a series of γ-ray events, indicating a flaring activity that lasted until at least our last data were analyzed, in 2014 October 4.

The radio galaxy 3C 120 ($z = 0.033$) presents an FRI morphology, but it also has a blazar-like radio jet, showing multiple superluminal components at parsec scales (Gómez et al. 2000, 2001, 2011), as well as at distances as large as 150 pc in projection from the core (Walker et al. 2001). This radio galaxy also reveals X-ray properties similar to Seyfert galaxies, with the X-ray spectral slope increasing with intensity (Maraschi et al. 1991), and a prominent iron emission line at a photon energy of 6.4 KeV. This implies that most of the X-ray emission comes from or near the accretion disk, rather than in the jet. In addition, the observed strong correlation between dips in the X-ray emission and the ejection of new superluminal components in the radio jet (Marscher et al. 2002; Chatterjee et al. 2009) reveals a clear connection between the accretion disk and the radio jet.

In this paper we present the first association of γ-ray emission and the ejection of new superluminal components in a FRI radio galaxy, 3C 120. This resembles the recent findings on the FRII radio galaxy 3C 111 (Grandi et al. 2012b). We present the radio data set analyzed in this study, as well as methods used to reduce radio data in Section 2; in Section 3 we present the analysis and results of the *Fermi*-LAT data; in Section 4 we study the radio emission at 15 and 43 GHz in the parsec scale jet; Section 5 presents the connection between the γ-ray and radio emission, and in Section 6 we discuss our findings.

The cosmological values adopted from Planck's results (Planck Collaboration et al. 2014) are $\Omega_m = 0.3$, $\Omega_\Lambda = 0.7$, and $H_0 = 68\ \mathrm{km\ s^{-1}\ Mpc^{-1}}$. With these values, at the redshift of 3C 120 ($z = 0.033$) 1 mas corresponds to a linear distance 0.67 pc, and a proper motion of 1 mas $\mathrm{yr^{-1}}$ corresponds to an apparent speed of $2.21c$.

2. RADIO DATA ANALYSIS

To study the structure of the radio jet in 3C 120 we have collected data from two of the most extended Very Long Baseline Array (VLBA) monitoring programs: the MOJAVE[11] and the VLBA-BU-BLAZAR programs.[12] This radio data set consists of 46 epochs of VLBA data at 15 GHz taken from the MOJAVE survey, covering the observing period from 2008 June to 2013 August, and 21 epochs of VLBA data at 43 GHz from the VLBA-BU-BLAZAR program, covering the period from 2012 January to 2014 May.

The reduction of the VLBA 43 GHz data has been performed using a combination of `AIPS` and `Difmap` packages, as described in Jorstad et al. (2005). VLBA data at 15 GHz have been calibrated by the MOJAVE team, following the procedure described in Lister et al. (2009a). For comparison across epochs all the images have been convolved with a mean beam of 0.3×0.15 and 1.2×0.5 mas for the VLBA-BU-BLAZAR and MOJAVE programs, respectively.

To determine the structural changes in the radio jet we have modeled the radio emission through fitting of the visibilities to circular Gaussian components using `Difmap` (Shepherd 1997). Fitted values for each component are the flux density, separation and position angle (PA) from the core, and size. These are tabulated in Tables 1 and 2 for the 15 and 43 GHz data, respectively.

[11] http://www.physics.purdue.edu/MOJAVE/
[12] http://www.bu.edu/blazars/research.html

3. *FERMI*-LAT DATA ANALYSIS

The LAT data collected during 72 months of operation (from 2008 August 4 to 2014 August 4)[13] were analyzed using the *Fermi*-LAT ScienceTools software (version v9r32p5) and the P7REP_SOURCE_V15 set of instrument response functions (Ackermann et al. 2012).[14] The time intervals when the rocking angle of the LAT was greater than 52° were rejected and a cut to select a maximum zenith angle of 100° of the events was applied to exclude γ-rays originating from cosmic ray interactions with the Earth's atmosphere.

The detection significance of a source is provided by the $\mathrm{TS} = 2[\log L(\text{source}) - \log L(\text{no source})]$, where $L(\text{source})$ is the maximum likelihood value for a model with an additional source at a specified location and $L(\text{no source})$ is the maximum likelihood value for a model without the additional source (Mattox et al. 1996). When the TS is less than 10 or the ratio of the flux uncertainty to the flux is more than 0.5, a 2σ upper limit of the flux is provided. Depending on the TS value, the upper limits are calculated using the profile ($\mathrm{TS} \geqslant 1$) or the Bayesian ($\mathrm{TS} < 1$) method as described in the second LAT catalog (2FGL catalog; Nolan et al. 2012). All errors reported in the figures or quoted in the text are 1σ statistical errors. The estimated systematic errors on the flux, 10% at 100 MeV, decreasing to 5% at 560 MeV, and increasing to 10% at 10 GeV, refer to uncertainties on the effective area of the instrument.[15]

3.1. The 72 Month Average Spectrum

We performed both binned and unbinned likelihood analyses following the standard LAT data analysis procedures, obtaining consistent results. Here we present results from binned analyses to be consistent with published data (Ackermann et al. 2011). We accumulated 72 months of data to obtain the average γ-ray spectral properties of the source. The adopted model included all 2FGL sources within 15° of 3C 120 (R.A.(J2000) = 68°.2962313, decl.(J2000) = 5°.3543389). The studied source was modeled with a power law. All spectral parameters of the sources more than 10° from the center of the Region of Interest (RoI) were fixed to the 2FGL values. The Galactic diffuse emission was modeled using the standard diffuse emission model *gll_iem_v05_rev1.fit* while isotropic γ-ray emission and the residual cosmic ray contamination in the instrument were modeled using the template *iso_source_v05.txt*.

3C 120 was detected in the 100 MeV–100 GeV band with a TS value of 107 ($\sim 10\sigma$). The source is steep (photon index $\Gamma = 2.7 \pm 0.1$) and weak with a flux of $F_{>100\mathrm{MeV}} = 2.5 \pm 0.4 \times 10^{-8}$ photon $\mathrm{cm^{-2}\ s^{-1}}$, in agreement with the result of Abdo et al. (2010). As noted by the same authors, a Flat Spectrum Quasar, PKS 0423+05, is located at only ~1.6 degrees from the radio galaxy. In our analysis, the blazar is soft ($\Gamma = 2.6 \pm 0.1$) and slightly fainter ($F_{>100\mathrm{MeV}} = 1.77 \pm 0.36) \times 10^{-8}$ photon $\mathrm{cm^{-2}\ s^{-1}}$) than 3C 120.

[13] Mission Elapsed Time (MET) Start Time = 239557417:MET End Time = 428803203.
[14] Science Tools and instrument response functions are available from the *Fermi* Science Support Center: http://fermi.gsfc.nasa.gov/ssc/data/analysis.
[15] http://fermi.gsfc.nasa.gov/ssc/data/analysis/LAT_caveats_pass7.html

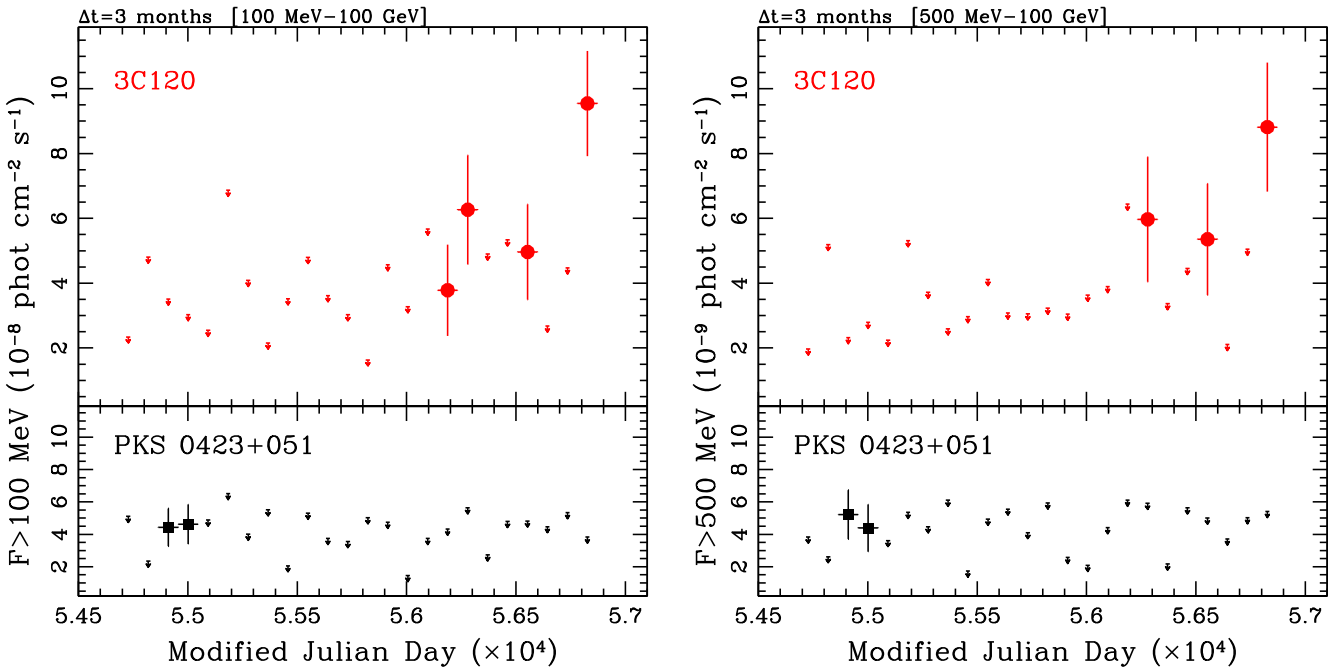

Figure 1. *Fermi*-LAT light curves of 3C 120 covering 72 month of survey (from 2008 August 4 to 2014 August 6) obtained considering two different energy bands: 100 MeV–100 GeV (left panel) and 500 MeV–100 GeV (right panel). A bin width of 3 months is adopted. A 2σ upper limit flux is shown (arrow) when the source is not detected (TS < 10). For comparison the light curves of the nearby FSRQ (PKS 0423+051) at 1°.6 from 3C 120 are also shown in the same energy ranges. There is not significant overlapping, as 3C 120 and PKS 0423+051 appear to be active in different time intervals.

Table 1
VLBA 15 GHz Model-fit Components' Parameters

VLBA 15 GHz						
Epoch (year)	Epoch (MJD)	Name	Flux (mJy)	Distance From C0 (mas)	Pos. Angle (°)	FWHM (mas)
2008.48	54642.50	C0	768 ± 38	···	···	0.31 ± 0.20
	···	C1	271 ± 14	0.65 ± 0.08	−115.2 ± 6.7	0.49 ± 0.16
	···	E0	117 ± 6	3.51 ± 0.24	−112.1 ± 3.6	0.79 ± 0.47
	···	E1	392 ± 20	1.50 ± 0.04	−109.3 ± 1.4	0.32 ± 0.08
	···	E1a	429 ± 21	1.14 ± 0.04	−106.2 ± 1.7	0.33 ± 0.08
2008.58	54677.50	C0	604 ± 30	···	···	0.22 ± 0.17
	···	C1	443 ± 22	0.35 ± 0.03	−115.8 ± 5.3	0.31 ± 0.07
	···	E0	123 ± 6	3.77 ± 0.26	−111.2 ± 3.7	0.88 ± 0.53
	···	E1	455 ± 23	1.75 ± 0.04	−109.9 ± 1.3	0.38 ± 0.09
	···	E1a	740 ± 37	1.31 ± 0.04	−110.0 ± 1.7	0.48 ± 0.09

(This table is available in its entirety in machine-readable form.)

3.2. Light Curves

Gamma-ray light curves were produced by dividing the analyzed time interval in temporal segments and repeating the likelihood analysis with only the normalizations of the sources within 10° free to vary. The spectral slopes of all the sources in the RoI were kept fixed to the best fit values of the 72 month likelihood analysis.

At first we produced a light curve from 2008 August 4 to 2014 August 4 with a bin size of 3 months in the 100 MeV–100 GeV energy band. The light curve shown in Figure 1 (left upper panel) indicates that 3C 120 was active starting from 2012. Abdo et al. (2010) reported also a detection between 2008 November and 2009 February. Our new analysis, which was performed with up-dated background files and new instrument response functions, provides only a flux upper limit for the same time interval (second bin of the light curve). Although we cannot claim a detection, the calculated TS value is however high (TS = 9.2, corresponding to $\sim 3\sigma$) and only slightly below the usually adopted detection threshold (TS = 10).

Considering that PKS 0423+051 is at only 1°.6 from 3C120, that both sources have steep spectra and, that the LAT point-spread function (PSF) is very broad at MeV energies, we decided to explore the 3 month light curve of the quasar to check for possible confusion effects. As shown in Figure 1, PKS 0423+051 and 3C 120 flare in different periods and exhibit light curves with different patterns, suggesting a negligible (mutual) contamination.

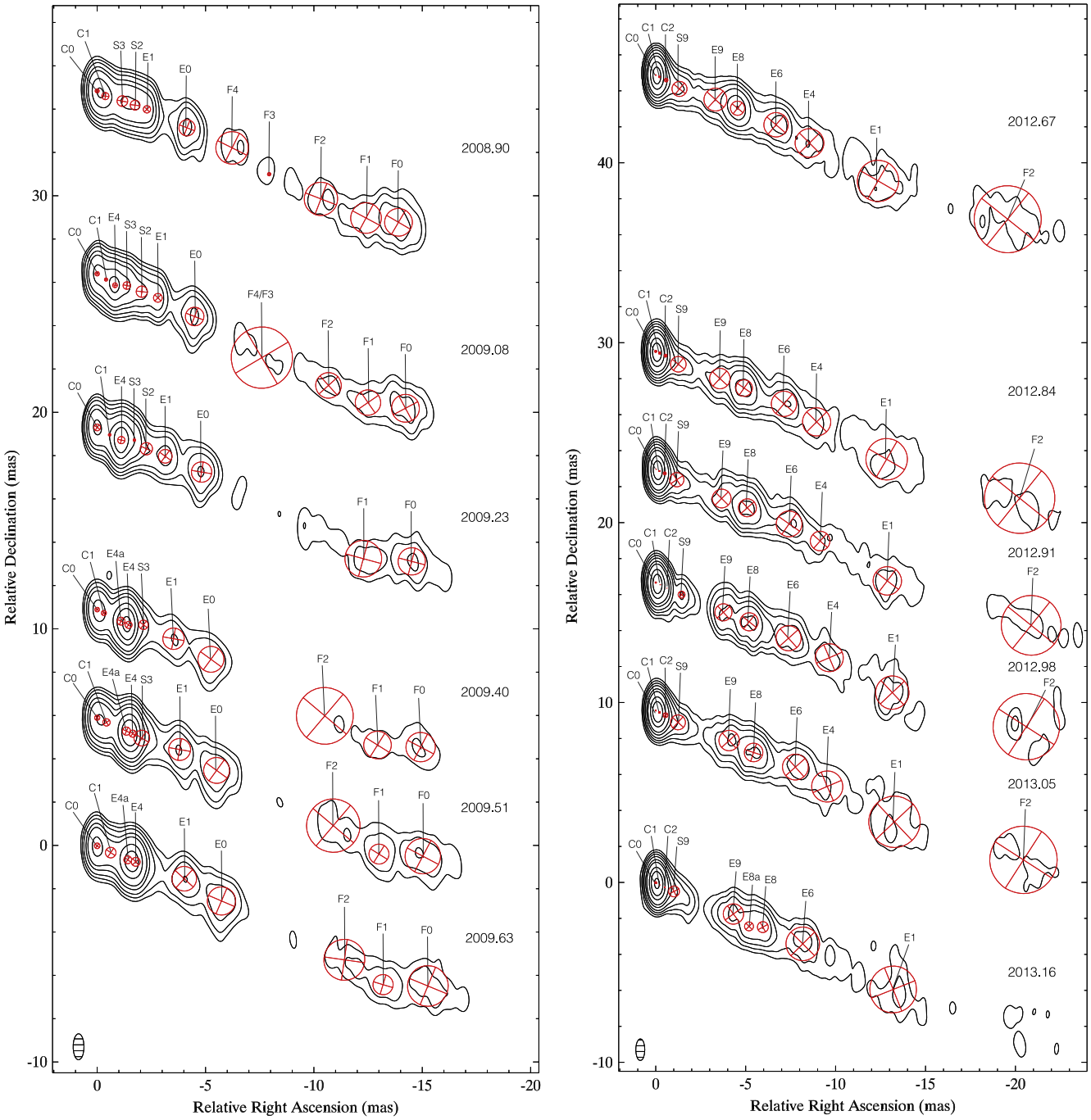

Figure 2. Sequence of total intensity 15 GHz VLBA images from the MOJAVE monitoring program of 3C 120 with a common restoring beam of 1.2 × 0.5 mas at 0°. The separation among images is proportional to the time elapsed between observing epochs. Contours are traced at 0.0015, 0.004, 0.009, 0.02, 0.05, 0.1, 0.3, 0.6, 1.2 Jy. Red circles represent model-fit components.

As further test, we also performed a variability study considering only photons with energy >500 MeV. Above this energy, the 68% containment angle (i.e., the radius of the circle containing 68% of the PSF) is indeed comparable or smaller than the separation of the two sources. The 500 MeV−100 GeV light curves (Figure 1, right panel) are similar to those obtained taking also into account softer photons, supporting the previous conclusion on negligible confusion effects.

Finally, we reduced the integration time interval of each bin to 15 days to better constrain the time of the γ-ray detections, shown in Table 3. In this case the analysis has been extended until 2014 October to confirm the flare at the end of 2014 September reported in Tanaka et al. (2014). Our analysis yields a γ-ray flux of $2.52 \pm 0.86 \times 10^{-8}$ photon cm^{-2} s^{-1} in MJD 56924–56939 for the 2014 September event (see Table 3).

4. THE PARSEC SCALE JET AT 15 AND 43 GHz

4.1. VLBA Data at 15 GHz

The study of the jet evolution at 15 GHz has been performed on the series of 46 VLBA images obtained by the MOJAVE monitoring program—a subset of these images is displayed in

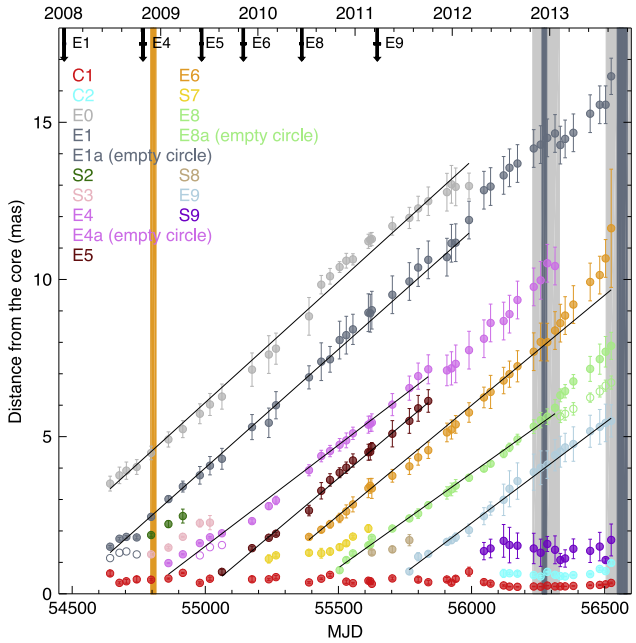

Figure 3. Distance from the core vs. time for the 15 GHz model-fit components with linear fits overlaid. Downward black arrows mark the time of ejection of each component. Gray vertical lines indicate γ-ray detections in the 15 day bin (dark gray) and 3 month bin (light gray) light curves in the energy band 500 MeV–100 GeV. The orange vertical line marks the optical flare reported in Kollatschny et al. (2014) (see text).

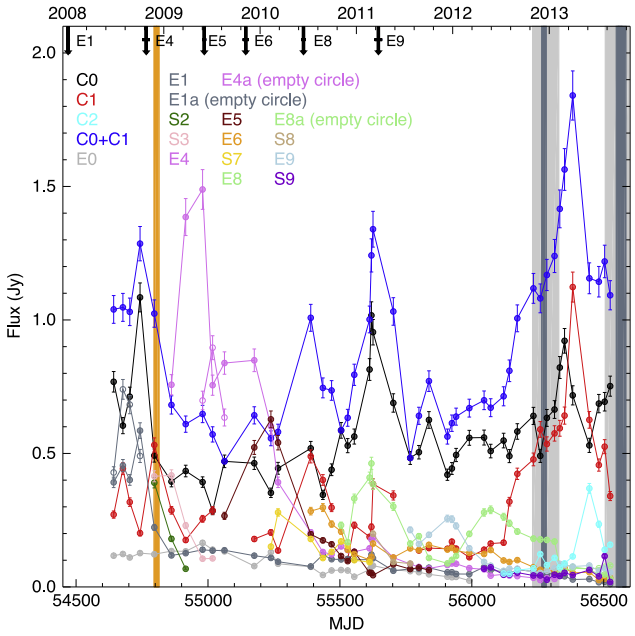

Figure 4. Light curves of the 15 GHz model-fit components, including the added total flux density of the core and component C1 (C0+C1). Arrows and vertical lines are as indicated in Figure 3.

Table 2
VLBA 43 GHz Model-fit Components' Parameters

VLBA 43 GHz						
Epoch (year)	Epoch (MJD)	Name	Flux (mJy)	Distance From c0 (mas)	Pos. Angle (°)	FWHM (mas)
2012.07	55953.50	c0	708 ± 43	···	···	0.08 ± 0.03
	···	d7	34 ± 13	0.13 ± 0.01	−124.8 ± 11.2	0.13 ± 0.04
	···	d10	346 ± 26	0.13 ± 0.01	−123.7 ± 8.6	0.13 ± 0.03
2012.18	55991.50	c0	756 ± 45	···	···	0.08 ± 0.03
	···	d7	66 ± 16	0.28 ± 0.05	−123.7 ± 20.4	0.16 ± 0.03
	···	d10	264 ± 22	0.13 ± 0.02	−126.2 ± 11.5	0.14 ± 0.03
2012.25	56019.50	c0	372 ± 26	···	···	0.06 ± 0.03
	···	d7	42 ± 13	0.41 ± 0.08	−122.8 ± 14.2	0.18 ± 0.03
	···	d10	186 ± 18	0.13 ± 0.01	−113.1 ± 6.1	0.08 ± 0.03

(This table is available in its entirety in machine-readable form.)

Figure 2, where contours represent the total intensity with model-fit components (red circles) overlaid.

We detected in total 25 components, apart from the core, although some of them characterize more probably the underlying flux density than knots that have been ejected from the core and move along the jet. The radio core is usually defined as the bright, compact feature at the upstream end of the jet, which may correspond to a recollimation shock (i.e., Gómez et al. 1997) at millimeter wavelengths and to the optically thin–thick transition at centimeter wavelengths.

Components E-F and C are robustly identified moving and standing features, respectively, and the rest of the model-fit components are required by the data, but cannot be cross-identified across the epochs and may represent, e.g., emission from the underlying jet flow. The core, identified with component C0, is considered stationary across epochs. Plots of the separation from the core and flux density evolution of the fitted components are shown in Figures 3 and 4, respectively.

We fit the trajectories with respect to the core for all the superluminal knots that can be followed for a significant number of epochs, as plotted in Figure 3. In order to have a better determination of the time of ejection of each component, namely the time when a new knot crosses the radio core, we use linear fits for the component separation versus time. Note that in some cases we have found evidence for components merging, splitting, or a clear acceleration in their motion (e.g., Homan et al. 2009, 2015). In those cases we have considered only the initial epochs with a clear linear fit, as we are mainly

interested in determining the time of ejection of each component. The time of ejection, angular and apparent velocities of the components are tabulated in Table 4.

We find that superluminal components move with apparent velocities between 5 and 6*c*, in agreement with previous findings (Gómez et al. 2001, 2008, 2011; Jorstad et al. 2005). This agrees also with recent MOJAVE results (Lister et al. 2013) where the 3C 120 kinematics, together with the radio galaxy 3C 111, departs from the others in the sample. These two radio galaxies seem to be the only ones displaying clear superluminal motions and with apparent speeds that do not commonly change with distance from the core.

From 2008 June to the beginning of 2012a stationary feature, C1, is found at a distance that shifts between ∼0.4–0.7 mas from the core. We identify this component with that reported by León-Tavares et al. (2010) at 0.72 ± 0.25 mas from the core, which is assumed by the authors to be related to optical flares when new components cross its position. Starting in 2012 the innermost 1 mas region of the jet changes, so that two stationary components can be found, C1 and C2. An extra component, labeled S9, is also required to fit some extended and weak flux density at ∼1.5 mas from the core.

As can be seen in Figures 2 and 4, the presence of two stationary components (C1 and C2) within the innermost 1 mas is associated with an increase in flux density and a more extended structure of the core. Component C1 is observed to progressively increase its flux density between mid 2012 and the beginning of 2013, when both the core and C1 are in a high flux density state. Three months later component C2 also shows an increase in flux density. These changes in the innermost structure of the jet are associated with the ejection of a new component, d11, revealed by the 43 GHz VLBA data (see Section 4.2), which extends our study of the jet until 2014 May.

Two other radio flares in the core have been also observed, one at the end of 2008 (2008.76 ± 0.10 year) and a second one at the beginning of 2011 (2011.15 ± 0.05 year). The flare in 2011 is associated with the ejection of a weak radio component from the core, E9, for which we estimate the time of ejection in 2011.23 ± 0.04.

The radio core flare at the end of 2008 is instead associated with the ejection of a bright superluminal knot, E4, in 2008.82 ± 0.04 year. The light curves of the different components shown in Figure 4 reveal the unusually large flare experienced by E4. By mid 2009 it has doubled its flux density, reaching a peak of ∼1.5 Jy and becoming brighter than the core itself. During the high state of flux density of E4 another component, named E4a, appears very close to it, suggesting an increase in extension of component E4 during the flare, as can be seen in Figures 2–4. In this case we consider more appropriate to take into account a flux-density-weighted distance between that of E4 and E4a to estimate the distance from the core of the new component E4 during its high state of flux density. The same method is used for components E1 and E1a, as we considered E1a an extension of E1 soon after this component is ejected from the core at the beginning of 2008. A similar splitting of components was also observed previously in 43 GHz VLBA images of 3C 120 (Gómez et al. 2001).

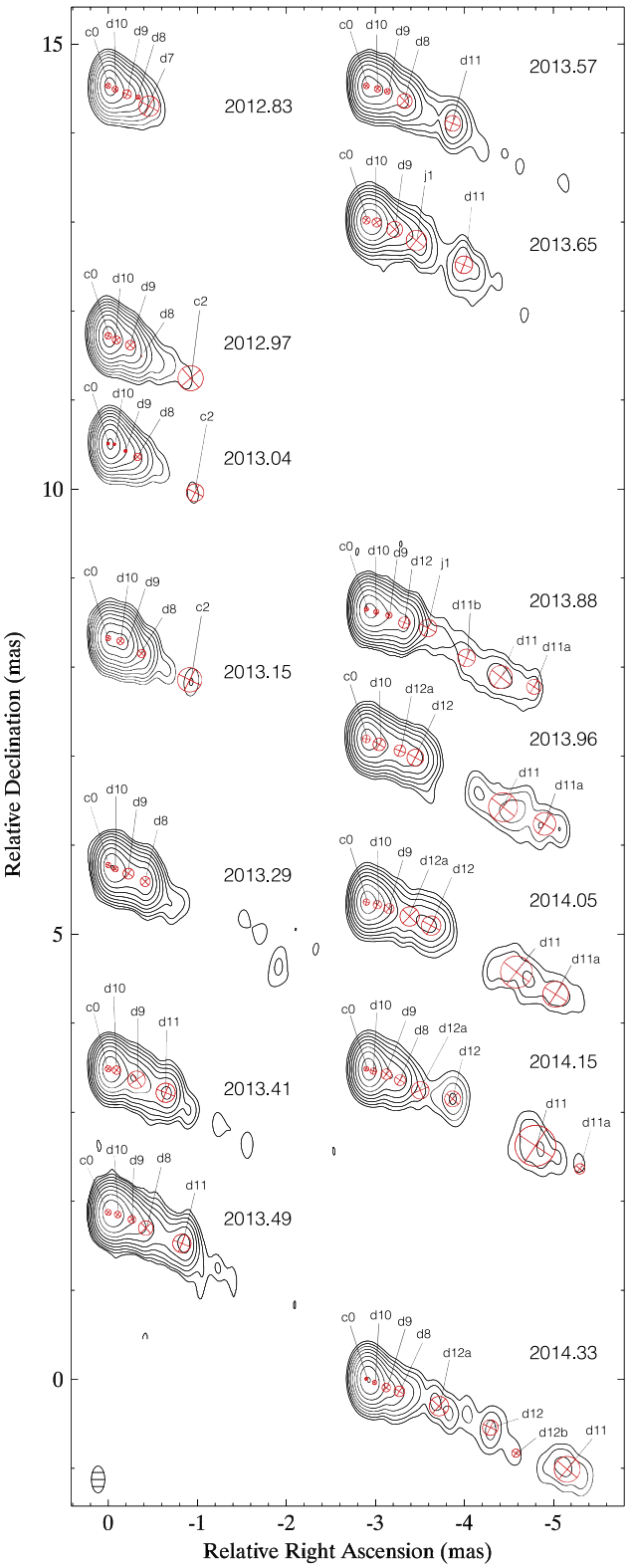

Figure 5. Sequence of total intensity 43 GHz VLBA images from the VLBA-BU-BLAZAR monitoring program of 3C 120 with a common restoring beam of 0.3 × 0.15 mas at 0°. Red circles represent modelfits components. Contours are traced at 0.16%, 0.35%, 0.77%, 1.7%, 3.77%, 8.33%, 18.41%, 40.71%, 90% of the peak intensity, 1.82 Jy beam^{-1}.

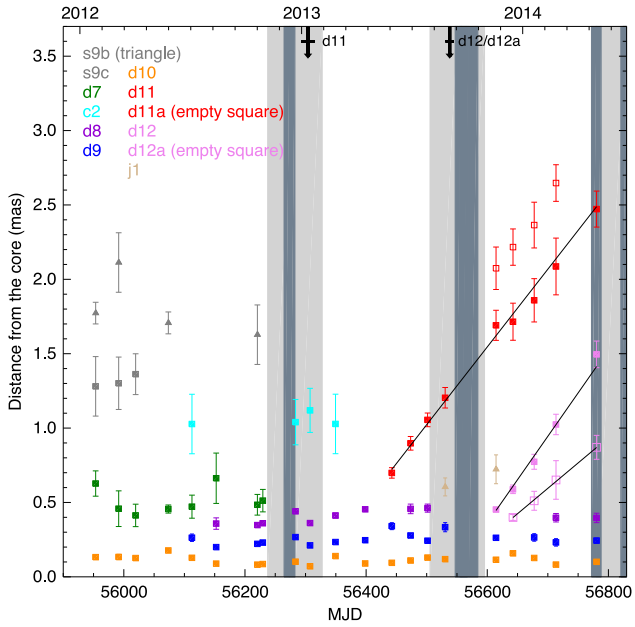

Figure 6. Distance from the core vs. time for the 43 GHz model-fit components with linear fits overlaid. Downward black arrows mark the time of ejection of each component. Gray vertical lines indicate γ-ray detections in the 15 day bin (dark gray) and 3 month bin (light gray) light curves in the energy band 500 MeV–100 GeV.

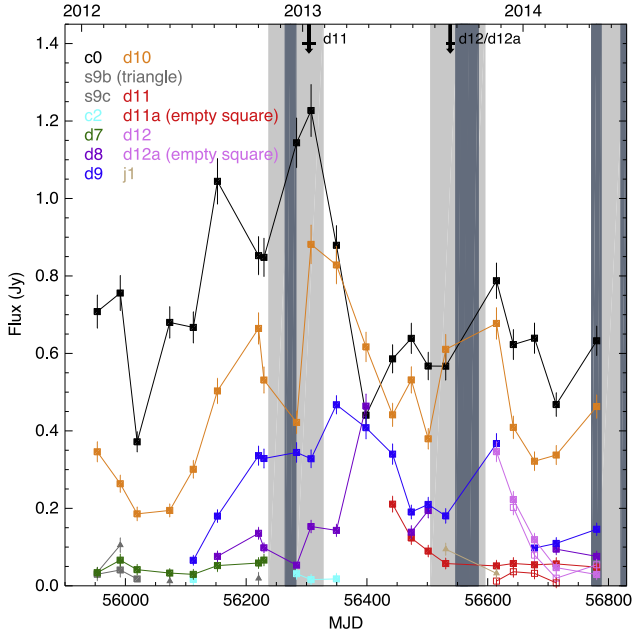

Figure 7. Light curves of the 43 GHz model-fit components. Arrows and vertical lines are as indicated in Figure 6.

The extended emission structure of components E1 and E4 (associated with components E1a and E4a) is consistent with Aloy et al. (2003) relativistic hydrodynamic simulations, where the passage of a new perturbation from a series of recollimation shocks results in extended emitting regions due to light-travel time delays between the front and the back of the perturbation.

Figure 4 shows also the light-curve obtained from adding the flux densities of C0 and C1. The stationary component C1 is usually located at a distance from the core of the order or smaller than the observing beam, therefore in many epochs it is difficult to disentangle its flux density from that of the core. For instance, the combination of the C0+C1 flux density reveals a high state leading to the ejection of component E8 in mid 2010. It is also particularly remarkable the increase in flux density of the C0+C1 complex in mid 2013 leading to the ejection of a new component, d11, seen at 43 GHz (see below).

4.2. VLBA Data at 43 GHz

We modeled the 43 GHz jet in the same manner as for the 15 GHz data, finding a total of 16 components, although as in the case of the 15 GHz data, some of them are most probably related to the underlying continuum flow and it is difficult to follow them along the jet. In each epoch we identify the core with c0 and we consider it a stationary feature.

Figure 5 shows a sequence of VLBA 43 GHz images in total intensity, where red circles represent model-fit components. The displayed images cover the observing period from 2012 October to 2014 May, when 3C 120 was detected at γ-ray frequencies.

As observed in the 15 GHz data, starting in mid 2012 we find an increase in the flux density and extension of the core, requiring up to three stationary components, d10, d9, and d8, to model the innermost 0.5 mas structure (see Figures 6 and 7). Because of the different angular resolution and opacity with respect to that obtained at 15 GHz, it is difficult to establish a one-to-one connection among the components at 43 and 15 GHz for the innermost jet region. We tentatively identify components s9b and s9c with substructures of component S9 seen at 15 GHz. Furthermore, during the enhanced activity of the source starting in mid 2012 it is not clear whether d10, d9, and d8 at 43 GHz—and C1, C2 at 15 GHz—correspond to actual physical structures in the jet, like recollimation shocks, or they trace the underlying emission of the jet.

The radio core persists in a flaring state until 2013 January. After this, the peak in flux density moves from the core along the jet, crossing progressively the three stationary features close to it (d10, d9 and d8). When the perturbation crosses the last stationary component, d8, we can clearly discern a new knot, d11, that emerges from the first 0.5 mas in 2013.4 years (see Figure 5). From the progressive flaring of stationary features close to the core we can infer the extension of the crossing emitting region, obtaining $\sim$0.35 mas. This is significantly larger that the FWHM obtained from the model-fit of d11 (see Table 2), which suggests that d11 is in fact part of a more extended region, resembling the results obtained from relativistic hydrodynamical simulations (Aloy et al. 2003). Fitting of the separation versus distance for d11 yields a proper motion of 1.91 ± 0.09 mas yr^{-1}, which corresponds to an apparent velocity of $4.22 \pm 0.22c$. The estimated time of ejection, that is, when component d11 crossed the radio core at 43 GHz, is 2013.03 $\pm$ 0.03.

A similar situation takes place also in the second half of 2013, when the core, together with components d10 and d9, starts to bright and a new component, d12, appears at $\sim$0.45 mas. We note also that another component, d12a, appears very close in time and position to component d12, although it displays a significantly slower proper motion. Component d12 moves at 2.1 ± 0.2 mas yr^{-1} ($4.7 \pm 0.3c$), while component d12a moves at 1.2 ± 0.2 mas yr^{-1} ($2.6 \pm 0.5c$). We note, however, that the estimated time of ejection for d12 and d12a, 2013.67 $\pm$ 0.02 year and 2013.64 $\pm$ 0.07 year,

Table 3
γ-ray Detections of 3C 120 in the Energy Range 0.5–100 GeV with a Bin Size of 15 Days

MJD	Date	Flux	Err	TS
56264–56279	2012 Dec 03–2012 Dec 18	1.41	0.60	10.6
56549–56564	2013 Sep 14–2013 Sep 29	1.65	0.54	21.6
56564–56579	2013 Sep 29–2013 Oct 14	1.31	0.53	13.3
56774–56789	2014 Mar 27–2014 May 12	1.15	0.52	10.4
56819–56834	2014 Jun 11–2014 Jun 26	1.47	0.59	13.8
56924–56939	2014 Sep 24–2014 Oct 09	2.52	0.86	18.4

Notes. We report the integration time in MJD and date, the flux with the corresponding error in 10^{-8} photon cm^{-2} s^{-1} and the TS value associated to each γ-ray detection.

Table 4
Time of Ejection, Proper Motions and Apparent Velocities of Model-fit Components at 15 GHz

Name	T_{ej} (year)	μ (mas yr^{-1})	β_{app}
E0	2007.29 ± 0.06	2.81 ± 0.05	6.21 ± 0.11
E1	2008.01 ± 0.02	2.76 ± 0.05	6.10 ± 0.11
E4	2008.82 ± 0.04	2.35 ± 0.05	5.19 ± 0.11
E5	2009.42 ± 0.02	2.60 ± 0.06	5.75 ± 0.13
E6	2009.85 ± 0.03	2.56 ± 0.05	5.66 ± 0.11
E8	2010.45 ± 0.02	2.20 ± 0.03	4.86 ± 0.07
E9	2011.23 ± 0.04	2.32 ± 0.09	5.12 ± 0.19

respectively, is the same within the uncertainties. Both components therefore originated simultaneously in the millimeter very long baseline interferometry (VLBI) core, although they propagate at quite different velocities afterwards.

Time delays stretch the shocked emission in the observer's frame, so that with the necessary angular resolution multiple sub-components associated with a single shock could be distinguished in the jet, but in this case they would have similar apparent velocities, in contrast with what it is observed for components d12 and d12a. Trailing components have a smaller velocity than the leading perturbation, but they are released on the wake of main perturbation (Agudo et al. 2001), instead of being ejected from the core, as occurs for component d12a. On the other hand, relativistic hydrodynamic simulations show that a single perturbation in the jet inlet leads to the formation of a forward and reverse shock (Gómez et al. 1997; Aloy et al. 2003; Mimica et al. 2009). Therefore, the fact that components d12 and d12a are ejected from the core at the same time but with different velocities suggests that they may correspond to the forward and reverse shock of a perturbation.

5. CONNECTION BETWEEN γ-RAY AND RADIO EMISSION

Our analysis of the *Fermi*-LAT data (see Figure 1 and Table 3) shows a prolonged γ-ray activity in the radio galaxy 3C 120 between 2012 December and 2014 September–October, when the source reaches a flux of $F_{>500\mathrm{MeV}} = 2.5 \pm 0.8 \times 10^{-8}$ photon cm^{-2} s^{-1}, about an order of magnitude larger than in previous detections. Three clear periods of γ-ray activity are found at the end of 2012 (56264–56279 MJD), 2013 September–October (56549–56579 MJD), and 2014 May–October (56774–56939 MJD).

The γ-ray activity in 2012 December is accompanied by an increase in the radio core flux density, as well as in the innermost stationary components, at both 15 and 43 GHz (see Figures 4 and 7), leading to the ejection of component d11 in 2013.13 ± 0.03 (see also Figure 6). From the estimated proper motion of d11 we infer that in the last epoch of the 15 GHz data this component is still in the innermost region of the jet as imaged at 15 GHz, crossing the stationary component C2.

After this first γ-ray detection the source remains in a quiescent state until 2013 August, when another γ-ray event covering the period from 2013 August to October is detected. The 15 days binning analysis (see Table 3) constrains the main flaring activity to 2013 September–October (56549–56579 MJD), coincident with the flaring of the radio core at 43 GHz and the ejection of the d12–d12a pair of components (see Figures 5–7).

There is also indication of the beginning of a new flaring activity in the 43 GHz radio core associated with the last γ-ray flaring activity starting in 2014 May, but further VLBI images are required to confirm the ejection of a new component in this event.

We therefore can conclude that there is a clear association between the γ-ray and radio emission in 3C 120, such that every period of γ-ray activity is accompanied by flaring of the VLBI radio core and subsequent ejection of a new superluminal component in the jet. However, not all ejections of superluminal components are related to enhanced γ-ray emission, detectable by *Fermi*-LAT, as occurred for components E4, E5, E6, E8, and E9. The case of component E4 is particularly interesting. Abdo et al. (2010) report a γ-ray detection in 2008 December, coincident with an increase of the 15 GHz radio core flux, leading to the ejection of E4 in 2008.82 ± 0.04. This is also coincident with an optical flare in 2008 December, as reported by Kollatschny et al. (2014). We also note that E4 reached a peak flux of ∼1.5 Jy, significantly larger than any other component seen in our analysis. Despite this intense activity in the optical and radio core, our analysis of the *Fermi* data during this period does not provide a clear detection in γ-rays, although the calculated TS (corresponding to $\sim 3\sigma$) is only slightly smaller than the usually adopted detection threshold.

6. DISCUSSION

6.1. Motion of Components Along the Jet

The debate on the origin and location of the γ-ray emission in blazars has gained added interest since the launch of the *Fermi* satellite. Much of the current discussion lies in whether γ-rays are produced upstream of the millimeter VLBI core, as suggested by some γ-ray and radio correlations (e.g., Rani et al. 2013a, 2014) and the observed γ-ray spectral break at few GeVs (Abdo et al. 2009; Finke & Dermer 2010; Poutanen & Stern 2010; Tanaka et al. 2011; Rani et al. 2013b) or downstream, as suggested by coincidence of γ-ray flares with either the appearance of new superluminal components (e.g., Jorstad et al. 2010, 2013) or the passage of moving components through a stationary jet feature (Schinzel et al. 2012; Marscher 2013).

As observed in several blazars (Jorstad et al. 2010, 2013; Ramakrishnan et al. 2014), the interaction between traveling features and the stationary radio core appears to be a necessary condition for the production of γ-ray photons in 3C 120, but it is clearly not enough. Therefore, to understand the γ-ray

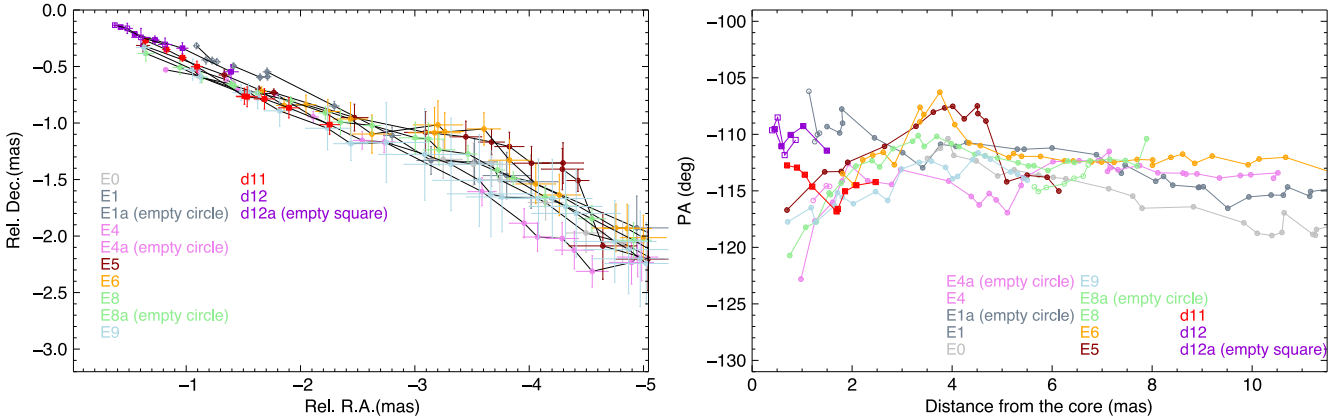

Figure 8. Positions (*l*eft) and position angles as a function of distance from the core (*r*ight) for the model-fit components at 15 (circles) and 43 GHz (squares). For clarity errors bars are shown only in the plot of the components' position.

emission in 3C 120, and more generally in AGN, it is necessary to address the question of what physical changes in the jet can produce γ-ray emission.

We note that the beginning of the γ-ray activity in 3C 120 occurs after a sustained period of low activity in the jet. As indicated in Table 4, during the time period analyzed new components are seen in the jet of 3C 120 roughly every 8 months; however, no new components are detected in the jet between the ejection of E9 in 2011.23 $\pm$ 0.04 and component d11 in 2013.03 $\pm$ 0.03, implying a lack of activity in the jet for almost 2 years. Note that after the ejection of d11 the source resumes its activity with the ejection of component d12, again roughly 8 months later.

Analysis of the components' proper motions (see Table 4) reveals a clear pattern of decreasing apparent velocities, from the 6.21 $\pm$ 0.11c of E0 to 5.12 $\pm$ 0.19c of E9. Furthermore, when the core resumes the ejection of components after a 2 years inactivity, the apparent velocities measured for d11 and d12 have further decreased to 4.22 $\pm$ 0.22c and 4.70 $\pm$ 0.31c, respectively. Component d12a shows an even smaller velocity of 2.75 $\pm$ 0.45c, but we believe this component differs for the other components seen previously in 3C 120 in which it is probably associated with a reserve shock.

Note that model-fits at 43 and 15 GHz trace the motion of components continuously throughout the jet. We also find no evidence for acceleration (only component E6 shows a clear acceleration at ~8 mas from the core), hence we consider that the proper motions measured at 43 GHz provide a good estimation for the expected values should these components be detected later on at 15 GHz, reassuring our finding for a progressive decrease in the apparent velocity of the components from ~6.2c to 4.2c in a time span of approximately 6.4 years, from 2007.3 to 2013.7. This progressive change in the apparent velocity of components could be due to a change in the velocity and/or orientation of the components. Considering that the 6.4 years time span measured roughly agrees with the 12.3 $\pm$ 0.3 year full period determined by the precessing jet model of Caproni & Abraham (2004), we favor the case in which it is produced by a change in the orientation of the components with respect to the observer.

Figure 8 shows the motion of components along the jet, as well as their PA with distance from the core. We observe that components E1-E1a (and presumably E0) are ejected with a PA of around -110° and they travel toward the southwest direction while the other components at 15 GHz are ejected with a PA between -117° and -123° and move initially in a less southern direction. Components E5 and E6 present a significant change in their velocity vectors at a distance of ~3 mas from the core, as observed previously for other components and interpreted as the interaction with the external medium or a cloud (Gómez et al. 2000, 2008). Components d11 and d12–d12a are ejected with a PA of around -110°, similar to that observed previously for E1-E1a. Note that in a precession model components E1 and d12 would have similar projected velocity vectors while differing in their orientation with respect to the observer. Despite the initially different PAs, components move following parallel paths after the initial ~4–5 mas. Rather than a precession of the whole jet, we therefore favor the model in which the jet consists of a broad funnel through which components—not filling the whole jet width—are ejected and travel at differ PAs, as supported also by previous observations of 3C 120 (Gómez et al. 2011) and other sources in the MOJAVE sample (Lister et al. 2013).

Considering that the slower apparent velocities of d11 and d12 are related to the first γ-ray detections, we conclude that these components are most likely ejected with a smaller viewing angle. This should increase the Doppler factor, leading to the enhanced γ-ray emission measured since the end of 2012, and a significant increase in the total flux of the core and innermost stationary features (see Figure 7). However, we cannot completely rule out the possibility that the smaller apparent velocities are just due to greater viewing angles, or slowing of the components' velocity.

It is possible to estimate the required minimum Lorentz factor, $\Gamma_{\rm min} = (1 + \beta_{\rm app}^2)^{1/2} = 6.3$, using the observed maximum apparent velocity of 6.2c. To minimize the required reorientation of the components, we can assume that the maximum apparent velocity is obtained for the angle that actually maximizes the apparent velocity, given by $\theta = \arccos(\beta)$, where β is the component's velocity in units of the speed of light. Using our previous estimation of $\Gamma_{\rm min} = 6.3$, we obtain a viewing angle of $\theta \sim 9\overset{\circ}{.}2$ for the maximum apparent velocity of 6.2c measured for component E0, in agreement with Hovatta et al. (2009). Given that the observed decrease in the apparent velocity is probably produced by a decrease in the viewing angle, the smallest observed apparent velocity of 4.2c for d11 requires $\theta \sim 3\overset{\circ}{.}6$. These values agree with the precession model of Caproni &

Abraham (2004), for which the authors estimate $\Gamma = 6.8 \pm 0.5$ and a variation of the viewing angle between $(6.3 \pm 0.^{\circ}8)$ and $(3.3 \pm 0.^{\circ}8)$. We should note however that our measured change in the apparent velocities is shifted from the periodicity phase predicted by Caproni & Abraham (2004) model.

This change in the orientation from $\theta \sim 9.^{\circ}2$ to $\theta \sim 3.^{\circ}6$ would lead to an increase in the Doppler factor from $\delta \sim 6.2$ to $\delta \sim 10.9$, enhancing the γ-ray emission above the flux detectable by *Fermi*.

In summary, all these evidence suggest that the observed γ-ray emission in 3C 120 depends strongly on the orientation of component's motion with respect to the observer, so that only when they are best oriented *and* a new superluminal component pass through the radio core a clear γ-ray detection is obtained.

Superluminal components are associated with shocks moving along the jet, hence the inferred values for the velocity—provided there is an estimation of the jet orientation—correspond to the pattern velocity of the shock, not the actual flow velocity. The detection of the forward and reserve shocks of the perturbation associated with d12 and d12a, respectively, allows to obtain a direct calculation of the jet bulk flow velocity. For the estimated viewing angle of $\sim 3.^{\circ}6$ during the ejection of components d12 and d12a we obtain the corresponding pattern velocities of $\Gamma_{\rm d12} = 6.7$ and $\Gamma_{\rm d12a} = 5$. Hence, we can conclude that the jet bulk flow velocity is restricted to be $5 \leqslant \Gamma_{\rm j} \leqslant 6.7$.

6.2. Gamma-ray Location and Emission Mechanism

Our first γ-ray detection at the end of 2012 is associated with the passage of component d11 through the millimeter VLBI core, whose time of ejection is coincident with the 3 months-bin γ-ray detection, and is $\sim$34 days (0.09 year) after the 15 days-bin γ-ray detection. On the other hand, Marscher et al. (2002) and Chatterjee et al. (2009) have measured a mean delay of 0.18 year ($\sim$66 days) between X-ray dips and the ejection of new superluminal components. Considering that most of the X-ray emission in 3C 120 originates from the disk-corona system, close to the central BH, we can consider this time delay as the distance in time between the BH and the millimeter VLBI core. A mean apparent motion of ~ 2 mas yr^{-1} corresponds to a rate of increase in projected separation from the core of ~ 0.24 pc yr^{-1}—or slightly smaller if we allow for some initial acceleration of the components.

The measured delay of 34 days between the 15 days-bin γ-ray detection and the passage of d11 from the millimeter VLBI core locates the γ-ray emission upstream of the millimeter VLBI core, at a distance about half of that between the BH and the core. Relativistic 3D hydrodynamic simulations of Aloy et al. (2003) show that time delays stretch significantly the observed size of components, so that our VLBI observations could detect only some portions of the component, depending on the strength of the forward/reverse shock and Doppler factor (i.e., viewing angle). Considering also that we have estimated for component d11 a size of ~ 0.35 mas (0.2 pc) once it is clearly detached from the core, it is possible that the 15 days-bin γ-ray detection could correspond to the passing of the forward section of the d11 perturbation through the millimeter VLBI core, while later on our VLBI images identify only the back section, as it is precisely seen in the numerical simulations of Aloy et al. (2003). In this case the flaring in γ-rays would more closely mark the crossing of the d11 perturbation through the millimeter VLBI core.

The second γ-ray event is instead associated with the ejection of components d12 and d12a. In this case the time of ejection of these two components is also coincident with the 3 months bin γ-ray detection, but the finer time sampling of the 15 day γ-ray light curve constrains the γ-ray production to $\sim$33 days after. Hence we conclude that in the second γ-ray event the high energy emission is produced downstream of the millimeter VLBI core, at a projected distance of ~ 0.13 pc from its position—smaller if we consider that the shock responsible for the γ-ray emission is the slower moving d12a.

Reverberation mapping studies of the broad-line-region (BLR) in 3C 120 suggest an inclined disk model with an extension from 12 ± 7 light days (~ 0.01 pc) to 28 ± 9 light days (~ 0.025 pc), from the BH (Grier et al. 2013; Kollatschny et al. 2014). These studies also found evidence of radial stratification in the BLR as well as infall and rotation related to the BH gravity. Therefore the BLR extends to about half of the estimated distance between the BH and the millimeter VLBI core, severely limiting the external photon field from the BLR at the location of the millimeter VLBI core. Hence we favor synchrotron self Compton as the mechanism for the production of γ-ray photons in the case of the second γ-ray event in late 2013, although we cannot discard the contribution from another external photon field, such the sheath or the external ionized cloud.

The external Compton process with photons coming from the BLR could be instead a possibility for the first γ-ray event, as our findings point to a γ-ray dissipation zone between the BH and the radio core, on the limit of the extension of the BLR.

The different orientation of the components within the broader jet funnel supports also a model in which they interact with the sheath of the jet (see also Gómez et al. 2000, 2008). In this case the observed γ-ray activity can be produced by Compton scattering of photons from the jet sheath, as proposed by Marscher et al. (2010) to explain the γ-ray activity seen in PKS 1510–089.

Grandi et al. (2012b) obtain similar results for the FRII radio galaxy 3C 111, associating the γ-ray activity with the ejection of a new radio component from the core, and confining the γ-ray dissipation region within 0.1 pc at a distance of almost 0.3 pc from the BH. These two radio galaxies have other similarities as they are both BLRGs and they show a connection between the radio jet and the corona-disk system (Marscher et al. 2002; Chatterjee et al. 2011). In addition, the apparent motions of superluminal components detected in their jets detach from those of the other radio galaxies in the MOJAVE sample (Lister et al. 2013).

This research has been supported by the Spanish Ministry of Science and Innovation grants AYA2010-14844, and AYA2013-40825 P, and by the Regional Government of Andalucía (Spain) grant P09-FQM-4784. The VLBA is an instrument of the National Radio Astronomy Observatory, a facility of the National Science Foundation of the USA operated under cooperative agreement by Associated Universities, Inc. (USA). This work has made use of data from the MOJAVE database that is maintained by the MOJAVE team (Lister et al. 2009b). This research was partly supported by the Russian Foundation for Basic Research grant 13-02-12103 and by the Academy of Finland project 274477.

REFERENCES

Abdo, A. A., Ackermann, M., Ajello, M., et al. 2009, ApJ, 707, 1310
Abdo, A. A., Ackermann, M., Ajello, M., et al. 2010, ApJ, 720, 912
Abramowski, A., Acero, F., Aharonian, F., et al. 2012, ApJ, 746, 151
Ackermann, M., Ajello, M., Albert, A., et al. 2012, ApJS, 203, 4
Ackermann, M., Ajello, M., Allafort, A., et al. 2011, ApJ, 743, 171
Agudo, I., Gómez, J.-L., Martí, J.-M., et al. 2001, ApJL, 549, L183
Aharonian, F., Akhperjanian, A. G., Bazer-Bachi, A. R., et al. 2006, Sci, 314, 1424
Aloy, M.-Á., Martí, J.-M., Gómez, J.-L., et al. 2003, ApJL, 585, L109
Caproni, A., & Abraham, Z. 2004, MNRAS, 349, 1218
Chatterjee, R., Marscher, A. P., Jorstad, S. G., et al. 2011, ApJ, 734, 43
Chatterjee, R., Marscher, A. P., Jorstad, S. G., et al. 2009, ApJ, 704, 1689
Finke, J. D., & Dermer, C. D. 2010, ApJL, 714, L303
Gómez, J. L., Marscher, A. P., Alberdi, A., Jorstad, S. G., & Agudo, I. 2001, ApJL, 561, L161
Gómez, J. L., Marscher, A. P., Alberdi, A., Jorstad, S. G., & García-Miró, C. 2000, Sci, 289, 2317
Gómez, J. L., Marscher, A. P., Jorstad, S. G., Agudo, I., & Roca-Sogorb, M. 2008, ApJL, 681, L69
Gómez, J. L., Martí, J. M., Marscher, A. P., Ibáñez, J. M., & Alberdi, A. 1997, ApJL, 482, L33
Gómez, J. L., Roca-Sogorb, M., Agudo, I., Marscher, A. P., & Jorstad, S. G. 2011, ApJ, 733, 11
Grandi, P., Torresi, E., & FERMI-LAT Collaboration 2012a, arXiv:1205.1686
Grandi, P., Torresi, E., & Stanghellini, C. 2012b, ApJL, 751, L3
Grier, C. J., Peterson, B. M., Horne, K., et al. 2013, ApJ, 764, 47
Hada, K., Giroletti, M., Kino, M., et al. 2014, ApJ, 788, 165
Harris, D. E., Massaro, F., Cheung, C. C., et al. 2011, ApJ, 743, 177
Homan, D. C., Kadler, M., Kellermann, K. I., et al. 2009, ApJ, 706, 1253
Homan, D. C., Lister, M. L., Kovalev, Y. Y., et al. 2015, ApJ, 798, 134
Hovatta, T., Valtaoja, E., Tornikoski, M., & Lähteenmäki, A. 2009, A&A, 494, 527
Jorstad, S. G., Marscher, A. P., Larionov, V. M., et al. 2010, ApJ, 715, 362
Jorstad, S. G., Marscher, A. P., Lister, M. L., et al. 2005, AJ, 130, 1418
Jorstad, S. G., Marscher, A. P., Smith, P. S., et al. 2013, ApJ, 773, 147
Kataoka, J., Stawarz, Ł., Cheung, C. C., et al. 2010, ApJ, 715, 554
Kollatschny, W., Ulbrich, K., Zetzl, M., Kaspi, S., & Haas, M. 2014, A&A, 566, A106
León-Tavares, J., Lobanov, A. P., Chavushyan, V. H., et al. 2010, ApJ, 715, 355
Lister, M. L., Aller, H. D., Aller, M. F., et al. 2009a, AJ, 137, 3718
Lister, M. L., Aller, M. F., Aller, H. D., et al. 2013, AJ, 146, 120
Lister, M. L., Cohen, M. H., Homan, D. C., et al. 2009b, AJ, 138, 1874
Maraschi, L., Chiappetti, L., Falomo, R., et al. 1991, ApJ, 368, 138
Marscher, A. P. 2013, in American Astronomical Society Meeting Abstracts, 221, 339.53
Marscher, A. P., Jorstad, S. G., Gómez, J.-L., et al. 2002, Nature, 417, 625
Marscher, A. P., Jorstad, S. G., Larionov, V. M., et al. 2010, ApJL, 710, L126
Mattox, J. R., Bertsch, D. L., Chiang, J., et al. 1996, ApJ, 461, 396
Mimica, P., Aloy, M.-A., Agudo, I., et al. 2009, ApJ, 696, 1142
Nolan, P. L., Abdo, A. A., Ackermann, M., et al. 2012, ApJS, 199, 31
Planck Collaboration, Ade, P. A. R., Aghanim, N., et al. 2014, A&A, 571, A16
Poutanen, J., & Stern, B. 2010, ApJL, 717, L118
Ramakrishnan, V., León-Tavares, J., Rastorgueva-Foi, E. A., et al. 2014, MNRAS, 445, 1636
Rani, B., Krichbaum, T. P., Fuhrmann, L., et al. 2013a, A&A, 552, A11
Rani, B., Krichbaum, T. P., Lott, B., Fuhrmann, L., & Zensus, J. A. 2013b, Advances in Space Research, 51, 2358
Rani, B., Krichbaum, T. P., Marscher, A. P., et al. 2014, A&A, 571, L2
Schinzel, F. K., Lobanov, A. P., Taylor, G. B., et al. 2012, A&A, 537, A70
Shepherd, M. C. 1997, in ASP Conf. Ser. 125, Astronomical Data Analysis Software and Systems VI, ed. G. Hunt & H. Payne, 77
Tanaka, Y. T., Cutini, S., Ciprini, S., et al. 2014, The Astronomer's Telegram, 6529, 1
Tanaka, Y. T., Stawarz, Ł., Thompson, D. J., et al. 2011, ApJ, 733, 19
Walker, R. C., Benson, J. M., Unwin, S. C., et al. 2001, ApJ, 556, 756

4.2 A multi-wavelength polarimetric study of the blazar CTA 102 during a Gamma-ray flare in 2012

The following article has been published in *The Astrophysical Journal* on November 1st, 2015 and it is presented here in its original form.

The reference for this article is: Casadio C., Gómez J. L., Jorstad S. G., Marscher A. P., et al., 2015b, ApJ, 813, 51.

The authors are: Carolina Casadio, José L. Gómez, Svetlana G. Jorstad, Alan P. Marscher, Valeri M. Larionov, Paul S. Smith, Mark A. Gurwell, Anne Lähteenmäki, Iván Agudo, Sol N. Molina, Vishal Bala, Manasvita Joshi, Brian Taylor, Karen E. Williamson, Arkady A. Arkharov, Dmitry A. Blinov, George A. Borman, Andrea Di Paola, Tatiana S. Grishina, Vladimir A. Hagen-Thorn, Ryosuke Itoh, Evgenia N. Kopatskaya, Elena G. Larionova, Liudmila V. Larionova, Daria A. Morozova, Elizaveta Rastorgueva-Foi, Sergey G. Sergeev, Merja Tornikoski, Ivan S. Troitsky, Clemens Thum, Helmut Wiesemeyer.

The Astrophysical Journal, 813:51 (14pp), 2015 November 1 doi:10.1088/0004-637X/813/1/51

A MULTI-WAVELENGTH POLARIMETRIC STUDY OF THE BLAZAR CTA 102 DURING A GAMMA-RAY FLARE IN 2012

Carolina Casadio[1], José L. Gómez[1], Svetlana G. Jorstad[2,3], Alan P. Marscher[2], Valeri M. Larionov[3,4], Paul S. Smith[5], Mark A. Gurwell[6], Anne Lähteenmäki[4,7], Iván Agudo[1], Sol N. Molina[1], Vishal Bala[2], Manasvita Joshi[2], Brian Taylor[2], Karen E. Williamson[2], Arkady A. Arkharov[8], Dmitry A. Blinov[3,9], George A. Borman[10], Andrea Di Paola[11], Tatiana S. Grishina[3], Vladimir A. Hagen-Thorn[3], Ryosuke Itoh[12], Evgenia N. Kopatskaya[3], Elena G. Larionova[3], Liudmila V. Larionova[3], Daria A. Morozova[3], Elizaveta Rastorgueva-Foi[4,13], Sergey G. Sergeev[10], Merja Tornikoski[4], Ivan S. Troitsky[3], Clemens Thum[14], and Helmut Wiesemeyer[15]
[1] Instituto de Astrofísica de Andalucía, CSIC, Apartado 3004, E-18080 Granada, Spain
[2] Institute for Astrophysical Research, Boston University, 725 Commonwealth Avenue, Boston, MA 02215, USA
[3] Astronomical Institute, St. Petersburg State University, Universitetskij Pr. 28, Petrodvorets, 198504 St. Petersburg, Russia
[4] Aalto University Metsähovi Radio Observatory, Metsähovintie 114, FI-02540 Kylmälä, Finland
[5] Steward Observatory, University of Arizona, Tucson, AZ 85716, USA
[6] Harvard-Smithsonian Center for Astrophysics, Cambridge, MA 02138, USA
[7] Aalto University Department of Radio Science and Engineering, P.O. Box 13000, FI-00076 Aalto, Finland
[8] Pulkovo Observatory, St. Petersburg, Russia
[9] University of Crete, Heraklion, Greece
[10] Crimean Astrophysical Observatory, Nauchnij, Ukraine
[11] INAF, Osservatorio Astronomico di Roma, Roma, Italy
[12] Department of Physical Sciences, Hiroshima University, Higashi-Hiroshima, Hiroshima 739-8526, Japan
[13] School of Maths Physics, University of Tasmania, Private Bag 37, Hobart, TAS 7001, Australia
[14] Instituto de Radio Astronomía Milimétrica, Granada, Spain
[15] Max-Planck-Institut für Radioastronomie, Bonn, Germany
Received 2015 July 27; accepted 2015 August 25; published 2015 October 28

ABSTRACT

We perform a multi-wavelength polarimetric study of the quasar CTA 102 during an extraordinarily bright γ-ray outburst detected by the *Fermi* Large Area Telescope in 2012 September–October when the source reached a flux of $F_{>100\ \mathrm{MeV}} = 5.2 \pm 0.4 \times 10^{-6}$ photons cm^{-2} s^{-1}. At the same time, the source displayed an unprecedented optical and near-infrared (near-IR) outburst. We study the evolution of the parsec-scale jet with ultra-high angular resolution through a sequence of 80 total and polarized intensity Very Long Baseline Array images at 43 GHz, covering the observing period from 2007 June to 2014 June. We find that the γ-ray outburst is coincident with flares at all the other frequencies and is related to the passage of a new superluminal knot through the radio core. The powerful γ-ray emission is associated with a change in direction of the jet, which became oriented more closely to our line of sight ($\theta \sim 1.^{\circ}2$) during the ejection of the knot and the γ-ray outburst. During the flare, the optical polarized emission displays intra-day variability and a clear clockwise rotation of electric vector position angles (EVPAs), which we associate with the path followed by the knot as it moves along helical magnetic field lines, although a random walk of the EVPA caused by a turbulent magnetic field cannot be ruled out. We locate the γ-ray outburst a short distance downstream of the radio core, parsecs from the black hole. This suggests that synchrotron self-Compton scattering of NIR to ultraviolet photons is the probable mechanism for the γ-ray production.

Key words: galaxies: active – galaxies: jets – quasars: individual (CTA 102) – techniques: interferometric – techniques: photometric – techniques: polarimetric

Supporting material: machine-readable tables

1. INTRODUCTION

The Blazar CTA 102 (B2230+114) is classified as a highly polarized quasar, characterized by optical polarization exceeding 3% (Moore & Stockman 1981). Its high variability at optical wavelengths (Pica et al. 1988; Osterman Meyer et al. 2009) and its spectral properties also identify it as an optically violent variable quasar (Maraschi et al. 1986). Microvariability of CTA 102 at optical wavelengths has been investigated by Osterman Meyer et al. (2009), who found that faster variability is associated with higher flux states.

The variability in this source occurs at other frequencies as well: flares at centimeter and millimeter wavelengths have been registered in the past, as well as an X-ray flare detected by the *Rossi X-ray Timing Explorer* in late 2005 (Osterman Meyer et al. 2009). A radio flare in 1997 was related to the ejection of a new knot from the core (Savolainen et al. 2002; Rantakyrö et al. 2003; Jorstad et al. 2005), and another, in 2006, was connected with both the ejection of a new superluminal feature and the interaction between this component and a recollimation shock at 0.1 mas (Fromm et al. 2011).

The radio morphology on arcsecond scales (from images with the Very Large Array at 6 and 2 cm) reveals a central core with two weak components located at opposite sides (Spencer et al. 1989; Stanghellini et al. 1998). At higher angular resolution, CTA 102 has been regularly observed since 1995 within the Very Long Baseline Array (VLBA) 2 cm Survey (e.g., Zensus et al. 2002) and its successor, the MOJAVE program (e.g., Lister et al. 2009). MOJAVE images show that the jet in CTA 102 extends toward the southeast up to ~15 mas

from the core, which corresponds to a de-projected distance of ∼2.7 kpc using the estimated viewing angle of 2°.6 obtained by Jorstad et al. (2005).

Kinematic studies of the MOJAVE data report apparent velocities between 1.39c and 8.64c (Lister et al. 2013). Higher apparent speeds, up to $\beta_{\rm app} \sim 18c$, have been reported in higher-resolution VLBA observations at 43 GHz by Jorstad et al. (2001, 2005). Apart from superluminal features, the jet of CTA 102 also displays standing features: two stationary components, A1 and C, have been observed at a distance of ∼0.1 and 2 mas from the core, respectively (Jorstad et al. 2001, 2005), and interpreted as recollimation shocks (Fromm et al. 2013b).

Recent MOJAVE polarimetric multifrequency observations (Hovatta et al. 2012) reveal a rotation measure gradient across the jet width at 7 mas from the core, which suggests the presence of a helical magnetic field in the jet. A similar result is reported in Fromm et al. (2013b), where the different observing frequencies reveal bends and helical structures in many parts of the jet.

CTA 102 was detected by the *Fermi Gamma-ray Space Telescope* in the first Large Area Telescope (LAT) catalog with a flux ($E > 100$ MeV) of $14.70 \pm 0.97 \times 10^{-8}$ photons cm^{-2} s^{-1} (Abdo et al. 2010a) and confirmed in the second catalog (Ackermann et al. 2011). In late 2012, the blazar exhibited an extraordinarily bright γ-ray outburst detected by the LAT, reaching a flux of $5.17 \pm 0.44 \times 10^{-6}$ photons cm^{-2} s^{-1} between 0.1 and 200 GeV. During the 2012 event, an unprecedented optical and near-infrared (near-IR) outburst was observed, as reported by Larionov et al. (2012) and Carrasco et al. (2012), respectively.

In this paper, we perform a radio to γ-ray multi-wavelength analysis in order to study the flaring activity of CTA 102 during the 2012 event. In Section 2, we present the multi-wavelength data set collected for the analysis, and we describe the methods used to reduce the data. In Section 3, we describe the characteristics of the emission at the different frequencies during the 2012 flare event. In Section 4, we study the kinematics and the flux density variability of the parsec scale jet. In Section 5, we perform the discrete cross-correlation analysis between light curves. In Section 6, we analyze the polarized emission of the source at millimeter and optical wavebands. We present our discussions and conclusions in Sections 7 and 8.

We adopt the cosmological values from the most recent *Planck* satellite results (Planck Collaboration et al. 2014): $\Omega_m = 0.3$, $\Omega_\Lambda = 0.7$, and $H_0 = 68$ km s^{-1} Mpc^{-1}. With these values, at the redshift of CTA 102 ($z = 1.037$), 1 mas corresponds to a linear distance of 8.31 pc, and a proper motion of 1 mas yr^{-1} corresponds to an apparent speed of 55.2c.

2. OBSERVATIONS AND DATA REDUCTION

We are interested in studying the multi-spectral behavior of CTA 102 during the γ-ray flare that occurred between 2012 September and October. For this, we have collected data from millimeter to γ-ray wavelengths, extending our study from 2004 June to 2014 June. In particular, the *Fermi* data extend from the start of the mission (2008 August) to 2013 September, X-ray and UV data cover the observing period from 2009 August to 2013 June, optical and NIR data from 2004 June to 2013 October, and the combined radio light curves cover the entire period from 2004 June to 2014 June.

In the millimeter-wave range, we use data at (1) 350 GHz (0.85 mm) and 230 GHz (1.3 mm), obtained with the Submillimeter Array (SMA) at Mauna Kea, Hawaii; (2) 230 GHz (1.3 mm) and 86.24 GHz (3.5 mm) with the 30 m Telescope of Institut de Radioastronomie Millimétrique (IRAM) at the Pico Veleta Observatory (Spain); (3) 43 GHz (7 mm) with the VLBA; and (5) 37 GHz (8 mm) with the 13.7 m Telescope at Metsähovi Radio Observatory of Aalto University (Finland).

NIR photometric data (JHK filters) were obtained at the Perkins Telescope at Lowell Observatory (Flagstaff, AZ) using the MIMIR instrument (Clemens et al. 2007) and at the 1.1 m Telescope of the Main Astronomical Observatory of the Russian Academy of Sciences located at Campo Imperatore, Italy (see Hagen-Thorn et al. 2008 for details).

We have collected optical photometric data in the *UBVRI* bands from numerous telescopes: (1) the 2.2 m Telescope of Calar Alto Observatory (Almería, Spain)[16]; (2) the 2 m Liverpool Telescope of the Observatorio del Roque de Los Muchachos (Canary Island, Spain); (3) the 1.83 m Perkins Telescope of Lowell Observatory (Flagstaff, AZ); (4) the 1.54 m and 2.3 m telescopes of Steward Observatory (Mt. Bigelow and Kitt Peak, AZ)[17]; (5) the 40 cm LX-200 Telescope of St. Petersburg State University (St. Petersburg, Russia); (6) the 70 cm AZT-8 Telescope of the Crimean Astrophysical Observatory (Nauchnij, Ukraine); (7) the 1.5 m Kanata Telescope in Higashi-Hiroshima Observatory (Japan)[18]; and (8) the Ultraviolet and Optical Telescope (UVOT) on board the *Swift* satellite. Optical data are in part also in polarimetric mode, mostly in the *R* band, except for items (4) and (5) listed above (see Schmidt et al. 1992; Hagen-Thorn et al. 2008, respectively, for details). In the UV range, we use UVOT data from *Swift* in the three available filters: UVW2 (2030 Å), UVM2 (2231 Å), and UVW1 (2634 Å). We have also obtained X-ray data in the energy range 0.3–10 keV from the X-ray Telescope on board the *Swift* satellite.

At the highest photon energies considered here, we have analyzed γ-ray data from the LAT of the *Fermi Gamma-ray Space Telescope*.

2.1. γ-Ray Data Analysis

We have analyzed the γ-ray data of the field containing CTA 102 from *Fermi* LAT from 2008 August to 2013 September, producing a light curve between 0.1 and 200 GeV with an integration time of 1 day. We used the *Fermi* Science Tools version v9r33p0 and instrument response function P7REP_SOURCE_V15, considering data inside a region of interest (ROI) of 15° radius centered on CTA 102. We followed the unbinned likelihood procedure as described at http://fermi.gsfc.nasa.gov/ssc/data/analysis/scitools/.

The procedure starts with the selection of good data and time intervals through the tasks *gtselect* and *gtmktime* and follows with the creation of an exposure map for each day (tasks *gtltcube*, *gtexpmap*) and the modeling of data through a maximum-likelihood method (*gtlike*). In this last step, we used a model that includes CTA 102 and 42 other point sources inside the ROI, according to the second *Fermi* Gamma-ray Catalog (2FGL; Ackermann et al. 2011). The model also takes

[16] Observations performed under MAPCAT (Monitoring AGN with the Calar Alto Telescopes); see Agudo et al. (2012).
[17] Data taken from the Steward Observatory monitoring project; see Smith et al. (2009).
[18] Data published in Itoh et al. (2013).

into account the diffuse emission from our Galaxy (*gll_iem_v05.fit*) and the extragalactic γ-ray background (*iso_source_v05.txt*). We searched for the flux normalization of CTA 102 by fixing the spectral index of the other point sources while varying both the flux and spectral index of our target. The γ-ray spectrum of CTA 102 was modeled with a log parabola curve corresponding to the spectral model given in the 2FGL catalog. We considered a successful detection when the test statistic TS $\geqslant$ 10, which corresponds to a signal-to-noise ratio $\gtrsim 3\sigma$ (Nolan et al. 2012).

2.2. X-ray, UV, Optical, and NIR

We collected X-ray and UV data from 2009 August to 2013 June from the *Swift* archive. The X-ray data in the energy range 0.3–10 keV were calibrated following the procedure described in Williamson et al. (2014). The UVOT data reduction was performed via the UVOTSOURCE tool, with a sigma value of 5 adopted to compute the background limit. Optical and NIR data were reduced and calibrated following the procedures outlined in Jorstad et al. (2010).

All of the magnitudes of the optical and NIR data have been corrected for Galactic extinction with values reported in the NASA Extragalactic Database[19] for each filter (Schlafly & Finkbeiner 2011). For the UV data, we obtained the absolute extinction value at each wavelength $A(\lambda)$ from Equation (1) in Cardelli et al. (1989). After the correction, we transformed magnitudes into fluxes using the formula reported in Mead et al. (1990) and Poole et al. (2008).

2.3. Photopolarimetric Millimeter VLBA and Single-dish Data

Multi-epoch very long baseline interferometer (VLBI) images provide ultra-high angular resolution that can be used to determine the location in the jet where flaring activity occurs. We therefore have collected data from the VLBA-BU-BLAZAR program,[20] which consists of monthly monitoring of γ-ray bright blazars with the VLBA at 43 GHz (7 mm). The data set consists of 80 total and polarized intensity images from 2007 June to 2014 June. We restore the images with a common convolving beam of 0.4 $\times$ 0.2 milliarcseconds (mas). Since the resolution of the longest baselines of the VLBA is less than half of these dimensions, we employ model fitting to define and determine the parameters of the very fine-scale structure. The data reduction was performed with a combination of the Astronomical Image Processing System (AIPS) and the Differential Mapping software (Difmap), as described in Jorstad et al. (2005). The electric vector position angle (EVPA) calibration follows the procedure discussed in Jorstad et al. (2005), which combines the comparison between VLA and VLBA integrated EVPA values at those epochs for which VLA data are available with the method of Gómez et al. (2002) that utilizes the stability of the instrumental polarization (D-terms).

The IRAM 30 m Telescope's total flux and polarimetric data in this paper were acquired under the POLAMI (Polarimetric AGN Monitoring at the IRAM 30 m Telescope) program (see I. Agudo et al. 2015, in preparation) and reduced and calibrated following the procedures introduced in Agudo et al. (2006, 2010, 2014).

[19] http://ned.ipac.caltech.edu/

[20] http://www.bu.edu/blazars/research.html

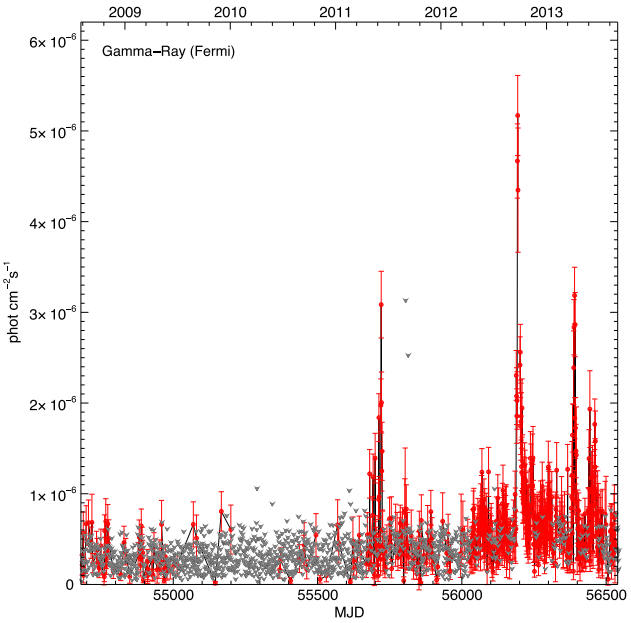

Figure 1. *Fermi* LAT γ-ray light curve between 0.1 and 200 GeV, with an integration time of 1 day. Red points represent the detections (TS $>$ 10), and gray arrows correspond to upper limits when the source is not detected (TS $<$ 10).

The Submillimeter Array data of CTA 102 came from an ongoing monitoring program at the SMA to determine the fluxes of compact extragalactic radio sources that can be used as calibrators at millimeter wavelengths (Gurwell et al. 2007). Observations of available potential calibrators are from time to time observed for 3–5 minutes, and the measured source signal strength are calibrated against known standards, typically solar system objects (Titan, Uranus, Neptune, or Callisto). Data from this program are updated regularly and are available at the SMA website.[21]

3. MULTI-WAVELENGTH OUTBURST

Figure 1 displays the γ-ray light curve of CTA 102 in the energy range 0.1–200 GeV during the period of major activity (2011 June–2013 April) obtained with an integration time of 1 day. Following Jorstad et al. (2013), we can define a γ-ray outburst as a period when the flux exceeds a threshold of 2×10^{-6} photons cm^{-2} s^{-1}. Although this is an arbitrary limit, it conforms to a visual inspection of the γ-ray light curve of CTA 102.

The first outburst takes place in 2011 June (MJD 55719–55721), when the source displays a one-day peak flux of $3.1 \pm 0.37 \times 10^{-6}$ photons cm^{-2} s^{-1}. The second, brightest outburst occurs at the end of 2012 September (2012.73), when the source remains above 2×10^{-6} photon cm^{-2} s^{-1} for 14 days (from MJD 56188 to 56202), reaching a peak of $5.2 \pm 0.4 \times 10^{-6}$ photons cm^{-2} s^{-1} on MJD 56193. During this outburst, the γ-ray flux increases by a factor of 10 in just 6 days. The third flare occurs in 2013 April (MJD 56387–56394) and lasts 8 days. On this occasion (MJD 56392), the blazar reaches a peak of $2.9 \pm 0.4 \times 10^{-6}$ photons cm^{-2} s^{-1}.

We compare the daily γ-ray light curve with the X-ray, UV, optical, NIR, and radio light curves in Figure 2. Table 1 lists

[21] http://sma1.sma.hawaii.edu/callist/callist.html

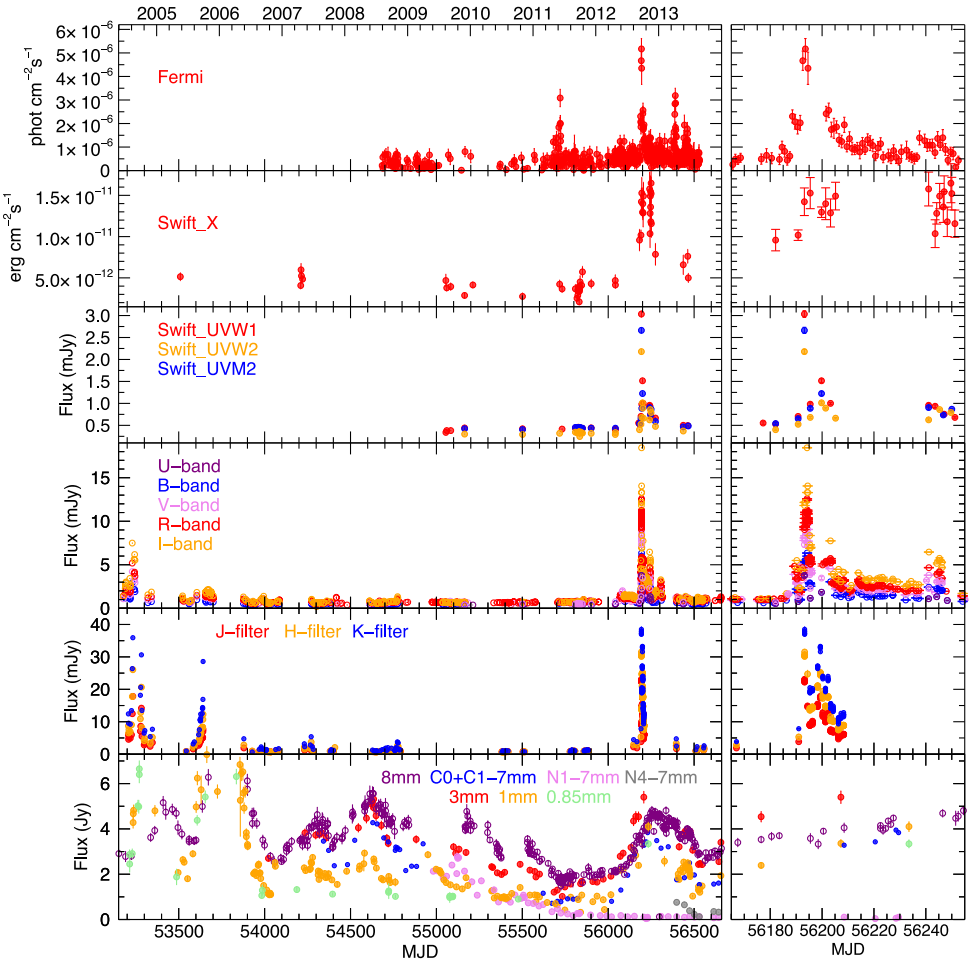

Figure 2. Light curves of CTA 102 from γ-ray to millimeter wavelengths. From top to bottom: γ-ray, X-ray, UV, optical, NIR, and millimeter-wave data. Left panel: data from 2004 May to 2014 January. Right panel: expanded view during the γ-ray outburst between 2012 August and November.

Table 1
Multi Wavelength Data

γ-Ray Data	Flux	Energy Band
Epoch (MJD)	(photons cm^{-2} s^{-1})	(GeV)
54684.2	2.15e-07 ± 1.11e-07	0.1–200
54688.2	5.68e-07 ± 2.30e-07	0.1–200
54689.2	10.00e-08 ± 8.30e-08	0.1–200
X-ray data		
Epoch (MJD)	Flux (photons cm^{-2} s^{-1})	Energy Band (KeV)
53509.4	5.14e-12 ± 4.74e-13	0.3–10
54210.2	4.07e-12 ± 4.13e-13	0.3–10
54212.1	5.97e-12 ± 7.67e-13	0.3–10

(This table is available in its entirety in machine-readable form.)

the multi-wavelength data used in our analysis. The brightest γ-ray outburst, in 2012 September, is accompanied by similarly bright flares at all of the other wavebands. This is, however, not the case for the other two orphan γ-ray flares (γ-ray outbursts with no correspondence at any of the other observing bands), with the exception of a millimeter-wave flare that follows the third γ-ray flare in 2013 April.

Analyzing the multi-wavelength flare in 2012, we observe that the X-ray light curve contains a double-peak structure, where the first peak is almost coincident with the γ-ray outburst and the second peak occurs ∼50 days later. The limited sampling of the X-rays prevents a deeper analysis of the overall X-ray behavior associated with this flare. The UV and optical bands exhibit a rapid and pronounced increase in the light curves coinciding with the γ-ray flare. In the optical light curve, we distinguish a secondary, weaker flare after ∼50 days, close to the second X-ray peak, as well as a third, smaller outburst that occurs ∼70 days after the second peak. In the UV it is also possible to distinguish a secondary flare delayed by ∼50 days with respect to the main flare, but the sampling of the data is insufficient to specify the behavior in more detail. In the NIR light curve, we observe a large flare coincident with the γ-ray flare, but there is no further sampling after this. A detailed analysis of the NIR flare shown in Figure 3 reveals that the event consists of three sub-flares covering almost the entire period of high γ-ray flux from MJD 56193 to 56202.

The radio light curve also exhibits an increase in flux density during the 2012 γ-ray outburst, but with a much longer timescale, lasting ∼200 days. The 1 mm light curve and 7 mm light curves of features C0 and C1 peak on ∼MJD 56230,

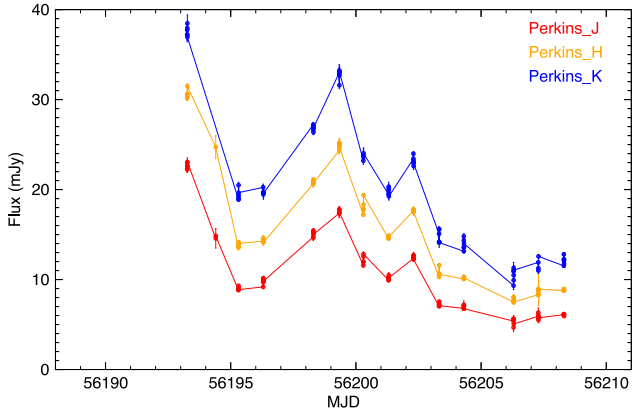

Figure 3. Expanded view of the NIR light curve in the *J*, *H*, and *K* bands during the period of the main γ-ray outburst.

about 1 month after the γ-ray flare. The 3 mm light curve follows a similar trend, starting to increase on ∼MJD 56000. Our limited time sampling between MJD 56208 and 56412 shows a peak on MJD 56207, very close to the γ-ray flare, although we cannot rule out the possibility that the actual peak is closer to that at 1 mm.

4. THE PARSEC-SCALE JET

4.1. Physical Parameters of Components

VLBA images of CTA 102 at some selected epochs are displayed in Figures 4–6. To carry out an analysis of the jet kinematics and flux density variability, we have fit with `Difmap` the complex visibilities with a model source consisting of components described by circular Gaussian brightness distributions. For each epoch, we obtained a model fit that provides information about the flux density (S), distance (r), and position angle (Θ) relative to the core and the FWHM size (a) of each component. The core (labeled C0), considered stationary over the entire period, is identified with the unresolved component in the northwestern (upstream) end of the jet. It is the brightest feature in the jet at most of the epochs. Polarization information has been obtained with an IDL program that calculates the mean values of the degree of polarization (m) and EVPA (χ) over the image area defined by the FWHM size of each component. The uncertainties of both m and χ correspond to the standard deviations of their respective distributions. Model-fit parameters for all components and epochs are reported in Table 2.

The accuracy of the model-fit parameters for each component depends on its brightness temperature, so that smaller uncertainties are expected for more compact components and higher flux densities. We have therefore established a criterion for quantifying the errors in the model-fit parameters that is directly related to the observed brightness temperature, $T_{\rm b} = 7.5 \times 10^8\ S/a^2$ (e.g., Jorstad et al. 2005), where $T_{\rm b}$ is measured in Kelvins (K), S in Janskys (Jy), and a in milliarcseconds (mas).

First, we select a representative sample of epochs and components with a wide range of S, a, and r values. For each one of these components, we compute the error in the fitted parameters by analyzing how the reduced χ^2 of the fit and resulting residual map change when varying the fitted parameters one at a time. We set a limit on the maximum allowed variation of the reduced χ^2 of 20%, corresponding to an increase by a factor of ∼1.5 in the peak levels of the residual map. According to this criterion, we assign a series of uncertainties in position and flux density to the components in the sample. We then relate the derived uncertainties with the measured brightness temperature, obtaining the following relations:

$$\sigma_{xy} \approx 1.3 \times 10^4\ T_{\rm b}^{-0.6}, \quad (1)$$

$$\sigma_S \approx 0.09\ T_{\rm b}^{-0.1}, \quad (2)$$

where σ_{xy} and σ_S are the uncertainties in the position (R.A. or decl.) and flux density, respectively. These relations have been used to compute the errors in the position and flux density for all of the fitted components. To account for the errors in the flux calibration, we have added in quadrature a 5% error to the uncertainty in flux density. The uncertainties in the sizes of components are also expected to depend on their brightness temperatures. Following Jorstad et al. (2005), we have assigned a 5% error to the sizes of the majority of components (those with flux densities $\geqslant$50 mJy and sizes of 0.1–0.3 mas) and a 10% error for more diffuse components.

Plots of separation and flux density versus time for the model-fit jet components, including the core, are presented in Figures 7 and 8. Besides the core, we have identified seven main components that could be traced reliably across multiple epochs. Component E1, located at ∼2 mas from the core, is a weak and extended feature that appears to be quasi-stationary across some epochs, or to move with a significantly slower velocity than other moving components (see Figure 7). A stronger and more compact component, C1, can be distinguished from the core at most of the observed epochs, located at a mean distance of $r \sim 0.1$ mas. Both quasi-stationary features have been observed previously by Jorstad et al. (2005) and Fromm et al. (2013a, 2013b) and interpreted as recollimation shocks in the jet. We identify five other moving components, N1, N2, N3, N4, and S1. Component S1 seems, however, to have a different nature: it appears to form in the wake of component N1 at a distance of ∼0.5 mas, and it is observed over only four epochs afterward. Its properties are similar to those expected and observed previously for trailing components (Agudo et al. 2001; Gómez et al. 2001; Jorstad et al. 2005). Linear fits of separation versus time have been obtained for the other moving components, N1, N2, N3, and N4, based on only those initial epochs at which an accurate position is obtained (see also Figure 7). This yields the estimates for the apparent velocities and times of ejection (epoch at which the component coincides with the core) listed in Table 3.

Since we cannot directly measure the radial velocities of the jet features, a common approach to disentangle the contributions of the component's Lorentz factor and viewing angle in the observed proper motion is the use of the flux variability (e.g., Jorstad et al. 2005; Hovatta et al. 2009). Following Jorstad et al. (2005), we use causality arguments to infer the variability Doppler factor

$$\delta_{\rm var} = \frac{s D_{\rm L}}{c \triangle t_{\rm var} (1+z)}, \quad (3)$$

where s is the disk-equivalent angular diameter (where $s = 1.6a$ for a Gaussian component fit with FWHM $= a$ measured at the

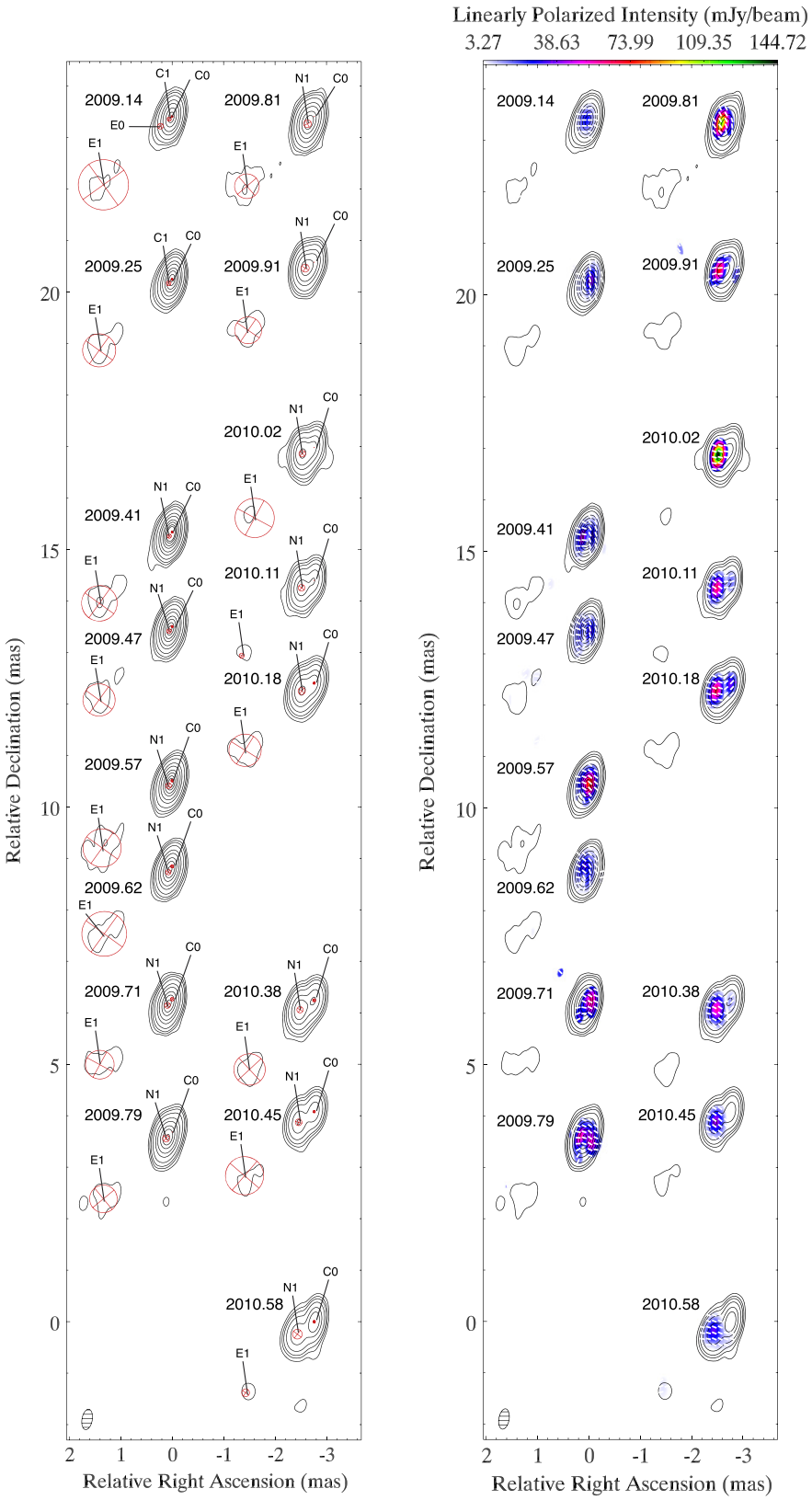

Figure 4. Sequence of 43 GHz VLBA images displaying epochs from 2009 February to 2010 August, when we observe the appearance of component N1. The images are restored with a common beam of 0.4 × 0.2 mas at −10° and are separated by a distance proportional to the time elapsed between observing epochs. Left panel: contours (total intensity) are traced at 0.003, 0.008, 0.04, 0.1, 0.3, 0.6, 1.2, 1.8, 2.5, and 3.0 Jy beam^{-1} and $I_{\rm peak}$ = 4.2 Jy beam^{-1}. Red circles represent model-fit components. Right panel: same contours (total intensity) as in the left panel plus colors that represent linearly polarized intensity and white sticks symbolizing linear polarization angle.

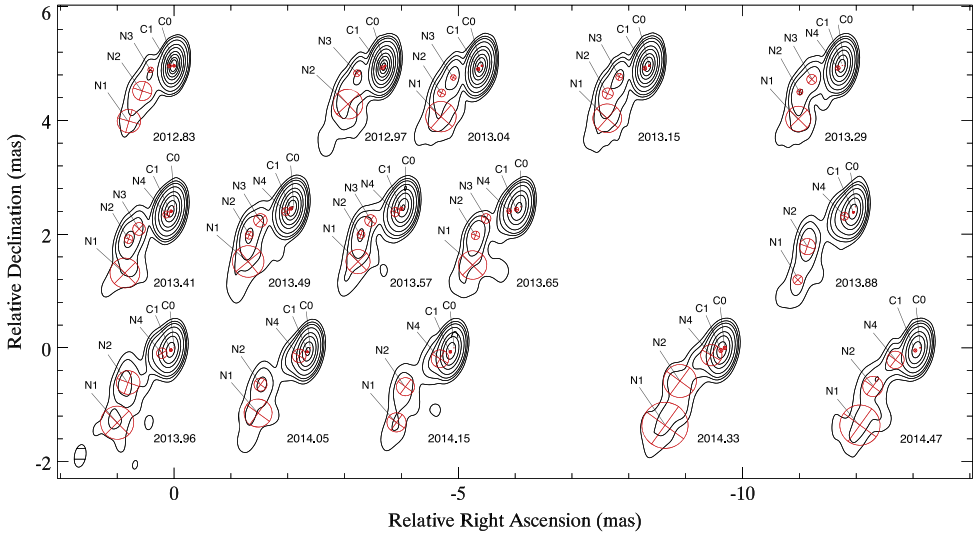

Figure 5. Sequence of total intensity 43 GHz VLBA images from 2012 October to 2014 June, covering the epochs from which we start observing component N4. Peak intensity is $I_{\rm peak} = 3.6$ Jy beam^{-1} and contours are traced at 0.003, 0.008, 0.04, 0.1, 0.3, 0.6, 1.2, 1.8, 2.5, and 3.0 Jy beam^{-1}.

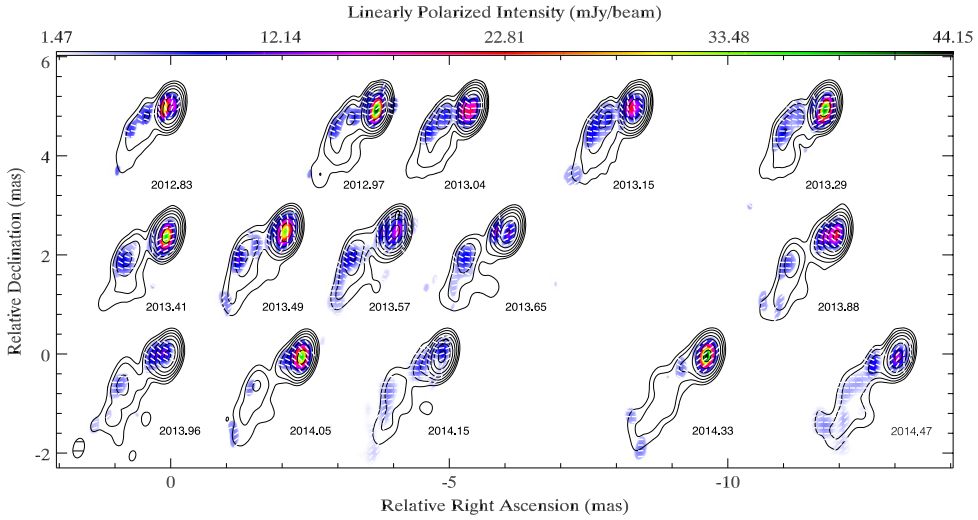

Figure 6. Same as Figure 5, but with linearly polarized intensity in colors and white sticks symbolizing linear polarization angle.

epoch of maximum flux), and $D_{\rm L}$ is the luminosity distance. The variability timescale is defined as $\Delta t_{\rm var} = dt/\ln(S_{\rm max}/S_{\rm min})$, where $S_{\rm max}$ and $S_{\rm min}$ are the measured maximum and minimum flux densities, respectively, and dt is the time in years between $S_{\rm max}$ and $S_{\rm min}$ (Burbidge et al. 1974). This definition of $\delta_{\rm var}$ is valid under the assumption that the flux density variability timescale corresponds to the light-travel time across the component, which is valid as long as the radiative cooling time is shorter than the light crossing time and expansion time. Combining the estimated value of $\delta_{\rm var}$ with the measured apparent velocity, $\beta_{\rm app} = \beta \sin\theta/(1 - \beta\cos\theta)$, where θ and β are the viewing angle and velocity (in units of the speed of light) of the component, we can calculate the variability Lorentz factor, $\Gamma_{\rm var}$, and viewing angle, $\theta_{\rm var}$, using (Hovatta et al. 2009)

$$\Gamma_{\rm var} = \frac{\beta_{\rm app}^2 + \delta_{\rm var}^2 + 1}{2\delta_{\rm var}} \quad (4)$$

and

$$\theta_{\rm var} = \arctan\frac{2\beta_{\rm app}}{\beta_{\rm app}^2 + \delta_{\rm var}^2 - 1}. \quad (5)$$

Physical parameters of the moving components obtained from this method are reported in Table 4.

4.2. Kinematics and Flux Density Variability

By inspecting the light curves in Figure 8, we can identify two flaring periods in the core: a prolonged first event that extends from mid-2007 to the beginning of 2009, and a second one between mid-2012 and the beginning of 2013, in coincidence with the main γ-ray flare.

The peak flux of the first flare occurs between 2008 June and July, when both components C0 and C1 increase their flux densities, reaching a combined value of $\sim$4.2 Jy. Due to the proximity of C1 to the core, it is not always possible for the model-fitting routine to clearly distinguish the two components, leading to high uncertainties in the flux ratio of the two

Table 2
VLBA 43 GHz Model-fit Components' Parameters

Epoch (year)	Epoch (MJD)	Flux (mJy)	Distance from C0 (mas)	Pos. Angle (°)	Major Axis (mas)	Degree of Polarization (%)	EVPAs (°)
			Component C0				
2007.45	54264.5	3086 ± 313	...	...	0.017 ± 0.001	...	...
2007.53	54294.5	3423 ± 347	...	...	0.034 ± 0.002	1.5 ± 0.2	71.2 ± 5.7
2007.59	54318.5	2340 ± 239	...	...	0.038 ± 0.002	2.4 ± 0.1	76.4 ± 5.4
2007.66	54342.5	3163 ± 321	...	...	0.045 ± 0.002	1.6 ± 0.1	71.9 ± 6.6
2007.74	54372.5	2743 ± 279	...	...	0.045 ± 0.002	1.4 ± 0.1	82.9 ± 8.4
			Component C1				
2007.66	54342.5	296 ± 37	0.07 ± 0.01	119.2 ± 3.2	0.062 ± 0.003	1.6 ± 0.1	65.5 ± 7.1
2007.74	54372.5	307 ± 37	0.09 ± 0.01	104.4 ± 4.8	0.031 ± 0.002	2.2 ± 0.1	−80.8 ± 6.3
2007.83	54405.5	168 ± 25	0.13 ± 0.02	119.5 ± 3.2	0.116 ± 0.006	2.6 ± 0.2	79.3 ± 5.9
2008.04	54482.5	575 ± 64	0.08 ± 0.01	146.2 ± 1.9	0.070 ± 0.003	0.7 ± 0.1	37.8 ± 5.5
2008.16	54524.5	894 ± 96	0.09 ± 0.01	−166.3 ± 7.4	0.062 ± 0.003	0.5 ± 0.1	38.2 ± 5.6

(This table is available in its entirety in machine-readable form.)

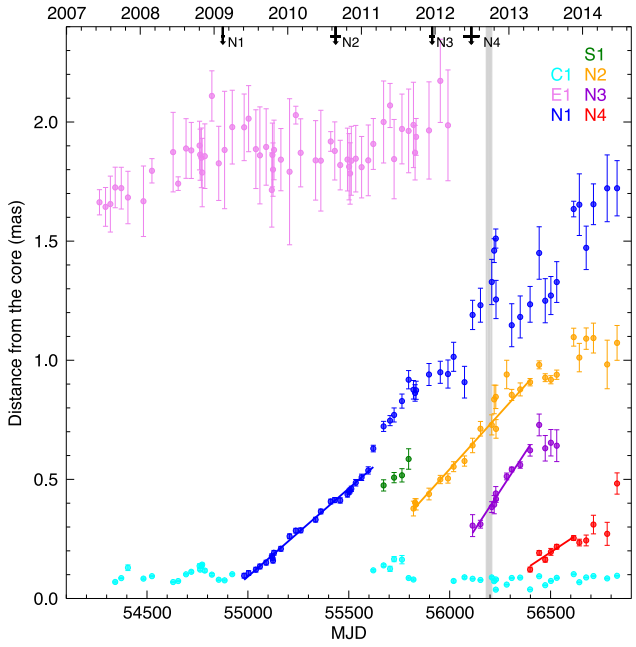

Figure 7. Distance from the core vs. time for the 43 GHz model-fit components, with linear fits overlaid. Downward black arrows mark the time of ejection of each component with the respective error bar. The gray vertical stripe indicates the epoch of the γ-ray flare.

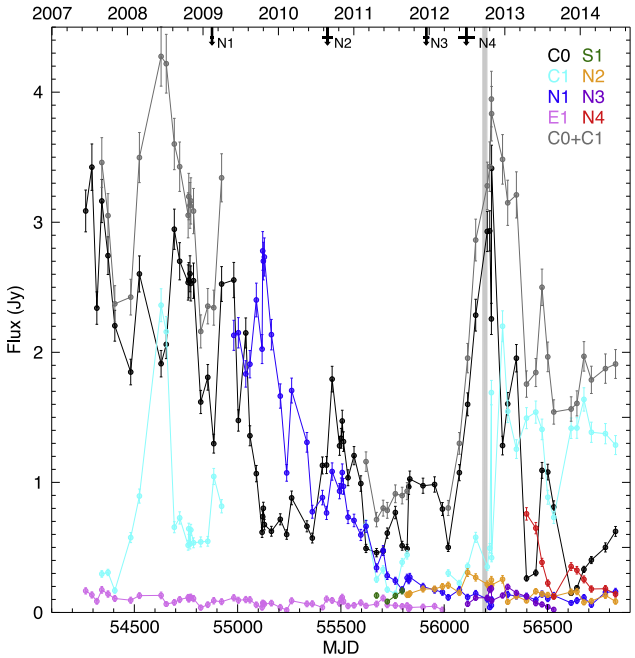

Figure 8. Light curves of 43 GHz model-fit components. Downward arrows and the gray vertical stripe indicate the same as in Figure 7.

features, as well as uncertainties in the position of C1. Because of this, Figure 8 also shows the combined flux density of the core and component C1, providing the data needed to follow the total flux density within the core region of CTA 102.

The second flare in the millimeter-wave core began in mid-2012, reaching its peak flux density at the end of 2012 October, close to the γ-ray flare (see Figure 8; Section 5). After the peak, the core region (C0 plus C1) remains in a high flux state until the last observing epoch, with a combined flux density oscillating around ∼2 Jy.

Both flares in the core region are associated with the appearance of subsequent superluminal components. In the case of the first such flare, component N1 appears as a bright

Table 3
Kinematics of Moving Jet Features

Name	N.Epoch	μ (mas yr^{-1})	$\beta_{\rm app}$ (c)	T_{ej} (year)
N1	26	0.27 ± 0.01	14.9 ± 0.2	2009.12 ± 0.02
N2	18	0.35 ± 0.01	19.4 ± 0.8	2010.65 ± 0.07
N3	10	0.49 ± 0.03	26.9 ± 1.8	2011.96 ± 0.07
N4	6	0.21 ± 0.02	11.3 ± 1.2	2012.49 ± 0.11

and well-defined feature that moves along the jet at 14.9 ± 0.2 c (see Figures 7–8 and Table 3). We also note that the ejection of component N1 corresponds to a change in the innermost structure of the compact jet, after which component C1 is no

Table 4
Physical Parameters of Moving Jet Features

Name	$\Delta t_{\rm var}$ (year)	$a_{\rm max}$[a] (mas)	$\delta_{\rm var}$	$\theta_{\rm var}$ (°)	$\Gamma_{\rm var}$
N1	0.70	0.14	14.6	3.9	14.9
N2	1.12	0.33	22.4	2.5	19.6
N3	0.28	0.09	26.1	2.2	26.2
N4	0.20	0.08	30.3	1.2	17.3

Note.
[a] FWHM of the model-fit component calculated at the epoch of maximum flux.

longer detected for almost two years. The second core flare leads to the ejection of component N4, which is significantly weaker than component N1 and has the slowest proper motion of the analyzed components (see Figures 7–8 and Table 3).

The values of the variability Doppler factors listed in Table 4 correspond to a progressive increase with time, from 14.6 for component N1 to 30.3 for component N4. Previous estimations of the variability Doppler factor in CTA 102 range between 15.6 (Hovatta et al. 2009) and 22.3 ± 4.5 (Jorstad et al. 2005), making N4 the superluminal knot with the highest Doppler factor to date. According to our analysis, this unusually large value is due to a progressive re-orientation in the direction of ejection of knots, from $\theta_{\rm var} = 3.^\circ9$ for component N1 to $\theta_{\rm var} = 1.^\circ2$ for N4, which travels almost directly along the line of sight. This change in the jet orientation is readily apparent when analyzing each component's position angle shortly after the time of ejection, as well as their subsequent trajectories, as shown in Figure 9.

This smaller viewing angle of the jet with respect to the observer during the second radio flare, which appears to last until the end of our VLBA data set (2014 June), is also in agreement with the significant differences observed between the ejections of components N1 and N4. While component N1 is clearly identified in the jet as a bright ($\gtrsim$2 Jy) component soon after its ejection, most of the increase in the total flux density during the second radio flare appears to be associated with the core region (C0+C1), with component N4 representing only a small fraction of the flare. The smaller viewing angle of the jet also leads to a more difficult identification of component N4, which is not clearly discerned from the core until 2014 May (2014.33). Further support for the re-orientation of the jet toward the observed is also obtained from the analysis of the polarization, discussed in Section 6.

5. CROSS-CORRELATION ANALYSIS

To quantify the relationship among the light curves at the different wavebands, we perform a discrete cross-correlation analysis. The z-transformed discrete correlation function (ZDCF) described by Alexander (1997) has been designed for unevenly sampled light curves, as in our case. We use the publicly available *zdcf_v1.2* and *plike_v4.0.f90* programs,[22] with a minimum number of 11 points inside each bin, as recommended for a meaningful statistical interpretation. We compute the DCF between each pair of light curves, including data from 100 days before to 100 days after the main γ-ray outburst. Time sampling of the light curves ranges from one day for the γ-ray data to tens of days in the case of some other wavebands (see Figure 2).

Figure 10 displays the ZDCF analysis for the optical-γ (upper panel) and UV-γ (lower panel) data. We find that the correlation peaks between the γ-ray light curve and the optical and UV light curves give a time lag of 0.70 ± 1 and $1.23^{+5.00}_{-4.09}$ days, respectively, where a positive lag means that the γ-ray variations lead. We therefore conclude that the variations at the three wavelengths are essentially coincident within the uncertainties.

The sparser sampling of the X-ray data, as well as its double-peaked structure, precludes a reliable ZDCF analysis. However, we note that the first X-ray data peak is coincident with the γ-ray flare, and the second brighter X-ray flare occurs ∼50 days later (see Figure 2). The triple-flare structure of the NIR light curve during the γ-ray flare (see Figure 3) also prevents a unique interpretation of a cross-correlation analysis. Nevertheless, from inspection of the light curves, we see that the first, brightest peak in the NIR light curve (56193 MJD) is simultaneous with the γ-ray outburst within an uncertainty of one day, corresponding to the time sampling of both light curves.

We obtain no significant correlation between the millimeter-wave and γ-ray light curves. This can be due to the different timescales associated with the emission at these wavebands, as also suggested for other blazars (e.g., 1156+295; Ramakrishnan et al. 2014). The rise time for the millimeter-wave band is of the order of months, while for the γ-rays it is of the order of a few days. We note, however, that the 1, 3, and 7 mm light curves contain a significant flare coincident with the γ-ray outburst.

6. POLARIZED EMISSION

Figure 11 shows the optical and millimeter-wave linear polarization between MJD 54000 and 56900, covering the period of the γ-ray flare. To solve for the $\pm n\pi$ ambiguity in the EVPA, we assume the slowest possible variation in time, applying a $\pm\pi$ rotation between two consecutive measurements when the magnitude of the EVPA change would otherwise exceed $\pi/2$.

No significant increase in the degree of polarization at millimeter wavelengths is observed during the γ-ray flare, but the EVPAs display a progressive rotation starting about one year prior to the γ-ray flare. Figure 11 shows that between 2007 and mid-2011 the EVPAs at 3 and 1 mm are distributed around a mean value of ∼100°. After this, the polarization at millimeter wavelengths starts a slow rotation by almost 80° in one year (from 2011 July to 2012 August) until the flare epoch. In coincidence with the γ-ray flare, the rate of EVPA rotation in the VLBI core and stationary component C1 increases significantly, leading to a rotation of almost 200° in one year. Subsequently, component N4 appears and the EVPAs of both C1 and N4 rotate again toward values similar to those at 1 and 3 mm, reaching ∼−100°. It is possible that during the flare, while the new superluminal component N4 is crossing the core zone, the EVPAs of the innermost region at 7 mm rotate due to the passage of the component. After this, when N4 can be distinguished from C1 and C0, the EVPAs at 7 mm again follow the general behavior of the EVPAs at shorter millimeter wavelengths. A similar discrepancy between the 1–3 and 7 mm EVPAs occurs between mid-2009 and mid-2010, when

[22] http://www.weizmann.ac.il/weizsites/tal/research/software/

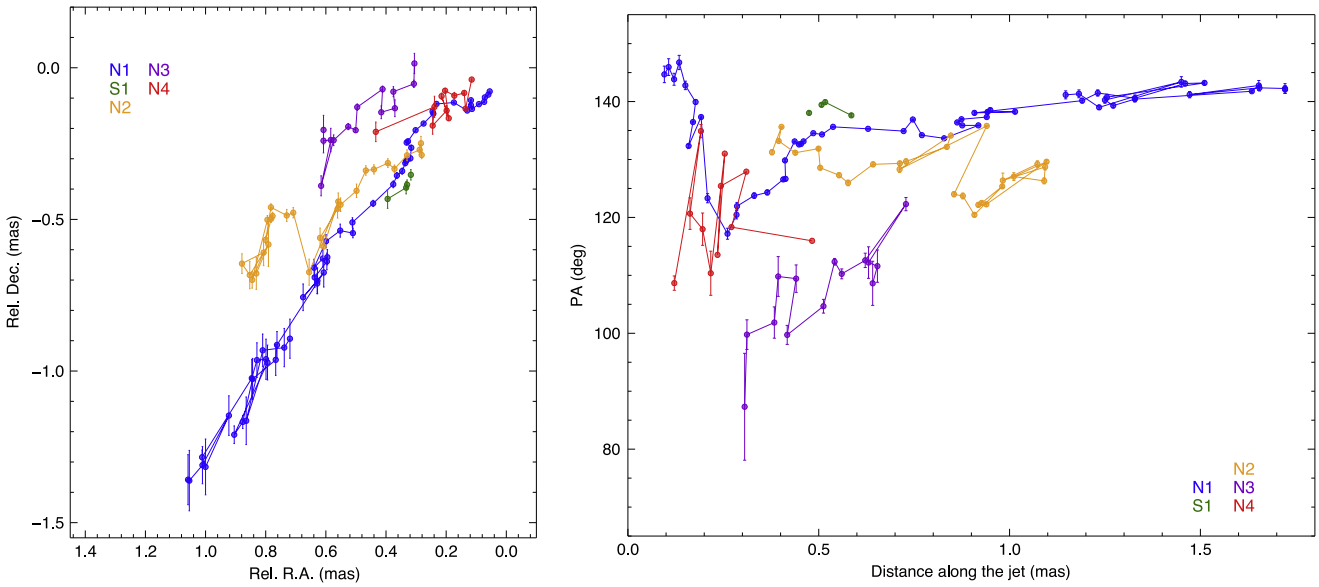

Figure 9. Trajectories (left panel) and position angles as a function of distance from the core (right panel) of the moving components in the jet.

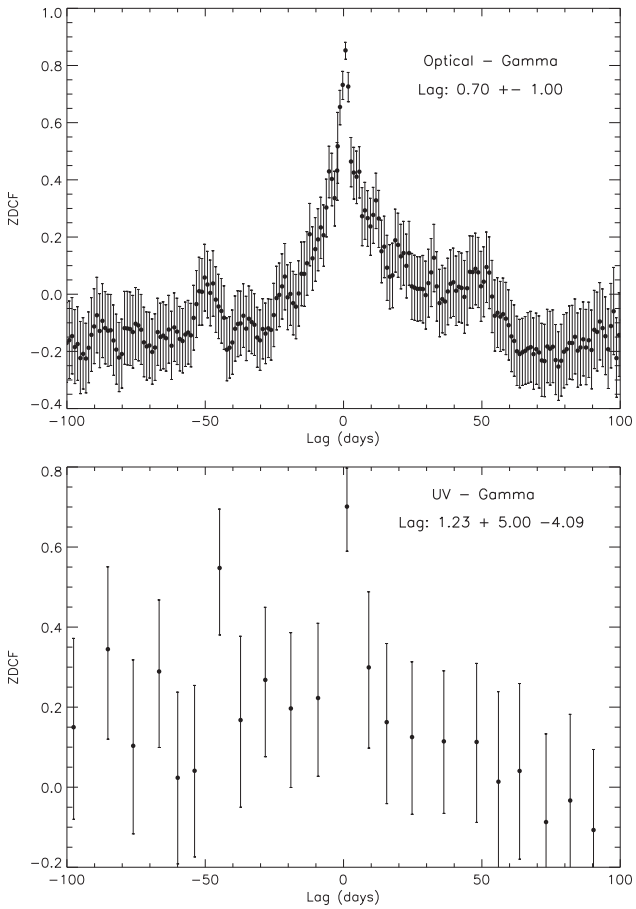

Figure 10. Z-transformed discrete correlation function between optical and γ-ray data (upper panel) and UV and γ-ray data (lower panel). In each panel, we report the time lag corresponding to the correlation peak with its respective 1σ error (see Alexander 2013 for more details).

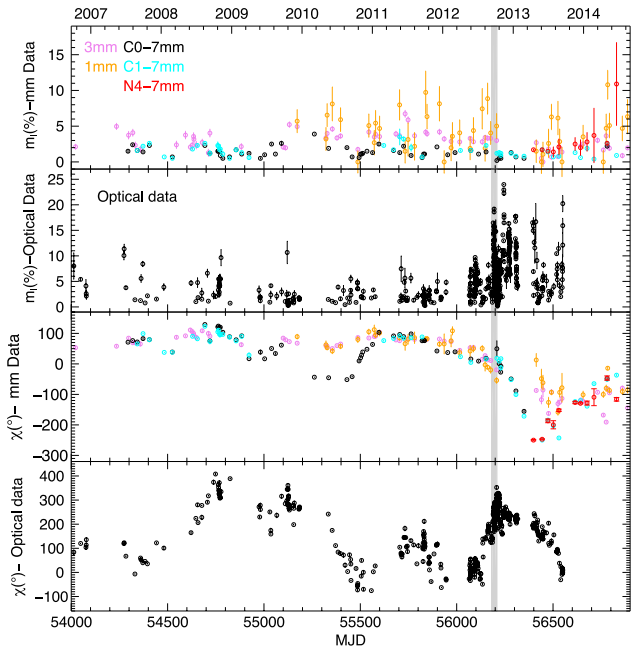

Figure 11. Optical and millimeter-wave linear polarization over the period MJD 54000–56800. The first two panels display the degree of millimeter-wave and optical polarization, respectively. The third and fourth panels display the EVPAs at millimeter and optical wavelengths, respectively. The gray vertical stripe indicates the epoch of the main γ-ray flare.

component N1 is ejected and becomes brighter than the core until mid-2010 (see Figure 8).

We can then distinguish the rapid rotation of polarization vectors observed in the VLBI components at 7 mm after the flare from the slower rotation observed at 1 and 3 mm. The latter leads to a rotation of the mm-EVPAs of $\sim$200° over 3 years (from 2011 July to 2014 August). This progressive

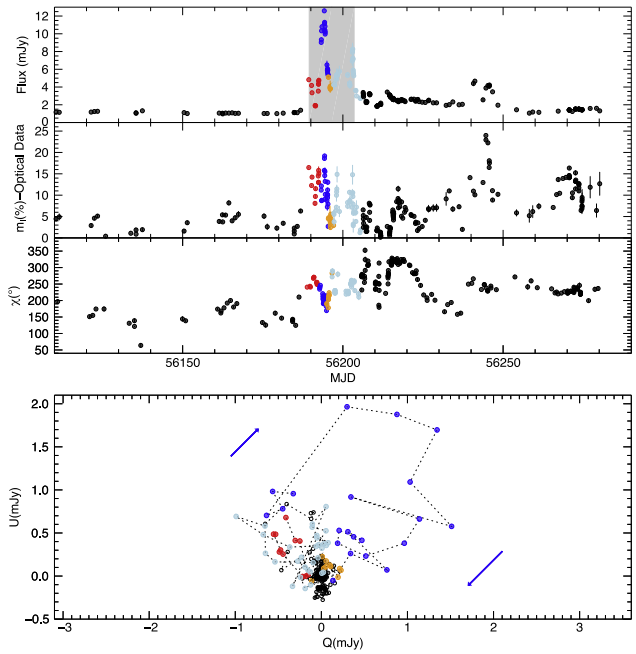

Figure 12. Upper panel displays, from top to bottom, the light curve, degree and time evolution of polarization, and EVPA at optical frequencies. Each colored mark corresponds to the period over which we plot the U and Q Stokes parameters in the lower panel. Blue points mark a clockwise rotation cycle that occurs in coincidence with the total intensity peak. The gray vertical stripe indicates the time range of the main gamma-ray flare.

rotation in the EVPAs can be produced by a change in the orientation of the innermost jet, which would be in agreement with the larger Doppler factor and smaller viewing angle of component N4 associated with the γ-ray event, as discussed previously (see Section 4).

The optical polarization executes rapid and pronounced changes in both degree of polarization and EVPA associated with the γ-ray flare. Figure 12 displays an expanded view of the optical polarization data near the time of the γ-ray flare, with four different time ranges marked in different colors. Before the peak at optical frequencies on MJD 56194, the source undergoes a period of rapid changes in both total and polarized emission (marked in red), and the EVPAs rotate by almost 30°. The plot of Stokes parameters U versus Q in Figure 12 reveals a clear clockwise rotation of the EVPAs (marked in blue), in coincidence with the main flare in total flux and a rapid change in the degree of polarization. This clockwise rotation has been previously reported by Larionov et al. (2013a).

If we assume a model in which a relativistic shock does not cover the entire cross-section of the jet and is moving down the jet following helical magnetic field lines, which also propagate downstream, then we expect to observe a rotation in the EVPA. This should be accompanied by a change in the degree of polarization, with a minimum in the middle of the rotation, where the flaring region contains magnetic field lines with opposite polarity (e.g., Vlahakis 2006; Marscher et al. 2008; Larionov et al. 2013b). Evidence of a helical magnetic field in CTA 102 jet can also be found in the detection of negative circular polarization (Gabuzda et al. 2008) and in a gradient in the rotation measure across the jet width at about 7 mas from the core (Hovatta et al. 2012), both in MOJAVE observations.

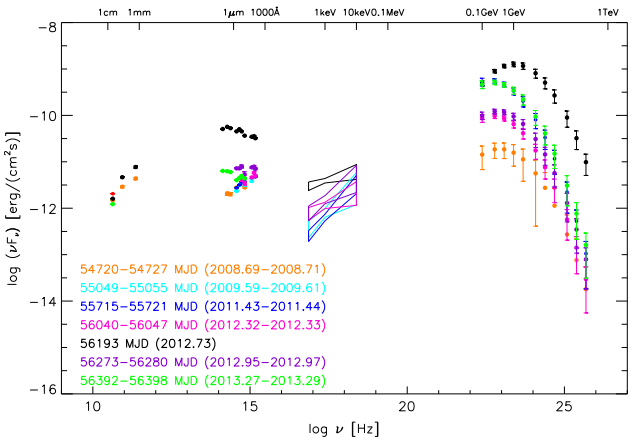

Figure 13. Spectral energy distribution of CTA 102 from millimeter-wave to γ-ray frequencies during the brightest γ-ray flare (black) and at other observing epochs, as labeled in the figure and discussed in the text.

7. SPECTRAL ENERGY DISTRIBUTION

We have computed the spectral energy distribution (SED) of the source from millimeter to γ-ray wavelengths at several epochs (see Figure 13): two epochs between MJD 54720 and MJD 55055, corresponding to γ-ray quiescent states; the epochs of the first γ-ray flare (MJD 55715–55721), the main flare (MJD 56193), and the third γ-ray flare (MJD 56392–56398); one epoch of a quiescent state between the first and second flares (MJD 56040–56047), and a second one between the second and third flares (MJD 56273–56280). For the main γ-ray flare, all data are simultaneous except for the millimeter-wave data, which corresponds to MJD 56208. For the other epochs, we have considered a range of time (as indicated in Figure 13) in order to cover the entire energy range.

By examining Figure 13, we observe that, during the multi-wavelength flare in 2012 (black points), both the synchrotron and the inverse-Compton peaks increased. The synchrotron peak frequency during the flare is close to 10^{14} Hz, at the upper end of the frequency range 10^{12}–10^{14} Hz of synchrotron peaks observed in luminous blazars (Ghisellini & Tavecchio 2008). At the same time, we also observe a shift in the inverse-Compton peak to higher frequencies, which leads to a hardening of the spectrum between 0.1 and 1 GeV. We note that neither of the other two, weaker γ-ray flares displays a similar shift in the peak of the inverse-Compton spectrum. In particular, the weaker first and third γ-ray flares display a very similar inverse-Compton spectrum, peaking at nearly the same frequency, with only a minor hardening toward higher energies during the third flare. The shift of the γ-ray peak toward higher frequencies during the main γ-ray flare can be explained by a change in the viewing angle—leading to an increase in Doppler factor—of the emitting region, in support of our hypothesis of a reorientation of the jet toward the line of sight during the multi-wavelength flare (see Sections 4 and 6).

The ratio of the inverse-Compton to synchrotron peaks is of the order of 10, which is not sufficiently large to rule out synchrotron self-Compton (SSC) scattering as the main mechanism for the production of the γ-ray emission (e.g., Sikora et al. 2009).

8. DISCUSSION AND RESULTS

We have presented a multi-wavelength polarimetric study of the quasar CTA 102 during an unprecedented γ-ray outburst that was observed between 2012 September 23 and October 2. We find that the γ-ray outburst occurred simultaneously with flares from millimeter to X-ray wavelengths, with the exception that the 1 and 7 mm light curves peak almost one month after the shorter-wavelength flares. However, all of the millimeter-wave light curves begin to increase before the shorter-wavelength outburst, but took longer times to reach maximum flux and then to decay.

Our DCF analysis confirms the coincidence between the γ-ray flare and the optical-UV flare. The same analysis does not provide unambiguous correlation between the X-ray or NIR and the γ-ray light curves because of the multi-peak structure of the flare at these two frequencies and the relatively sparse sampling.

The *Fermi* LAT daily light curve reveals two more γ-ray outbursts apart from that in 2012: one in 2011 June and the other in 2013 April. Both outbursts are weaker and "orphan." Only the bright outburst in 2012 September–October is coincident with flares at the other wavelengths and with the emergence of a new superluminal knot from the radio core.

We have combined our multi-wavelength study of light curves with an analysis of multi-epoch VLBA observations at 43 GHz that provide the necessary angular resolution to follow the evolution of the jet during the outburst. In the 43 GHz VLBA images, we observe the ejection of multiple superluminal knots from the radio core during the analyzed period, but only one of these knots, N4, is associated with a γ-ray flare. Component N4 was ejected in 2012.49 $\pm$ 0.11, within a time range between 47 and 127 days before the main γ-ray flare in 2012 (2012.73), when the radio core started to increase in flux density. The interaction between a traveling feature and the stationary radio core appears to have triggered a number of γ-ray outbursts in blazars (e.g., Morozova et al. 2014; Ramakrishnan et al. 2014) and radio galaxies (Grandi et al. 2012; Casadio et al. 2015). However, not every ejection of a new knot leads to a γ-ray flare. For instance, it is not clear why a γ-ray flare is associated with N4 in CTA 102 and not with the other moving radio components.

From the analysis of model-fit components at 43 GHz, we deduce that the jet changed its orientation with respect to the observer when component N4 was ejected. This is derived from an analysis of the variability Doppler factor and viewing angle, which indicates that a progressive increase in the Doppler factor occurred, caused by a re-orientation of the jet toward the line of sight. This led to a minimum viewing angle of $\theta \sim 1.^{\circ}2$ when component N4 was ejected during the γ-ray outburst. This change in the orientation of the jet is supported by the observed progressive, slow rotation of the millimeter-wave EVPAs starting almost one year before the ejection of N4 and the γ-ray flare. We therefore conclude that the γ-ray emission in CTA 102 is related to a decrease in the viewing angle of the jet.

This correlation between γ-ray activity and orientation of the jet has been already observed in other BL Lac objects (Marscher et al. 2008; Larionov et al. 2010; Rani et al. 2014), quasars (Abdo et al. 2010b; Raiteri et al. 2011; Jorstad et al. 2013), and radio galaxies (Casadio et al. 2015), although there are different interpretations regarding the cause of the change in orientation. Some authors consider a bent or precessing jet, while others suggest a helical jet with the radiating component following this helical path. A helical trajectory could also be the consequence of magnetic field lines twisting around a conical or parabolic jet (Vlahakis 2006).

In the case of CTA 102, there are indications of a helical magnetic field structure (Gabuzda et al. 2008; Hovatta et al. 2012). We associate the fast variability in the polarized optical emission, as well as the clockwise rotation displayed in the EVPAs during the outburst, with the helical path followed by the superluminal component in its motion along the outwardly propagating magnetic field lines. On the other hand, a number of similar rotations of the millimeter-wave and optical polarization vectors occurred in both the clockwise and counterclockwise directions over the entire 2004–2014 monitoring period. This can be interpreted in terms of random walks of a turbulent magnetic field (Jones 1988; D'Arcangelo et al. 2007; Marscher 2014). Early results from the RoboPol program show that, while many EVPA rotations related to γ-ray flares can be produced by a random walk process, some are not (Blinov et al. 2015). If the rotation associated with a γ-ray flare is caused by a helical geometry of the magnetic field, then future such outbursts should be accompanied by similar clockwise rotations.

The observed long-term rotation in millimeter-wave polarization vectors, together with the slower proper motion associated with component N4, suggests a change in the jet orientation, so that it becomes more closely aligned with the line of sight during the ejection of component N4 and the multi-wavelength flare.

The close timing of the γ-ray, X-ray, UV, and optical flares suggests co-spatiality of the emission at all these frequencies. Knot N4 was 0.025–0.07 mas downstream of the core when the γ-ray flare occurred, i.e., it had not yet reached the feature C1 at $\sim$0.1 mas. This is confirmed by the increase in flux density in the 7 mm core during the γ-ray outburst. Hence, we conclude that the bright γ-ray outburst occurred inside the millimeter-wave core region.

We observe component N4 for the first time in the VLBA images on 2013 April (MJD 56398), when it was located at $r \sim$ 0.12 mas. The γ-ray flare in 2013 April occurred between MJD 56387 and 56394. Therefore, a possible interpretation of this flare is the passage of component N4 through C1, interpreted by Fromm et al. (2013a) as a possible recollimation shock.

If the radio core were located within $\sim$1 pc of the black hole (BH), then the accretion disk or the broad-line region could provide the necessary photon field to explain the high-energy emission through external Compton scattering. The 43 GHz radio core in CTA 102 must be coincident with, or downstream of, the 86 GHz core that is located at a distance of 7.5 $\pm$ 3.2 pc ($\sim 8.5 \times 10^4$ gravitational radii for a BH mass of $\sim 8.5 \times 10^8 M_{\odot}$; Zamaninasab et al. 2014) from the BH (Fromm et al. 2015). A similar scaled distance, $\sim 10^4$–10^5 gravitational radii, has been determined also for two radio galaxies, 3C 111 and 3C 120 (Marscher et al. 2002; Chatterjee et al. 2009, 2011) and two blazars, BL Lac and 3C 279 (Marscher et al. 2008; Abdo et al. 2010b). For a mean viewing angle of the jet of CTA 102 of $2.^{\circ}6$ (Jorstad et al. 2005; Fromm et al. 2015), the distance of N4 from C0 is 4.6–13 pc, hence the γ-ray outburst took place more than 12 pc from the BH. At this location, there should be a negligible contribution of photons from the disk or the broad-line region, or from the dusty torus (located $\sim$1.6 pc from the BH; Pacciani et al. 2014), for

external Compton scattering to produce the high-energy flare. The lack of a suitably strong external source of photons favors SSC scattering of NIR to UV photons by electrons in the jet with energies ∼10 times the rest-mass energy as the source of the γ-ray emission. The ratio of γ-ray to infrared (synchrotron) luminosity is $\lesssim$10, sufficiently low to be consistent with the SSC process.

9. CONCLUSION

Our study of the time variability of the multi-wavelength flux and linear polarization of the quasar CTA 102 confirms its erratic blazar nature, revealing both strong connections across wavebands in one outburst and no obvious connections for other events. The bright γ-ray outburst in late 2012 was accompanied by contemporaneous flares at longer wavelengths up to at least 8 mm, with the increase in millimeter-wave flux starting before the γ-ray activity. The polarization vector at both optical and millimeter wavelengths rotated from the time of the γ-ray peak until ∼150 days later. A new superluminally moving knot, N4—the feature with the highest Doppler beaming factor during our monitoring, according to our analysis—was coincident with the core in the 43 GHz VLBA images 47–127 days prior to the γ-ray peak. We conclude that the outburst was so luminous because the jet (or, at least, the portion of the jet where most of the emission occurs) had shifted to a direction closer to the line of sight than was previously the case. The time delay between the epoch when N4 crossed the centroid of the core (feature C0) and the epoch of peak γ-ray emission implies that the main flare took place $\gtrsim$12 pc from the BH. At this distance, the only plausible source of seed photons for inverse-Compton scattering is NIR to UV emission from the jet itself. The ratio of γ-ray to infrared luminosity is only ∼10 at the peak of the outburst, low enough to be consistent with SSC high-energy emission.

Multiple superluminal knots appeared in the jet during the 7 years covered by our VLBA observations. These include a very bright component (N1) ejected in 2009.12 ± 0.02 and associated with a significant millimeter-wave flare in the core region (∼4.2 Jy). Yet, only component N4 is related to a flare at γ-ray energies. Two strong "orphan" γ-ray flares have no apparent optical counterparts. A strong millimeter-wave event with neither a γ-ray nor optical counterpart can be explained by an inability of the event to accelerate electrons up to energies $\sim 10^4 mc^2$ needed to radiate at such frequencies, although the reason for this inability is unclear. Orphan γ-ray flares might be explained by a knot crossing a region where there is a higher local density of seed photons for inverse-Compton scattering (Marscher et al. 2010; MacDonald et al. 2015). Indeed, the second orphan flare corresponds to the time of passage of knot N4 through stationary feature C1 (located ∼0.1 mas from the core), which could be such a region.

During the multi-wavelength outburst we observe intra-day variability in the optical polarized emission, as well as a clockwise rotation in optical EVPAs. This rotation could be caused by a spiral path traced by the knot moving along helical magnetic field lines that propagate outwards relativistically. Alternatively, the various rotations of the polarization vector seen in our data set, which are in the clockwise and counterclockwise direction over different time ranges, could be mainly random walks caused by a turbulent magnetic field.

CTA 102 displays the complex behavior characteristic of the blazar class of active galactic nuclei. Nevertheless, we have found possible connections between variations in the multi-wavelength flux and polarization and in the structure of the jet in some events. Continued monitoring of CTA 102 and other bright blazars at multiple wavebands with as dense a sampling as possible, combined with millimeter-wave VLBI imaging, can eventually determine which connections are robust and the extent to which stochastic processes dominate the behavior of blazars.

This research has been supported by the Spanish Ministry of Economy and Competitiveness (MINECO) grant AYA2013-40825-P. The research at Boston University (BU) was funded in part by NASA Fermi Guest Investigator grants NNX14AQ58G and NNX13AO99G, and Swift Guest Investigator grant NNX14AI96G. I.A. acknowledges support by a Ramón y Cajal grant of the MINECO. The VLBA is operated by the National Radio Astronomy Observatory. The National Radio Astronomy Observatory is a facility of the National Science Foundation operated under cooperative agreement by Associated Universities, Inc. The PRISM camera at Lowell Observatory was developed by K. Janes et al. at BU and Lowell Observatory, with funding from the NSF, BU, and Lowell Observatory. St. Petersburg University team acknowledges support from Russian RFBR grant 15-02-00949 and St. Petersburg University research grant 6.38.335.2015. This research was conducted in part using the Mimir instrument, jointly developed at Boston University and Lowell Observatory and supported by NASA, NSF, and the W.M. Keck Foundation. The Mimir observations were performed by Lauren Cashman, Jordan Montgomery, and Dan Clemens, all from Boston University. This research is partly based on data taken at the IRAM 30 m Telescope. IRAM is supported by INSU/CNRS (France), MPG (Germany), and IGN (Spain). The Submillimeter Array is a joint project between the Smithsonian Astrophysical Observatory and the Academia Sinica Institute of Astronomy and Astrophysics and is funded by the Smithsonian Institution and the Academia Sinica. Data from the Steward Observatory spectropolarimetric monitoring project were used. This program is supported by Fermi Guest Investigator grants NNX08AW56G, NNX09AU10G, and NNX12AO93G. The Metsähovi team acknowledges the support from the Academy of Finland to our observing projects (numbers 212656, 210338, 121148, and others).

REFERENCES

Abdo, A. A., Ackermann, M., Ajello, M., et al. 2010a, ApJ, 715, 429
Abdo, A. A., Ackermann, M., Ajello, M., et al. 2010b, Natur, 463, 919
Ackermann, M., Ajello, M., Allafort, A., et al. 2011, ApJ, 743, 171
Agudo, I., Gómez, J.-L, Marti, J.-M., et al. 2011, ApJL, 549, L183
Agudo, I., Krichbaum, T. P., Ungerechts, H., et al. 2006, A&A, 456, 117
Agudo, I., Molina, S. N., Gómez, J. L., et al. 2012, IJMPS, 8, 299
Agudo, I., Thum, C., Gómez, J. L., & Wiesemeyer, H. 2014, A&A, 566, A59
Agudo, I., Thum, C., Wiesemeyer, H., & Krichbaum, T. P. 2010, ApJS, 189, 1
Alexander, T. 1997, in Astrophysics and Space Science Library 218, Astronomical Time Series, ed. D. Maoz, A. Sternberg & E. M. Leibowitz (Dordrecht: Kluwer), 163
Alexander, T. 2013, arXiv:1302.1508
Blinov, D., Pavlidou, V., Papadakis, I., et al. 2015, MNRAS, 453, 1669
Burbidge, G. R., Jones, T. W., & Odell, S. L. 1974, ApJ, 193, 43
Cardelli, J. A., Clayton, G. C., & Mathis, J. S. 1989, ApJ, 345, 245
Carrasco, L., Luna, A., Porras, A., & Mayya, D. Y. 2012, ATel, 4442, 1
Casadio, C., Gómez, J. L., Grandi, P., et al. 2015, ApJ, 808, 162
Chatterjee, R., Marscher, A. P., Jorstad, S. G., et al. 2009, ApJ, 704, 1689
Chatterjee, R., Marscher, A. P., Jorstad, S. G., et al. 2011, ApJ, 734, 43
Clemens, D. P., Sarcia, D., Grabau, A., et al. 2007, PASP, 119, 1385

D'Arcangelo, F. D., Marscher, A. P., Jorstad, S. G., et al. 2007, ApJL, 659, L107
Fromm, C. M., Perucho, M., Ros, E., Savolainen, T., & Zensus, J. A. 2015, A&A, 576, A43
Fromm, C. M., Perucho, M., Ros, E., et al. 2011, A&A, 531, A95
Fromm, C. M., Ros, E., Perucho, M., et al. 2013a, A&A, 551, A32
Fromm, C. M., Ros, E., Perucho, M., et al. 2013b, A&A, 557, A105
Gabuzda, D. C., Vitrishchak, V. M., Mahmud, M., & O'Sullivan, S. P. 2008, MNRAS, 384, 1003
Ghisellini, G., & Tavecchio, F. 2008, MNRAS, 387, 1669
Gómez, J.-L., Marscher, A. P., Alberdi, A., Jorstad, S. G., & Agudo, I. 2001, ApJL, 561, L161
Gómez, J., Marscher, A., Alberdi, A., et al. 2002, Polarization Calibration of the VLBA Using the D-terms, Tech. Rep., National Radio Astronomy Observatory, VLBA Scientific Memo
Grandi, P., Torresi, E., & Stanghellini, C. 2012, ApJL, 751, L3
Gurwell, M. A., Peck, A. B., Hostler, S. R., Darrah, M. R., & Katz, C. A. 2007, in ASP Conf. Ser. 375, From Z-Machines to ALMA: (Sub) Millimeter Spectroscopy of Galaxies, ed. A. J. Baker et al. (San Francisco, CA: ASP), 234
Hagen-Thorn, V. A., Larionov, V. M., Jorstad, S. G., et al. 2008, ApJ, 672, 40
Hovatta, T., Lister, M. L., Aller, M. F., et al. 2012, AJ, 144, 105
Hovatta, T., Valtaoja, E., Tornikoski, M., & Lähteenmäki, A. 2009, A&A, 494, 527
Itoh, R., Fukazawa, Y., Tanaka, Y. T., et al. 2013, ApJL, 768, L24
Jones, T. W. 1988, ApJ, 332, 678
Jorstad, S. G., Marscher, A. P., Larionov, V. M., et al. 2010, ApJ, 715, 362
Jorstad, S. G., Marscher, A. P., Lister, M. L., et al. 2005, AJ, 130, 1418
Jorstad, S. G., Marscher, A. P., Mattox, J. R., et al. 2001, ApJS, 134, 181
Jorstad, S. G., Marscher, A. P., Smith, P. S., et al. 2013, ApJ, 773, 147
Larionov, V., Blinov, D., & Jorstad, S. 2012, ATel, 4397, 1
Larionov, V. M., Blinov, D. A., Jorstad, S. G., et al. 2013a, EPJWC, 61, 4019
Larionov, V. M., Jorstad, S. G., Marscher, A. P., et al. 2013b, ApJ, 768, 40
Larionov, V. M., Villata, M., & Raiteri, C. M. 2010, A&A, 510, A93
Lister, M. L., Aller, M. F., Aller, H. D., et al. 2013, AJ, 146, 120
Lister, M. L., Cohen, M. H., Homan, D. C., et al. 2009, AJ, 138, 1874
MacDonald, N. R., Marscher, A. P., Jorstad, S. G., & Joshi, M. 2015, ApJ, 804, 111
Maraschi, L., Ghisellini, G., Tanzi, E. G., & Treves, A. 1986, ApJ, 310, 325
Marscher, A. P. 2014, ApJ, 780, 87
Marscher, A. P., Jorstad, S. G., D'Arcangelo, F. D., et al. 2008, Natur, 452, 966
Marscher, A. P., Jorstad, S. G., Gómez, J.-L., et al. 2002, Natur, 417, 625
Marscher, A. P., Jorstad, S. G., Larionov, V. M., et al. 2010, ApJL, 710, L126
Mead, A. R. G., Ballard, K. R., Brand, P. W. J. L., et al. 1990, A&AS, 83, 183
Moore, R. L., & Stockman, H. S. 1981, ApJ, 243, 60
Morozova, D. A., Larionov, V. M., Troitsky, I. S., et al. 2014, AJ, 148, 42
Nolan, P. L., Abdo, A. A., Ackermann, M., et al. 2012, ApJS, 199, 31
Osterman Meyer, A., Miller, H. R., Marshall, K., et al. 2009, AJ, 138, 1902
Pacciani, L., Tavecchio, F., Donnarumma, I., et al. 2014, ApJ, 790, 45
Pica, A. J., Smith, A. G., Webb, J. R., et al. 1988, AJ, 96, 1215
Planck Collaboration, Ade, P. A. R., Aghanim, N., et al. 2014, A&A, 571, A16
Poole, T. S., Breeveld, A. A., Page, M. J., et al. 2008, MNRAS, 383, 627
Raiteri, C. M., Villata, M., Aller, M. F., et al. 2011, A&A, 534, A87
Ramakrishnan, V., León-Tavares, J., Rastorgueva-Foi, E. A., et al. 2014, MNRAS, 445, 1636
Rani, B., Krichbaum, T. P., Marscher, A. P., et al. 2014, A&A, 571, L2
Rantakyrö, F. T., Wiik, K., Tornikoski, M., Valtaoja, E., & Bååth, L. B. 2003, A&A, 405, 473
Savolainen, T., Wiik, K., Valtaoja, E., Jorstad, S. G., & Marscher, A. P. 2002, A&A, 394, 851
Schlafly, E. F., & Finkbeiner, D. P. 2011, ApJ, 737, 103
Schmidt, G. D., Stockman, H. S., & Smith, P. S. 1992, ApJL, 398, L57
Sikora, M., Stawarz, Ł., Moderski, R., Nalewajko, K., & Madejski, G. M. 2009, ApJ, 704, 38
Smith, P. S., Montiel, E., Rightley, S., et al. 2009, arXiv:0912.3621
Spencer, R. E., McDowell, J. C., Charlesworth, M., et al. 1989, MNRAS, 240, 657
Stanghellini, C., O'Dea, C. P., Dallacasa, D., et al. 1998, A&A, 131, 303
Vlahakis, N. 2006, in ASP Conf. Ser. 350, Blazar Variability Workshop II: Entering the GLAST Era, ed. H. R. Miller et al. (San Francisco, CA: ASP), 169
Williamson, K. E., Jorstad, S. G., Marscher, A. P., et al. 2014, ApJ, 789, 135
Zamaninasab, M., Clausen-Brown, E., Savolainen, T., & Tchekhovskoy, A. 2014, Natur, 510, 126
Zensus, J. A., Ros, E., Kellermann, K. I., et al. 2002, AJ, 124, 662

4.3 Resume and contextualization

The most interesting result we derive comparing both multi-wavelength studies is that, despite they belong to very different class of AGN, the radio galaxy 3C 120 and the blazar CTA 102 display similar properties when they experience γ-ray outbursts.

In particular, we found that γ-ray outbursts with a counterpart at millimeter wavebands or in coincidence also with flares at X-ray, UV, optical and Near-Infrared frequencies as occurs in CTA 102, are always associated with the ejection of a new superluminal component, meaning the passage of the component through the mm-VLBI core. On the other hand we have that not all ejections of new components are associated to γ-ray events.

In both sources we found evidences of changes in the direction of motions of superluminal components, where components associated to γ-ray outbursts move in a direction closer to our line of site. We then infer that γ-ray flares are detected when a new superluminal component is ejected at a smaller viewing angle. In the case of CTA 102 we also observe two orphan γ-ray flares (without counterparts at the other wavebands); only one probably associated to the passage of the new superluminal component through a recollimation shock close to the core.

The γ-ray dissipation regions are located in both cases in the parsec-scale jet, closer to the mm-VLBI core and far from the central engine. The difficulty of having contribution from external photon fields at such distances supports the synchrotron self Compton mechanism as responsible for γ-ray photons.

Many blazars show characteristics similar to those described above during high-energy events. I report below some studies where I contributed and where we found some of the behaviors described.

We found evidences of γ-ray outbursts triggered by the passage of a new superluminal component through the mm-VLBI core in many blazars, being both FSRQ objects as the FSRQs 1156+295 (Ramakrishnan et al., 2014), PKS 1510-089 (Aleksić et al., 2014) and 3C 454.3 (Jorstad et al., 2013) and BL Lac objects as the BL Lac 0954+658 (Morozova et al., 2014). In Morozova et al. (2014) and Ramakrishnan et al. (2014) we also observe minor γ-ray flares associated to the passage of the superluminal knot through a standing recollimation shock close to the mm-VLBI core, as occurs in CTA 102. The passage of the new emerging knot through three recollimation shock

inside the core it is a possible scenario also to explain the triple structure of three γ-ray and optical flares observed in 3C 454.3 between autumn 2009 and autumn 2010 (Jorstad et al., 2013). In 3C 454.3 the repeated pattern suggests the same mechanism and location for all the three flares which occurred in coincidence also with X-ray, optical and millimeter outbursts.

However, not always γ-ray flares have a counterpart at millimeter wavelengths; orphan flares have been observed in other blazar besides CTA 102. For example, in Lico et al. (2014) we analyzed VLBA observations at 15, 24 and 43 GHz of the blazar Mrk 421 from January to December 2011 in coincidence with three γ-ray flares of similar intensity detected by *Fermi* in March, September and November 2011, obtaining that only the March event was associated to an increase in flux at all the three radio wavelengths.

In many blazars, γ-ray and optical flares occur very close in time as we observe for example in 4C 38.41 and BL Lacertae (Raiteri et al., 2012, 2013) and often in coincidence also with millimeter and X-ray flares as occur in 3C 454.3 (Jorstad et al., 2013) and 0954+658 (Morozova et al., 2014). But sometimes γ-ray and optical flares occur before millimeter and X-ray outbursts that instead take place in the same emitting region downstream the location of the γ-ray event, as we found in OJ 248 (Carnerero et al., 2015) and BL Lacertae (Raiteri et al., 2013). In these two objects (OJ 248 and BL Lacertae) as also in 4C 38.41, we adopt a geometrical interpretation for the observed flares considering, as we have in 3C 120 and CTA 102, that the jet or the different emitting regions change their orientation over time and resulting oriented closer to the line of sight during high energy events.

Changes in polarization of these objects are frequently observed during outbursts. In some cases we have evidences of both shocks, that would produce an increase in the degree of polarization and a methodical change in the EVPAs orientation (see § 2.3), and turbulent processes. This is the case of 3C 454.3 where the degree of optical linear polarization display a general increase during an outburst but it drops significantly when the γ-ray peak occurs (Jorstad et al., 2013). Instead in other cases the increase in the degree of optical polarization is in coincidence with an optical and γ-ray flare and a wide rotation of optical EVPAs is also observed during the outburst, as we found in OJ 248 (Carnerero et al., 2015) and 0954+658 (Morozova et al., 2014). In the latter, optical EVPAs are observed to rotate smoothly more than 300° in one direction and

this can be related to the spiral path followed by the component along helical magnetic field lines, as we also suggest for CTA 102 (see sketch represented in Figure 4.1).

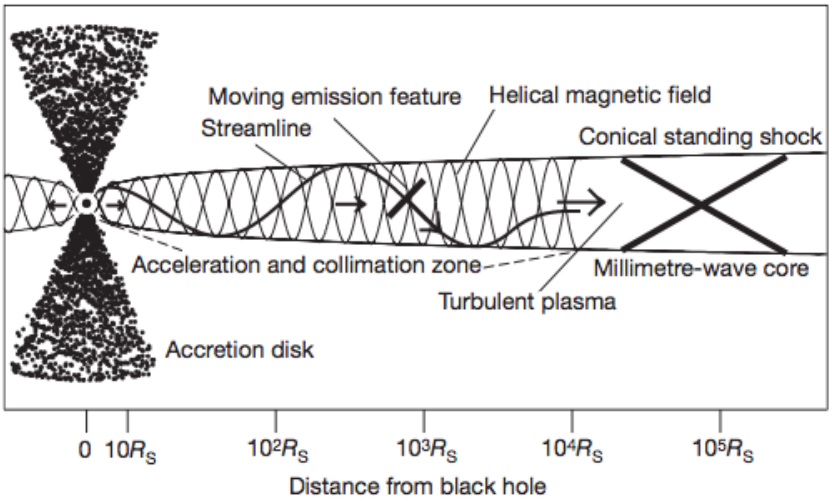

Figure 4.1: Inner jet model. A moving shock propagates along the jet following helical magnetic field lines. The millimeter core is here the first recollimation shock and in this sketch is located at almost 10^5 Schwarzschild radii (R_s), as in the case of 3C 120 and CTA 102. Reproduced from Marscher et al. (2008).

The scenario offered by radio galaxies at high energies is not so wide as for blazars. This is mainly because radio galaxies are less powerful objects and because they usually are oriented at larger viewing angles, having for this less probability of emitting up to γ-ray frequencies. Only a small fraction of radio galaxies has been detected at γ-ray frequencies, as we mentioned in § 3.2, and before 3C 120, the connection between a γ-ray outburst and the ejection of a new superluminal component from the mm-VLBI core, has been observed only in another radio galaxy, the FRII radio galaxy 3C 111 (Grandi et al., 2012). The radio galaxy 3C 120 is then the first FRI radio galaxy where we observe this. The other famous FRI radio galaxy which has experienced many high energy (100 MeV<E<100 GeV energies) and very high energies events (E>100 GeV) events over time is the radio galaxy M 87. Despite many events registered from this source, no new components have been clearly observed emerging from the core during these events; only evidences of brightening in the region close to the core (Acciari et al., 2009) or time-lag between flaring peaks at 43 and 22 GHz (Hada et al., 2014) have been observed as evidences of newborn components in coincidence with VHE flares

in 2008 and 2012, respectively. In Hada et al. (2014) we found that from February to March 2012, when M 87 exhibited an elevated state at VHE, the radio core at 22 and 43 GHz increased its flux density while the peculiar emitting region HST-1, which is a possible candidate for the γ-ray photons production, was in a low state of flux. Another interesting result we obtained in Hada et al. (2014) is that the HE light curve generated with *Fermi* data showed an increase before the VHE event while it was stable during the event.

To conclude we want to remark an important result coming out from our multi-wavelengths studies of 3C 120 and CTA 102 that is the need of considering the millimeter core as a recollimation shock. We found in fact that in both sources the γ-ray flares occurred close to the 43 GHz core that in both cases is located far away from the central engine, at almost 10^5 Schwarzschild radii (R_s) (Marscher et al., 2002; Fromm et al., 2015), resembling the situation in Figure 4.1. Similar distances between the black hole and the mm-wave core, of the order of 10^4-10^5 R_s, were founded in others blazars (Marscher et al., 2008, 2010) as well as in the radio galaxy 3C 111 Chatterjee et al. (2011). Very different is instead the distance between the mm-wave core and the black hole in the nearby radio galaxy M 87, where the 43 GHz core results located at few tens of Schwarzschild radii (Hada et al., 2011). We will focus again our attention on this topic in the next Chapter.

5

Polarimetric studies on the radio galaxies 3C 120 and M 87: revealing the nature of C80 and HST-1

The radio galaxies 3C 120 and M 87 are very well known and well studied AGN due to their proximity, their bright and knotty jets and some other peculiarities which make them interesting subjects of study.

As we learned in Chapter 4, they are both gamma-ray emitters, with M 87 being also a TeV emitter, although we know from previous studies that M 87 jet is not oriented at a so small viewing angle as we would expect in order to have emission up to very high energies. This, together with the lack of prominent low energy flares in nuclear regions during some VHE events puts some doubts on the location and mechanism of the VHE emission observed in this source. In the past, besides the core also the peculiar emitting region named HST-1, and located at a de-projected distance of $\gtrsim 120$ pc downstream of the nucleus, has been considered a possible candidate for the VHE emission. During the VHE event registered in 2005, radio, optical and X-ray outbursts have been registered from HST-1, while the nucleus was in a low state of flux (Harris et al., 2006). Three more VHE events have been registered after the 2005 event: in 2008, 2010 and 2012. The 2008 and 2012 events suggest the core as possible site for the

TeV emission while the peculiar knot HST-1 remained quiescent (Acciari et al., 2009; Hada et al., 2014).

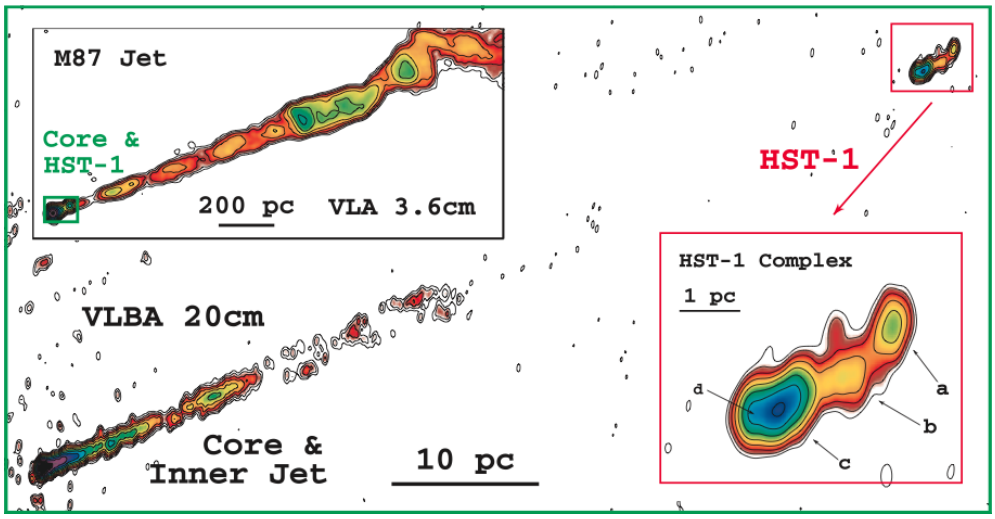

Figure 5.1: M 87 and HST-1 multi-scale images. Two images of the M 87 jet with the VLBA at 20 cm (main image) and with the VLA at 3.6 cm (upper left inset panel). In the VLA image a green box indicates the portion of the jet represented in the VLBA image. The red box on the bottom right displays a zoom of the HST-1 region in the VLBA image. Reproduced from Cheung et al. (2007).

The 2010 event complicated more the scenario because no prominent low energy flares have been detected in the core nor in the HST-1 region. A key aspect of this scenario is the nature of the peculiar knot HST-1 which is still matter of debate, so far. With the sufficient resolution (VLBA observations) we observe a jet that becomes progressively fainter due to radiative cooling until it stops to emit, resuming surprisingly after many parsecs where HST-1 is located, as we appreciate in Figure 5.1. To explain the resume of the emission at such large distances from the nucleus we need some mechanism of particles acceleration occurring in the HST-1 region, as it could be recollimation shock (see § 2.3).

The hypothesis of a recollimation shock is supported by many previous studies: in Stawarz et al. (2006) authors found that a reconfinement nozzle is expected in the position of HST-1 due to interaction of the jet with the external medium; also semi-analytical and numerical magneto-hydrodinamic (MHD) models support the hypothesis of the recollimation shock (Gracia et al., 2009; Bromberg & Levinson, 2009; Nalewajko,

2012) as well as VLBI observations in Asada & Nakamura (2012) showing that HST-1 corresponds to the location at which the jet of M 87 changes from a parabolic to a conical shape. There are, however, no conclusive observational indications for the existence of a stationary feature in HST-1 region associated with the recollimation shock as expected from numerical simulations (Gomez et al., 1995; Gómez et al., 1997) and observed in other sources (Agudo et al., 2012; Cohen et al., 2014). Only in early 1.7 GHz VLBA observations in Cheung et al. (2007) the authors reported an upper limit of $0.25c$ for the apparent motion of the upstream region of HST-1 (labeled by these authors as HST-1d).

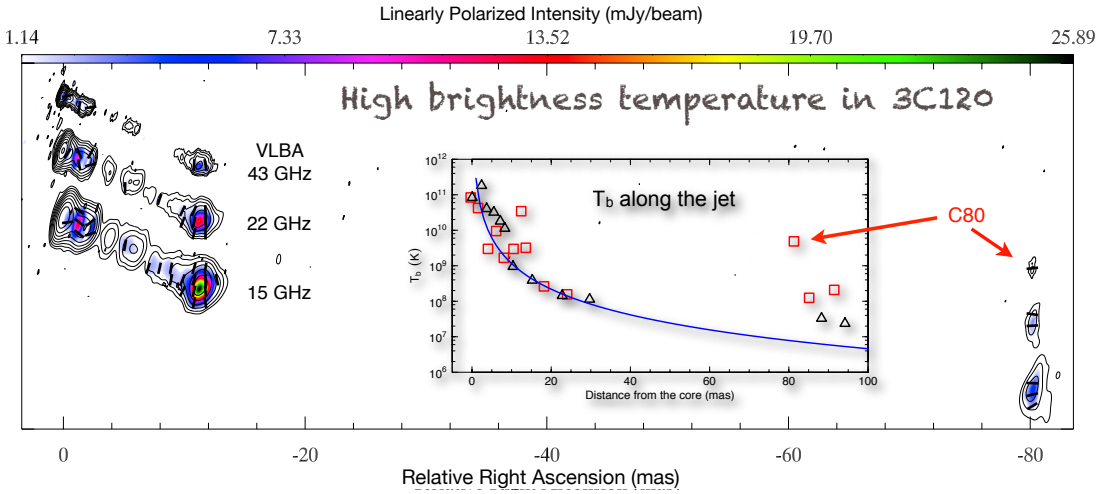

Figure 5.2: 3C 120 and C80 VLBA images. VLBA observations of 3C 120 in November 2007 at 43 (top), 22 (middle) and 15 (bottom) GHz; reproduced from Roca-Sogorb et al. (2010). Inset panel shows the observed brightness temperature for different components along the jet, with the red squares and black triangles representing different epochs. The blue line represents the expected decline with distance from the core.

Another radio galaxy where we find a similar peculiarity is the radio galaxy 3C 120. Also in this source the jet resumes its emission at almost 80 mas ($\gtrsim$140 pc, de-projected, considering a viewing angle $<20°$ (Roca-Sogorb et al., 2010)) from the core, as we appreciate in Figure 5.2. Our research group discovered for the first time the emitting region at $\sim$80 mas (named C80) from polarimetric VLBA observations of 3C 120 performed in November 2007. In Roca-Sogorb et al. (2010) the authors reported an unusually high brightness temperature for component C80 which they explained due to a strong stationary shock located in that region.

5. Polarimetric studies on the radio galaxies 3C 120 and M 87: revealing the nature of C80 and HST-1

The bright blazar-like jet of 3C 120 has a very rich structure, displaying both superluminal components and stationary features suggestive of a helical configuration seen in projection (Walker et al., 2001) which could be associated to bot the jet geometry and the magnetic field structure (Gómez et al., 2001b). Another very interesting finding in this radio galaxy is the observed connection between the activity in the accretion disk and the subsequent appearance of a new component in the radio jet suggesting the accretion disk as the origin site of jets in this radio galaxy (Marscher et al., 2002; Chatterjee et al., 2009). Also the linearly polarized emission resulted a powerful tool in revealing more details of this radio galaxy: the source of Faraday Rotation in the inner jet seems to be mainly associated to foreground clouds and not to the plasma in the jet (Gómez et al., 2011).

In the light of findings in Roca-Sogorb et al. (2010), we decided to performed a detailed analysis of the unusual emitting region at 80 mas through new multi-frequency polarimetric VLBA images (Agudo et al., 2012). In Agudo et al. (2012) we also compared observational properties with simulated images of conical recollimation shocks obtained by Dr. Timothy V. Cawthorne using the models described in Cawthorne & Cobb (1990) and Cawthorne (2006). I performed the calibration and imaging of the majority of data presented in Agudo et al. (2012), following the procedure described in § 3.2.

5.1 A recollimation shock 80 mas from the core in the jet of the radio galaxy 3C 120: observational evidence and modeling

The following article has been published in *The Astrophysical Journal* on June 20th, 2012 and it is presented here in its original form.

The reference for this article is: Agudo I., Gómez J. L., Casadio C., Cawthorne T. V., Roca-Sogorb M., 2012, ApJ, 752, 92.

The authors are: Iván Agudo, José L. Gómez, Carolina Casadio, Timothy V. Cawthorne and Mar Roca-Sogorb.

The Astrophysical Journal, 752:92 (9pp), 2012 June 20 doi:10.1088/0004-637X/752/2/92

A RECOLLIMATION SHOCK 80 mas FROM THE CORE IN THE JET OF THE RADIO GALAXY 3C 120: OBSERVATIONAL EVIDENCE AND MODELING

Iván Agudo[1,2], José L. Gómez[1], Carolina Casadio[1], Timothy V. Cawthorne[3], and Mar Roca-Sogorb[1]
[1] Instituto de Astrofísica de Andalucía, CSIC, Apartado 3004, 18080 Granada, Spain; jlgomez@iaa.es
[2] Institute for Astrophysical Research, Boston University, 725 Commonwealth Avenue, Boston, MA 02215, USA
[3] School of Computing, Engineering and Physical Science, University of Central Lancashire, Preston PR1 2HE, UK
Received 2012 March 13; accepted 2012 April 12; published 2012 May 30

ABSTRACT

We present Very Long Baseline Array observations of the radio galaxy 3C 120 at 5, 8, 12, and 15 GHz designed to study a peculiar stationary jet feature (hereafter C80) located ∼80 mas from the core, which was previously shown to display a brightness temperature ∼600 times larger than expected at such distances. The high sensitivity of the images—obtained between 2009 December and 2010 June—has revealed that C80 corresponds to the eastern flux density peak of an arc of emission (hereafter A80), downstream of which extends a large (∼20 mas in size) bubble-like structure that resembles an inverted bow shock. The linearly polarized emission closely follows that of the total intensity in A80, with the electric vector position angle distributed nearly perpendicular to the arc-shaped structure. Despite the stationary nature of C80/A80, superluminal components with speeds up to $3 \pm 1\,c$ have been detected downstream from its position, resembling the behavior observed in the HST-1 emission complex in M87. The total and polarized emission of the C80/A80 structure, its lack of motion, and brightness temperature excess are best reproduced by a model based on synchrotron emission from a conical shock with cone opening angle $\eta = 10^{\circ}$, jet viewing angle $\theta = 16^{\circ}$, a completely tangled upstream magnetic field, and upstream Lorentz factor $\gamma_u = 8.4$. The good agreement between our observations and numerical modeling leads us to conclude that the peculiar feature associated with C80/A80 corresponds to a conical recollimation shock in the jet of 3C 120 located at a de-projected distance of ∼190 pc downstream from the nucleus.

Key words: galaxies: active – galaxies: individual (3C 120) – galaxies: jets – polarization – radio continuum: galaxies

Online-only material: color figures

1. INTRODUCTION

The radio galaxy 3C 120 is a very active and powerful emitter of radiation at all observed wavebands. While classified as a Seyfert 1 (Burbidge 1967), its spectrum shows broad emission lines and a complex optical morphology which has been interpreted as the result of a past merger (García-Lorenzo et al. 2005). Variability in the emission lines has allowed reverberation mapping to yield a black hole mass of $\sim 3 \times 10^7\,M_{\odot}$ (Wandel et al. 1999). In X-rays, it is the brightest broad-line radio galaxy, with the X-ray spectrum becoming softer when the intensity increases (Maraschi et al. 1991), suggesting that the soft X-rays are dominated by the disk instead of the beamed jet. This has made it possible to establish a clear connection between the accretion disk and the radio jet through coordinated X-ray and radio observations (Marscher et al. 2002; Chatterjee et al. 2009). Along with 3C 111, 3C 120 is one of only two broad-line radio galaxies detected by *Fermi*-LAT in the GeV photon energy range, such emission being most probably the result of beamed radiation from the relativistic jet observed at intermediate viewing angles (Kataoka et al. 2011).

At radio wavelengths, 3C 120 has a blazar-like one-sided superluminal radio jet extending up to hundreds of kiloparsecs (Walker et al. 1987, 1988; Muxlow & Wilkinson 1991). Due to its proximity ($z = 0.033$), and to its bright millimeter emission (Agudo et al. 2010), Very Long Baseline Array (VLBA) observations at high frequencies (22, 43, and 86 GHz) show a very rich inner jet structure containing multiple superluminal components with apparent velocities up to $6c$ (Gómez et al. 1998, 1999; Homan et al. 2001; Jorstad et al. 2005; Marscher et al. 2007). Continued monthly monitoring with the VLBA at 22 and 43 GHz has revealed rapid changes in the total and linearly polarized intensity, interpreted as resulting from the interaction of the jet components with the external medium (Gómez et al. 2000, 2001). Longer wavelength very long baseline interferometry (VLBI) observations have shown evidence for the existence of an underlying helical jet structure (Walker et al. 2001), which has been interpreted as the result of jet precession (Hardee et al. 2005; Caproni & Abraham 2004)

Combination of the information from a sequence of 12 monthly polarimetric VLBA observations of 3C 120 at 15, 22, and 43 GHz has allowed imaging of the linearly polarized emission within the innermost ∼10 mas jet structure, revealing a coherent in time Faraday screen and polarization angles (Gómez et al. 2008). Gradients in Faraday rotation and degree of polarization across and along the jet are observed, together with a localized region of high (∼6000 rad m^{-2}) Faraday rotation measure (RM) between approximately 3 and 4 mas from the core. The existence of this localized region of high RM, together with the observation of uncorrelated changes in the RM screen and RM-corrected polarization angles, suggests that a significant fraction of the Faraday RM found in 3C 120 originates in foreground clouds, rather than in a sheath intimately associated with the emitting jet (Gómez et al. 2011).

VLBA observations of 3C 120 in 2007 November revealed a component (hereafter C80) located at 80 mas (which corresponds to a de-projected distance of ∼190 pc for a viewing angle of 16°) with a brightness temperature $T_b \approx 5 \times 10^9$ K, which is about 600 times higher than expected at such distances from the core (Roca-Sogorb et al. 2010). Analysis of

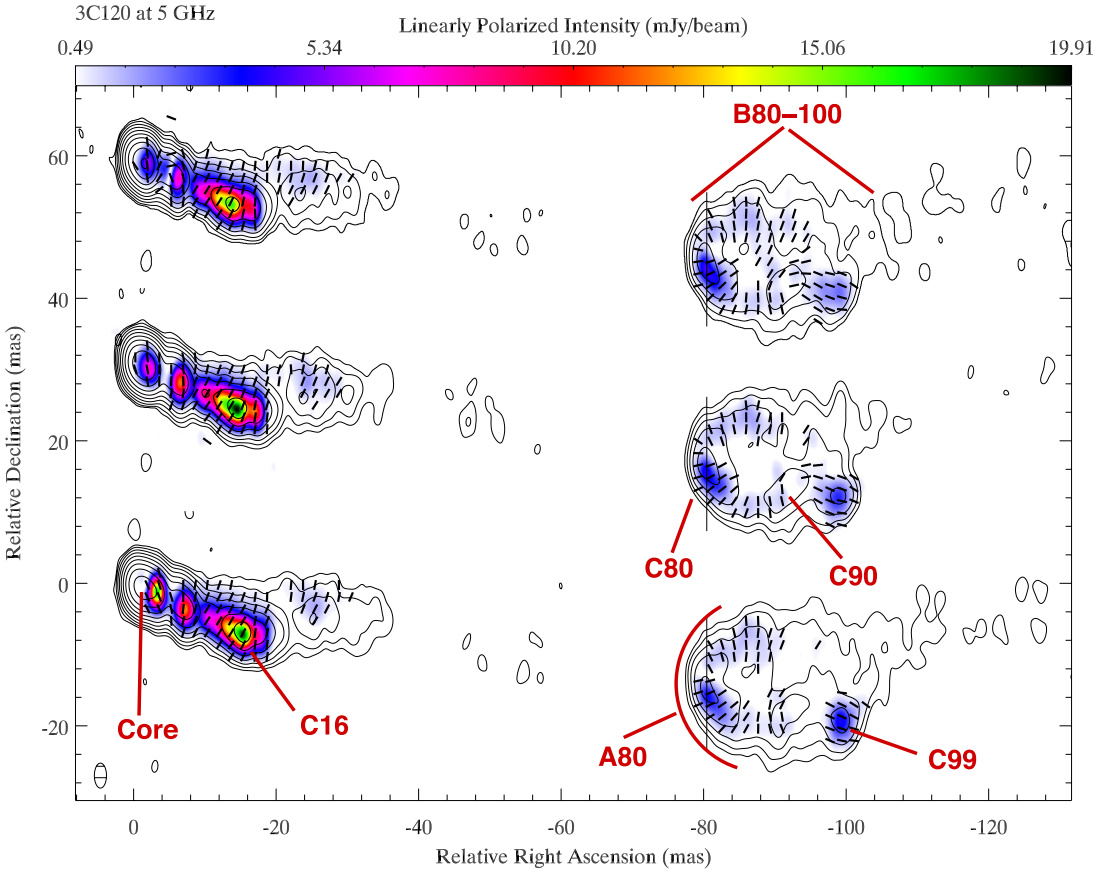

Figure 1. Sequence of VLBA images of 3C 120 at 5 GHz taken on 2009 December 14, 2010 March 14, and 2010 June 21 (from top to bottom). Vertical separations are proportional to the time difference between epochs. Total intensity contours are overlaid at 0.03%, 0.07%, 0.17%, 0.41%, 1.02%, 2.49%, 6.11%, 14.98%, 36.72%, and 90% of the total intensity peak at 1.53 Jy beam^{-1}. A common convolving beam of FWHM 3.5 × 1.7 mas at 0° was used for all images and is shown in the lower left corner. Gray-scale images (on a linear scale shown at the top) show the linearly polarized intensity. Black sticks (or unit length) indicate the polarization electric vector position angle, uncorrected for Faraday rotation. The vertical lines at ∼80 mas from the core indicate the location where the transverse cuts of the fractional polarization of the jet shown in Figure 5 were performed.

(A color version of this figure is available in the online journal.)

previous observations (starting in 1982) shows that this component was not detected at frequencies higher than 5 GHz before 2007 April, when it was first observed at 15 GHz. After this epoch C80 appears in all images (even at the highest frequencies) at the same location without significant changes in its flux density. Roca-Sogorb et al. (2010) conclude that the unusually high T_b of C80 could be explained by a helical shocked jet model—and perhaps some flow acceleration—but it seems very unlikely that this corresponds to the usual shock that emerges from the core and travels downstream to the location of C80, requiring some other intrinsic process capable of providing a local amplification in the density of high energy particles and/or magnetic field.

Here we present the results from a new observing program designed to study the nature of the C80 feature. Such a study is complemented with semi-dynamical and semi-analytical simulations to help us interpret the structure of C80 and its surrounding jet region. The paper is organized as follows. In Section 2, we describe the new VLBA observations presented here and their data reduction procedures; in Section 3, we report on the results that are obtained directly from the observations; we present the numerical models used to reproduce these observations in Section 4. Finally, in Section 5 we summarize our main results and draw the conclusions from this work.

At the redshift of 3C 120, and under the standard ΛCDM cosmology (with $H_0 = 71$ km s^{-1} Mpc^{-1}, $\Omega_M = 0.27$, and $\Omega_\Lambda = 0.73$) that we assume in this work, an angular separation of 1 mas in the sky corresponds to a projected linear distance of 0.65 pc, and a proper motion of 1 mas yr^{-1} is translated to a superluminal speed 2.19 times larger than the speed of light.

2. OBSERVATIONS

The new multi-frequency and polarimetric VLBA images of the jet in 3C 120 presented in this paper were obtained from observations performed on 2009 December 14, 2010 March 14, and 2010 June 21. The corresponding observations, that employed all ten antennas of the VLBA, were performed at 5, 8, and 12 GHz (see Figures 1–3), and used a two-bit signal sampling to record in a 32 MHz bandwidth per circular polarization at a recording rate of 256 Mbits s^{-1}.

Calibration of the data was performed within the AIPS software package following the standard procedure for VLBI polarimetric observations (Leppänen et al. 1995). To correct for opacity effects on the higher frequency observations (>8 GHz) we used the recorded variation of the system temperature on every station to solve for the receiver temperature and zenith opacity. The final images were obtained following the standard hybrid-mapping procedure through an iterative process that

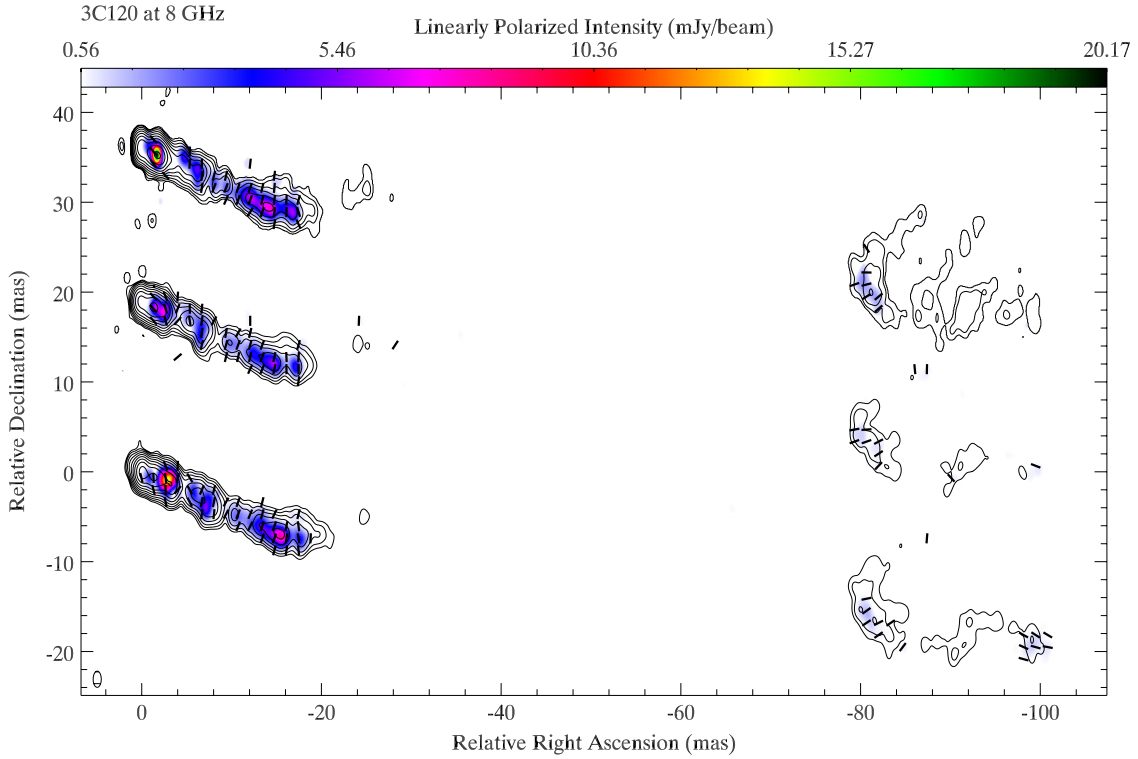

Figure 2. Same as Figure 1 but for the 8 GHz images. Contour levels are drawn at 0.11%, 0.23%, 0.49%, 1.03%, 2.17%, 4.58%, 9.64%, 20.30%, 42.74%, and 90% of the total intensity peak at 1.04 Jy beam^{-1}. A common convolving beam of FWHM 1.8 × 0.9 mas at 0° was used for all images.
(A color version of this figure is available in the online journal.)

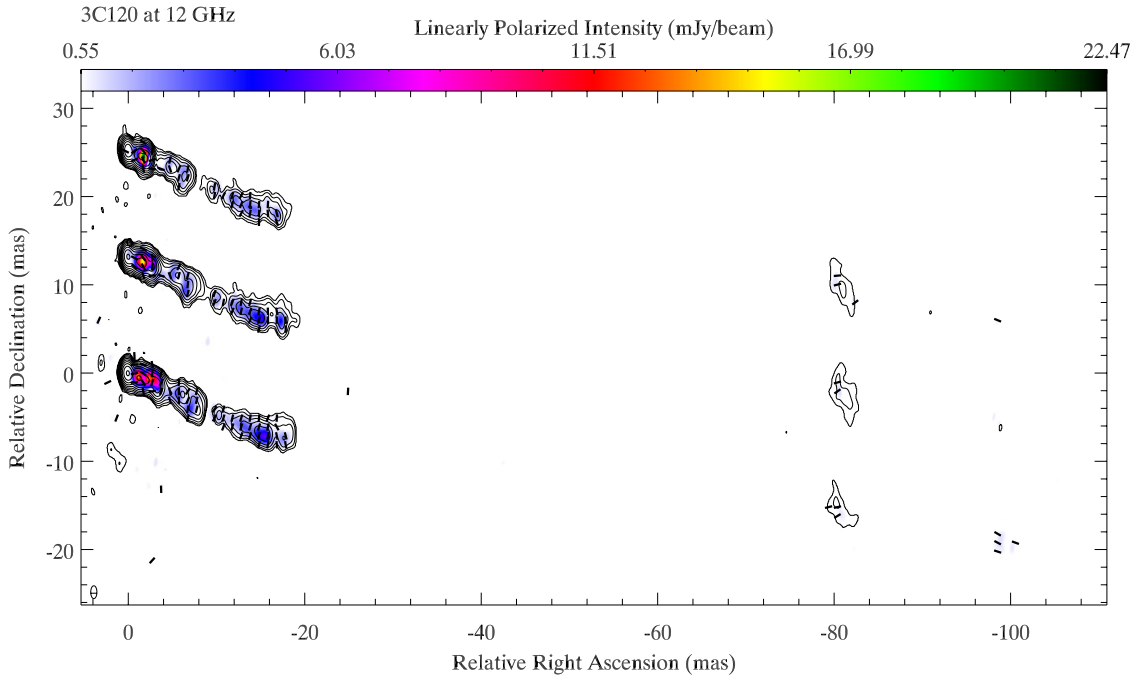

Figure 3. Same as Figure 1 but for the 12 GHz images. Contour levels are drawn at 0.17%, 0.34%, 0.69%, 1.38%, 2.76%, 5.54%, 11.13%, 22.34%, 44.83%, and 90% of the total intensity peak at 0.75 Jy beam^{-1}. A common convolving beam of FWHM 1.5 × 0.7 mas at 0° was used for all images.
(A color version of this figure is available in the online journal.)

employed both AIPS and the DIFMAP package (Shepherd 1997).

For the calibration of the absolute orientation of the electric vector position angle (EVPA) we employed both a set of VLA observations of our polarization calibrators (NRAO150, OJ287, 3C 279, and 3C 454.3) from the VLA/VLBA Polarization Calibration Program[4] and the information extracted by the comparison of the D-terms at different observing epochs

[4] http://www.vla.nrao.edu/astro/calib/polar/

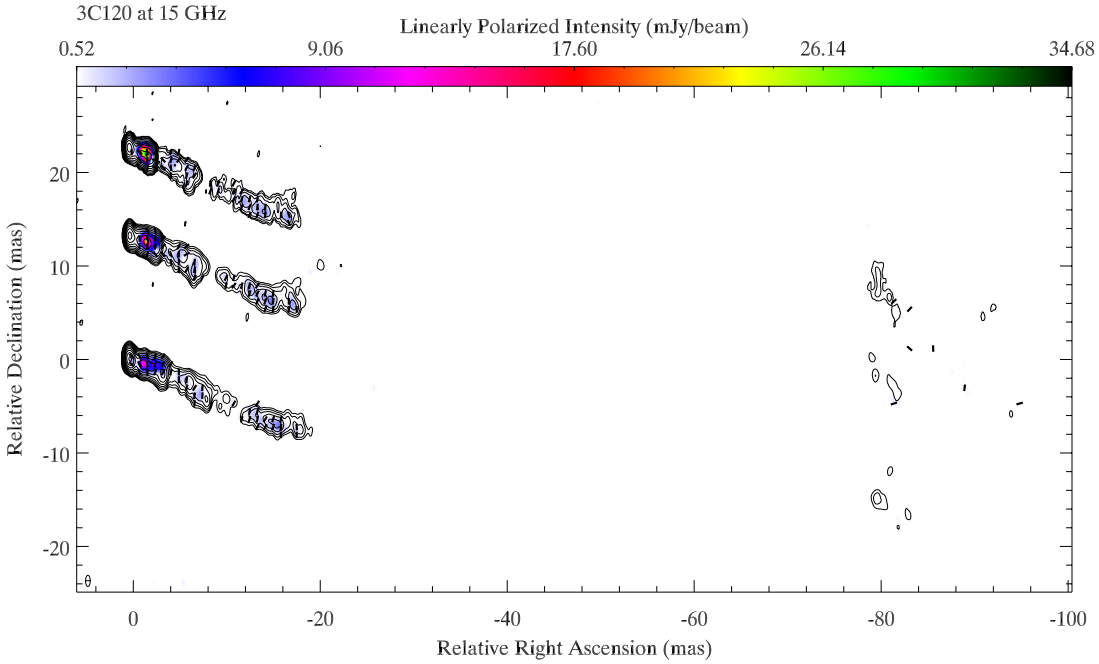

Figure 4. Same as Figure 1 but for the 15 GHz images obtained and calibrated by the MOJAVE team (see the text). From top to bottom, the three images correspond to VLBA observations performed on 2009 December 10, 2010 March 10, and 2010 July 12. Contour levels are drawn at 0.13%, 0.27%, 0.56%, 1.15%, 2.38%, 4.92%, 10.17%, 21.04%, 43.52%, and 90% of the total intensity peak at 0.73 Jy beam^{-1}. A common convolving beam of FWHM 1.2 × 0.5 mas at 0° was used for all images.
(A color version of this figure is available in the online journal.)

(see Gómez et al. 2002). The useful input from the first of these two methods was rather limited in our case because the VLA/VLBA Polarization Calibration Program does not include data at 12 GHz, and the program was halted at the end of 2009 to focus on EVLA commissioning, hence preventing us from getting the calibration at 5 and 8 GHz for the latest two observing epochs in 2010. However, we verified that the 5 and 8 GHz D-terms were very stable during our three observations. Gómez et al. (2002) showed that in this case the D-terms can be used to calibrate those observing epochs without an independent EVPA calibration. This allowed us to calibrate the 5 and 8 GHz EVPAs of the latest two observing epochs by rotating their corresponding D-terms to match those of the fully calibrated first observing epoch.

At 12 GHz there are no available independent polarization data from our sources to estimate the adequate EVPA calibration. However, we used the publicly available total-intensity and linear-polarization 15 GHz VLBA images of 3C 120 taken (and calibrated) by the MOJAVE team[5] on dates close to those of our multi-frequency observations (see Figure 4). These 15 GHz EVPA images allowed us to calibrate our 12 GHz EVPA on nearby epochs by fitting Faraday rotation profiles at 5, 8, and 15 GHz to find the correct EVPA calibration at 12 GHz. The stability of the D-terms at 12 GHz was also used as a cross-check for the final calibration at this frequency. The final errors in our absolute calibration of the EVPA at all our observing frequencies are estimated to be ∼5°.

3. RESULTS

3.1. The Inner ∼20 mas of the Jet

Figures 1–4 show the new 5, 8, 12, and 15 GHz VLBA images of 3C 120 in total and linearly polarized intensity, as well as their corresponding EVPA distribution. These new images show a straight jet within the inner ∼20 mas that contains a bright and highly polarized knot at ∼16 mas from the core (C16). The EVPA of C16 is distributed perpendicular to the jet axis. The same EVPA orientation is found in the C16 counterparts at 8, 12, and 15 GHz (see Figures 2–4) where the images show an increasingly rich structure of jet knots with observing frequency all along the innermost 20 mas of the jet. The multi-frequency polarization properties of C16 match those of the C12 jet feature reported by Gómez et al. (2011). This, together with the total flux dominance of both C16 and C12 in regions $\gtrsim$10 mas from the core and the fact that C16 lies in the jet region expected from the position of C12 and the typical proper motions in the jet of 3C 120 (∼2 mas yr^{-1}, Gómez et al. 2001), allows us to identify both components as representing the same jet moving knot.

3.2. Bright Emission Region between 80 and 100 mas from the Core: B80-100

The jet feature at ∼80 mas from the core (C80) is detected in all new images presented in this work from 5 to 15 GHz (Figures 1–4). No other jet feature is detected in the jet downstream of C80 in the 12 and 15 GHz images presented here. However, the new 5 GHz images show an emission region in an arc from north to south around the eastern side of C80, having the shape of an inverted bow shock, similar to those observed at the end of the large-scale jets of FR-II radio galaxies (e.g., Perley et al. 1984). Perhaps because of the lack of sensitivity, this arc of emission (that we have labeled as A80) was not detected by our previous short-integration VLBA observations of the source at 5 GHz (see Roca-Sogorb et al. 2010; Gómez et al. 2011), where only the detection of C80, the brightest region in A80, was reported.

Together with C80/A80, the new 5 GHz images show a bubble-like extended emission—region larger than ∼20 mas

[5] http://www.physics.purdue.edu/MOJAVE/

along the jet axis—from the sharp edge near the location of C80, and ∼20 mas across the jet axis. This emission structure will be called B80-100 hereafter (see Figure 1). Neither the total intensity nor the polarized emission is symmetric with regard to the jet axis in B80-100. The maxima in total and linearly polarized intensity are both located on the southern side of the bubble, which resembles the behavior of the jet in 3C 120 within the first ∼10 mas (Gómez et al. 2000, 2001, 2008).

Further downstream from C80 (but still within B80-100), C90, a more extended jet region reported by Roca-Sogorb et al. (2010) and Gómez et al. (2011) at observing frequencies below 8 GHz, starts to be resolved in our new images (Figures 1 and 2). Our 8 GHz images in 2009 and 2010 show the jet emission around C90 as a slightly more extended and sparser jet region than in the image taken in 2007 November 30 by Gómez et al. (2011) at the same frequency. C90 is better observed in our 5 GHz images that map the entire B80-100 at higher sensitivity. This provides a reliable superluminal speed measurement of C90 ($v_{C90} = 3.4 \pm 1.0\,c$), which contrasts with the stationary character of C80 (Roca-Sogorb et al. 2010) located ∼10 mas upstream in the jet.

Our new images also show a bright and compact jet region located ∼99 mas from the core—reported here for the first time—that we have labeled C99. Our kinematic study of this feature also reveals superluminal proper motion ($v_{C99} = 3.0 \pm 1.1\,c$) of similar magnitude and direction downstream from the jet than C90. The superluminal character of the flow downstream from C80 resembles the behavior near the HST-1 knot in M87 as reported by Cheung et al. (2007), who suggested HST-1 as the site of a recollimation shock in the jet of M87 (see also Stawarz et al. 2006; Asada & Nakamura 2012).

Given the typical superluminal motions previously detected in 3C 120 on smaller jet scales (∼4c; Gómez et al. 2001), we consider it unlikely that C90—as identified by Roca-Sogorb et al. (2010) and Gómez et al. (2011)—can be identified with C99 at earlier epochs, given the exceedingly large proper motion that would be needed ($\gtrsim 9c$, which has not previously been observed in the jet of 3C 120). Our 5 GHz images show that C99's flux density increases progressively from 2009 December 14 to 2010 June 21, which provides a better explanation for why C99 was not detected in our previous 5 GHz observations in 2007 November 30.

3.3. Arc of Emission at ∼80 mas from the Core: A80

As shown in Figure 1 (see also Figures 2–4), the linearly polarized emission in A80 closely follows that of the total intensity, with values of the degree of polarization up to ∼30% (see also Figure 5), and the EVPAs distributed nearly perpendicular to the arc-shaped structure of A80, as expected in the case of a shock front.

The observations presented here show a nearly constant flux density evolution of C80/A80, and confirm the large brightness temperature as well as its stationarity, both within our new observing epochs and with regard to the reported position of C80 at earlier epochs. These properties appear remarkably similar to those expected in the case of conical recollimation shocks (e.g., Cawthorne & Cobb 1990; Gómez et al. 1995, 1997; Agudo et al. 2001; Cawthorne 2006; Nalewajko 2009) and will be discussed in detail in the next session.

Interestingly, the region of B80-100 close to the jet axis and downstream from the sharp edge of A80 appears unpolarized in our 5 GHz images. In contrast, weak linear polarization emission (with EVPA nearly perpendicular to the local jet axis) starts to be discerned further downstream at ∼10 mas from the eastern edge of A80. The strong linear polarization emission of C99 shows its EVPA distribution parallel to the jet axis, which, together with the measured superluminal motion, may be an indication of a traveling plane shock wave perpendicular to the axis.

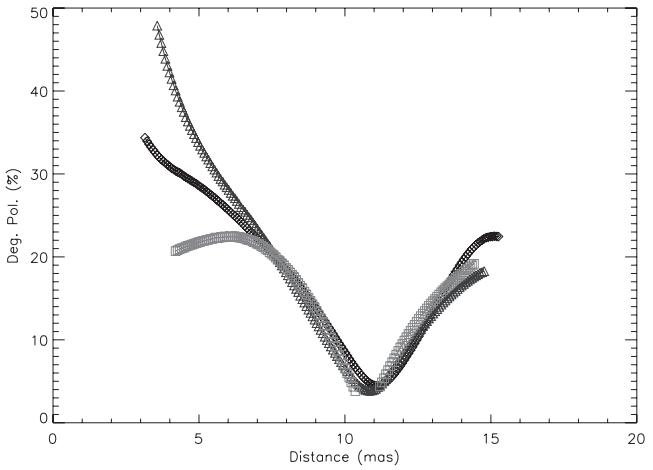

Figure 5. 5 GHz fractional polarization across the A80 jet structure through the slices (from south to north) marked in Figure 1. Diamonds correspond to epoch 2009 December 14, triangles to epoch 2010 March 14, and squares to 2010 June 21.

3.4. Faraday Rotation Screen Between 5 and 15 GHz

Figure 6 shows the RM image of 3C 120 for 2009 December made by combining the data between 5 and 15 GHz. The RM images for the other two epochs of our observations show very similar results to those for 2009 December and are therefore not shown. As can be seen in the inset panels of Figure 6, we obtain good fits to a λ^2 law of the EVPAs throughout the jet, except at longer wavelengths in the innermost ∼4 mas, probably due to beam depolarization and opacity.

The RM screen shown in Figure 6 is in excellent agreement with that obtained for observations taken in 2007 November (see Figure 7 in Gómez et al. 2011), providing further confirmation for the stationarity of the Faraday screen in 3C 120 claimed previously (Gómez et al. 2008). Note, however, that relatively rapid changes (in scales of tens of months) in the RM have also been observed in the innermost ∼2 mas of the jet (Gómez et al. 2011). Our new observations also confirm the negative gradient in RM with distance along the jet, including a sign reversal at ∼8 mas from the core. The motion of component C16 along the jet during the two-year time span between the 2007 observations of Gómez et al. (2011) and ours have allowed the mapping of the RM further downstream, revealing an RM of -79 ± 2 rad m^{-2}, fully consistent with the RM gradient along the jet mentioned previously.

Component C80/A80 has a small RM of 20 ± 2 rad m^{-2}, leading to a Faraday rotation in the EVPAs at our longest observing wavelength of 6 cm (5 GHz) of 4°, within the estimated error in our absolute calibration of the EVPAs. We therefore can conclude that our EVPA maps of C80/A80 are not affected by Faraday rotation.

4. A CONICAL SHOCK MODEL FOR A80

The structure and polarization of the A80 feature point toward an origin in the kind of shock that can occur when the internal pressure of a jet adjusts as a result of changes to its environment.

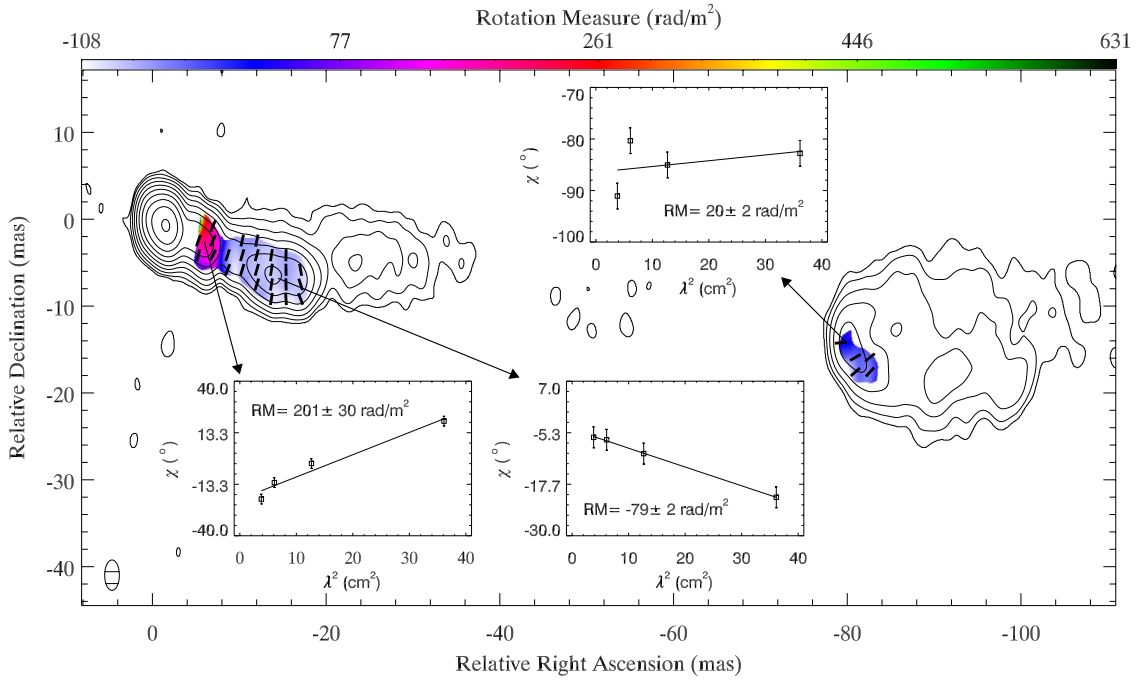

Figure 6. Rotation measure image of 3C 120 between 5 and 15 GHz for observations taken on 2009 December 14. Contours show the 5 GHz total intensity image (see Figure 1). Black sticks indicate the RM-corrected EVPAs. Inset panels show sample fits to a λ^2 law of the EVPAs at some particular locations. The convolving beam is shown in the lower left corner.

(A color version of this figure is available in the online journal.)

This type of structure has been suggested as the origin of the HST-1 knot in M87 (Stawarz et al. 2006; Asada & Nakamura 2012). A jet that is initially freely expanding may become underpressured and is therefore recollimated by a conical shock converging away from the nucleus. Such shocks may reflect from the jet axis, producing a second conical shock diverging away from the nucleus that further adjusts the collimation of the jet. The result is a structure consisting of a pair of point-to-point conical shocks that have been found to occur both in experiments and numerical simulations (e.g., Gómez et al. 1995). In A80, there is no evidence for a converging shock—the shape of the structure, particularly in polarized intensity, suggests a diverging cone that will divert the flow away from the axis causing a drop in pressure. This therefore appears to indicate that A80 has arisen because the jet has rapidly become overpressured, perhaps as a result of a sudden drop in external pressure at this point. Though this seems the most probable explanation it is possible that the jet has encountered a small object—perhaps a molecular cloud typical of the narrow-line emission regions in AGNs—near the axis of the jet, and that the conical shock represents the resulting wake. This explanation seems less probable because it depends on the lucky chance that the obstacle is near the jet axis, but it is in agreement with previous indications for a jet/cloud collision at distances closer to the core (Gómez et al. 2000).

Here, the A80 feature is modeled as a diverging conical shock using the models described by Cawthorne & Cobb (1990) and Cawthorne (2006). These models assume the plasma to be a relativistic gas with sound speed $c/\sqrt{3}$.

Previous monitoring of the proper motions in 3C 120 (e.g., Gómez et al. 2000, 2001; Walker et al. 2001; Homan et al. 2001; Marscher et al. 2002; Jorstad et al. 2005) shows that the maximum apparent velocity observed is $\sim 6c$. From this it is possible to estimate the maximum viewing angle, $\theta_{\rm max} = 19^\circ$, and the minimum Lorentz factor of the jet, $\gamma_u = 6$ (e.g., Gómez et al. 2000). The value $\beta_{\rm app} = 6$ is therefore assumed, being also relevant to the components labeled L5 to L8 by Walker et al. (2001) in the region upstream from C80. This value is used to constrain the properties of the upstream flow. The 5 GHz images presented in this paper are used to constrain the properties of the shock wave.

The projected semi-opening angle η_p of the conical shock is best estimated from the polarized intensity images presented earlier in this paper (Figure 1). The cone axis is taken to be a line inclined at approximately 7° from EW, pointing directly back to the radio core structure. The opening angle deduced from the distribution of polarized flux density is about 90°, but after convolution of model structures with the elliptical beam, the best fit to this is found from a projected opening angle in the region of 80° corresponding to $\eta_p = 40^\circ$. The angle between the polarization rods on either side of the structure (measured where the polarized flux density is brightest) is in the region of 90°. Since the model polarization E rods are orthogonal to the projected edge of the conical structure, a value of $\eta_p = 40^\circ$ corresponds to an angle of 100° between the polarization rods on the two sides. However, after convolution, this angle is reduced to approximately 90°, in agreement with the images, as a result of the influence of the polarized structure nearer the axis. A value of η_p much less than 40° would be hard to reconcile with both a symmetrical cone structure and an axis pointing back to the core region; if the axis is maintained at its inclination of 7° to EW, then the southern edge of the cone would then exclude much of the observed flux density. Values of η_p significantly greater than 40° result in simulated polarization images that are inconsistent with those observed in that they do not reproduce the observed saddle point between the two sides of the polarization image. Hence, a value for η_p in the region of 40° seems to offer the best chance of modeling the observed structure of A80 and is therefore used in what follows.

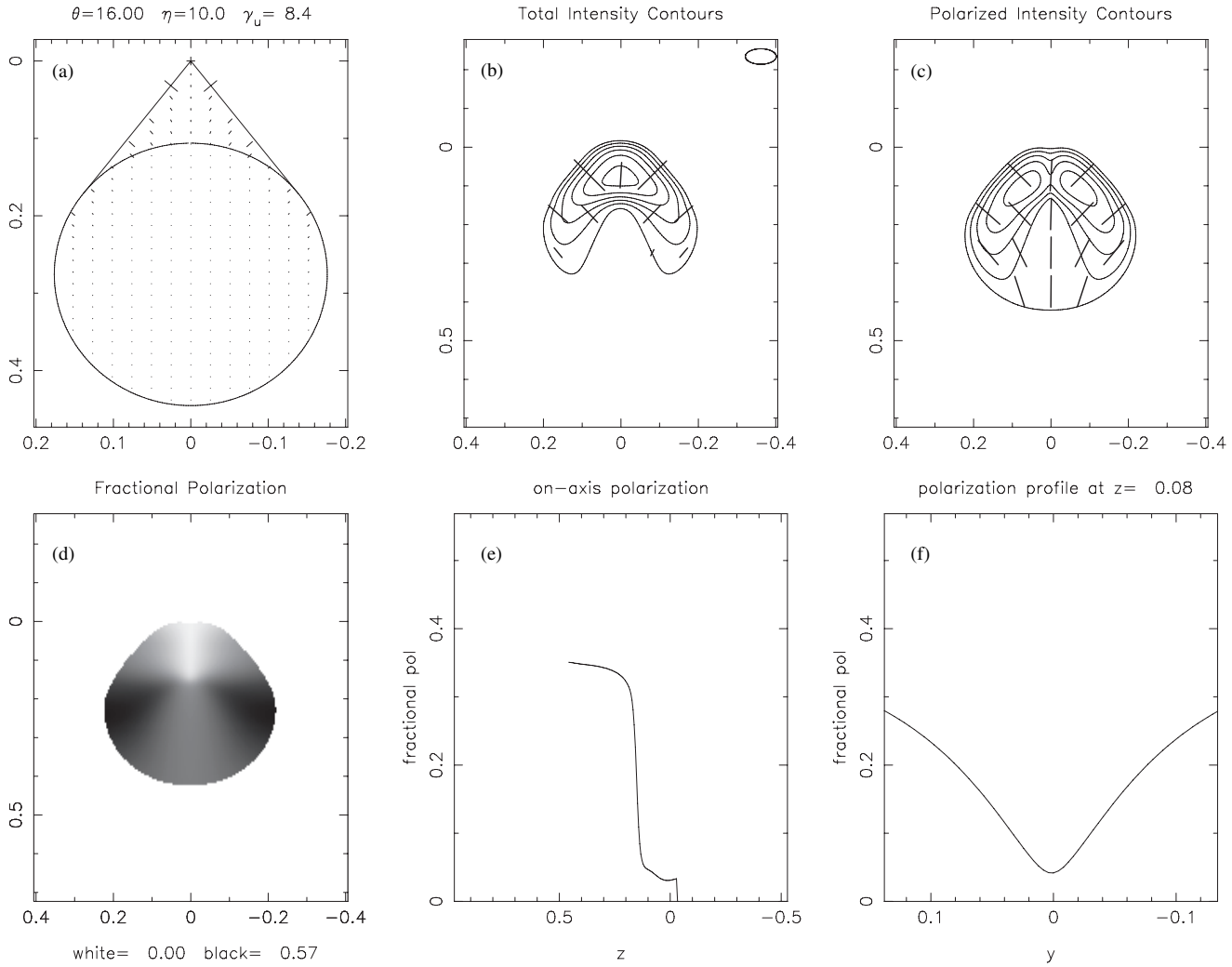

Figure 7. Simulated images and plots corresponding to model 3 (see Table 1). Plots of the six panels are as follows: (a) outline of the shock structure and the (unconvolved) polarization rods of length proportional to P, (b) contours of I after convolution with a beam chosen to match in shape that of the observations; the convolved polarization is shown by rods parallel to the E field and of length proportional to P, (c) contours of convolved P, with polarization angle χ shown by the orientation of rods of constant length, (d) variation of fractional polarization (from the convolved images), (e) along the jet axis, and (f) across the jet through the region of the I peak. In all six plots the units of distance are scaled so that the height of the cone (from apex to base) is unity.

The true semi-opening angle η is related to η_p by

$$\tan \eta_p = \frac{\tan \eta}{\cos\theta(1 - \tan^2\theta \tan^2 \eta)^{1/2}}, \quad (1)$$

which can be solved numerically for η in terms of η_p and θ.

A further constraint is provided by the requirement that, in the rest frame of the upstream flow, the shock wave must advance toward the stationary plasma at speed greater than the sound speed, $c/\sqrt{3}$. This requires that

$$\beta_u \gamma_u \sin \eta > 1/\sqrt{2}. \quad (2)$$

For each value of θ, a unique model can be computed using the procedures described in Cawthorne (2006) provided inequality (2) is satisfied. Parameters appropriate to several models are given in Table 1 and the corresponding model images have been computed assuming that the upstream magnetic field is completely disordered. The plausible range of θ is quite restricted: values below about 10° are ruled out by inequality (2), while values above 18.°9 cannot yield apparent superluminal speeds as high as $\simeq 6c$.

The simulated images corresponding to models 1–4 resemble the observations of A80 shown in Figure 1. The total intensity (I) images in Figure 7 show a bow wave pattern, while the simulated polarized intensity (P) images show a similar pattern that is divided by a saddle point at the position of maximum I. The polarization E rods in the two elongated P features are approximately perpendicular to the direction of elongation, which corresponds to the outline of the conical shock wave. Models 1–4 produce simulations that differ mainly in two ways: first, the structures become more compact as θ increases, because the emission from the far side of the shock wave becomes relatively weaker, and second, the degree of polarization increases as θ increases, mainly because the shock becomes stronger (the compression factor of the shock κ decreases) as a result of increasing values of η and the upstream flow velocity (β_u).

The model best matching the degrees of polarization found in the images is model 3. In this model, the degree of polarization rises to about 30% near the edges of A80 in the region of the peak in total intensity, and levels as high as this are seen in this region on the southern side of A80 (as shown in the profiles plot of Figure 5).

Table 1
Model Parameters for Different Values of θ

Model	θ (°)	β_u	η (°)	κ	ξ (°)	β_d	δ_u	$\delta_{d,\max}$	$\delta_{d,\max}/\delta_u$	R_1	R_2
(1)	(2)	(3)	(4)	(5)	(6)	(7)	(8)	(9)	(10)	(11)	(12)
1	12	0.9874	7.5	0.76	1.2	0.9849	4.63	4.73	1.02	2.9	3.0
2	14	0.9895	8.8	0.50	3.2	0.9826	3.62	5.33	1.47	40.3	27.5
3	16	0.9929	10.0	0.31	5.0	0.9815	2.61	5.26	2.02	600	395
4	18	0.9974	11.2	0.14	6.9	0.9810	1.40	5.19	3.71	68,900	39,300

Notes. For all these models the upstream magnetic field was assumed to be completely tangled. Columns are as follows: (1) model number; (2) angle θ between the axis and the line of sight; (3) β_u, upstream flow velocity as a fraction of c; (4) η, the (deprojected) semi-opening angle; (5) κ, the compression factor at the shock front; (6) ξ, the angle through which the flow is deflected; (7) β_d, the downstream flow velocity expressed as a fraction of c; (8) δ_u Doppler factor upstream of the conical shock; (9) $\delta_{d,\max}$, maximum Doppler factor downstream of the conical shock; (10) $\delta_{d,\max}/\delta_u$, ratio of maximum downstream to upstream Doppler factor; (11) intensity ratio R_1 between the downstream and upstream emission; and (12) a new estimate, R_2, of the downstream to upstream intensity with downstream intensity weighted by the Doppler shift.

The simulated images for model 3 are shown in Figure 7. The model is reasonably successful in reproducing the observed structure in the vicinity of the I peak. However, further downstream the observed polarization rods turn to become orthogonal to the axis, whereas the model polarization rods turn in the opposite sense. On axis, the model polarization rods are parallel to the axis, but where on-axis polarization is seen in the observations, at distances greater than about 10 mas from the working surface, the rods are either orthogonal or oblique to the axis. It seems that if the conical shock model is appropriate, then it is the dominant influence on the polarized emission only within about 10 mas of the apex.

Another way in which the model is successful is in its prediction of a very large ratio of upstream to downstream intensity. The observations of Roca-Sogorb et al. (2010) have shown that C80 (the brightest hot spot in A80) represents an increase in the intensity of emission with respect to the underlying jet by a factor of approximately 600, a figure that they found difficult to explain without invoking acceleration of the jet. If this is due to the formation of a shock structure, then the ratio of the upstream to downstream intensity should be about 600 or greater. If the Doppler factors of the upstream and downstream flows are δ_u and δ_d, respectively, and the compression ratio is κ, then the intensity ratio should be approximately

$$R_1 = \frac{I_d}{I_u} = \kappa^{(5\alpha-6)/3}\left(\frac{\delta_d}{\delta_u}\right)^{(2-\alpha)},$$

where $\alpha \simeq -1$ is the spectral index for C80 (Roca-Sogorb et al. 2010). In estimating the value of R_1 the largest downstream Doppler factor $\delta_{d,\max}$ (for flow at angle $\theta - \xi$ to the line of sight) has been assumed. The values of κ, $\delta_{d,\max}$ for the downstream flow closest to the line of sight and R_1 are shown in Table 1. Because $\delta_d < \delta_{d,\max}$ for most of the downstream flow, R_1 is likely to be an overestimate of the intensity ratio, and so a second estimate based on an intensity-weighted average of the downstream Doppler factor, R_2, has also been included in the table.

Table 1 shows that as θ increases from 12° to 18°, so the downstream to upstream brightness ratios, R_1 and R_2, increase very rapidly. The greater part of this effect is due to the compression of the plasma (indicated by the value of κ) and its effect on the magnetic field and particle density. However the increase in the value of $\delta_{d,\max}/\delta_u$ is also significant. This occurs because (1) δ_u is decreasing because θ is increasing and β is also increasing in the regime where $\sin\theta > \gamma_u^{-1}$, and (2) because δ_d is varying only weakly, which occurs because although β_d decreases and θ_d increases, the shock becomes stronger and parts of the downstream flow are directed closer to the observer's line of sight.

From Table 1 it is clear that parameters similar to those of model 3 ($\theta = 16°$), which gave the closest match for the fractional polarization values, should have a downstream to upstream brightness ratio of order several hundred. It therefore seems likely that such models can reasonably reproduce both the observed polarization structures and the very high ratio of downstream to upstream intensity demanded by Roca-Sogorb et al. (2010).

A few variants on the models described here have been investigated to determine whether they might explain the transverse polarization rods seen on the downstream side of C80. First a poloidal magnetic field component was added, as described by Cawthorne (2006). The influence of the poloidal field on the polarization is strongest on the near side of the shock front, producing transverse polarization rods near the peak in I, where none are seen. The effect is negligible on the far side of the shock, which extends further downstream toward the region where transverse polarization rods would be desirable. The possibility that the upstream flow might be converging slightly has also been investigated, as suggested by Nalewajko (2009). The effect was to increase the degree of polarization at a given value of θ, but otherwise the simulated images were very similar. It seems that neither of these modifications helps to explain the larger scale polarization properties beyond A80. It is possible that allowing for a more complex upstream field structure might explain the entire polarization structure of B80-100 but, on the other hand, it seems likely that the conical shock is not the dominant influence on polarization toward the downstream edge of the B80-100 structure. Indeed, the superluminal motion found for C90 and C99 suggests that instead the polarization structure downstream of A80 may be the result of moving plane-perpendicular shock waves that appear in the wake of the A80 conical shock.

It is worth noting that, although the upstream Doppler factor is rather low in model 3 ($\simeq 2.6$) the jet to counterjet ratio is still reasonably high, giving

$$\frac{I_{\rm jet}}{I_{\rm counterjet}} = \left(\frac{1+\beta_u\cos\theta}{1-\beta_u\cos\theta}\right)^{2-\alpha} \simeq 1.2\times10^4$$

for $\alpha \simeq -0.5$, as expected nearer the core.

5. SUMMARY AND CONCLUSIONS

The first analysis of the properties of component C80 was carried out by Roca-Sogorb et al. (2010), who concluded that although a helical shocked jet model—including perhaps some bulk flow acceleration—could explain the unusually large brightness temperature, it appears unlikely that it corresponds to the usual shock that moves from the core to the location of C80. Rather, Roca-Sogorb et al. (2010) proposed the need for an alternative process capable of explaining the high brightness temperature of C80, its appearance in high-frequency images after 2007 April, and its apparent stationarity. One of the possible alternatives considered by these authors involved a stationary shock at the location of C80 with emission suddenly enhanced by the arrival of a region of enhanced particle number in the jet flow, such as the one proposed to explain the kinematic and flux evolution properties of the HST-1 knot in M87 (Stawarz et al. 2006).

The main goal of the new observations presented here is to further constrain the physical processes taking place in the jet of 3C 120 that have led to the extreme properties of C80. Thanks to the increased sensitivity achieved by our new observations we report on the existence of the A80 arc of total intensity and linear polarization associated with C80, as part of a larger bulge of emission that extends ∼20 mas along and across the jet. Most importantly, the polarization vectors are distributed perpendicularly to the semi-circular shape of A80, as would be expected for the case of a compression by a shock front. This evidence, together with the excess in brightness temperature displayed by C80/A80 and its stationarity in flux and position, supports the model suggested by Roca-Sogorb et al. (2010) in which C80/A80 corresponds to a standing shock. More specifically, our modeling suggests a conical recollimation shock. Indeed, our simulations based on the synchrotron emission from a conical shock, as described by Cawthorne (2006), reproduce quite closely the observed total and linearly polarized emission structure, the electric vector distribution, and the increased brightness temperature of C80/A80, allowing constraints on the values of the jet flow in 3C 120 and the geometry of the conical shock at ∼80 mas from the core. In particular, our simulations provide the cone opening angle $\eta = 10^\circ$, the jet viewing angle $\theta = 16^\circ$ at the location of A80, and the upstream Lorentz factor $\gamma_u = 8.4$.

An important issue to investigate further is the origin of the recollimation shock at such large distances from the core of emission in relativistic jets as in 3C 120 and presumably in M87. While for M87 it has been proposed that the recollimation originates from the transition between a parabolic to a conical shape (Asada & Nakamura 2012), in 3C 120 we suggest that the most plausible cause is a sudden drop in the external pressure, leading to the formation of a conical shock wave opening away from the nucleus.

The study of the nature of C80—and the structure of its related arc of emission A80—that we present in this paper was only possible thanks to the high angular resolution provided by the VLBA and its large sensitivity and good performance for polarimetric observations. The use of synthetic images of the total intensity and linear polarization of conical shocks has also proven to be a powerful tool to interpret the nature of jet structures, and to constrain the physical and geometrical properties of such structures and the jet plasma that forms them. Studies similar to that presented here can be carried out for a number of cases—additional potential examples might be the HST-1 and K1 knots in M87 (Stawarz et al. 2006) and 3C 380 (Papageorgiou et al. 2006). Performing these studies will be important to obtain relevant information on the relativistic jets and their surrounding medium.

This research has been supported by the Spanish Ministry of Economy and Competitiveness grant AYA2010-14844 and by the Regional Government of Analucía grant P09-FQM-4784. We thank Dr. P. A. Hughes of the University of Michigan for useful discussion on the physics of recollimation shocks. The VLBA is an instrument of the National Radio Astronomy Observatory, a facility of the National Science Foundation operated under cooperative agreement by Associated Universities, Inc. This research has made use of the MOJAVE database maintained by the MOJAVE team (Lister et al. 2009).

REFERENCES

Agudo, I., Gómez, J. L., Martí, J. M., et al. 2001, ApJ, 549, L183
Agudo, I., Thum, C., Wiesemeyer, H., & Krichbaum, T. P. 2010, ApJS, 189, 1
Asada, K., & Nakamura, M. 2012, ApJ, 745, L28
Burbidge, E. M. 1967, ApJ, 149, L51
Caproni, A., & Abraham, Z. 2004, MNRAS, 349, 1218
Cawthorne, T. V. 2006, MNRAS, 367, 851
Cawthorne, T. V., & Cobb, W. K. 1990, ApJ, 350, 536
Chatterjee, R., Marscher, A. P., Jorstad, S. G., et al. 2009, ApJ, 704, 1689
Cheung, C. C., Harris, D. E., & Stawarz, Ł. 2007, ApJ, 663, L65
García-Lorenzo, B., Sánchez, S. F., Mediavilla, E., González-Serrano, J. I., & Christensen, L. 2005, ApJ, 621, 146
Gómez, J. L., Marscher, A. P., & Alberdi, A. 1999, ApJ, 521, L29
Gómez, J. L., Marscher, A. P., Alberdi, A., Jorstad, S. G., & Agudo, I. 2001, ApJ, 561, L161
Gómez, J. L., Marscher, A. P., Alberdi, A., Jorstad, S. G., & Agudo, I. 2002, VLBA Scientific Memorandum 30 (http://www.vlba.nrao.edu/memos/sci/sci30memo.ps)
Gómez, J. L., Marscher, A. P., Alberdi, A., Jorstad, S. G., & García-Miró, C. 2000, Science, 289, 2317
Gómez, J. L., Marscher, A. P., Alberdi, A., Martí, J. M., & Ibáñez, J. M. 1998, ApJ, 499, 221
Gómez, J. L., Marscher, A. P., Jorstad, S. G., Agudo, I., & Roca-Sogorb, M. 2008, ApJ, 681, L69
Gómez, J. L., Martí, J. M., Marscher, A. P., Ibáñez, J. M., & Alberdi, A. 1997, ApJ, 482, L33
Gómez, J. L., Martí, J. M., Marscher, A. P., Ibáñez, J. M., & Marcaide, J. M. 1995, ApJ, 449, L19
Gómez, J. L., Roca-Sogorb, M., Agudo, I., Marscher, A. P., & Jorstad, S. G. 2011, ApJ, 733, 11
Hardee, P. E., Walker, R. C., & Gómez, J. L. 2005, ApJ, 620, 646
Homan, D. C., Ojha, R., Wardle, J. F. C., et al. 2001, ApJ, 549, 840
Jorstad, S. G., Marscher, A. P., Lister, M. L., et al. 2005, AJ, 130, 1418
Kataoka, J., Stawarz, Ł., Takahashi, Y., et al. 2011, ApJ, 740, 29
Leppänen, K. J., Zensus, J. A., & Diamond, P. J. 1995, AJ, 110, 2479
Lister, M. L., Aller, H. D., Aller, M. F., et al. 2009, AJ, 137, 3718
Maraschi, L., Chiappetti, L., Falomo, R., et al. 1991, ApJ, 368, 138
Marscher, A. P., Jorstad, S. G., Gómez, J. L., et al. 2002, Nature, 417, 625
Marscher, A. P., Jorstad, S. G., Gómez, J. L., et al. 2007, ApJ, 665, 232
Muxlow, T. W. B., & Wilkinson, P. N. 1991, MNRAS, 251, 54
Nalewajko, K. 2009, MNRAS, 395, 524
Papageorgiou, A., Cawthorne, T. V., Stirling, A., Gabuzda, D., & Polatidis, A. G. 2006, MNRAS, 373, 449
Perley, R. A., Dreher, J. W., & Cowan, J. J. 1984, ApJ, 285, L35
Roca-Sogorb, M., Gómez, J. L., Agudo, I., Marscher, A. P., & Jorstad, S. G. 2010, ApJ, 712, L160
Shepherd, M. C. 1997, in ASP Conf. Ser. 125, Astronomical Data Analysis Software and Systems VI, ed. G. Hunt & H. E. Payne (San Francisco, CA: ASP), 77
Stawarz, Ł., Aharonian, F., Kataoka, J., et al. 2006, MNRAS, 370, 981
Walker, R. C., Benson, J. M., & Unwin, S. C. 1987, ApJ, 316, 546
Walker, R. C., Benson, J. M., Unwin, S. C., et al. 2001, ApJ, 556, 756
Walker, R. C., Walker, M. A., & Benson, J. M. 1988, ApJ, 335, 668
Wandel, A., Peterson, B. M., & Malkan, M. A. 1999, ApJ, 526, 579

5.2 The radio galaxy M 87 and its peculiar knot at 900 mas from the core

In Giroletti et al. (2012) we presented a monitoring of the radio galaxy M 87 and its peculiar feature HST-1 combining new data taken with the European VLBI Network (EVN) and archival VLBA images, respectively at 5 and 1.7 GHz, for a total of 24 observations between November 2006 and October 2011. In Figure **??**87-GiM 87-Gin appreciate the evolution in morphology of the HST-1 region from the January 2007 to August 2011, with gaussian components obtained from the model-fits overlaid to the images. The main results obtained in Giroletti et al. (2012) are as follows: i) the HST-1 extension in the radio band is of $\gtrsim$50 mas and it is formed by sub-structures on smaller angular scales, ii) two sub-components within HST-1 (*comp 1* and *comp 2* in Figure 5.3) moved regularly with superluminal velocity (v=4c) with a displacement of $\sim$88 mas over the observing period – as we appreciate from the plot in Figure 5.4, iii) a slower moving component (*comp 2b*, in Figures 5.3 and 5.4) observed from August 2008 to May 2009 in the wake of the superluminal *comp 2*, resembling the characteristics of "trailing" components that appear behind a major flow disturbance in numerical simulations (Agudo et al., 2001) and have been observed in other sources (Gómez et al., 2001b; Jorstad et al., 2005), iv) after 2010 a new component (*comp 3*, in Figures 5.3 and 5.4) appeared upstream *comp 2* and in a position similar to that of the previous *comp 2b*.

As mentioned at the beginning of this Chapter, a possible scenario to explain the emission in HST-1 is that of a recollimation shock located in that region which accelerates electrons that consequently emit via synchrotron process. In order to test this hypothesis Dr. Manel Perucho performed new numerical simulations involving the physics of a jet characterized by many recollimation shocks and where a new perturbation (moving component) moves downstream the jet and interacts with recollimation shocks. Relativistic hydrodynamical (RHD) simulations and resulting synthetic images have been performed using RHD models described in Perucho et al. (2010). To obtain a series of strong recollimation shocks the jet is launched with an initial over-pressure 10 times larger than the external medium. A magnetic field in equipartition with particle energy density and oriented predominantly in the direction of the jet axis is assumed. In Figure 5.5 are displayed the rest-mass density, pressure, specific internal energy and

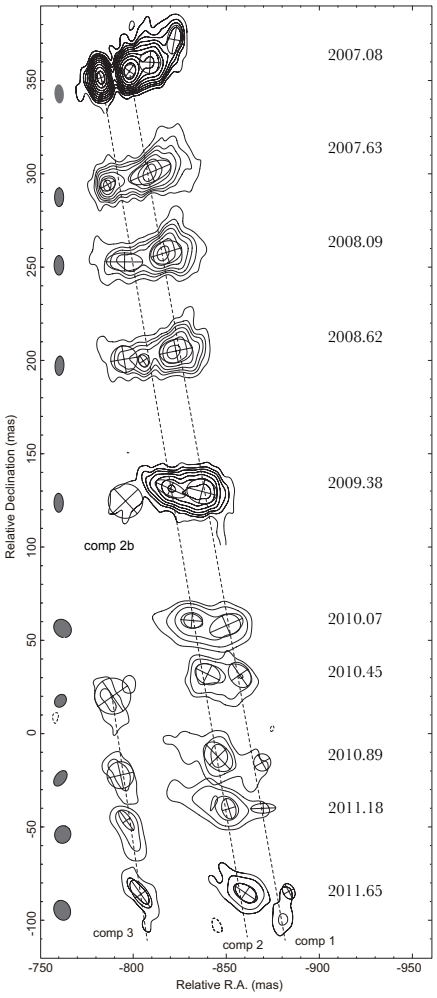

Figure 5.3: HST-1 evolution from January 2007 to August 2011. Total intensity images of HST-1 at 1.7 GHz (VLBA) from 2007.8 to 2009.38 and 5 GHz (EVN) from 2010.07 to 2011.65. Model-fit components are overlaid to the images. Images are spaced vertically proportionally to the time interval between the relative epochs. Adapted from Giroletti et al. (2012).

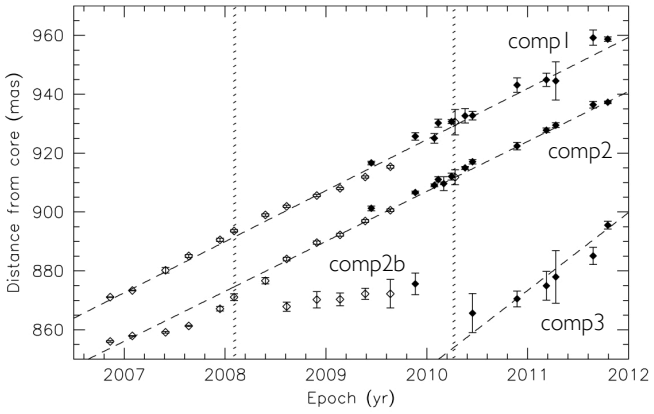

Figure 5.4: Kinematics of sub-components in HST-1 region. This plot represents the distance from the core of model-fit components within HST-1 as a function of time. Note the new component, *comp*3, appearing in late 2010 in a position similar of previous *comp 2b*. The two parallel linear fits matching the positions of *comp 1* and *comp 2* indicate that both components move regularly with the same velocity. From Giroletti et al. (2012).

Lorentz factor along the jet for the stationary model. When we introduce a perturbation, consisting of an increase by a factor of 8 in the pressure of plasma injected into the jet, a shock wave forms. This shock moves along the jet and interacts with the second recollimation shock leading to a significant increase in pressure in that region, as we appreciate in Figure 5.6.

Computing the synchrotron emission which results from the hydrodynamical simulation (for details of the numerical model used see Gomez et al. (1995); Gómez et al. (1997); Aloy et al. (2003)) we obtain a sequence of 15 total intensity images displayed in Figure 5.7. We only show, for clarity, the portion of jet where the moving feature interacts with the recollimations shock. The interaction between both shocks (the stationary and the moving one) leads to a significant increase in the particle and magnetic field energy density and a new superluminal component appears in total intensity images, as we appreciate in the third image from the top in Figure 2.11. The appearance of the new superluminal component is in agreement with our VLBI observations in Giroletti et al. (2012) where *comp 3* appears in a position similar to that of previous *comp 2b*, see Figure 5.3.

What is important to note in Figure 5.3 is that the quasi-stationary component

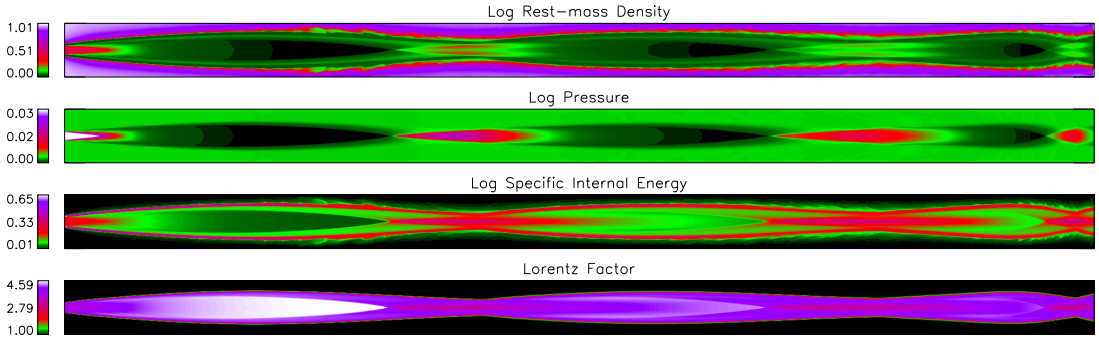

Figure 5.5: The stationary jet model in RHD simulation. Relativistic hydrodynamical simulation of a jet with an initial over-pressure 10 times larger than the external medium, leading to a set of recollimation shocks. Reproduced from Casadio et al. (2013).

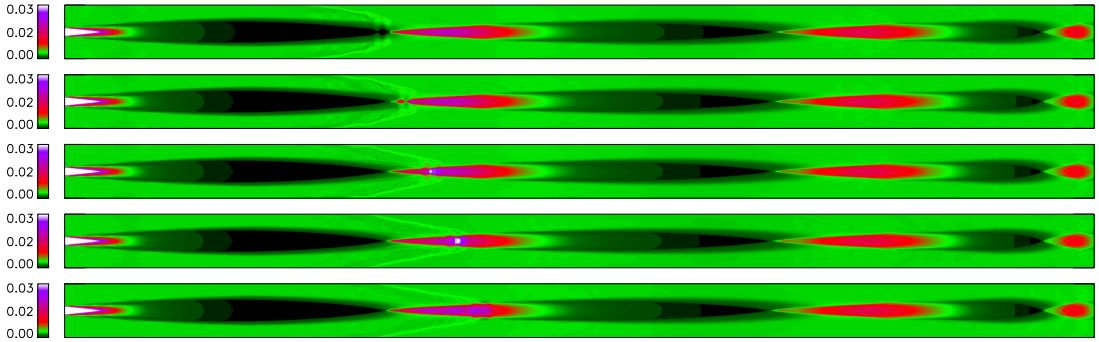

Figure 5.6: The jet model with the introduction of a moving shock wave. Five snap-shots in the time evolution (from top to bottom) of the jet particle pressure after the introduction of a perturbation, consisting in an increase by a factor of 8 in the jet inlet pressure. The perturbation interacts with the second recollimation shock leading to a significant increase in pressure. From Casadio et al. (2013).

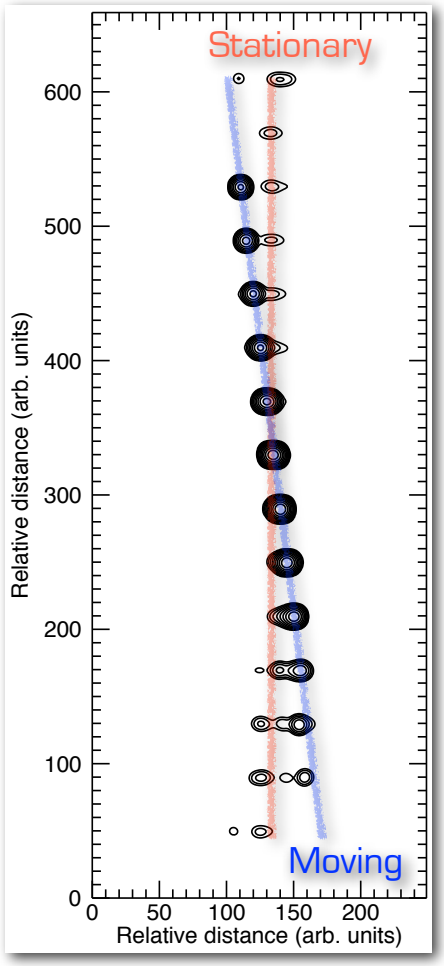

Figure 5.7: Simulated synchrotron emission maps. Fifteen snap-shots in the time evolution (from top to bottom) of the simulated synchrotron emission maps obtained using the relativistic hydrodynamical models shown in Figure 5.5 and 5.6 as imput. Only the region corresponding to the interaction of the moving component with the recollimation shock is shown for clarity. Note that the passage of the perturbation through the recollimation shock (visible in the first five and last four epochs) leads to the appearance of a new superluminal component.

associated with the recollimation shock, as it appears in the first five and last four images, is significantly fainter than the new superluminal component and its position shifts with the passage of the moving shock, as seen in previous numerical simulations (Gómez et al., 1997).

To test this on the source we performed new polarimetric observations of the radio galaxy M 87 with the VLBA at 2.2 and 5 GHZ (project BC210, PI Carolina Casadio) and with the JVLA at 15, 22 and 43 GHz in A-configuration (project 12B-153, PI Carolina Casadio). The VLBA array at these two frequencies provide the necessary sensitivity to detect the faint emission associated to the recollimation shock in HST-1 and the sufficient resolution to follow the kinematics and flux density evolution of subcomponents in that region. The VLBA observing epochs obtained are three, separated by 6 months each: 09 March 2013, 29 January 2014, 14 July 2014. Here we present only the first epoch (09 March 2013), the other two epochs will be analyzed in the future. Observations with the JVLA, providing lower resolution but a greater field of view, were intended to study the fainter underlying emission and to probe the polarized emission structure along the jet of M 87, also in the light of results obtained in Agudo et al. (2012) on the radio galaxy 3C 120. They consist in 7 observing blocks, approximately three hours-long, observed between 2012 October 28 and 2012 December 22.

The calibration and imaging of VLBA data was performed using a combination of `AIPS` and `Difmap` tools as described in § 3.2 and as we did also in previous studies. During the hybrid imaging (for more details see § 3.2), we applied a gaussian taper to the visibility data at 2.2 GHz in order to detect the emission in HST-1 region. The taper subtracts weight to long baselines, increasing the sensitivity to extended structures but at lower resolution. Then, the resulting beam in the HST-1 image at 2.2 GHz is bigger (14.66×12.85 mas) respect to the corresponding image of M 87 jet (8.8×4.61 mas) at the same frequency. The resolution in 5 GHz image is instead a little higher (3.95×2.06 mas). It was not possible to detect emission in HST-1 region at 5 GHz but, considering the sensitivity achieved at both frequencies (∼0.1-0.2 mJy/beam), we can estimate an upper limit for the peak flux density of HST-1 at 5 GHz of 0.5 mJy/beam (∼ 5-σ).

The VLBA images at 2.2 and 5 GHz of the epoch 09 March 2013 are shown in Figure 5.8 and 5.9, respectively. Figure 5.8 contains also an inset panel showing the HST-1 image obtained with the taper together with circular components obtained fitting the

visibility data. The HST-1 region at 2.2 GHz can be model fitted with two separated circular components, one located at ∼913 mas from the core and a second one at ∼953 mas. Comparing the positions of these two components with those detected in Giroletti et al. (2012) we found they can be associated to *comp 3* and *comp 2*, respectively, as we appreciate from Figure 5.10. We obtained a peak flux density for HST-1 at 2.2 GHz of 2.1 mJy/beam, associated to *comp 3* which results brighter than *comp 2* in our epoch.

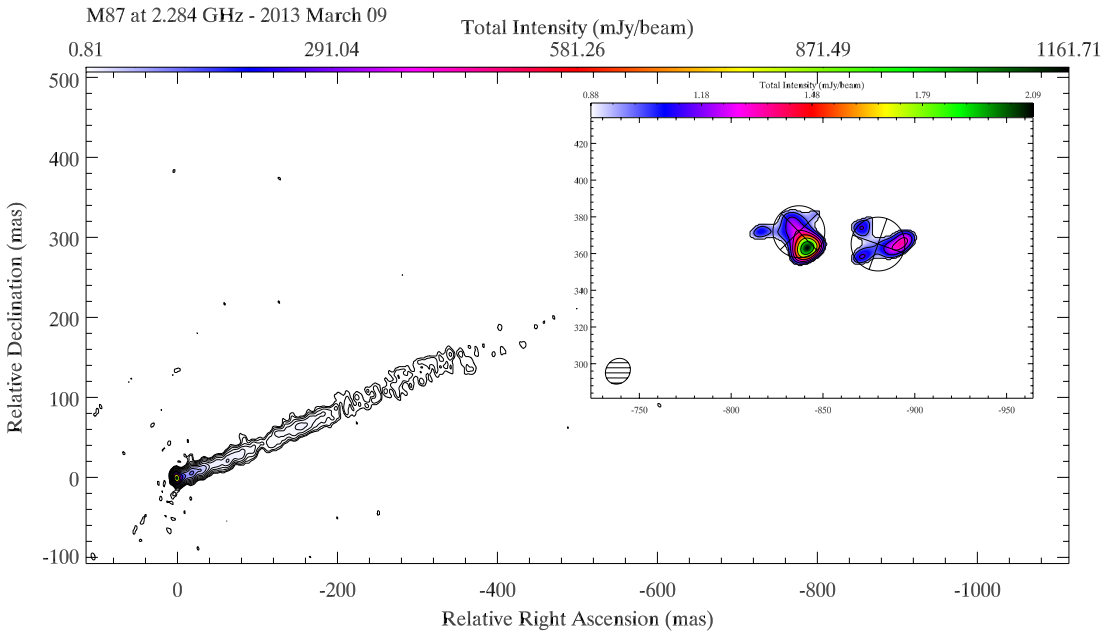

Figure 5.8: M 87 at 2.2 GHz (VLBA). VLBA observation at 2.2 GHz of M 87 on 09 March 2013. Total intensity is shown in contours and colors. Contours are traced at 0.07, 0.13, 0.23, 0.42, 0.76, 1.38, 2.51, 4.56, 8.28, 15.03, 27.29, 49.56 and 90% of the peak brightness of 1.16 Jy/beam. The restoring beam is 8.8×4.61 mas at 15.8°. The panel inside the figure shows a zoom of the HST-1 region, obtained with a taper and resulting in a beam of 14.66×12.85 mas at -38.2×. Modelfits components in HST-1 are overlaid to the image and contours plot, where contours are traced at 38.3, 44.2, 50.9, 58.7, 67.7, 78.1, 90% of the peak brightness of 2.1 mJy/beam.

If we put the values of flux density found in context with previous epochs (Giroletti et al., 2012) we observe a significant decrease in the flux density of HST-1 starting from 2011 as supported also by the EVN image at 5 GHz of HST-1 in March 2012 (Hada et al., 2014) where the peak flux density in HST-1 region is <1 mJy/beam although in the same period the radio galaxy M 87 underwent an elevated VHE state of flux. The difference we observe between March 2012 and March 2013 data is that in March

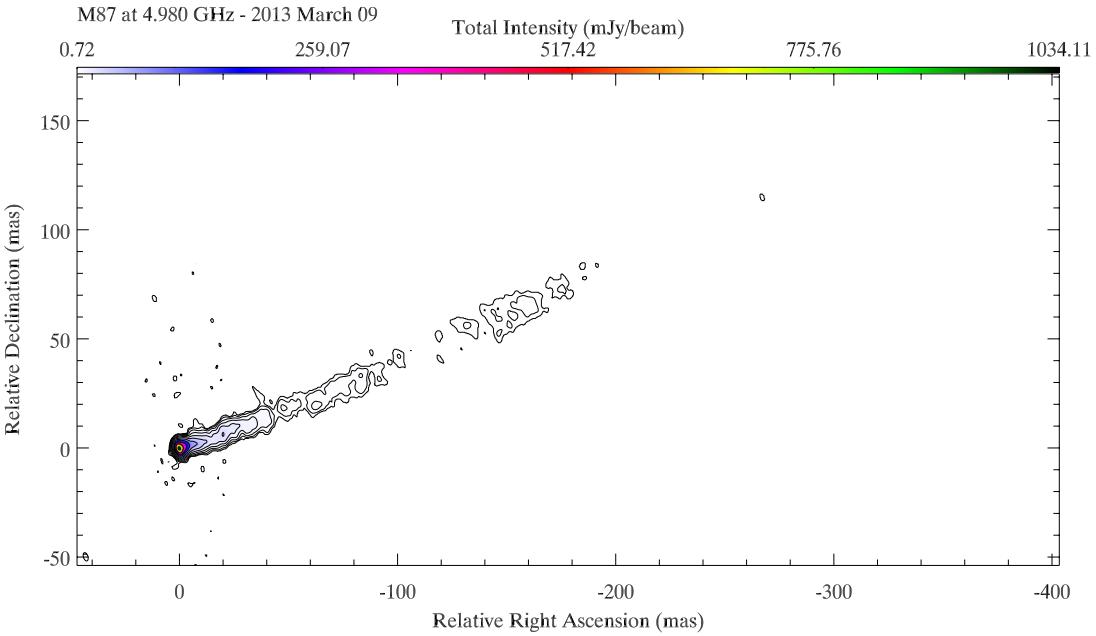

Figure 5.9: M 87 at 5 GHz (VLBA). VLBA observation at 5 GHz of M 87 on 09 March 2013. Total intensity is shown in contours and colors. Contours are traced at 0.07, 0.14, 0.29, 0.6, 1.23, 2.51, 2.14, 10.51, 21.5, 43.99, 90% of the peak brightness of 1.034 Jy/beam. The restoring beam is 3.95×2.06 mas at 18.03°.

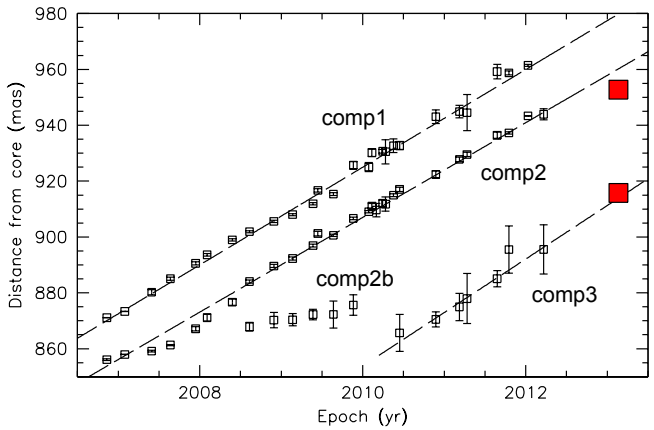

Figure 5.10: New subcomponents positions in HST-1 region. Distances of compact components in HST-1 as a function of time as registered in Giroletti et al. (2012). The two red squares represent the position of our two Gaussian model-fit components detected in HST-1 in the image at 2.2 GHz with the VLBA on 2013 March 9 (Figure 5.8).

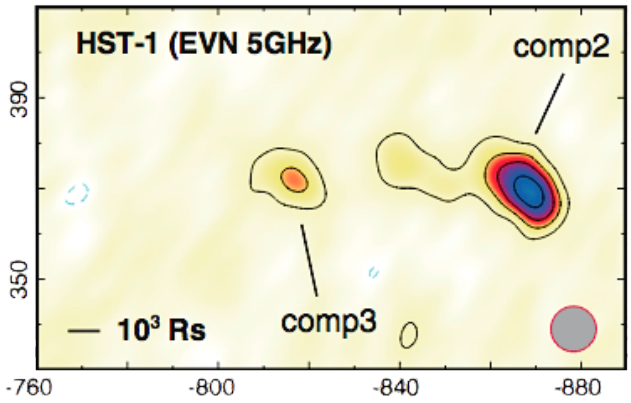

Figure 5.11: HST-1 at 5 GHz (EVN). EVN image of HST-1 at 5 GHz in 2012 March. Total intensity is shown in contours and colors. Contours are traced at -1, 1, 2, 2.8, 4 times 3σ (0.24 mJy/beam). A 10.0 mas circular restoring beam is used. Reproduced from Hada et al. (2014).

2012, where we found again both *comp 3* and *comp 2* as it is shown in Figure 5.11, *comp 2* is the brighter one while it is the opposite in March 2013. This, together with the lack of detection of *comp 1* present in the previous epochs (see Figure 5.3 and 5.4), suggests that subcomponents in HST-1 region become weaker as they move downstream, probably due to adiabatic expansion.

The decrease in flux of HST-1 is also confirmed by our JVLA data. In Figure 5.12 we present the polarimetric JVLA image of M 87 at 15 GHz on 2012 November 25. In the image the core has a peak flux density of ∼2.9 Jy/beam and HST-1 a total flux of ∼9 mJy. The better sensitivity achieved by the new JVLA clearly stands up when we compare our image with an image obtained in 2006 with the old VLA at the same frequency in Figure 5.13. Comparison between flux density values obtained in 2012 and previous VLA archive data that we used to produced the images displayed in Figure 5.13 and 5.14, reveals a significant decrease in the flux density of HST-1 while the core remains stable or even brighter respect to the past. In Figure 5.14 we report an image of HST-1 with the VLA during 2003 (left) and 2006 (right). In those epochs the core has a peak flux density of 2.3 and 1.9 Jy/beam, respectively, hence resulting fainter than our 2012 observation.

Instead the HST-1 region results brighter in both previous epochs than in 2012, with a total flux of ∼27 mJy in 2003 and ∼52 mJy in 2006. In our JVLA image we also detect polarized emission up to ∼20 arcseconds from the core, represented in colors in

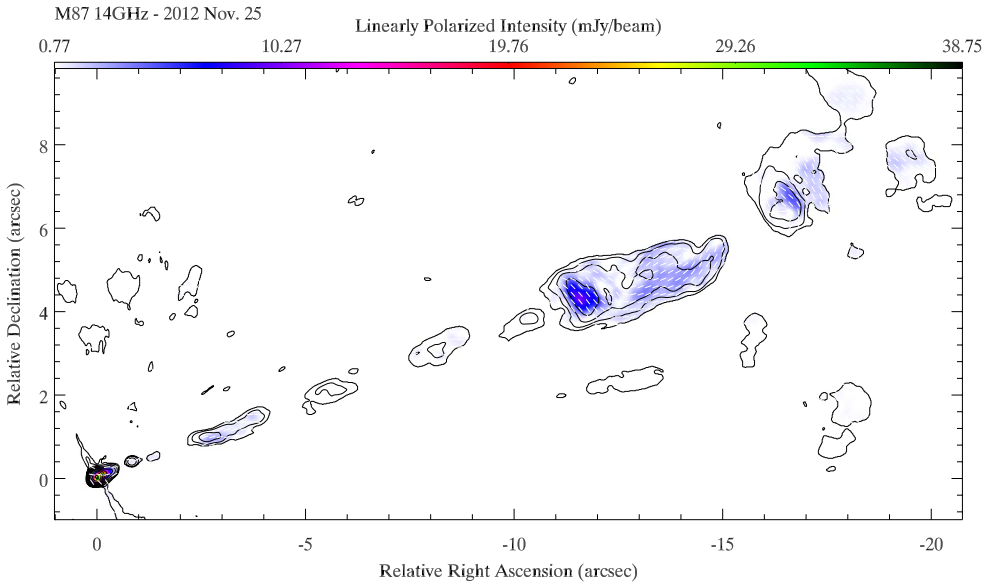

Figure 5.12: M 87 - JVLA observation at 15 GHz. JVLA observation at 15 GHz of M 87 in 2013 November 25. Total intensity is shown in contours and polarized flux in colors. White bars, of unit length, indicate the magnetic field direction (uncorrected for Faraday rotation). Contours are traced at 0.04, 0.09, 0.22, 0.52, 1.24, 2.91, 6.87, 16.19, 19.38, 17.90% of the peak brightness of 2.93 Jy/beam. The restoring beam is 0.17×0.165 arcseconds at -47°.

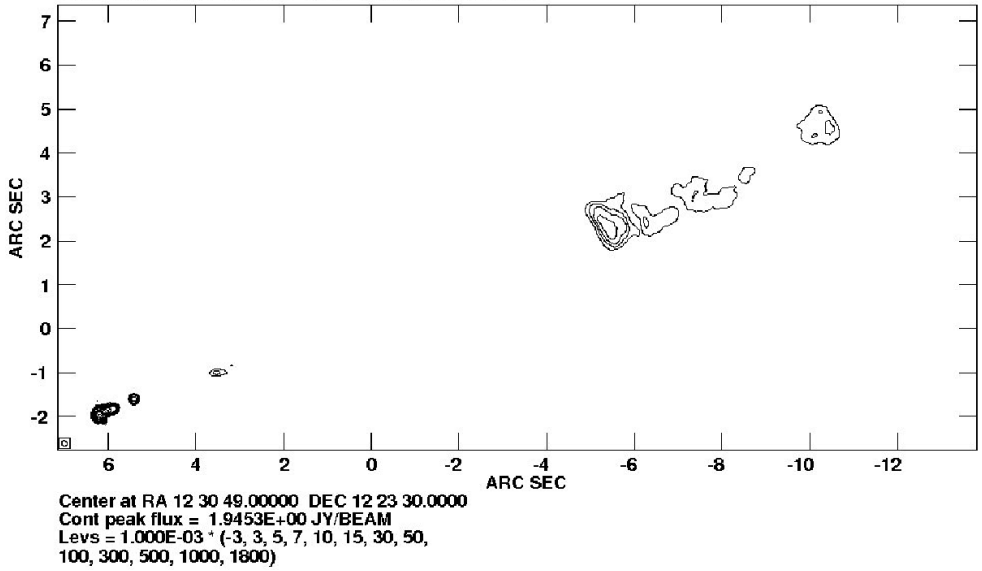

Figure 5.13: M 87 - VLA observation at 15 GHz. VLA observation at 15 GHz of M 87 in 2006. Contours represent the total intensity and they are traced at -3, 3, 5, 7, 10, 15, 30, 50, 100, 300, 500, 1000, 1800 mJy/beam. The peak flux density is 1.9 Jy/beam.

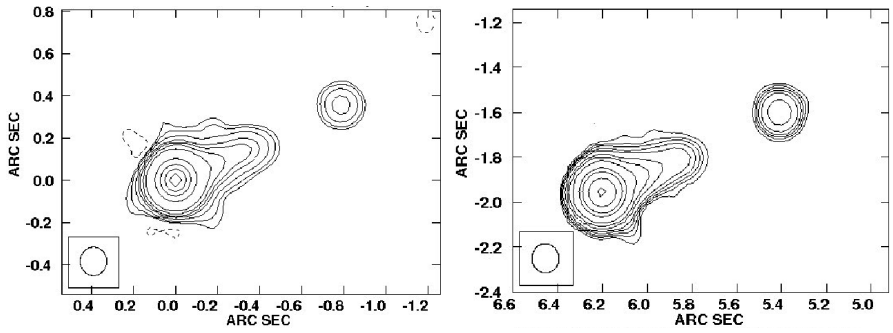

Figure 5.14: VLA observations at 15 GHz of M 87 in 2003 (left) and 2006 (right), reproduced using VLA archive data. Contours represent the total intensity and they are traced at -2, 3, 5, 10, 20, 30, 50, 100, 500, 1000, 1500, 2000 mJy/beam (left) and at -3, 3, 5, 7, 10, 15, 30, 50, 100, 300, 500, 1000, 1800 mJy/beam (right).

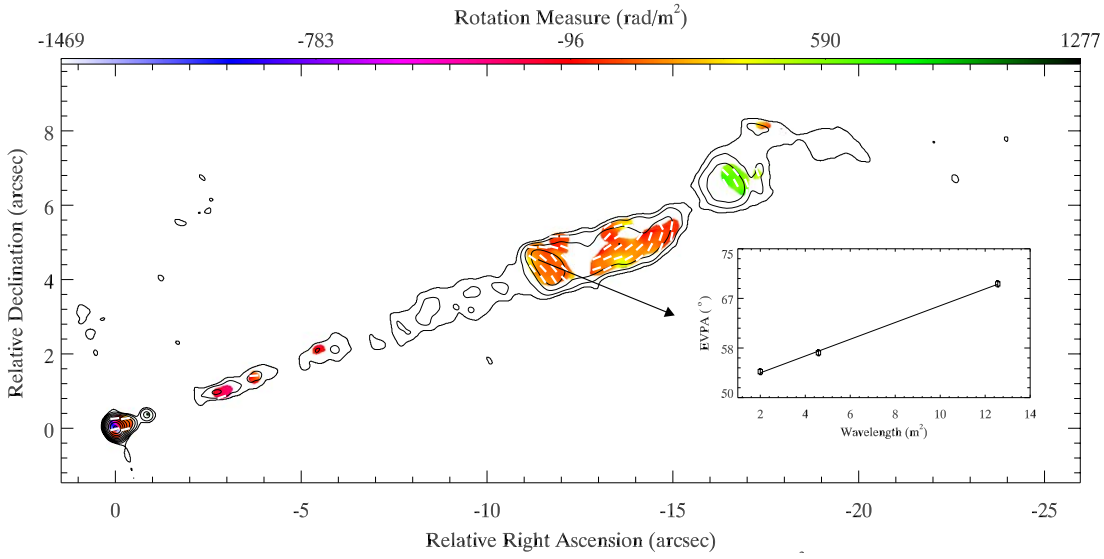

Figure 5.15: Rotation Measure along the M 87 jet. JVLA image at 8.4 GHz in total intensity (in contours) with superimposed (in colors) the rotation measure values along the jet of M 87. The white bars are the Faraday-corrected EVPAs. Inset panel shows the λ^2 fit to the EVPAs in the area of knot A, yielding RM=246±30 rad/m^2.

Figure 5.12, where the peak of polarized flux is in the jet of M 87, as expected, but it is interesting also to observe that also the region at ∼12 arcseconds has a high value of polarized flux. The emitting region at ∼12 arcseconds, usually called knot A, has been interpreted by magnetohydrodynamic models as a relativistic shock launched from the HST-1 complex (Nakamura et al., 2010), but still not clear evidences about its nature and its relation with HST-1 have been observed so far.

We also estimated the rotation measure (RM) due to Faraday rotation (see § 2.1.1.4) along the jet of M 87. For this purpose we analyzed archival JVLA data, corresponding to 8.4 GHz A-configuration observations, performed in June 2011 (program SB0514). We then use 8, 15 and 22 GHz data to extract the information of the EVPAs orientation along the jet at the three wavelengths, obtaining the rotation measure map shown in Figure 5.15. The inset panel in Figure 5.15 gives the rotation measure (RM=246±30 rad/m^2) for the region of knot A. In Figure 5.15 is shown the JVLA image at 8.4 GHz where EVPAs in knot A have been corrected for the rotation measure found. Since a value of RM≈246 rad/m^2 applied to EVPAs at 8.4 GHz translates in a rotation of almost 18°, the Faraday-corrected EVPAs in Figure 5.15 do not differ so much from not corrected EVPAs in 15 GHz JVLA image represented in Figure 5.12. In any case the rotation measure map indicates regions where a Faraday rotation screen, that could be either internal or external, is present and may affect the polarized emission from the source.

To conclude, what we obtained about the peculiar structure HST-1 comparing results from numerical simulations and previous observations (Giroletti et al., 2012) is that the evolution in flux, morphology and velocity pattern of subcomponents in HST-1 region resembles what we observe in numerical simulations when a moving shocks interacts with a stationary recollimation shock. This means that HST-1 may mark the location of a recollimation shock. The hypothesis of a recollimation shock is also supported by other previous studies, as reported at the beginning of the Chapter. Its location coincides with the transition of the jet from a parabolic to a conical geometry, at $\sim 5\times10^5 R_s$ (Asada & Nakamura, 2012). This distance in Schwarzschild radii remembers the location of mm-VLBI cores in many blazars and distant radio galaxies as we reported in § 4.3. In many of these AGN (i.e. CTA 102, 3C 120, 3C 111) the core is seen as a recollimation shock in order to explain high energy events occurring therein which are often associated with ejection of new superluminal components from the core

as well as changes in polarized emission. Then, due to the proximity of the radio galaxy M 87 (D∼16.7 Mpc), what we call "core" and we do not resolve in the mm-VLBI observations of the others AGN, it is instead formed by the portion of jet of M 87 which we observe up to the HST-1 location. In M 87 we are then able to distinguish between the mm-VLBI core and another possible recollimation shock at $\sim 5\times10^5 R_s$ (HST-1). This could also explain why in some occasions we considered the core as responsible for the very high-energy events and in other occasions HST-1, while in all the other AGN we are not able to distinguish between recollimations shocks inside the core if there are more than one. This may indicate that a recollimation shock is expected in AGN jets between 10^4-$10^5 R_s$, independently from the power of jets such as we observe the same in radiogalaxies and blazars. Probably the mm-VLBI core is formed by many recollimation shocks, as indicated by higher resolution space VLBI (*RadioAstron*) and 3mm VLBI observations (GMVA) in the case of BL Lac (Gómez et al., 2016) and M 87 (Hada et al., 2016), respectively.

5. Polarimetric studies on the radio galaxies 3C 120 and M 87: revealing the nature of C80 and HST-1

6
Conclusions

This Thesis for the mention of Philosophiae Doctor (PhD) is focused on the study of relativistic jets in active galactic nuclei (AGN). These are produced by the mass accretion onto a super massive black hole (SMBH) lurking at the center of the host galaxy, and are well known for emitting profusely across the whole electromagnetic spectrum. They are also observed in other multiple astrophysical sites involving accretion onto compact objects, such as microquasars and GRBs. Despite decades of study, there are many aspects related to the physics of relativistic jets in AGN that still remain unclear. For instance, we do not know how jets are formed, accelerated, and collimated from the accretion disk around the SMBH. It is largely unknown what is the role played by the magnetic field in the jet dynamics, or in the actual jet formation. We do not know where the very high energy emission (γ-rays) is produced, and whether it is mainly due to synchrotron self-Compton, or inverse Compton scattering of ambient (external to the jet) photons. Thanks to the *Fermi* gamma-ray satellite, launched by NASA in 2008, we are extending our knowledge of the γ-ray activity in many AGN. We are also in the era of very high resolution mm-VLBI observations that give us the opportunity of studying deeper in the jet, probing the regions where jets are formed. Multi-waveband

observations, combined with mm-VLBI observations, can therefore provide the information to determine how jets are formed and what are the sites and mechanisms for the production of γ-ray photons.

We performed two multi-wavelength studies, on the radio galaxy 3C 120 and the blazar CTA 102, during unprecedented γ-ray flares for both sources (Casadio et al., 2015a,b). The *Fermi* satellite registered in September-October 2012 an extraordinary bright γ-ray outburst in the blazar CTA102, and between December 2012 and October 2014 a prolonged γ-ray activity in the radio galaxy 3C120. In both studies the analysis of Fermi data has been compared with a series of 43 GHz VLBA images from the Boston University blazar monitoring program, in which our group collaborate, providing the necessary spatial resolution to probe the parsec scale jet evolution during the high energy events. For the study of 3C 120 we also collected 15 GHz VLBA data from the MOJAVE program in order to extend the analysis of the radio jet to a wider observing period. In the case of CTA 102 our our observations covered the entire electromagnetic spectrum, from millimeter wavelengths, to infrared, optical, X and gamma-ray energies. Millimeter, near-infrared and optical data were collected as part of a large international collaboration in which many research groups, including our own, participate and in which I significantly contributed in the acquisition and analysis of the data.

From both multi-wavelength analysis we obtain that, despite representing very different class of AGN, the radio galaxy 3C 120 and the blazar CTA 102 display very similar properties during γ-ray events. In particular we obtain that the γ-ray outbursts are associated with the passage of new superluminal components through the VLBI core. However, not all ejections produce detectable γ-ray flares and components responsible for the γ-ray emission are not necessary bright components. The key aspect to detect γ-ray emission seems to be the orientation of the emitting region. In fact, we find that components associated with the γ-ray flares move in a direction closer to our line of sight; this would lead to an increase in the Doppler factor, enhancing the γ-ray emission above the flux detectable by *Fermi*. This new result is in agreement with the geometrical interpretation adopted to explain observed high energy flares in other studies in which I have participated (e.g. Raiteri et al., 2012, 2013; Carnerero et al., 2015). In the case of CTA 102 the hypothesis of a change in the jet orientation over time is also supported by the slow rotation over an extended period ($\sim$3 years) observed in the polarization vectors (EVPAs) at millimeter wavelengths. The analysis

of the polarized emission at optical wavelengths shows instead intra-day variability and a clear clockwise rotation of the EVPAs during the γ-ray flare, which we associate with the path followed by the new superluminal component that moves along helical magnetic field lines. This is in agreement with theoretical models in which helical magnetic field are responsible for the jet formation, acceleration, and collimating (Blandford & Payne, 1982; Blandford & Znajek, 1977).

In both 3C 120 and CTA 102 the mm-VLBI core is located parsecs away from the black hole, at a distance of $\sim 10^4$-10^5 Schwarzschild radii, in agreement also with findings for other AGNs (Marscher et al., 2008, 2010; Chatterjee et al., 2011). The location of the γ-ray dissipation zone close to the mm-VLBI core in both sources, at such distances from the black hole that is difficult to have contributions of photons from the disk or the broad line region and probably also from the molecular torus, lead us to suggest the synchrotron self Compton (SSC) mechanism for the production of γ-ray photons in both sources. Also the SED, in the case of CTA 102, sustains the SSC mechanism, revealing also a different high energy spectrum for the bright γ-ray flare with respect to that of the "orphan flares".

Another consequence of locating the γ-ray emission in the mm-VLBI core, and far from the black hole, is that we need a mechanism to reaccelerate particles in situ, as for example happens in recollimation shocks. For this it is important to understand the nature of recollimation shocks and what could be the observational evidences associated to these shocks. For this purpose we have performed polarimetric studies of the jets in the radio galaxies 3C 120 (Agudo et al., 2012) and M 87 (Casadio et al., 2013); both aimed to understand the nature of the peculiar emitting regions C80 and HST-1, located hundreds of parsecs away from the core of the jet. With the improved sensitivity of our new polarimetric VLBA images of 3C 120, we analyzed in detail the observational properties of the emitting region at $\sim$80 mas from the core, whose detection was first reported in Roca-Sogorb et al. (2010). These authors suggest the possibility of a stationary shock at the location of C80 in order to explain the observed extreme properties, such as the unusually high brightness temperature. We discovered that C80 is the peak emission of a more extended structure whose upstream edge has an arc morphology (A80). The linearly polarized emission also follows this arc structure with polarization vectors distributed perpendicularly to the arc, as would be expected in the case of a shock front, where the magnetic field component parallel to

shock is compressed and amplified. This evidence, together with the high brightness temperature of C80 and the stationarity over time of C80/A80, while superluminal motions have been detected in the flow downstream C80/A80, supports the hypothesis of a recollimation shock. Moreover, the agreement between our findings and numerical simulations lead us to conclude that the emitting region C80 corresponds in fact to a recollimation shock located ∼190 pc from the core of the jet.

The situation observed in 3C 120 is very similar to what we have in the radio galaxy M 87 with its peculiar feature HST-1. In Giroletti et al. (2012) we observe that the extended emitting region named HST-1 is formed by superluminal subcomponents that seem to be released by the stationary upstream end of HST-1. This, and in the light of our findings for C80, lead us to suggest that HST-1 can also be associated with a recollimation shock. This implies that HST-1 may be the responsible for the high energy emission previously observed in M 87, although we rule out its implication in the TeV flare in March 2012 as we pointed out in Hada et al. (2014). In fact, between 2011 and 2013, HST-1 was found to be in a low flux state, confirmed also by our new VLBA and JVLA observations.

References

Abdo, A. A., Ackermann, M., Ajello, M., Allafort, A., Antolini, E., Atwood, W. B., Axelsson, M., Baldini, L., Ballet, J., Barbiellini, G., et al., 2010, ApJS, 188, 405 44

Abdo, A. A., Ackermann, M., Ajello, M., Allafort, A., Antolini, E., Atwood, W. B., Axelsson, M., Baldini, L., Ballet, J., Barbiellini, G., et al., 2010, The Astrophysical Journal, 715, 429, URL http://stacks.iop.org/0004-637X/715/i=1/a=429 44

Abdo, A. A., Ackermann, M., Ajello, M., Atwood, W. B., Axelsson, M., Baldini, L., Ballet, J., Band, D. L., Barbiellini, G., Bastieri, D., et al., 2009, ApJS, 183, 46 44

Acciari, V. A., Aliu, E., Arlen, T., Bautista, M., Beilicke, M., Benbow, W., Bradbury, S. M., Buckley, J. H., Bugaev, V., Butt, Y., et al., 2009, Science, 325, 444, 0908.0511 87, 90

Acero, F., Ackermann, M., Ajello, M., Albert, A., Atwood, W. B., Axelsson, M., Baldini, L., Ballet, J., Barbiellini, G., Bastieri, D., et al., 2015, ApJS, 218, 23 44

Ackermann, M., Ajello, M., Allafort, A., Antolini, E., Atwood, W. B., Axelsson, M., Baldini, L., Ballet, J., Barbiellini, G., Bastieri, D., et al., 2011, ApJ, 743, 171 44

Ackermann, M., Ajello, M., Atwood, W. B., Baldini, L., Ballet, J., Barbiellini, G., Bastieri, D., Becerra Gonzalez, J., Bellazzini, R., Bissaldi, E., et al., 2015, ApJ, 810, 14 44

Agudo, I., Gómez, J. L., Casadio, C., Cawthorne, T. V., & Roca-Sogorb, M., 2012, ApJ, 752, 92, 1203.2788 49, 52, 91, 92, 108, 119

Agudo, I., Gómez, J.-L., Martí, J.-M., Ibáñez, J.-M., Marscher, A. P., Alberdi, A., Aloy, M.-A., & Hardee, P. E., 2001, ApJ, 549, L183, astro-ph/0101188 103

Agudo, I., Jorstad, S. G., Marscher, A. P., Larionov, V. M., Gómez, J. L., Lähteenmäki, A., Gurwell, M., Smith, P. S., Wiesemeyer, H., Thum, C., et al., 2011, ApJ, 726, L13 32

Aleksić, J., Ansoldi, S., Antonelli, L. A., Antoranz, P., Babic, A., Bangale, P., Barres de Almeida, U., Barrio, J. A., Becerra González, J., Bednarek, W., et al., 2014, A&A, 569, A46, 1401.5646 85

Aloy, M.-Á., Martí, J.-M., Gómez, J.-L., Agudo, I., Müller, E., & Ibáñez, J.-M., 2003, ApJ, 585, L109 105

REFERENCES

Antonucci, R., 1993, ARA&A, 31, 473 8

Asada, K., & Nakamura, M., 2012, ApJ, 745, L28, 1110.1793 91, 114

Blandford, R. D., & Königl, A., 1979, ApJ, 232, 34 18, 23, 33

Blandford, R. D., & Levinson, A., 1995, ApJ, 441, 79 40

Blandford, R. D., & Payne, D. G., 1982, MNRAS, 199, 883 2, 33, 119

Blandford, R. D., & Rees, M. J., 1978, Phys. Scr, 17, 265 33

Blandford, R. D., & Znajek, R. L., 1977, MNRAS, 179, 433 2, 33, 119

Bonnoli, G., Tavecchio, F., Ghisellini, G., & Sbarrato, T., 2015, MNRAS, 451, 611 41

Bromberg, O., & Levinson, A., 2009, ApJ, 699, 1274, 0810.0562 90

Carnerero, M. I., Raiteri, C. M., Villata, M., Acosta-Pulido, J. A., D'Ammando, F., Smith, P. S., Larionov, V. M., Agudo, I., Arévalo, M. J., Arkharov, A. A., et al., 2015, MNRAS, 450, 2677, 1505.00916 86, 118

Casadio, C., Gómez, J. L., Giroletti, M., Giovannini, G., Hada, K., Fromm, C., Perucho, M., & Martí, J.-M., 2013, in *European Physical Journal Web of Conferences*, volume 61 of *European Physical Journal Web of Conferences*, p. 6004 106, 119

Casadio, C., Gómez, J. L., Grandi, P., Jorstad, S. G., Marscher, A. P., Lister, M. L., Kovalev, Y. Y., Savolainen, T., & Pushkarev, A. B., 2015a, ApJ, 808, 162 iii, vii, 32, 43, 53, 118

Casadio, C., Gómez, J. L., Jorstad, S. G., Marscher, A. P., Larionov, V. M., Smith, P. S., Gurwell, M. A., Lähteenmäki, A., Agudo, I., Molina, S. N., et al., 2015b, ApJ, 813, 51, 1508.07254 iii, vii, 43, 53, 118

Cawthorne, T. V., 2006, MNRAS, 367, 851 36, 92

Cawthorne, T. V., & Cobb, W. K., 1990, ApJ, 350, 536 36, 92

Chatterjee, R., Marscher, A. P., Jorstad, S. G., Markowitz, A., Rivers, E., Rothschild, R. E., McHardy, I. M., Aller, M. F., Aller, H. D., Lähteenmäki, A., et al., 2011, ApJ, 734, 43 32, 88, 119

Chatterjee, R., Marscher, A. P., Jorstad, S. G., Olmstead, A. R., McHardy, I. M., Aller, M. F., Aller, H. D., Lähteenmäki, A., Tornikoski, M., Hovatta, T., et al., 2009, ApJ, 704, 1689, 0909.2051 92

Cheung, C. C., Harris, D. E., & Stawarz, Ł., 2007, ApJ, 663, L65 32, 90, 91

Cohen, M. H., Meier, D. L., Arshakian, T. G., Homan, D. C., Hovatta, T., Kovalev, Y. Y., Lister, M. L., Pushkarev, A. B., Richards, J. L., & Savolainen, T., 2014, ApJ, 787, 151, 1404.0976 91

Dermer, C. D., Schlickeiser, R., & Mastichiadis, A., 1992, A&A, 256, L27 27

Donato, D., Ghisellini, G., Tagliaferri, G., & Fossati, G., 2001, A&A, 375, 739 27

Fanaroff, B. L., & Riley, J. M., 1974, MNRAS, 167, 31P 3

Fossati, G., Maraschi, L., Celotti, A., Comastri, A., & Ghisellini, G., 1998, MNRAS, 299, 433 27

Fromm, C. M., Perucho, M., Ros, E., Savolainen, T., & Zensus, J. A., 2015, A&A, 576, A43, 1412.1317 88

Gabuzda, D. C., Knuettel, S., & Reardon, B., 2015, MNRAS, 450, 2441, 1503.03411 23

Ghisellini, G. (ed.), 2013, *Radiative Processes in High Energy Astrophysics*, volume 873 of *Lecture Notes in Physics, Berlin Springer Verlag* 11, 14, 26

Ghisellini, G., Celotti, A., Fossati, G., Maraschi, L., & Comastri, A., 1998, MNRAS, 301, 451 27

Ghisellini, G., Tavecchio, F., Foschini, L., Ghirlanda, G., Maraschi, L., & Celotti, A., 2010, MNRAS, 402, 497 41

Giroletti, M., Hada, K., Giovannini, G., Casadio, C., Beilicke, M., Cesarini, A., Cheung, C. C., Doi, A., Krawczynski, H., Kino, M., et al., 2012, A&A, 538, L10 iv, vii, 32, 103, 104, 105, 109, 110, 114, 120

Gomez, J. L., Alberdi, A., & Marcaide, J. M., 1993, A&A, 274, 55 35

Gómez, J. L., Guirado, J. C., Agudo, I., Marscher, A. P., Alberdi, A., Marcaide, J. M., & Gabuzda, D. C., 2001a, MNRAS, 328, 873 32

Gómez, J. L., Lobanov, A. P., Bruni, G., Kovalev, Y. Y., Marscher, A. P., Jorstad, S. G., Mizuno, Y., Bach, U., Sokolovsky, K. V., Anderson, J. M., et al., 2016, ApJ, 817, 96, 1512.04690 115

Gómez, J.-L., Marscher, A. P., Alberdi, A., Jorstad, S. G., & Agudo, I., 2001b, ApJ, 561, L161 32, 92, 103

Gómez, J. L., Marscher, A. P., Alberdi, A., Jorstad, S. G., & Agudo, I., 2002, VLBA Scientific Memorandum No. 30 52

Gómez, J.-L., Marscher, A. P., Alberdi, A., Jorstad, S. G., & García-Miró, C., 2000, Science, 289, 2317 28

REFERENCES

Gómez, J.-L., Marscher, A. P., Alberdi, A., Martí, J. M., & Ibáñez, 1998, ApJ, 499, 221 32

Gómez, J. L., Marscher, A. P., Jorstad, S. G., Agudo, I., & Roca-Sogorb, M., 2008, ApJ, 681, L69 23

Gómez, J. L., Martí, J. M., Marscher, A. P., Ibáñez, J. M., & Alberdi, A., 1997, ApJ, 482, L33 37, 91, 105, 108

Gomez, J. L., Marti, J. M. A., Marscher, A. P., Ibanez, J. M. A., & Marcaide, J. M., 1995, ApJ, 449, L19 36, 37, 91, 105

Gómez, J. L., Roca-Sogorb, M., Agudo, I., Marscher, A. P., & Jorstad, S. G., 2011, ApJ, 733, 11, 1102.1943 92

Gracia, J., Vlahakis, N., Agudo, I., Tsinganos, K., & Bogovalov, S. V., 2009, ApJ, 695, 503, 0901.2634 90

Grandi, P., Torresi, E., & Stanghellini, C., 2012, ApJ, 751, L3 87

Hada, K., Doi, A., Kino, M., Nagai, H., Hagiwara, Y., & Kawaguchi, N., 2011, Nature, 477, 185 37, 88

Hada, K., Giroletti, M., Kino, M., Giovannini, G., D'Ammando, F., Cheung, C. C., Beilicke, M., Nagai, H., Doi, A., Akiyama, K., et al., 2014, ApJ, 788, 165, 1405.1082 iv, vii, 87, 88, 90, 109, 111, 120

Hada, K., Kino, M., Doi, A., Nagai, H., Honma, M., Akiyama, K., Tazaki, F., Lico, R., Giroletti, M., Giovannini, G., et al., 2016, ApJ, 817, 131, 1512.03783 115

Harris, D. E., Cheung, C. C., Biretta, J. A., Sparks, W. B., Junor, W., Perlman, E. S., & Wilson, A. S., 2006, ApJ, 640, 211, astro-ph/0511755 89

Högbom, J. A., 1974, A&AS, 15, 417 51

Homan, D. C., Attridge, J. M., & Wardle, J. F. C., 2001, ApJ, 556, 113 21

Homan, D. C., & Wardle, J. F. C., 1999, AJ, 118, 1942 21

Hughes, P. A., 1991, Journal of the British Astronomical Association, 101, 128 16, 17, 21

Hughes, P. A., Aller, H. D., & Aller, M. F., 1985, ApJ, 298, 301 36, 38

—, 1989, ApJ, 341, 54 35

Jorstad, S. G., Marscher, A. P., Lister, M. L., Stirling, A. M., Cawthorne, T. V., Gear, W. K., Gómez, J. L., Stevens, J. A., Smith, P. S., Forster, J. R., et al., 2005, AJ, 130, 1418 28, 32, 34, 42, 55, 103

Jorstad, S. G., Marscher, A. P., Mattox, J. R., Aller, M. F., Aller, H. D., Wehrle, A. E., & Bloom, S. D., 2001, ApJ, 556, 738 40, 53, 55

Jorstad, S. G., Marscher, A. P., Smith, P. S., Larionov, V. M., Agudo, I., Gurwell, M., Wehrle, A. E., Lähteenmäki, A., Nikolashvili, M. G., Schmidt, G. D., et al., 2013, ApJ, 773, 147 54, 85, 86

Jorstad, S. G., Marscher, A. P., Stevens, J. A., Smith, P. S., Forster, J. R., Gear, W. K., Cawthorne, T. V., Lister, M. L., Stirling, A. M., Gómez, J. L., et al., 2007, AJ, 134, 799 24, 37

Kellermann, K. I., 2013, Bulletin of the Astronomical Society of India, 41, 1 5

Kellermann, K. I., Sramek, R., Schmidt, M., Shaffer, D. B., & Green, R., 1989, AJ, 98, 1195 2

Konigl, A., 1981, ApJ, 243, 700 37

Leppanen, K. J., Zensus, J. A., & Diamond, P. J., 1995, AJ, 110, 2479 48

Lico, R., Giroletti, M., Orienti, M., Gómez, J. L., Casadio, C., D'Ammando, F., Blasi, M. G., Cotton, W., Edwards, P. G., Fuhrmann, L., et al., 2014, A&A, 571, A54, 1410.0884 86

Lister, M. L., Aller, M., Aller, H., Hovatta, T., Kellermann, K. I., Kovalev, Y. Y., Meyer, E. T., Pushkarev, A. B., Ros, E., MOJAVE Collaboration, et al., 2011, ApJ, 742, 27 54

Lister, M. L., Aller, M. F., Aller, H. D., Homan, D. C., Kellermann, K. I., Kovalev, Y. Y., Pushkarev, A. B., Richards, J. L., Ros, E., & Savolainen, T., 2013, AJ, 146, 120 28

Lister, M. L., Cohen, M. H., Homan, D. C., Kadler, M., Kellermann, K. I., Kovalev, Y. Y., Ros, E., Savolainen, T., & Zensus, J. A., 2009, AJ, 138, 1874 28, 54

Lobanov, A. P., 1998, A&A, 330, 79 37

Lyutikov, M., Pariev, V. I., & Gabuzda, D. C., 2005, MNRAS, 360, 869 23

Marscher, A. P., 2005, Mem. Soc. Astron. Italiana, 76, 13 40

—, 2009, ArXiv e-prints 35

—, 2014, ApJ, 780, 87 41

Marscher, A. P., & Gear, W. K., 1985, ApJ, 298, 114 36, 38

Marscher, A. P., Jorstad, S. G., Agudo, I., MacDonald, N. R., & Scott, T. L., 2012, ArXiv e-prints 55

REFERENCES

Marscher, A. P., Jorstad, S. G., Aller, M. F., McHardy, I., Balonek, T. J., Teräsranta, H., & Tosti, G., 2004, in *X-ray Timing 2003: Rossi and Beyond*, edited by P. Kaaret, F. K. Lamb, & J. H. Swank, volume 714 of *American Institute of Physics Conference Series*, pp. 167–173 55

Marscher, A. P., Jorstad, S. G., D'Arcangelo, F. D., Smith, P. S., Williams, G. G., Larionov, V. M., Oh, H., Olmstead, A. R., Aller, M. F., Aller, H. D., et al., 2008, Nature, 452, 966 32, 87, 88, 119

Marscher, A. P., Jorstad, S. G., Gómez, J.-L., Aller, M. F., Teräsranta, H., Lister, M. L., & Stirling, A. M., 2002, Nature, 417, 625 88, 92

Marscher, A. P., Jorstad, S. G., Larionov, V. M., Aller, M. F., Aller, H. D., Lähteenmäki, A., Agudo, I., Smith, P. S., Gurwell, M., Hagen-Thorn, V. A., et al., 2010, ApJ, 710, L126 27, 88, 119

Marti, J. M. A., Muller, E., Font, J. A., & Ibanez, J. M., 1995, ApJ, 448, L105 36

McKinney, J. C., & Blandford, R. D., 2009, MNRAS, 394, L126 34

Mittal, R., Porcas, R., Wucknitz, O., Biggs, A., & Browne, I., 2006, A&A, 447, 515 37

Morozova, D. A., Larionov, V. M., Troitsky, I. S., Jorstad, S. G., Marscher, A. P., Gómez, J. L., Blinov, D. A., Efimova, N. V., Hagen-Thorn, V. A., Hagen-Thorn, E. I., et al., 2014, AJ, 148, 42 85, 86

Nakamura, M., Garofalo, D., & Meier, D. L., 2010, ApJ, 721, 1783 114

Nalewajko, K., 2012, MNRAS, 420, L48, 1111.0018 90

Nolan, P. L., Abdo, A. A., Ackermann, M., Ajello, M., Allafort, A., Antolini, E., Atwood, W. B., Axelsson, M., Baldini, L., Ballet, J., et al., 2012, ApJS, 199, 31 44

Pacholczyk, A. G., 1970, *Radio astrophysics. Nonthermal processes in galactic and extragalactic sources* 11, 16, 18, 19, 20, 21

Perucho, M., Martí, J. M., Cela, J. M., Hanasz, M., de La Cruz, R., & Rubio, F., 2010, A&A, 519, A41, 1005.4332 103

Poutanen, J., & Stern, B., 2010, ApJ, 717, L118 55

Pushkarev, A., Lister, M., Kovalev, Y., & Savolainen, T., 2014, in *Proceedings of the 12th European VLBI Network Symposium and Users Meeting (EVN 2014). 7-10 October 2014. Cagliari, Italy.*, p. 104 54

Raiteri, C. M., Villata, M., D'Ammando, F., Larionov, V. M., Gurwell, M. A., Mirzaqulov, D. O., Smith, P. S., Acosta-Pulido, J. A., Agudo, I., Arévalo, M. J., et al., 2013, MNRAS, 436, 1530, 1309.1282 86, 118

Raiteri, C. M., Villata, M., Smith, P. S., Larionov, V. M., Acosta-Pulido, J. A., Aller, M. F., D'Ammando, F., Gurwell, M. A., Jorstad, S. G., Joshi, M., et al., 2012, A&A, 545, A48, 1207.3979 86, 118

Ramakrishnan, V., León-Tavares, J., Rastorgueva-Foi, E. A., Wiik, K., Jorstad, S. G., Marscher, A. P., Tornikoski, M., Agudo, I., Lähteenmäki, A., Valtaoja, E., et al., 2014, MNRAS, 445, 1636 32, 85

Readhead, A. C. S., Pearson, T. J., Cohen, M. H., Ewing, M. S., & Moffet, A. T., 1979, ApJ, 231, 299 33

Roca-Sogorb, M., Gómez, J. L., Agudo, I., Marscher, A. P., & Jorstad, S. G., 2010, ApJ, 712, L160, 0912.2192 91, 92, 119

Rybicki, G. B., & Lightman, A. P., 1979, *Radiative processes in astrophysics* 11, 12, 25, 26

Schmidt, M., 1970, ApJ, 162, 371 6

Schwab, F. R., & Cotton, W. D., 1983, AJ, 88, 688 50

Sikora, M., Begelman, M. C., & Rees, M. J., 1994, ApJ, 421, 153 27

Sikora, M., Stawarz, Ł., Moderski, R., Nalewajko, K., & Madejski, G. M., 2009, ApJ, 704, 38, 0904.1414 41

Sokolov, A., Marscher, A. P., & McHardy, I. M., 2004, ApJ, 613, 725 55

Stawarz, Ł., Aharonian, F., Kataoka, J., Ostrowski, M., Siemiginowska, A., & Sikora, M., 2006, MNRAS, 370, 981, astro-ph/0602220 90

Tavecchio, F., Becerra-Gonzalez, J., Ghisellini, G., Stamerra, A., Bonnoli, G., Foschini, L., & Maraschi, L., 2011, A&A, 534, A86 27, 41

Tavecchio, F., Ghisellini, G., Bonnoli, G., & Ghirlanda, G., 2010, MNRAS, 405, L94 41

Urry, C. M., & Padovani, P., 1995, PASP, 107, 803 8

Valtaoja, E., & Teraesranta, H., 1996, A&AS, 120, C491 53

Valtaoja, E., & Terasranta, H., 1995, A&A, 297, L13 53

Wagner, S. J., & Witzel, A., 1995, ARA&A, 33, 163 28

Walker, R. C., Benson, J. M., Unwin, S. C., Lystrup, M. B., Hunter, T. R., Pilbratt, G., & Hardee, P. E., 2001, ApJ, 556, 756, astro-ph/0103379 92

Wardle, J. F. C., 2013, in *European Physical Journal Web of Conferences*, volume 61 of *European Physical Journal Web of Conferences*, p. 6001 23

REFERENCES

Whitney, A. R., Shapiro, I. I., Rogers, A. E. E., Robertson, D. S., Knight, C. A., Clark, T. A., Goldstein, R. M., Marandino, G. E., & Vandenberg, N. R., 1971, Science, 173, 225 29

Williamson, K. E., Jorstad, S. G., Marscher, A. P., Larionov, V. M., Smith, P. S., Agudo, I., Arkharov, A. A., Blinov, D. A., Casadio, C., Efimova, N. V., et al., 2014, ApJ, 789, 135, 1406.2719 54

Zwicky, F., 1963, AJ, 68, 301 5

—, 1965, ApJ, 142, 1293 5